

ABSTRACT

Title of Document: Quantification of the Past and Future Anthropogenic Effect on Climate Change Using the Empirical Model of Global Climate, an Energy Balance Multiple Linear Regression Model

Austin Patrick Hope, Doctor of Philosophy, 2020

Directed by: Professor Ross J. Salawitch, Department of Atmospheric and Oceanic Science, Department of Chemistry and Biochemistry, Earth System Science Interdisciplinary Center

and

Assistant Professor Timothy P. Canty, Department of Atmospheric and Oceanic Science, Marine Estuarine Environmental Sciences program

The current episode of global warming is one of, if not the, biggest challenge to modern society as the world moves into the 21st century. Rising global temperatures due to anthropogenic emissions of greenhouse gases are causing sea level rise, extreme heat waves, droughts and floods, and other major social and economic disruptions. To prepare for and potentially reverse this warming trend, the causes of climate change must not only be understood, but thoroughly quantified so that we can attempt to make reasonable predictions of the future rise in global temperature and its associated consequences. The project described in this dissertation seeks to use a simple model of global climate, utilizing an energy balance and multiple linear regression approach, to provide a quantification of historical temperature trends and use that knowledge to provide probabilistic projections of future temperature. By considering many different greenhouse gas and aerosol emissions scenarios along with multiple possibilities for the role of the

ocean in the climate system and the extent of climate feedbacks, I have determined that there is a 50% probability of keeping global warming beneath 2 °C if society can keep future emissions on the pathway suggested by the RCP 4.5 scenario, which includes moderately ambitious emissions reductions policies, and a 67% probability of keeping global warming beneath 1.5 °C if society can keep emissions in line with the very ambitious RCP 2.6 scenario. These probabilities are higher, e.g. more optimistic, than similar probabilities for the same scenarios given by the most recent IPCC assessment report. Similarly, we find larger carbon budgets than those from GCM analyses for any warming limitation target and confidence level, e.g. the EM-GC predicts a total carbon budget of 710 GtC for limiting global warming to 1.5 °C with 95% confidence. The results from our simple climate model suggest that the difference in future temperatures is related to an overestimation of recent warming by the IPCC global climate models. We postulate that this difference is partially due to an overestimation of cloud feedback processes in the global climate models. Importantly, though, I also reaffirm the consensus that anthropogenic emissions are driving current warming trends, and discuss both the effects of shifting the energy sector toward increase methane emissions and the timeline we have for emitting the remainder of our carbon budget – less than a decade if we wish to prevent global warming from exceeding the 1.5 °C threshold with 95% certainty.

QUANTIFICATION OF THE PAST AND FUTURE ANTHROPOGENIC EFFECT ON
CLIMATE CHANGE USING THE EMPIRICAL MODEL OF GLOBAL CLIMATE,
AN ENERGY BALANCE MULTIPLE LINEAR REGRESSION MODEL

by

Austin Patrick Hope

Dissertation submitted to the Faculty of the Graduate School of the
University of Maryland, College Park, in partial fulfillment
of the requirements for the degree of
Doctor of Philosophy
2020

Advisory committee:

Professor Ross Salawitch, Co-Advisor

Assistant Professor Timothy Canty, Co-Advisor

Professor Russell R. Dickerson

Assistant Professor Jacob Wenegrat

Associate Professor Ronald A. Yaros, Dean's Representative

© Copyright by
Austin Patrick Hope
2020

Dedication

I dedicate this body of work to my late grandfather, Dr. Hans Rath, MD, May 1928 – June 2017, whose commitment to education was only surpassed by his love for his grandchildren. My Papa (and my grandma) helped see all six of us grandkids through undergrad, and not only did my grandparents learn to acknowledge anthropogenic climate change thanks to hearing about my body of work here, they have high hopes for what my, my sister's, and my cousins' generation can do to fix the problem climate that previous generations have left for us. I'll do my best, Papa.

Acknowledgements

I'd like to thank everyone who has supported me during my time at UMD. First, to my advisors Ross and Tim, who have taught me so much over the years and helped me grow as a scientist. Second, to Brian, Walt, Nora, and especially Laura, a.k.a. the other members in our little "climate club", for providing support over the years and directly or indirectly helping develop the EM-GC. Third, to all other professors and students of the AChem group within AOSC, for the sense of community and regular feedback you have provided. Next, to my TA friends for camaraderie and to the AOSC office staff for incredible clarity and aid. And last, but far from least, to my family, who have always given me plenty of love and support, both emotional and financial, throughout my time at UMD. In particular, my sister has had to live with me for all three years of my "last year" as a grad student, and my parents has served as beta readers for several large writing efforts from our "climate club" over the past five years. I can't thank you enough for everything, and I hope I've made you proud!

I also thank NASA for funding this work under the NASA Climate Indicators and Data Products for Future National Climate Assessments (INCA) program (award NNX16AG34G).

Table of Contents

Dedication	ii
Acknowledgements	iii
Table of Contents	iv
List of Figures	vi
List of Tables	x
Abbreviations and Acronyms	xi
1. Introduction	1
1.1. Basics of Climate	5
1.1.1. Radiative Forcing	5
1.1.2. The Greenhouse Effect	9
1.1.3. Other Considerations	15
1.2. Previous Modeling Efforts	20
1.2.1. History of GCMs	20
1.2.2. The Representative Concentration Pathways	24
1.2.3. Multiple Linear Regression Climate Models	27
1.3. Goals and Accomplishments	31
2. Advanced Physics and Chemistry of Climate	36
2.1. Radiative Forcing by Species	37
2.2. Human Fingerprints on Global Warming	46
2.2.1. The “Hockey Sticks”: Multiple Strong Recent Correlations	46
2.2.2. Carbon Dioxide (CO ₂)	49
2.2.3. Other GHGs	55
2.2.3.1. Methane (CH ₄)	55
2.2.3.2. Nitrous Oxide (N ₂ O)	60
2.2.3.3. Halogenated Gases	61
2.2.4. Anthropogenic Aerosols	62
2.2.5. Final Comments on Anthropogenic Fingerprints and the Evolution of RF Over Time	66
2.3. Nonlinearity & Uncertainty of the Climate System	69
2.3.1. Considerations for a Linear Model of a Nonlinear Climate	72
2.3.2. Uncertainty in Future Projections	78
3. Forecasting Global Warming	83
3.1. Introduction	83
3.2. Empirical Model of Global Climate	91
3.2.1. Formulation	93
3.2.1.1. Model Inputs	100

3.2.1.2. Model Outputs	111
3.2.2. The Degeneracy of Earth’s Climate	115
3.2.3. Equilibrium Climate Sensitivity	119
3.3. Attributable Anthropogenic Warming Rate	124
3.4. Global Warming Hiatus	135
3.5. Future Temperature Projections	139
3.6. Methods	152
4. Examining the Human Influence on Global Climate Using an Empirical Model	171
4.1. Introduction	171
4.1.1. Previous Estimates of AAWR	173
4.1.2. Prior Projections of Future Temperature	174
4.1.3. Overview of This Work	181
4.2. Model Construction	181
4.2.1. EM-GC Core Equations	182
4.2.1.1. Model Inputs, Natural Factors	189
4.2.1.2. Model Inputs, Anthropogenic Factors	195
4.2.2. EM-GC Ocean Components	205
4.2.3. Climate Feedback and Sensitivity	211
4.3. Results and Analysis	213
4.3.1. AAWR from the EM-GC	219
4.3.2. Comparison to Previous AAWR Estimates	223
4.3.3. Comparison to AAWR from GCMs	232
4.3.3.1. Extracting AAWR from GCMs	242
4.3.4. The Effects of Aerosols and Climate Feedback on Future ΔT	245
4.3.5. Other RCPs and Comparisons to Projections from GCMs	257
4.3.6. The effect of increased future emissions of CH ₄	265
4.3.7. Response to Cumulative Emissions	267
4.4. Conclusions	274
5. Conclusion and Future Research Opportunities	278
5.1. Summary of Work Presented	278
5.2. Potential Future Work	280
5.2.1. Altering the Spatial and Temporal Resolution of the EM-GC	281
5.2.1.1. Other Ocean Temporal and Spatial Issues to Examine	283
5.2.2. Climate Relationships to Examine	286
5.2.3. Public Modeling	288
5.3. Final Comment	289
Bibliography	290

List of Figures

Ch1

Figure 1.1 – GMST vs Δ RF; Anthropocene	8
Figure 1.2 – Schematic of Earth’s Energy Balance	10
Figure 1.3 – GMST vs CO ₂ ; Deep Time	13
Figure 1.4 – Component Development of GCMs	22

Ch2

Figure 2.1 – Radiation Transmitted by the Atmosphere	39
Figure 2.2 – Total Δ RF of Climate by Anthropogenic Species	43
Figure 2.3 – Δ RF of Climate by Anthropogenic Species; Anthropocene	44
Figure 2.4 – GMST, GHGs, and Population; Common Era	47
Figure 2.5 – CO ₂ Yearly Emissions Rate vs Hemispheric Gradient	50
Figure 2.6 – Atmospheric Chemistry Fingerprints of Anthropogenic Activity	51
Figure 2.7 – Global Methane Budget, 2000 to 2009	56
Figure 2.8 – CO ₂ Emissions by Source; Anthropocene	68
Figure 2.9 – Comparison of GHG RF vs Aerosol RF Uncertainty	71
Figure 2.10 – The Ice-Albedo Feedback in CERES Data	75
Figure 2.11 – Rate of Temperature Change on Different Timescales	81

Ch3

Figure 3.1 – GHG abundance, 1950 to 2100	86
Figure 3.2 – RF of Climate Due to GHGs, 1950 to 2100	87

Figure 3.3 – Observed and GCM Simulated Global Warming, 1960 to 2060	90
Figure 3.4 – Observed and EM-GC Simulated Global Warming, 1860 to 2015, Without Ocean Oscillations	97
Figure 3.5 – Observed and EM-GC Simulated Global Warming, 1860 to 2015, With Ocean Oscillations	98
Figure 3.6 – Aerosol Δ RF Versus Time by Species, RCP 4.5, for AER RF ₂₀₁₁ = -0.9 W/m^2	101
Figure 3.7 – Aerosol Δ RF Versus Time, RCP 4.5 and 8.5, Various AER RF ₂₀₁₁ Scenarios	102
Figure 3.8 – Ocean Heat Content (OHC) Versus Time	110
Figure 3.9 – Observed and EM-GC Simulated Global Warming, 1860 to 2060, for Various AER Δ RF ₂₀₁₁ Scenarios	116
Figure 3.10 – Observed and EM-GC Simulated Global Warming, 1860 to 2060, for Various OHC Records	120
Figure 3.11 – Equilibrium Climate Sensitivity (ECS) from the Literature and EM-GC Simulations	122
Figure 3.12 – Sensitivity of Attributable Anthropogenic Warming Rate (AAWR) due to Δ RF of Aerosols	127
Figure 3.13 – Comparison of AAWR from the EM-GC and CMIP5 GCMs	128
Figure 3.14 – Observed and EM-GC Simulated Global Warming, 1995 to 2016	136
Figure 3.15 – Projected Rise in GMST, year 2060	140

Figure 3.16 – Projected Rise in GMST, year 2100	141
Figure 3.17 – Probability Distribution Functions of Rise in GMST, year 2060	144
Figure 3.18 – Probability Distribution Functions of Rise in GMST, year 2100	145
Figure 3.19 – Global Warming Projections, RCP 4.5	148
Figure 3.20 – Global Warming Projections, RCP 8.5	149
Figure 3.21 – Aerosol Indirect Effect Scaling Parameters	164
Ch4	
Figure 4.1 – Greenhouse gas abundances, 1950 to 2100, from the RCP scenarios	176
Figure 4.2 – Observed and GCM-Simulated Global Warming, 1970 to 2060	179
Figure 4.3 – Observed and EM-GC-Modeled ΔT , 1850 to 2019	186
Figure 4.4 – Ocean Heat Content (OHC) Records	187
Figure 4.5 – Blended Methane Scenarios	198
Figure 4.6 – Example Time Series of Total Aerosol ΔRF by Species	201
Figure 4.7 – Aerosol “Roads” Scaling Procedure	204
Figure 4.8 – Ocean Warming Profiles, CMIP5 (normalized) vs EM-GC (simplified)208	
Figure 4.9 – Measured and Modeled Global Temperature Anomaly: Fallacy of the Residual Method	215-6
Figure 4.10 – AAWR and ΔT_{2100} as a function of AER RF_{2011} and λ_{Σ}	217
Figure 4.11 – Probability Density Functions of AAWR and ΔT_{2100} , RCP 4.5	218
Figure 4.12 – AAWR as a Function of AER RF_{2011} , λ_{Σ} , and AER “Road”	229
Figure 4.13 – Observed and Modeled ΔT , 1850 to 2100, Varying AER ΔRF_{2011}	230

Figure 4.14 – Comparison of Values of AAWR, EM-GC vs CMIP5 GCMs	234
Figure 4.15 – Observed and Modeled ΔT , 1850 to 2100, Varying AER “Road” and ΔT_{OBS}	235
Figure 4.16 – AAWR from GCMs, Found Using Linear Fit and Regression	236
Figure 4.17 – Box-and-Whisker Plots of AAWR from GCMs	237
Figure 4.18 – AAWR from 41 GCMs (RCP 4.5) compared to empirical AAWR	244
Figure 4.19 – Global Warming Projections for RCP 4.5, 1950 to 2100	249
Figure 4.20 – EM-GC Temperature Comparisons for Time-Varying $1/\lambda$	252
Figure 4.21 – ΔT_{2100} as a function of AER RF_{2011} and λ_{Σ} , RCP 2.6 and 8.5	259
Figure 4.22 – Probability Density Functions of ΔT_{2100} , RCP 2.6 and 8.5	260
Figure 4.23 – Global Warming Projections for Various RCPs, 1950 to 2100	263
Figure 4.24 – Impact of CH_4 on EM-GC Projections	266
Figure 4.25 – ΔT as a Function of CO_2 Emissions, Ensemble Medians	268
Figure 4.26 – ΔT as a Function of CO_2 Emissions, RCP 8.5	269

List of tables

Ch3

Table 3.1 – Cumulative Probability of the Rise in ΔT Below a Specific Value, 2060 and 2100	146
Table 3.2 – Names of the 42 CMIP5 GCMs used in Fig. 3.3	156
Table 3.3 – AAWR from GCM RCP 4.5 Simulations in the CMIP5 Archive	157-60

Ch4

Table 4.1 – Natural Factor Input Sources	190
Table 4.2 – Anthropogenic Factor Input Sources	197
Table 4.3 – Comparison of Simulated Ocean Warming Profiles	210
Table 4.4 – Variation of AAWR Based on Start and End Year	224
Table 4.5 – ΔT_{2100} and $1/\lambda_{FINAL}$ as $1/\lambda$ Varies.	253
Table 4.6 – Carbon Budget Comparisons	270
Table 4.7 – Metrics for Future Carbon Budgets Leading to Crossing the Pairs Thresholds	273

Abbreviations and Acronyms

ΔT	Change in GMST from preindustrial (baseline 1850-1900)
AER RF	Change in RF due to Aerosols from preindustrial (1750)
AMO	Atlantic Multidecadal Oscillation
AMOC	Atlantic Meridional Overturning Circulation
AMV	Atlantic Multidecadal Variability
AR4	Working Group I Contribution to the IPCC 4 th Assessment Report
AR5	Working Group I Contribution to the IPCC 5 th Assessment Report
BW	Box-and-Whisker Plot
CERES	Clouds and the Earth's Radiant Energy System
CMIP5	Phase 5 of the Climate Model Intercomparison Project
EM-GC	Empirical Model of Global Climate
ENSO	El Niño – Southern Oscillation
ERF	Effective Radiative Forcing
GCM	Global Climate Model
GHG	Greenhouse Gas
GMST	Global Mean Surface Temperature
IO(D)	Indian Ocean Dipole
IPCC	Intergovernmental Panel on Climate Change
IR	Infrared (wavelengths, radiation, etc.)
LUC	Land Use Change
MLR	Multiple Linear Regression

OHC	Ocean Heat Content
OHE	Ocean Heat Export
PDO	Pacific Decadal Oscillation
PICR	Potsdam Institute for Climate Research
RCP	Representative Concentration Pathway
RF	Radiative Forcing (units: W/m ²)
S(A)OD	Stratospheric Aerosol Optical Depth
SSP	Shared Socioeconomic Pathway
SWV	Stratospheric Water Vapor
TCRE	Transient Climate Response to cumulative carbon Emissions
TSI	Total Solar Irradiance
UNFCCC	United Nations Framework Convention on Climate Change

Chapter 1: Introduction

Understanding Earth's climate, particularly the warming of atmospheric temperature at Earth's surface, is not only an important and highly active field of study, but an important social and political issue in modern society. It is a complex issue in all three of these areas, (academia, society, and policy,) even if the scientific community has reached a general consensus on the cause and general trend of recent global warming and is now to the point of refining our understanding of the climate system. Earth's climate is dynamic and complex because it integrates many factors – continental geography, the biologic and geologic carbon cycle, atmospheric and oceanic flow patterns, cloud cover and microphysics, aerosol and ozone chemistry, and even the color and texture of Earth's surface. This complexity has allowed many different methods of analyzing the climate system to arise.

At the most fundamental level, Earth's climate system works to correct energy imbalances at multiple scales: between hot and cold air masses, between the equator and the poles, or between incoming and outgoing radiation. Earth's overall energy balance, at zeroth order, concerns this third balance between the amount of incoming solar shortwave radiation and the amount of outgoing thermal and reflected radiation. Incoming radiation is a function of Earth's orbit around the Sun, (dominated by the sun's output and by orbital patterns known as the Milankovitch cycles,) and outgoing thermal radiation is a function of Earth's effective temperature as seen from space. Then, at first order, Earth's Global Mean Surface Temperature (GMST) has risen and fallen over geologic history in parallel with changes in the strength of the greenhouse effect and of surface albedo. These changes both alter the relationship between Earth's effective

temperature as seen from space and the temperature that life on Earth experiences at Earth's surface. Second and third order effects such as regional geography, the large-scale atmospheric circulation cells, and smaller-scale atmospheric waves and eddies then dictate weather patterns and local climate, which also affect variations in surface temperature at human-scale locations and time [*Wolff et al.*, 2020].

Multiple aspects of modern society respond to changes in surface temperatures at various spatial and temporal scales. While hour-by-hour local temperatures (and precipitation chances) affect how we dress and what we do on any given day, seasonal regional temperature and precipitation patterns affect crucial societal needs like agricultural production and water supply. These seasonal and regional patterns also affect critical natural phenomena like arctic sea ice cover [*Richter-Menge et al.*, 2019] and extreme weather events [*Herring et al.*, 2020]. Long-term GMST trends affect these seasonal, regional temperature and precipitation patterns enough to confidently and accurately predict these mid-scale patterns based on those large-scale trends. As such, it is reasonable and expected that we as a society have invested heavily in meteorology and climatology in order to understand and plan for any changes we might see in the future, whether it be a few days or a few decades in advance.

As surface temperatures affect human activity, so too can human activity affect surface temperatures. Agriculture, mining, and urban sprawl are significant ways in which humans have left obvious marks on Earth's surface. Multiple changes in Earth's atmospheric composition have also been observed, the most noticeable of which being a rapid rise in carbon dioxide (CO₂). The rise in CO₂ can be attributed to the rise of energy production driven by fossil fuel combustion, a consequence of worldwide

industrialization. Expected continued industrialization into the future would thus imply a continued rapid rise in CO₂ and other greenhouse gases (GHGs), leading to a large expected rise in GMST, unless the world can make a rapid switch to renewable forms of energy. While the link between GHGs and rising temperature has been well-established, the extent of future warming remains an open question.

Meteorological models have seen great advances in becoming fairly accurate and precise for the upcoming few days out to a week, but climate models have arguably been less well-constrained in their predictions. As stated in the IPCC Fifth Assessment Report [*Stocker et al.*, 2013] (hereafter **AR5**), the Global Climate Models (GCMs) used in Phase 5 of the Climate Model Intercomparison Project (CMIP5) [*K Taylor et al.*, 2012] show a wide range of predicted end-of-century transient temperatures even when using the same emissions scenario; this range becomes much wider when sampling across multiple different emission scenarios. The four Representative Concentration Pathway (RCP) scenarios, a subset of the scenarios ran in CMIP5, produce temperatures above the preindustrial baseline ranging from 0.3 to 1.7 °C (mean of roughly 1.0 °C) for the least-warming scenario and 2.8 to 5.0 °C (mean of roughly 4.1 °C) for the most-warming scenario. Equilibrium Climate Sensitivity (ECS), another metric of future climate defined as the temperature Earth reaches to equalize the energy imbalanced caused by CO₂ reaching levels twice their preindustrial value, shows a similar wide range of uncertainty: **AR5**'s "likely" range for ECS is 1.5 to 4.5 °C. A widely publicized recent paper suggests a more constrained likely range of 2.6 to 3.9 °C [*Sherwood et al.*, 2020].

There are other models and analytical methods that can be used to examine past and future climate. Reconstructions of atmospheric temperature and composition in

prehistoric and geologic time come from physical and chemical analyses of long-term proxies such as tree rings, ice and sediment cores, and coral reefs. Some scientists use these reconstructions to estimate ECS [Köhler *et al.*, 2010; Rohling *et al.*, 2012; Schmittner *et al.*, 2011], though the validity of using paleoclimate data to predict the future has been questioned [Friedrich *et al.*, 2016; Hopcroft and Valdes, 2015; Köhler *et al.*, 2015]. ECS and other estimates of future GMST can also come from models of low- and moderate-complexity, in contrast to the computationally intensive GCMs. These models can range from essentially single-equation calculations based solely on CO₂ [X Zeng and Geil, 2016] to multiple linear regression (MLR) models of varying complexity [Canty *et al.*, 2013; Chylek *et al.*, 2016; Lean and Rind, 2008] to the Integrated Assessment Models [Hartin *et al.*, 2015; Meinshausen *et al.*, 2008] and impulse response models [Myhre *et al.*, 2013; C J Smith *et al.*, 2018] that represent a range of physical processes.

The body of work presented here describes the advancement of and results from the Empirical Model of Global Climate (EM-GC), an energy balance model with MLR first constructed in 2012 at the University of Maryland [Canty *et al.*, 2013]. Research completed using the EM-GC is conducted to advance our understanding of the interplay between major components of Earth's climate system as it experiences global warming, and to produce a reliable projection of future GMST. These concepts can help to better inform global warming policy moving forward as well as provide quantitative evaluations of certain aspects of past and future GCM results. The remainder of this first chapter consists of a description of the basic physics and chemistry behind climate change (§1.1),

followed by a general history of climate modeling efforts (§1.2), and finally a more thorough listing of this project's goals and accomplishments to date (§1.3).

1.1 Basics of Climate

1.1.1 Radiative Forcing

Radiative forcing (RF) is defined by **AR5** as “a measure of the net change in the energy balance of the Earth system in response to some external perturbation”. It has units of W/m^2 , and is usually discussed in terms of a net change in energy balance acting at the tropopause [*Gregory et al.*, 2004]. In this system, positive value for RF signifies an energy imbbalance across the tropopause, with more energy entering the troposphere (and, by extension, the hydrosphere) than going out. Such an imbalance leads to a buildup of energy in these components of the Earth system that translates to an increase surface temperature. There are many potential “external perturbations” that can produce an RF effect on the climate system, either for the troposphere or for the whole Earth system. The most external of all potential perturbations would be astronomical changes such as varying solar energy output and shifts in Earth's orbit, but these astronomical changes are slow and small enough that the Earth system remains essentially in equilibrium, i.e. the RF at the top of the atmosphere remain ~ 0 at timescales applicable to modern society. As such, most climate science focuses on RF at the tropopause due to changes of the Earth's surface and atmosphere.

In the absence of an atmosphere, GMST would be determined solely by the balance between the amount of energy from the sun intercepted by the disc profile of Earth:

$$E_{in} = (1 - A)S(\pi R_E^2)$$

Eq 1.1

and the amount of energy emitted from Earth's total surface area:

$$E_{out} = \sigma T^4(4\pi R_E^2)$$

Eq 1.2

In the above equations, Earth is approximated as a perfect sphere with radius R_E , total albedo A , and mean surface temperature T . The quantity S is the measure of solar insolation at the distance of Earth's orbital radius, roughly 1370 W/m^2 , some of which gets reflected by Earth's total albedo (a combination of cloud reflectivity and surface albedo). Finally, σ is the Stefan-Boltzmann constant ($5.67 \times 10^{-8} \text{ W/m}^2/\text{K}^4$) used in calculating the relationship between the effective temperature and energy output of a radiating blackbody. Earth's albedo is roughly 0.3, implying an effective GMST of roughly 255 K, which can be reached by equating E_{in} and E_{out} in the above two equations.

The GMST at present is significantly warmer than 255 K, as most of the planet is well above the temperature where water freezes (273 K) instead of well below that temperature. This discrepancy is a result of a large positive RF on climate due to our atmosphere, relative to a planet whose energy balance is solely determined by its star, orbit, and albedo. Applying a positive RF to the climate system increases E_{in} at the surface by re-radiating energy that should be leaving the system, effectively lowering E_{out} . This forces GMST to increase until Earth's effective T is high enough that E_{out} once again balances E_{in} . This relationship between an object's temperature and energy output, while officially quartic (T^4 in Eq 1.2), can be approximated linearly around its current energy state. Relatively small changes in RF imply similarly small changes in T , and vice

versa. By assuming that T is relatively constant so that E_{out} varies roughly linearly as a function of T for nearby values of T, we can differentiate Eq 1.2 to give

$$\Delta \left(\frac{E_{out}}{a_E} \right) = (4\sigma T^3) \Delta T$$

Eq 1.3a

$$\Delta RF \approx c \Delta T$$

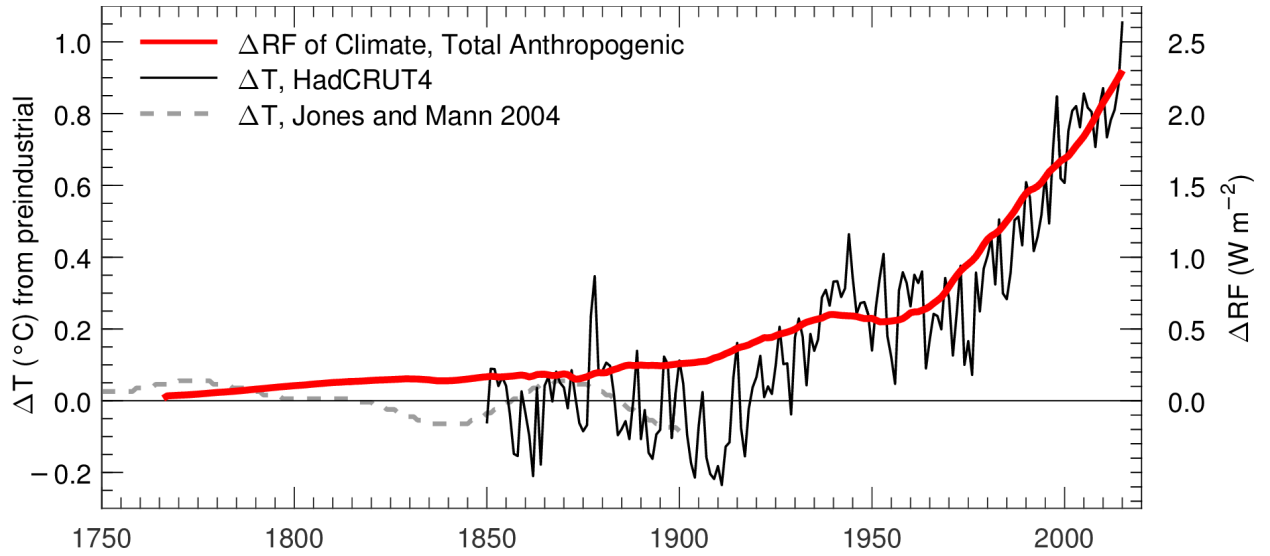
Eq 1.3b

Here, both sides of Eq 1.2 were divided by the surface area of Earth ($a_E = \pi R_E^2$) before taking the derivative, which was done to demonstrate the physical description of RF as being Watts (energy) per square meter (area).

This approximation of direct proportionality in Eq1.3b works well in comparing RF against T for Earth's recent history. Figure 1.3b of *Salawitch et al.* [2017], reproduced here as figure 1.1, demonstrates the parallel rises in the change in RF since preindustrial times due to the total of anthropogenic influences and in the change in GMST over the same century and a half. Equation 1.3b is, of course, a simplification of the Earth climate system. Specifically, taking the final values of the ΔRF and ΔT lines from figure 1.1 – roughly 2.3 W/m² and 0.9 °C, respectively – would give a value for c of roughly 2.56 W/m²/K. In comparison, *Bony et al.* [2006] and *Salawitch et al.* [2017] would suggest a value of 3.23 W/m²/K. Directly calculating $4\sigma T^3$ with a temperature of either 255 K (the albedo-only equilibrium GMST mentioned above) or 245 K (an approximation for the actual effective temperature of Earth's atmosphere as seen from space ¹) would suggest

¹ We can create a simple model of effective temperature a surface and an atmospheric layer, and assume that the atmosphere absorbs ~ 10% of the incoming solar energy that would otherwise reach the surface and ~80% of the outgoing thermal energy leaving the surface that would otherwise go to space. This two-equation, two-unknowns system with known S and A allows us to solve for the energy emitted by the surface and by the atmosphere itself, in turn determining $T_{ATM}=245$ K and $T_{SFC}=277$ K.

Figure 1.1 – GMST vs ΔRF ; Anthropocene



Reproduction of *Salawitch et al.* [2017] Figure 1.3b comparing the change in Earth's global mean surface temperature (ΔT , two different records) to the change in radiative forcing (ΔRF) over the past century and a half, commonly referred to as the Anthropocene.

values of $3.76 \text{ W/m}^2/\text{K}$ or $3.36 \text{ W/m}^2/\text{K}$, respectively. This variance though is typical of the kinds of uncertainty seen in GMST warming projections and is proof that the Earth climate system is much more complex than Eq 1.3b alone suggests. (For example, **AR5** states that the expected equilibrium rise in GMST due to a doubling of atmospheric CO_2 is anywhere from $2 \text{ }^\circ\text{C}$ to $4.5 \text{ }^\circ\text{C}$.) Still, this zeroth-order energy balance basis is a core feature of many climate models, which seek to quantify the complexity and nonlinearity of Earth's climate.

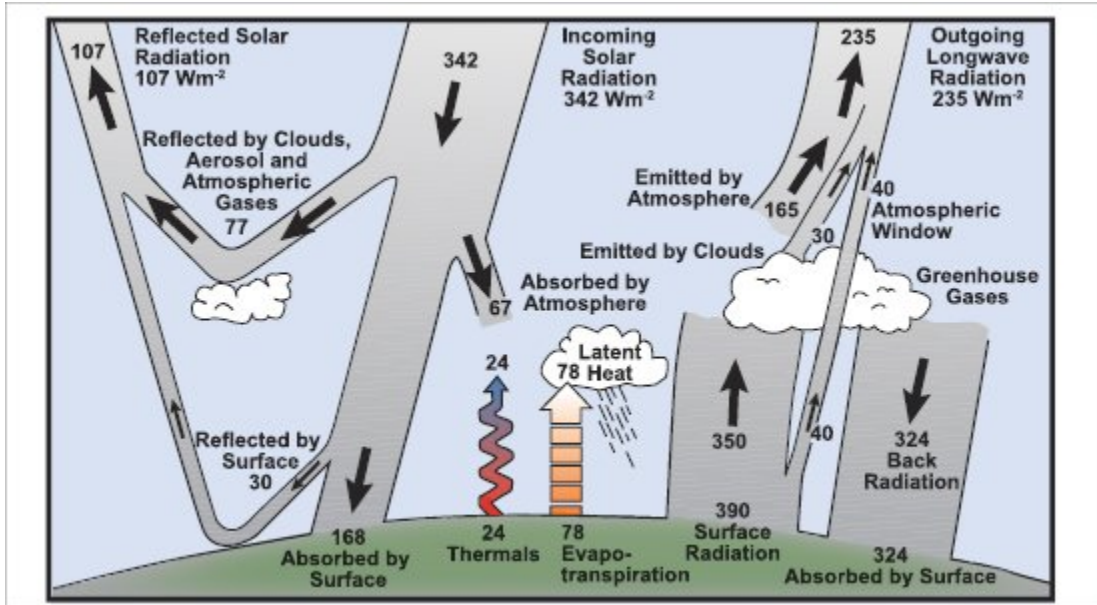
1.1.2 The Greenhouse Effect

The “greenhouse effect” is the term for the warming caused by the increase in RF from Earth's atmosphere. Many gases in our planet's atmosphere absorb thermal radiation from the Earth's surface and re-radiate that energy in all directions, including back down to the surface. This back-radiation provides the increase in RF that allows our planet to be significantly warmer, on average, than the 255K expected without an atmosphere.² The gases that provide this back-radiation are collectively known as greenhouse gases (GHGs).

A general schematic of how the greenhouse effect works can be seen in figure 7 of Kiehl & Trenberth [1997], reproduced here as figure 1.2. At the top of the atmosphere, Earth receives roughly 342 W/m^2 for each square meter of its surface (one-fourth of the 1370 W/m^2 received from the sun at Earth's orbital radius, accounting for spherical geometry). This incoming 342 W/m^2 is balanced by the total reflected solar radiation (107 W/m^2) and outgoing longwave radiation (235 W/m^2). Due to the back radiation of

² “Without an atmosphere” is of course a simplification itself, as an atmosphere-less Earth would also be missing the clouds and greenery that greatly affect albedo. For simplicity, the various components of the Earth system are treated as independent factors in this section.

Figure 1.2 – Schematic of Earth’s Energy Balance



Reproduction of *Kiehl & Trenberth* [1997] Figure 7 depicting a general summary of the flow & balance of energy in Earth’s atmosphere; color version retrieved from https://archive.ipcc.ch/publications_and_data/ar4/wg1/en/faq-1-1.html .

the atmosphere, though, the Earth's surface experiences a balance of 492 W/m^2 between absorbed radiation and the energy released through thermals, evapotranspiration, and surface radiation. This difference is why observed GMST ($287\text{-}8 \text{ K}$)³ is warmer than Earth's effective temperature as seen from space (255 K).

Global warming occurs when the strength of the greenhouse effect is increased. Over the past century and a half, this increase has been driven by anthropogenic activities, most notably the continuous and increasing emission of carbon dioxide (CO_2) due to the burning of fossil fuels, though other anthropogenic GHGs have also contributed noticeably to the greenhouse effect. As the atmospheric mixing ratio of GHGs increases, the equilibrium between radiation leaving the Earth's surface and energy coming back down is perturbed in favor of having more energy coming down than going up. Earth's surface then warms until the point that the thermal radiation leaving Earth's surface increases enough to re-establish equilibrium.

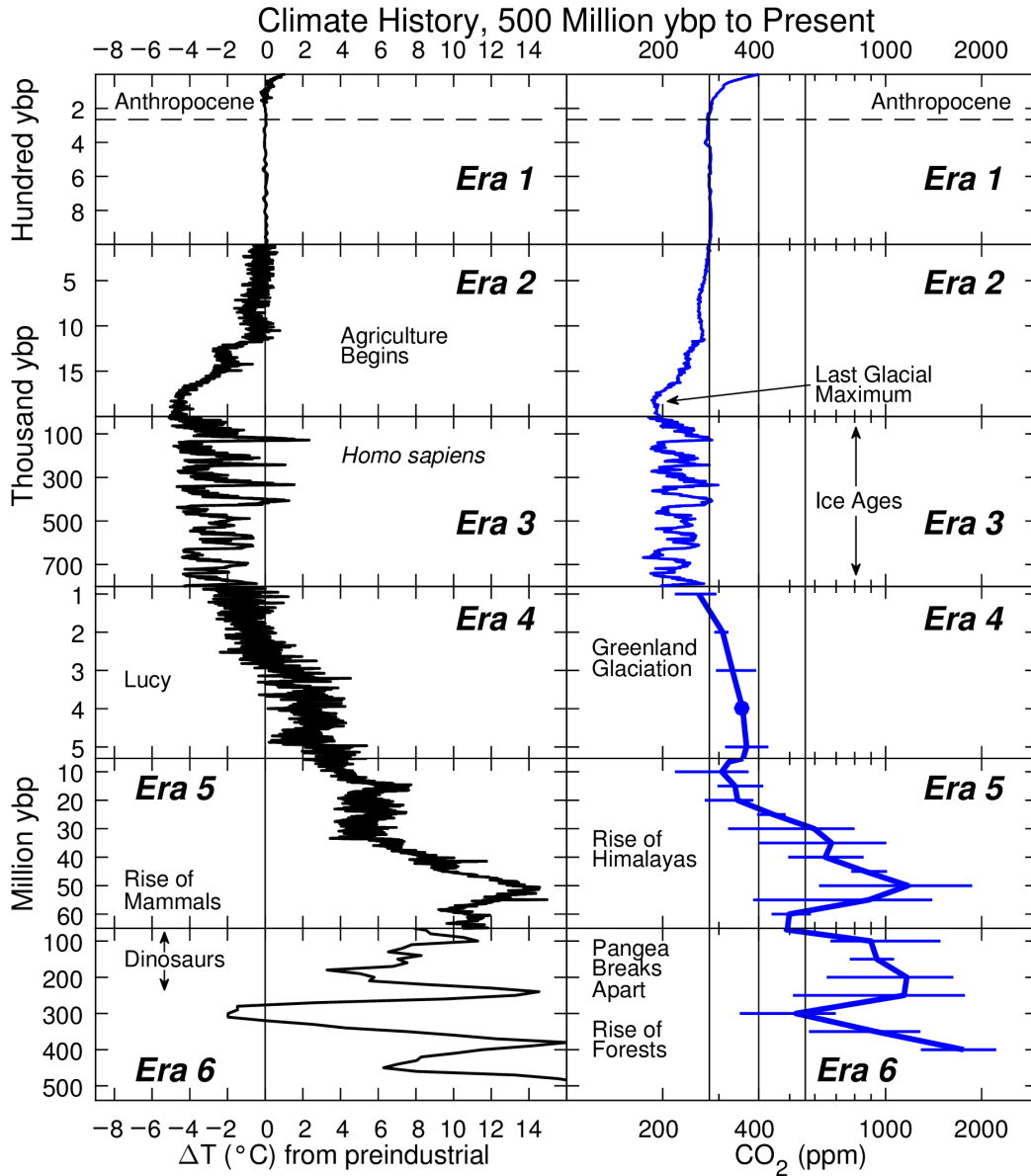
Humans are currently emitting CO_2 and other GHGs at such a rapid rate that Earth is not in radiative equilibrium. *Trenberth et al.* [2009] provide an update to figure 1.2 for the years 2000-2004, in which the Earth system was absorbing a net 0.9 W/m^2 instead of having a true balance between outgoing and incoming energy. Accounting for disequilibrium is one of the first-order changes that can be applied to Eq 1.3b, and is usually represented by energy leaving the atmosphere and entering the oceans [*Gregory*, 2000; *Schwartz et al.*, 2014]. Water has a much higher heat capacity than air, and there is much more mass of water in the oceans than mass of air in the atmosphere. These facts

³ Earth's current temperature, in a deterministic sense, is commonly cited as being $14\text{-}15 \text{ }^\circ\text{C}$. This is an estimate as quantification of Earth's immediate temperature is complicated and difficult, and it is warmer than the 277 K , or $4 \text{ }^\circ\text{C}$, mentioned earlier as the two-component model is highly simplified, likely not taking into account the complexities of the climate system that determine the actual current temperature.

considered together mean that the oceans take much longer to warm than the atmosphere immediately above. This temperature difference allows for heat to leave the warming atmosphere [Raper *et al.*, 2002] until oceans warm enough to also be in equilibrium with the atmospheric changes in RF. The exact delay to equilibrium is unknown but is thought to take centuries to millennia based on estimates of deep ocean circulation [Li *et al.*, 2013; Raper *et al.*, 2002], meaning the warming effects of fossil fuel burning will continue long after humans manage to stabilize atmospheric CO₂. It is important to make the distinction that reducing emissions to zero would cause a reduction in atmospheric CO₂ levels, not just a stabilization, and would neutralize and potentially reverse warming trends [MacDougall *et al.*, 2020].

The correlation between atmospheric CO₂ and GMST is not unique to the recent past – it exists deep into Earth’s geologic history, as can be seen in figure 1.1 of Salawitch *et al.* [2017], reproduced here as figure 1.3. The rates of change in CO₂ in the past were (to current resolution) slow enough that it is assumed that Earth remained close to equilibrium for most of its geologic past [Zeebe, 2012], with only a few instances of relatively rapid CO₂ change – which are often associated with major extinction events [Burgess *et al.*, 2014; Jourdan *et al.*, 2014; Penman *et al.*, 2014]. Even these geologically rapid changes occurred on the order of tens to hundreds of thousands of years, which is a noticeable difference from the current situation where the atmospheric mixing ratio is increasing at several parts per million (ppm) per year, expected to double from preindustrial levels on a timescale of just centuries.

Figure 1.3 – GMST vs CO₂; Deep Time



Reproduction of *Salawitch et al.* [2017] Figure 1.1 comparing the change in Earth's global mean surface temperature (ΔT) to the mixing ratio of carbon dioxide over geologic time, with uncertainty estimates included for CO₂ mixing ratio.

There is some debate as to whether rising CO₂ level caused previous global warming or vice versa. Examination of the glacial-interglacial cycle over the past million years is complicated due to a natural lag between the age of ice and the age of the air trapped in bubbles within the ice cores being studied [Loulergue *et al.*, 2007]. Further, the time it takes for air bubbles to become separated from the atmosphere above them is on the same order or magnitude as the time resolution available. As such, even when taking into account the diffusion of air in the compacting upper snow layers of an ice sheet, consensus is difficult to reach on near-synchronous events in the ice core record such as observed rises in temperature and CO₂. While there is little suggestion that large increases CO₂ noticeably precedes the onset of warming in major deglaciation events, there are some arguments that these rises are synchronous within resolution or at least have varied relative to each other over the glacial record [Parrenin *et al.*, 2013; Van Nes *et al.*, 2015] and other arguments suggesting that the warming consistently but barely begins shortly before a growth in CO₂ [Marcott *et al.*, 2014; Shakun *et al.*, 2012; Stips *et al.*, 2016; Toggweiler and Lea, 2010]. Even in these latter cases, while CO₂ lags the initialization of deglaciation, presumably caused by eccentricity in Earth's orbit, it then also amplifies the final extent of the deglaciation warming processes, showing the effect of CO₂ as a GHG; this process seem to happen with a hemispheric bias in this division of effects, as warming primarily in the southern hemisphere leads to CO₂ outgassing from the oceans, which then leads to advanced warming in the northern hemisphere. Either way, Earth's orbital cycles currently imply a slow return toward glaciation; instead, there are multiple lines of evidence linking the *current* rise in CO₂ to human activities (§2.2)

thus confidently showing the current episode of global warming to be an effect, not a cause, of rising GHGs in the atmosphere.

1.1.3 Other Considerations

Other anthropogenic and natural effects (i.e. aside from GHGs) apply direct or effective RF to Earth's climate system on timescales relevant to modern society, in addition to the ocean heat sink mentioned in the previous section. The other two major sources of anthropogenic RF on climate are the aerosols society emits, which have both direct and indirect effects on climate with large uncertainty on both, and alterations to Earth's albedo due to land use change (LUC). Natural sources of RF on climate (at human timescales) include the occasional volcanic eruptions that affect stratospheric aerosol optical depth (SAOD), slight changes in solar energy output associated with the eleven-year sunspot cycle (total solar irradiance, TSI), the global repercussions of the Pacific El Niño-Southern Oscillation pattern (ENSO), and middle-term variations in the atmosphere-ocean heat exchange in various ocean basins (e.g. the Atlantic Multidecadal Variation, AMV, the Pacific Decadal Oscillation, PDO, or the Indian Ocean Dipole, IOD). Quick, general qualitative descriptions of these phenomena follow below.

Anthropogenic aerosols are small particles of solids or liquids released into or produced within the atmosphere, which remain suspended in the air until they are removed, usually through deposition or precipitation. Aerosols come from various human activities, though primarily from fossil fuel combustion and agricultural burning. They can also be produced in situ after chemical or physical reactions of other anthropogenic pollutants; these other pollutants are thus called aerosol precursors. Anthropogenic aerosols provide direct changes to the RF on climate based on the radiative properties of

each aerosol type. Many aerosols (sulfates, nitrates, dust, and most organic aerosols) tend to reflect incoming solar radiation, causing a negative RF and a cooling effect, while others (black carbon and some organic aerosols) predominantly absorb and re-radiate the incoming solar energy more efficiently than other components of the atmosphere, providing a positive RF and a warming effect. These different aerosol species can also indirectly affect the RF of climate due to their influence on cloud formation, growth, and lifetime, thus affecting the energy balance, latent heat exchange, and albedo the clouds provide. Large-scale aerosol deposition, particularly black carbon on snow, can also alter Earth's surface albedo, making a semi-direct source of RF on climate from anthropogenic aerosols. The extent of the RF effect anthropogenic aerosols have on climate is an extant problem in the climate community due to the difficulty in quantifying both the direct effect [*Bond et al.*, 2013; *Kahn*, 2012; *Myhre*, 2009] and the large uncertainties in our understanding of the micro-scale of clouds [*Carslaw et al.*, 2013; *Morgan et al.*, 2006]. That said, the direct and indirect effects are both thought to generally provide negative RF, though the error bars for both approach 0 RF, with high confidence in the values for the direct effect but low confidence for the indirect effect [Table 8.5 of **AR5**]. This cooling effect is going away, as human health concerns (due to the small particle size or the toxicity of various aerosols) are generally prompting governments to increase industrial regulations and decrease the abundance of these particles in the atmosphere [*Smith and Bond*, 2014]. Thus, while aerosol cooling has offset some GHG warming over the past several decades, this “mask” is being removed, allowing previously “hidden” warming to be realized.

The RF effect of anthropogenic land use change (LUC) is small in comparison to GHGs, aerosols, or ocean warming, but is still a key systematic component to how humans have changed our climate and ecosystems over the course of human history. While some LUC acts to darken the surface of the planet by laying asphalt, the dominant pattern of LUC is the removal of darker-colored forest in favor of lighter-colored agricultural fields or, recently, concrete. The world is currently losing tens of millions of hectares of forest per year, with a total RF from 1750 to 2011 of $-0.15 \pm 0.10 \text{ W/m}^2$ [AR5]. These material changes to Earth's surface are long-lasting, so while the cooling effect might be seen as beneficial in a minor manner, the damage to the affected ecosystems and the associated disruptions to processes such as flooding, soil decay, and evapotranspiration must also be considered. The vegetation changes associated with LUC also, obviously, alter the carbon cycle, indirectly affecting how much of anthropogenic CO₂ emissions remains in the atmosphere

Volcanic aerosols affect the RF of climate when they puncture the tropopause and enter the stratosphere. The general stability of the stratosphere (contrasting the highly dynamic processes of troposphere) allows for these aerosols – mostly cooling sulfate aerosols and dust – to remain airborne for an extended period of time, on the order of months to years, and spread over a large area of the planet. These volcanic aerosols thus have an extended and noticeable negative RF of climate as they reflect and block incoming sunlight, increasing the optical depth of the stratosphere. Only the strongest volcanic eruptions have enough explosive force to send a significant quantity of aerosols high enough in the atmosphere to increase stratospheric aerosol optical depth (SAOD)

and provide a cooling effect on climate. These strong eruptions do not produce any long-term cooling, with their short-term effect on GMST lasting on the order of a year.

Total solar irradiance (TSI), while quoted as being the flat value of 1370 W/m^2 in first-order approximations, varies on short, medium, and long timescales. The long-term variations are a function of the sun's age and Earth's orbital parameters, but these changes generally⁴ happen too slowly to significantly affect Earth's climate system on decadal to century timescales. The daily and monthly changes in insolation are generally noisy and smaller in amplitude but produce a noticeable signal on the yearly-to-decadal time scale. This signal corresponds with the 11-year sunspot cycle. Even though sunspots are instances of the sun's surface being cooler than normal, they are associated with higher magnetic field activity and thus produce a larger amount of energy leaving the sun, resulting in higher TSI when more sunspots are present and lower TSI during sunspot minimums. The TSI cycle has an amplitude of slightly under 1 W/m^2 , giving a forcing at any point on the surface of slightly over 0.2 W/m^2 [Rind, 2009], and causes global temperature variation of $0.2 \text{ }^\circ\text{C}$ [G Masters, 1998] to $0.5 \text{ }^\circ\text{C}$ [J Zhou and Tung, 2013b] at the surface.

The El Niño-Southern Oscillation (ENSO) is an extensively studied atmospheric and oceanic phenomena most associated with the tropical Pacific region, where it is strongest⁵. Technically speaking, it is an internal aspect of the Earth's climate system, but it is often considered a forcing agent due to the causal effects on the rest of the planet [Chylek et al., 2016; Lean and Rind, 2008]. During positive (negative) ENSO events, the Pacific trade winds weaken (strengthen), causing warm surface water to pool further east

⁴ The Maunder Minimum and Medieval maximum being possible exceptions.

⁵ Other tropical ocean basins experience their own ENSO-like events, but to much lesser degrees.

(west) than it would in neutral conditions [*Rasmusson and Wallace, 1983*]. This shift disrupts the biologic carbon sink of the ocean by inhibiting (promoting) ecologic production in the cold-water upwelling off the South American coast. ENSO also disrupts the global-scale atmospheric circulation by moving the center of precipitation in the Pacific, which in turn affects the jet stream. These processes overall have the effect that GMST noticeably rises (falls) during a positive (negative) ENSO phase, driven largely by the inhibition (promotion) of cold-water upwelling to the ocean surface [*Yulaeva and Wallace, 1994*].

Larger ocean circulation and atmosphere-interaction patterns in each ocean basin can also affect climate, though causal relationships and the intensity of the effects are less certain than those associated with ENSO. In the Indian Ocean, the smallest of the three tropic-spanning basins, the most notable pattern appears to be the ENSO-like Indian Ocean Dipole (IOD) – which, as stated above, is a minor pattern compared to ENSO itself, though it does have some influence on the Indian monsoon [*Ashok et al., 2001*]. In the Atlantic Ocean, there is also an ENSO-like pattern, but more impactful to climate and large-scale weather patterns are the Atlantic Meridional Overturning Circulation (AMOC) and the surface patterns associated with AMOC. These surface patterns include the Gulf Stream (which transports warm water and mild climate/weather to the eastern seaboard of North American and western Europe) and the Atlantic Multidecadal Variation (AMV, surface temperature patterns in the north Atlantic associated with cold water formation). Direct measurements of the flow of the AMOC have only been available for a little over a decade [*Smeed et al., 2017*], so many groups have tried to model the overturning circulation [*L C Jackson et al., 2016; Rahmstorf et al., 2015*] or

find proxies for variation in the strength of this circulation [*Haustein et al.*, 2019; *Rahmstorf et al.*, 2015]. Here, we will use the AMV as a proxy for the AMOC; there is considerable debate in the climate community both for [*Boessenkool et al.*, 2007; *Knight et al.*, 2005; *Medhaug and Furevik*, 2011; *Meehl et al.*, 2011] and against [*Booth et al.*, 2012; *Haustein et al.*, 2019] this use. Finally, in the Pacific Ocean, two large-scale patterns of sea surface temperatures are the Pacific Decadal Oscillation (PDO) and the Interdecadal Pacific Oscillation (IPO). Both have been suggested to be the surface signal of an ocean-atmosphere interaction with decadal-scale influence on GMST [*England et al.*, 2014], while both have also been suggested to be primarily associated with long-term averages of ENSO [*Newman et al.*, 2003; *Verdon and Franks*, 2006].

1.2 Previous Climate Modeling Efforts

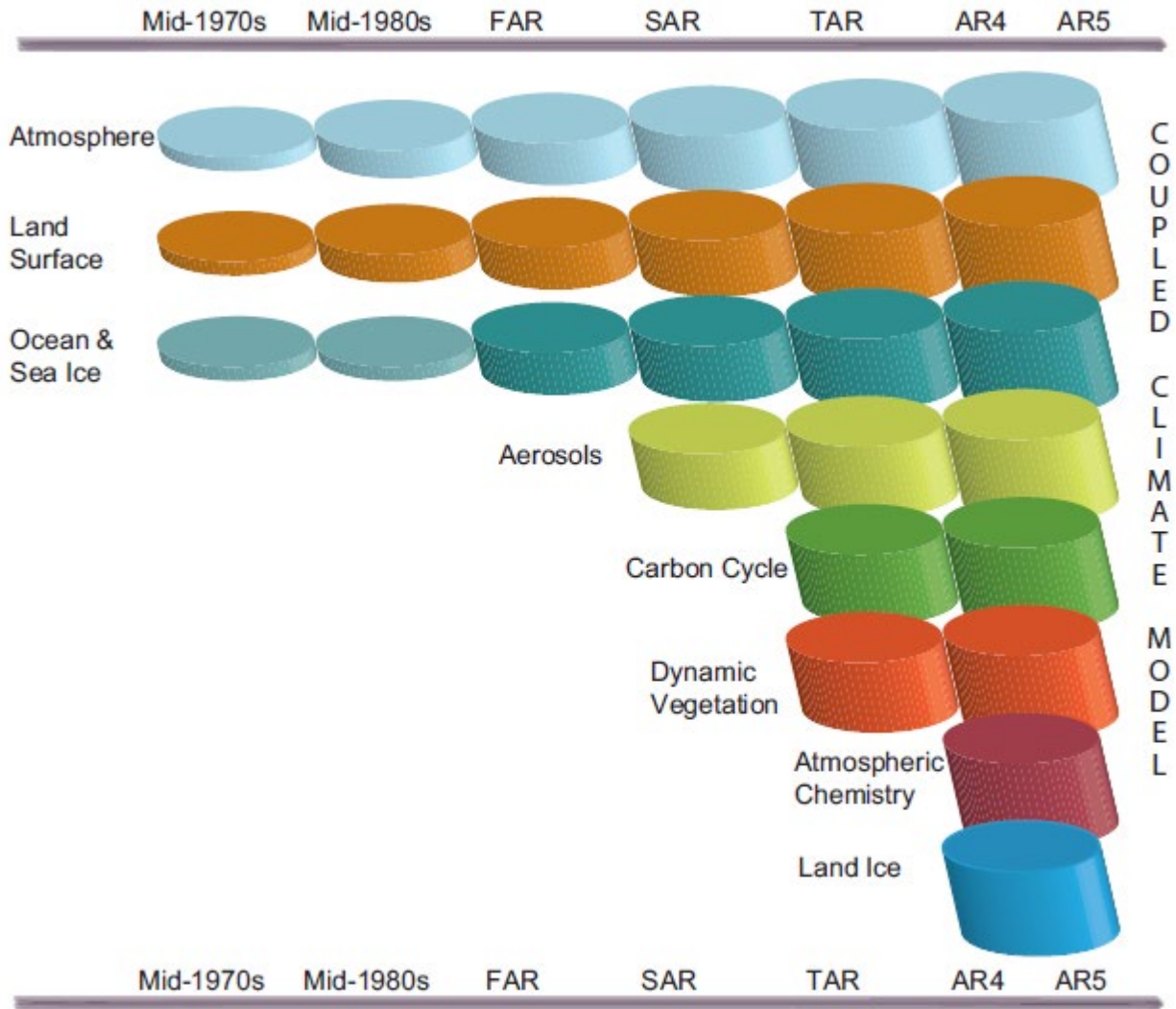
1.2.1 History of GCMs

Large-scale climate modeling efforts began as offshoots of numerical weather prediction in the late 1950s as some scientists sought theoretical models of the atmosphere, in contrast to observationally-forced models. These early General Circulation Models, for which the acronym GCM would later be recast as Global Climate Models, often relied on just a small set of equations and had a very coarse atmospheric “grid” with just a handful of vertical levels and horizontal divisions. As computing power grew, models moved from hemispheric and zonal divisions to horizontal grid cells several degrees a side, as well as increasing the number of vertical levels [*Edwards*, 2000]. This progress, which has continued to modern modeling efforts as computing power continues to increase, allows for more nuanced quantification of larger-scale processes and for quantification at all of smaller-scale patterns, all of which are necessary

for accurately modeling a system which is inherently not discretized – and one where long-term trends can be defined in averages of complex events (e.g. hurricane trends) or observed in very localized microclimates.

In addition to increasing resolution from the computation side, GCMs have grown significantly from a conceptual standpoint over the years. Early GCMs relied on modeling just general atmospheric flow, simple land surface interactions, and large-scale ocean processes. As computing power and scientific understanding have grown, modelers have added representation of aerosols (starting in the 1990s), dynamic vegetation and other key components of the carbon cycle (2000s), and atmospheric chemistry and land ice interactions (2010s) [*Edwards, 2000; Jakob, 2014*]. A schematic of the increase in processes included in GCMs from **AR5** is reproduced here as figure 1.4. These advances, along with the fine resolution allowed by higher computation power, can represent small-scale but important processes and feedbacks. The newer small-scale details also provide information that is influential on a personal level to citizens, constituents, businesses, and politicians, such as flooding or drought risk, tendency for severe weather, agricultural constraints, and attempts at definitive emissions budgets. Simple GCMs have also been paired with/included in Integrated Assessment Models (IAMs) to examine how the physical processes of the climate system interact with human demographics, politics, and economics (e.g. industry, commerce, and energy production). This coupling in IAMs can attempt to emulate human-behavior-based feedbacks that might not be seen when separate social and climate models are forced with static scenarios passed from one model to the other.

Figure 1.4; Component Development of GCMs



Reproduction of AR5 Figure 1.13

“The development of climate models over the last 35 years showing how the different components were coupled into comprehensive climate models over time. In each aspect (e.g., the atmosphere, which comprises a wide range of atmospheric processes) the complexity and range of processes has increased over time (illustrated by growing cylinders). Note that during the same time the horizontal and vertical resolution has increased considerably e.g., for spectral models from T21L9 (roughly 500 km horizontal resolution and 9 vertical levels) in the 1970s to T95L95 (roughly 100 km horizontal resolution and 95 vertical levels) at present, and that now ensembles with at least three independent experiments can be considered as standard.”

Problems in representing the climate system still exist even as GCMs have included more processes at higher resolution. Given the complexity of the Earth climate system, reducing the myriad of mechanisms to a computer model will necessarily involve parameterization of some real-world processes. Parameterization, the natural chaos of the system, numerical noise issues, and coding choices all contribute to the large amount of model spread seen in coordinated modeling efforts such as the Coupled Model Intercomparison Project, phase five (CMIP5) and phase 6 (CMIP6). In particular, differences in the quantification of cloud feedbacks (particularly in the tropics) accounts for roughly 70% of inter-model spread in future temperatures within CMIP5 [Vial *et al.*, 2013], and continued uncertainty in cloud feedback drives some of the excessive warming in CMIP6 [Zelinka *et al.*, 2020]. On top of cloud feedback spread, over half of CMIP5 models do not consider all aspects of the aerosol indirect effect [Chylek *et al.*, 2016; Wilcox *et al.*, 2013].

Coordinated modeling efforts such as CMIP5 are designed to deal with the above mentioned model uncertainty. For CMIP5, dozens of modeling centers around the world agreed on a specific set of emissions (for aerosols and in some instances GHGs) and atmospheric abundance (in other instances for GHGs) and physics scenarios that could be used for running their models within the comparison project. The CMIP5 scenarios included a handful that every involved modeling group agreed to run. Having multiple models running the exact same scenario(s) eliminates scenario uncertainty, allowing for CMIP5 to better examine the model uncertainty among member models. Notably, CMIP5 also aimed to examine uncertainty in the mechanisms for the carbon cycle and cloud processes [K Taylor *et al.*, 2012]. While the model spread due to cloud feedbacks is

somewhat problematic, seeing such a large signal can allow for modelers to easier identify specific mechanisms and best coding and analysis practices for current and future projects like CMIP6 – something that would be difficult to identify without controlling for scenario uncertainty. Indeed, one of the major projects within CMIP6 is examining and improving cloud feedbacks (CFMIP), although the general improvement in cloud microphysics seems to have produced a bias in the direction of the cloud feedback interaction, leading to excessive warming [Zelinka *et al.*, 2020].

1.2.2 The Representative Concentration Pathways

One class of emissions scenarios used in CMIP5 is the set of Representative Concentration Pathways (RCPs). Each RCP scenario was created by a separate integrated assessment model (IAM) group [Van Vuuren *et al.*, 2011a], based on the state of knowledge from the IPCC Fourth Assessment Report [Solomon, 2007], hereafter **AR4**, so as to inform **AR5**. The RCPs consist of four scenarios of GHG concentrations and other climate forcings out to year 2100, as well as a historical account of those quantities from 1765 to 2005. Global average and half-degree gridded data are available for most of the included quantities. The four RCP scenarios were developed such that sum of all forcings at the end of the 21st century totaled one of four values that spanned the literature at the time: 2.6 W/m², 4.5 W/m², 6.0 W/m², and 8.5 W/m² [Van Vuuren *et al.*, 2011a].

The RCP 8.5 scenario, at the time of development, represented the “business as usual” or “baseline” pathway for global emissions of GHGs, aerosols, and land use changes [Riahi *et al.*, 2011]. This scenario assumed continued growth in population, economic output, and all associated energy and resource consumption, while also assuming no climate change mitigation policies would be enacted. This projection did not

mean extreme growth in all areas; the continued trends instead imply moderate growth in global GDP and almost no improvements to per capita income or primary energy intensity. RCP 8.5 thus descended directly from the A2r scenario [Riahi *et al.*, 2007], a modification to the A2 SRES scenario [Nakicenovic *et al.*, 2000], and envisioned a world where fossil fuel technologies remain the most attractive options for energy production. Coal in particular supports roughly half of all global primary energy supply by 2100 according to RCP 8.5, the largest difference in energy portfolios between the RCPs [Riahi *et al.*, 2011]. The GHG emissions associated with RCP 8.5 were developed using the MESSAGE integrated assessment model.

RCP 6.0 was developed with the Asia-Pacific Integrated Model [Fujino *et al.*, 2006] using socio-economic assumptions that allow for global emissions of GHGs to peak around 2060 [Masui *et al.*, 2011]. Even as emissions decrease in the later part of the 21st century, global radiative forcing would still increase slightly before stabilizing at 6.0 W/m². This outcome is in contrast to RCP 8.5, wherein global radiative forcing would still be strongly rising at the end of the century and beyond. The emissions reduction and forcing stabilization are achieved by assuming the establishment of a global carbon market and decreased growth in primary energy needs from 2060 to 2100. Under this global incentive, the change in primary energy production is the main driver for the stabilization, as the relative shares of energy sources does not change significantly – e.g. renewables account for roughly 13% of primary energy in 2000 and only grow to roughly 16% by the end of the century; other sectors similarly do no change significantly [Masui *et al.*, 2011].

The global energy portfolio begins to shift away from fossil fuels significantly when considering RCP 4.5 [Thomson *et al.*, 2011]. The RCP 4.5 scenario arose from use of the GCAM integrated assessment model to synthesize multiple studies [Clarke *et al.*, 2007; S J Smith and Wigley, 2006; Wise *et al.*, 2009] concerning GHG emissions, other pollution controls, land use changes, and carbon pricing. In RCP 4.5, atmospheric GHG mixing ratios stabilize by 2080, as does global RF. To accomplish this outcome, global primary energy from fossil fuels stabilizes by midcentury. More than half of the growth after midcentury is attributed to massive increases in nuclear energy production, with renewables and biomass accounting for the rest. RCP 4.5 includes adoption of industrial-scale carbon capture and sequestration (CCS) to help decrease GHG emissions after fossil-fuel-produced primary energy stabilizes, and also includes afforestation to offset other CO₂ emissions [Thomson *et al.*, 2011].

Finally, RCP 2.6 was designed to limit global warming to 2°C above preindustrial, based on the state of science at the time [Van Vuuren *et al.*, 2011b]. Also known as RCP3-PD (Peak and Decline), the RCP 2.6 scenario requires global RF to peak at 3 W/m² by midcentury and then decline to 2.6 W/m² by 2100. This outcome requires GHG emissions to peak and begin declining in the near immediate future so that atmospheric mixing ratios peak by midcentury, and then requires negative emissions so that mixing ratios fall in the ensuing decades. This can only be accomplished through extensive use of CCS technologies (with over two-thirds of fossil-fuel-based primary energy production at the end of the century is assumed to have its carbon emission sequestered) including bio-energy-based CCS, and use of afforestation. RCP 2.6 also necessitates the enactments of extensive additional climate change policy actions from all

nations around the world – such as a global carbon market with rapid growth in carbon prices – and also assumes increased energy efficiency, decreased energy demand, and only moderate population growth [*Van Vuuren et al.*, 2011b].

Among the emissions and physics scenarios included for use in CMIP5, RCP 4.5 and RCP 8.5 were two of the scenarios designated as “core” simulations, intended to be run by nearly every participating GCM [*K Taylor et al.*, 2012]. For this reason, the research in this dissertation focuses on these two scenarios. Particular emphasis is given to RCP 4.5 as research closely associated to this dissertation [*Tribett et al.*, 2017] suggests both that RCP 8.5 is no longer the “business as usual” scenario as intended and that emissions associated with compliance to commitments to the Paris Climate Agreement approximate RCP 4.5 rather well, assuming continued improvements in carbon and methane emissions extend beyond the time frame of most commitments.

1.2.3 Multiple Linear Regression Climate Models

Multiple linear regression (MLR) is a simple yet elegant mathematical tool that attempts to recreate a response term given multiple explanatory variables. While it does not prove causation or even correlation by itself, well-educated choices of explanatory variables and experimental design can be used to support causation (provided there exists an underlying physical mechanism) or strongly rule out otherwise possible explanatory variables. While Earth’s climate system is highly complex and nonlinear, it is not unreasonable to use zeroth- and first-order physics in an attempt to examine specific variables with an MLR model.

Global warming has a strong enough effect on other aspect of climate change and on global society that it has reasonably been a focus of GCMs, MLR models, and other

climate analyses. Most MLR approaches to understanding global warming [Chylek *et al.*, 2020; Chylek *et al.*, 2014; Foster and Rahmstorf, 2011; Lean and Rind, 2008; 2009; Tung and Zhou, 2013; J Zhou and Tung, 2013a] use a one- or two-step process to separate the natural influences on GMST, e.g. ENSO, from the anthropogenic influences on GMST, e.g. GHG forcing. While there has been some criticism that MLRs oversimplify the complex mechanisms that affect GMST [Marvel, 2018], many of these criticisms can be addressed with proper experiment design (see §2.3.1, §4.2, and §4.3 in this dissertation). Any remaining minor criticisms of the MLR method for climate modeling can be outweighed by the power – provided by its simplicity – to perform thousands or even millions of runs in the time it takes the complex GCMs to complete a single run, allowing for sensitivity and scenario testing that is unavailable to GCMs.

The Empirical Model of Global Climate (EM-GC) originated from a class project that itself used the work of Lean & Rind [2008; 2009] as an instructional foundation. Their MLR model combines the natural forcings of ENSO, TSI, and SOD with an eight-component anthropogenic signal [Hansen *et al.*, 2007] to produce a modeled temperature record that explains 76% of the observed temperature record (from the Hadley Center) that had been examined. In particular, the anthropogenic component provided 0.199 ± 0.005 °C per decade of warming since the beginning of the satellite era (1979-2005). They also show how observed and modeled temperatures map spatially over the globe by repeating the MLR temperature analysis on each $5^\circ \times 5^\circ$ grid box [Lean and Rind, 2008] (hereafter **LR08**). With the coefficients from their analysis, they project GMST out to 2030, suggesting that GMST would increase at an average rate of 0.17 ± 0.03 °C per decade; they also examine the effect of a potential major volcanic eruption (affecting

SAOD) and an extreme positive ENSO event. Notable predictions include a strong GMST increase from 2009 to 2014 due to the TSI cycle amplifying anthropogenic effects and a relative lack of GMST increase from 2014 to 2019 due to a projected downturn in the TSI cycle [*Lean and Rind, 2009*].

Foster and Rahmstorf [2011] (hereafter **FR11**) examine five different temperature records with their MLR, three based on surface station data and two based on satellite sensing (and thus more representative to lower troposphere temperatures than surface temperatures). All five records show general consistency in their warming trends both before and after adjustment by the MLR analysis of **FR11**. This MLR examines the effect of the three previously mentioned natural factors – ENSO, TSI, and SOD – and then removes those effects from the temperature record to create the adjusted temperature records. With these three natural factors (and a seasonal cycle) removed, **FR11** name the (implicitly anthropogenic) remaining residual as the “global warming signal”, reporting a value of $0.17 \pm 0.01^{\circ}\text{C}$ per decade for the surface records (1979-2010). They do not directly consider anthropogenic RF as an input to their analysis.

Zhou & Tung [2013a] (hereafter **ZT13**) critically examine the work of both **LR08** and **FR11**, notably adding a LOWESS-filtered version of the Atlantic multidecadal oscillation (AMO) to their MLR. This addition produces substantially different estimates for the attributable anthropogenic warming rate in their MLR framework. While they essentially recreate **FR11**'s 0.17°C per decade when ignoring AMO, that value drops to 0.07°C per decade with AMO included. With their choices of AMO filtering and effective lags for the other natural inputs, they also argue that the pre-supposing of an anthropogenic signal by **LR08** caused an overshoot in their estimate of the anthropogenic

effect, evidenced by an apparent shift in the trends of the residual between the observational and modeled temperatures. As such, the ZT13 MLR uses a linear trend as an initial estimate for the anthropogenic signal during the MLR step, then add that linear trend back into their residual for their further analysis.

A simple MLR model from a group based at the Los Alamos National Lab [Chylek *et al.*, 2020; Chylek *et al.*, 2016; Chylek *et al.*, 2014] shows many similar results to results from the EM-GC [Canty *et al.*, 2013; Hope *et al.*, 2017]. The Los Alamos MLR model suggests a significant influence of the AMO on GMST [Chylek *et al.*, 2016; Chylek *et al.*, 2014] and an overstatement from GCMs of the influence of SAOD on GMST [Chylek *et al.*, 2020]. As with the EM-GC, the Los Alamos MLR model can test multiple versions of input regressors, both natural and anthropogenic, though their model does not include terms representing LUC, ocean heat export (OHE), or the influence of the Indian Ocean on climate. Chylek *et al.* [2016] state that the GMST record can be suitably reconstructed using just three regressors: anthropogenic total, solar, and AMO. Any addition of extra regressors does not provide a significant improvement in GMST hindcast accuracy for the increase in complexity. While the EM-GC can run with subsets of its available regressors, we prefer using the full set of regressors because slight improvements to fitting the GMST record can greatly increase the spread in projections of future GMST and the use of ENSO, in particular, helps explain why for instance 2016 was the warmest year on record [Hope *et al.*, 2017]. We prefer to account for as much uncertainty in future GMST as is reasonable.

1.3 Goals and Accomplishments

The body of work encompassed by this dissertation is the result of advancing the physics and data inputs of my research group's MLR climate model – the Empirical Model of Global Climate (EM-GC), first described in *Canty et al.* [2013] and first named in *Hope et al.* [2017]. Specifically, the updates I have made to the EM-GC between the *Canty et al.* [2013] version of the model and the submitted *Hope et al.* [2020] version of the model include:

- Rewriting the ocean heat export term from a purely mathematical estimate to the physics-based calculation from *Raper et al.* [2002]
- Adding an ocean surface temperature term into the ocean heat export expression to prevent the ocean from functioning as an infinite heat sink and later adding options to simulate different possibilities for the ocean warming profile as a function of depth
- Expanding the number of ocean heat content records that the EM-GC can use from two (with two modifications each, for a total of four) to eight (with depth dependencies and various averages, for a total of sixteen)
- Alter the treatment of feedback processes in response to ocean heat export forcing of climate
- Apply an area correction for the ocean heat export forcing of climate
- Updating the EM-GC aerosol scenarios to represent the aerosol RF estimates of **AR5** instead of those in **AR4**
- Reformatting the process of combining aerosol direct RF time series to sample the uncertainty in past aerosol total RF

- Including the aerosol scenarios of [*S Smith and Bond, 2014*] as options into the EM-GC
- Examining the evolution of Earth's albedo over the time period of the Clouds and the Earth's Radiant Energy System (CERES) record
- Examining the effect of stratospheric water vapor in the EM-GC
- Creating new methods to examine specific time periods within specific EM-GC runs, e.g. to seek the cause(s) of the so-called "global warming hiatus" in the early 21st century
- Testing new data record inputs for SOD, ENSO, AMV, and PDO
- Rewriting our projection analysis weighting method from a purely math/physics perspective to using **AR5**-directed probabilities based on the uncertain in the radiative forcing of climate due to anthropogenic aerosols
- Restating projected temperatures as a function of total carbon emissions instead of as a function of time, such that we can report policy relevant quantities such as transient climate response to cumulative carbon emissions (TCRE) and total/remaining carbon budget
- Allowing the model to run with a mix of anthropogenic GHG signals from various original scenarios, e.g. using times series for the three main GHGs and the class of halocarbons each from a different one of the four RCPs
- Creating four new CH₄ scenarios to bridge the gap between the RCP 8.5 and RCP 4.5 projections of atmospheric CH₄.

The advancements of the EM-GC to date have all helped to increase the power and rigor of the model in the hopes of my group addressing three main pillars of

projection uncertainty in climate models: scenario uncertainty, model difference, and internal variability. In addition to using the EM-GC to test all four RCPs more quickly than GCMs, our ability to mix the RCPs and test other projections of aerosols and CH₄ gives an even more complete picture of scenario uncertainty. Our ability to selectively chose the natural and anthropogenic inputs in any given ensemble, as well as selecting how much heat goes into the ocean and how the heat is distributed, simulates differences in model physics between GCMs. Natural internal variability is included in the EM-GC by means of the natural regressors considered; that is, the model does not attempt to simulate its own natural variability from physics principles. We can also show the effect of predicted natural variability from inputs such as TSI on future projections by comparing runs with their inclusion and exclusion.

Chapter 2 of this dissertation expands on the physics and chemistry of climate change by taking a more detailed look at some of the factors considered in the EM-GC. A large portion of chapter 2 is a recasting of my contributions to *Salawitch et al.* [2017]. This includes a detailed examination of the RF on climate from the different sources referenced in **AR5** and how they compare over time, as well as a closer look at methane emissions specifically. Chapter 2 also includes discussion of several influences on climate that were considered in the growth of the EM-GC but not directly addressed in either Chapter 3 [*Hope et al.*, 2017] or Chapter 4 [*Hope et al.*, 2020] – specifically, an analysis of how Earth’s albedo has changed over the recent past, the effect of the ocean warming profile as a function of depth, and the effect (or lack thereof) of stratospheric water vapor on modern climate change. Finally, Chapter 2 discusses some of the

considerations made in constructing a linear model of the nonlinear climate system, and how I address some of these concerns.

Chapter 3 of this dissertation, published as *Hope et al.* [2017], outlines the basic structure of the EM-GC and several of our core results. It discusses the inspiration behind the EM-GC before describing all of the inputs (as of summer 2016) in detail. Our group's central message, that the CMIP5 warming projections likely overpredict future warming, follows from use of the EM-GC in both of its main modes. We use the “best-fit mode” of the model to examine the Attributable Anthropogenic Warming Rate (AAWR) from our results and from CMIP, and we use the “spanning mode” of the model to create a large ensemble of future temperature projections. Chapter 3 also includes comments about the so-called “global warming hiatus” from 1998 to 2012.

Chapter 4 of this dissertation accounts for the important physics updates made between the publishing of the Chapter 3 material and present. This material was submitted to the AGU journal *Earth's Future* on 30 August 2020 and can be viewed online at <https://www.essoar.org/doi/10.1002/essoar.10504179.1> [*Hope et al.*, 2020]. While there are significant parallels between the two chapters in terms of structure and content, the updates are significant enough that one of our core messages has changed. These updates also shifted our group's focus solely to an ensemble-driven view of our modeling efforts, stemming from the “spanning mode” of Chapter 3. Chapter 4 here also includes updates to my contributions to *Bennett et al.* [2017], which are not otherwise present in this dissertation – namely, describing the implications that result from considering future temperature as a function of total emissions, and describing the effect of uncertainty in future methane emissions on our GMST projections.

Finally, Chapter 5 of this dissertation provides concluding remarks, including how the predictions made by the EM-GC have been validated to date and how our results fit into the goals of providing a comparison/check to GCMs and can inform policy, such as any agreements intended to follow-up the Paris Agreement [*Tribett et al.*, 2017]. This chapter concludes with future directions for the advancement and use of the EM-GC, for myself as well as future graduate students who further develop the EM-GC.

Chapter 2: Advanced Physics & Chemistry of Climate

While Chapter 1 introduced the concepts of radiative forcing (RF) and greenhouse gases (GHGs), Chapter 2 seeks to provide a more thorough exploration and explanation of these concepts, all of which underlie various components of the Empirical Model of Global Climate (EM-GC). In §2.1, I discuss further background information on the physics and history of the relationship between GHGs and RF. The specific physical properties and sources of three GHGs (CO₂, CH₄, and N₂O) and a fourth class of GHGs (halogenated gases) are discussed. The next section (§2.2) then focuses on the many links that show the anthropogenic signature of these GHGs in the atmosphere – that is, how we know the sources mentioned earlier have a noticeable effect on the atmosphere, and that the changes in RF are thus caused by humans – and what that means for future GHG concentrations.

The final section of this chapter (§2.3) deviates from the observationally-based background information, instead addressing more of the history and theory behind the structure of the EM-GC. Some climate scientists view multiple linear regression (MLR) as an insufficient method for analyzing the climate system, due to how the system is inherently nonlinear. I present justifications for some of the simplifications and assumptions that help build the EM-GC and address some of these concerns. In addition, I include the results of all of the background research that I did in support of the EM-GC that are not thoroughly described in either *Hope et al.* [2017] or *Hope et al.* [2020]. These include, but are not limited to, examinations of recent minor volcanoes and their effect on stratospheric aerosol optical depth (SAOD), the importance (or lack thereof) of

stratospheric water vapor (SWV), and an exploration of the albedo feedback process using data from the CERES satellite.

2.1 Radiative Forcing by Species

The thermal radiation involved in the greenhouse effect discussed above in §1.1.2 consists of photons in the infrared (IR) section of the electromagnetic spectrum.

Molecules of different gas or aerosol species in the atmosphere will absorb, transmit, and reflect photons of different wavelengths, depending on the atoms in each molecule and their physical arrangement. From a radiation standpoint, Earth's atmosphere is transparent to visible light (roughly 400-700nm wavelengths) but mostly opaque to thermal IR radiation (roughly 3-15 μ m). This property of the atmosphere allows for sunlight to pass through the atmosphere and be absorbed by Earth's surface. That surface energy is re-radiated in the IR spectrum and thus is mostly absorbed by the atmosphere. This "greenhouse effect", as mentioned before, is what keeps our atmosphere at a habitable temperature.

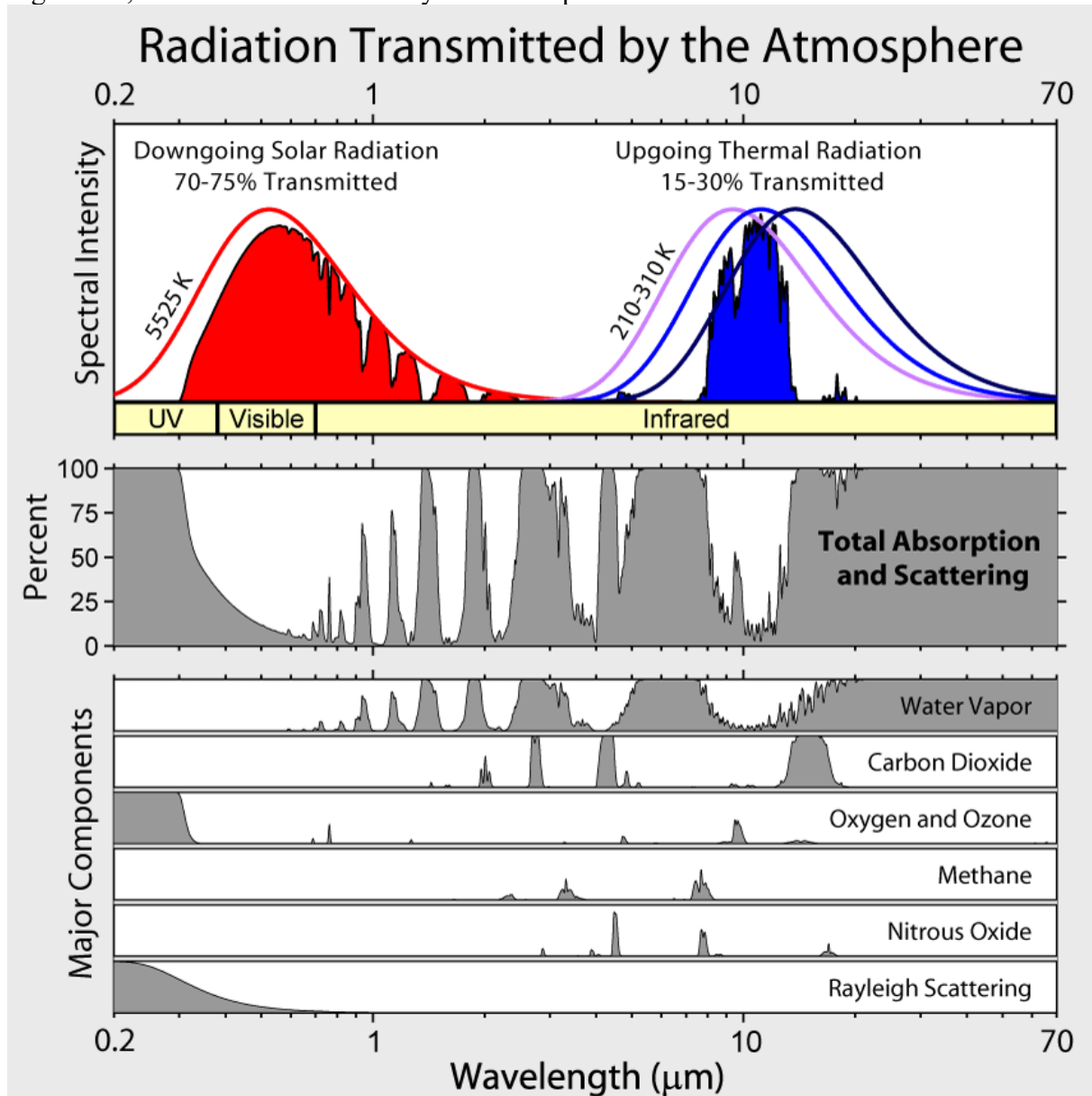
Any gas in the atmosphere that absorbs radiation in the thermal IR region of the electromagnetic spectrum is a greenhouse gas (GHG). A molecule with three or more atoms can bend and stretch in various ways when it is in higher energy states. If this bending and stretching causes the molecule's dipole moment – its internal distribution of electric charge – to change, then the associated change in the molecule's energy state matches the energy levels of IR photons that the molecule absorbs or emits. Other types of energy state transitions correspond to other electromagnetic waves: the higher-energy photons from X-rays and ultraviolet radiation can strip electrons from molecules, while the lower-energy photons of microwaves cause full-molecule rotation as opposed to

vibration and stretching. The presence of dipole-moment-changing vibrational modes are thus what allows a molecule to function as a GHG.

The most abundant GHG is water vapor. The abundance of water ranges from 0-5% of tropospheric air at any given location depending on thermodynamic conditions, such as evaporation from bodies of water and local weather (cloud formation and air parcel transport). In total, water vapor averages roughly 2.75% of the atmosphere, specifically with an estimated 37.5×10^{15} gallons of water vapor out of the 5.148×10^{18} kg of atmosphere. Water vapor also accounts for 66-85% of the greenhouse effect [Hausfather, 2008] because it absorbs a dominant portion of the IR radiation from Earth's surface. Specifically, water vapor absorbs almost all IR radiation near $3\mu\text{m}$ (i.e. $3 \pm 0.5\mu\text{m}$), between $5\mu\text{m}$ and $8\mu\text{m}$, and in the vast majority of the "far IR" (far IR includes wavelengths greater than $15\mu\text{m}$, though water vapor starts absorbing well at $18\mu\text{m}$), as shown in Figure 2.1.

While water vapor accounts for so much of the existing greenhouse effect, it is not a *driver* of current global warming. The amount of water that a parcel of air can hold is directly limited by the air parcel's temperature; past that maximum amount of water, the air is saturated or oversaturated, promoting precipitation. The water cycle thus strongly limits the lifetime of water vapor molecules in the atmosphere. The water cycle also thus provides a cap to the amount of water the atmosphere overall can hold, loosely being a function of global mean surface temperature (GMST). In this sense, water vapor can and does provide a positive atmospheric *feedback* but should not be considered a global warming *forcing* despite being the strongest GHG. That is, warmer (or cooler) atmospheric temperatures mean more (less) water can be held in air parcels, and more

Figure 2.1; Radiation Transmitted by the Atmosphere



Reproduction of figure created by Robert A. Rhode for the Global Warming Art project; figure accessed from Wikipedia.

Top panel shows relative amount of radiation that passes through the atmosphere from the sun downward (red) and from Earth's surface upward (shades of blue) as a function of wavelength, where the peak of each smooth spectra is dependent on each object's surface temperature. Departure downward from these smooth spectra thus represent the percent of radiation at those wavelengths that is absorbed by the atmosphere.

Middle panel explicitly quantifies the percent of radiation at each wavelength that is absorbed by the atmosphere, in grey.

Bottom panel breaks the grey absorption profile from the middle panel into its major components based on the atmospheric species & physics responsible for the absorption at each wavelength.

(less) water vapor means a stronger (weaker) greenhouse effect, further warming (cooling) atmospheric temperatures until a new equilibrium with the water cycle is reached. Unlike most other GHGs, water vapor has no significant direct anthropogenic source and is naturally kept near its equilibrium by weather processes.

After water vapor, CO₂ is the next largest constituent of Earth's atmosphere and second most abundant GHG, making it most abundant anthropogenic GHG. Carbon dioxide currently accounts for slightly over 0.04% of the atmosphere, or 400 parts per million by volume (ppmv) [<https://www.esrl.noaa.gov/gmd/ccgg/trends/>]. This abundance is much higher than the 270-280 ppmv commonly cited as the atmospheric mixing ratio of CO₂ before the Industrial Revolution began in the mid-1700s, which is also the approximate mixing ratio that the Earth system had upon exiting each of the past Ice Ages (figure 1.3). The effectiveness of CO₂ as a GHG can largely be attributed to the fact that it absorbs IR radiation in the "windows" left in water vapor's absorption spectrum, specifically the gaps from 3.5 to 5 μm and from 8 to 18 μm. That is, IR radiation that would normally be able to escape the Earth system due to not getting absorbed by CO₂ by excitation of vibrational modes. CO₂ has strong absorption peaks at roughly 4 μm and from 13 to 18 μm. This molecule also has two small absorption peaks between 9 and 11 μm. As the concentration of CO₂ (or any GHG) increases in the atmosphere, weak absorption peaks become stronger as more molecules are available to absorb at those wavelengths. Strong absorption peaks (i.e. those at wavelengths where ~100% of radiation is already absorbed) can even broaden slightly in wavelength-space. Both of these effects thus serve to close the atmospheric windows left by water vapor as

CO₂ mixing ratio (or that from any GHG) increases, strengthening the greenhouse effect and global warming.

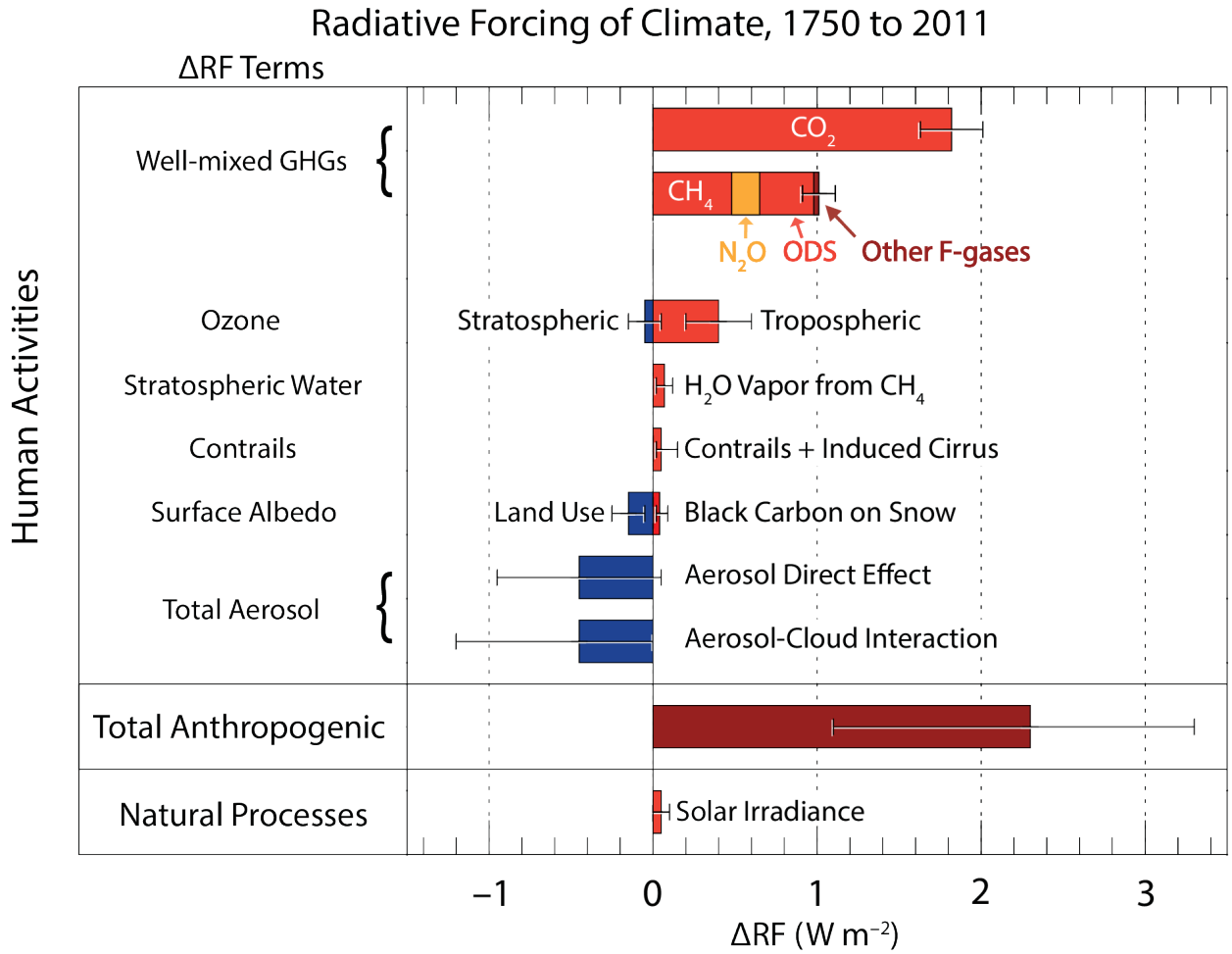
The most abundant GHGs after CO₂ are CH₄ and N₂O, two species whose current atmospheric mixing ratios are roughly 1.84 ppmv and 0.329 ppmv respectively. Like with CO₂, CH₄ and N₂O have their strongest absorption peaks in the windows of water vapor's absorption spectrum. Both have a strong peak between 7 μm and 9 μm, and both also have a strong peak at the shoulder of other strong absorption bands. The second strong peak of CH₄ sits between 3 μm and 4 μm on the high shoulder of water vapor's first absorption band, while the second strong peak of N₂O at 5 μm borders CO₂'s first peak. Compared to CO₂, CH₄ and N₂O are much better at absorbing IR radiation on a per molecule basis. In addition, CH₄ is even better still at absorbing on a per mass basis; CO₂ and N₂O have roughly the same molecular mass but are both roughly 3× more massive than a molecule of CH₄. The main reason for the greater strength of CH₄ and N₂O with respect to CO₂ is the difference in the saturation of each GHG's respective absorption regions of the spectrum.

As the concentration of a GHG increases in the atmosphere, or the concentration of another species that absorbs at the same wavelength(s) as that GHG similarly increases the likelihood of an IR photon from Earth's surface being absorbed by a particular molecule of that GHG does not rise in direct proportion. In the case of CO₂, there is already enough CO₂ (and water) in the atmosphere that all of CO₂'s absorption bands from 1 μm to 20 μm are saturated, either from CO₂ alone or from competition with absorption from water vapor. That is, the atmosphere is essentially opaque to all IR radiation at CO₂'s IR-active wavelengths. Quantitatively, this results in the radiative

forcing (RF) equation for CO₂ being dependent on the logarithm of CO₂'s mixing ratio – a lot of CO₂ is needed to produce a little bit more RF due to broadening of the existing absorption peaks. Conversely, each peak of the absorption spectra for CH₄ and N₂O are not fully saturated and exist on the weaker shoulders of absorption bands due to water vapor and CO₂; thus any added molecules of CH₄ or N₂O are a bit more likely to absorb any IR photons from Earth's surface than occurs for CO₂. As a result, the RF equations for CH₄ and N₂O vary as a function of the square root of mixing ratio of each molecule, as opposed to the logarithm of mixing ratio of CO₂.

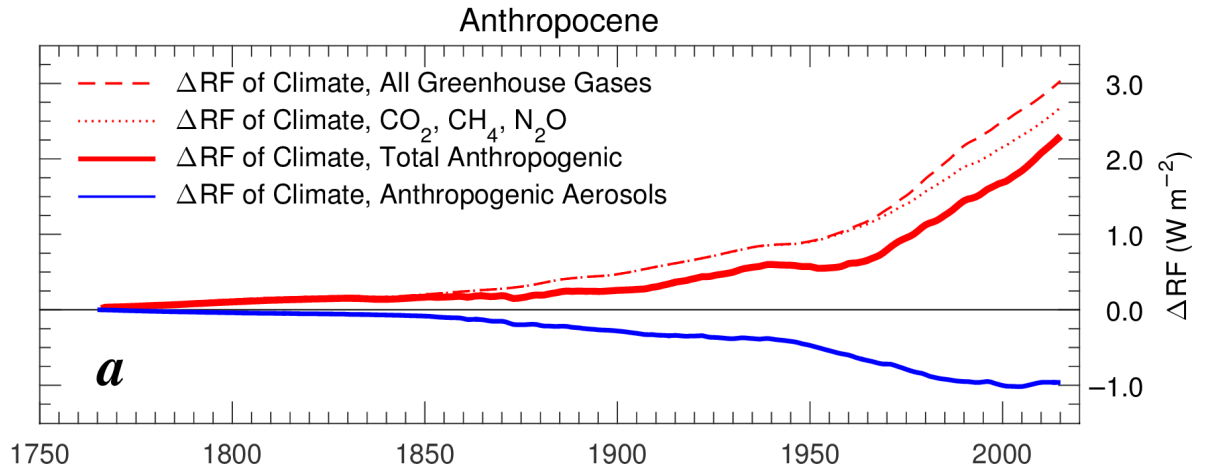
These effects can be summarized in a metric called global warming potential (GWP). This metric is calculated by integrating the RF over time of an atmospheric release of an instantaneous pulse of a given GHG and dividing that quantity by the same integral for instantaneous pulse release of the same mass of CO₂ [AR5, Ch8]. By definition, CO₂ has a GWP of 1 regardless of the time period for integration. On a twenty-year time horizon, when the carbon cycle does not have a significant secondary effect, the GWPs for CH₄ and N₂O are roughly 85 and 265, respectively. On a one-hundred-year time horizon, the short atmospheric lifetime of CH₄ causes its GWP to drop versus its twenty-year GWP. At the same time, the effect of the carbon cycle becomes more prominent and causes slight increases in GWP for all species. Thus, the GWPs for CH₄ and N₂O on the one-hundred-year time horizon are respectively 28 and 265 without consideration of carbon cycle feedbacks, or 34 and 298 when considered [AR5 table 8.7]. Water vapor, which has several unsaturated absorption peaks and is known to be a stronger GHG than CO₂, is not generally given a GWP due both to its rapid cycling time

Figure 2.2 – Total Δ RF of Climate by Anthropogenic Species



Reproduction of Salawitch et al. 2017 figure 1.4, detailing the total change in RF of climate from preindustrial to 2011, as stated in tables 8.2 and 8.6 of AR5.

Figure 2.3 – Δ RF of Climate by Anthropogenic Species; Anthropocene



Reproduction of Salawitch et al. 2017 Figure 1.3a. The bold red line here is the same as the bold red line in Figure 1.1.

and also because this compound is not emitted in appreciable amounts by human activities.

The large differences in GWP due to the saturation effects partially offset the larger differences in the concentrations of CO₂ (400ppmv), CH₄ (1.8ppmv), and N₂O (0.33ppmv). As such, the change in RF of these “big three anthropogenic GHGs” over the past few centuries ultimately are within one order of magnitude. This result is visualized in figure 1.4 of Salawitch et al. [2017], reproduced here as figure 2.2. The change in RF since 1750 due to CO₂, the most abundant GHG, is slightly over 1.8 W/m², while increases in CH₄ and N₂O have caused rises in their respective RF values of 0.48 and 0.17 W/m². Figure 2.2 places the “big three” in the class of Well-Mixed GHGs along with ozone depleting substances (ODSs) and other fluorinated gases (F-gases). Multiple different species make up the classes ODSs and other F-gases; all are rare in the atmosphere but also have incredibly high GWPs. Among these gases, no individual compound exerts a tremendous influence on the climate system, but as a group they have similar RF to CH₄ in their effect on Earth’s energy balance. Still, the historic change in RF due to all GHGs only outstrips the change from the “big three” by a small amount. This difference is also a recent development, which can be seen in figure 1.3a of [Salawitch et al., 2017], reproduced here as figure 2.3. (Take note that the solid red line in figure 2.3, representing the total RF due to humans, is the same as the solid red line in figure 1.1.) In figure 2.3, the dashed red line (all GHGs) and the dotted red line (“big three”) do not visually diverge until roughly 1970 (and then return to being parallel by roughly 1990). This recent divergence, combined with the fact that most ODSs and F-

gases are not produced in the natural environment, is part of the evidence supporting the notion that current global warming is caused almost entirely by humans.

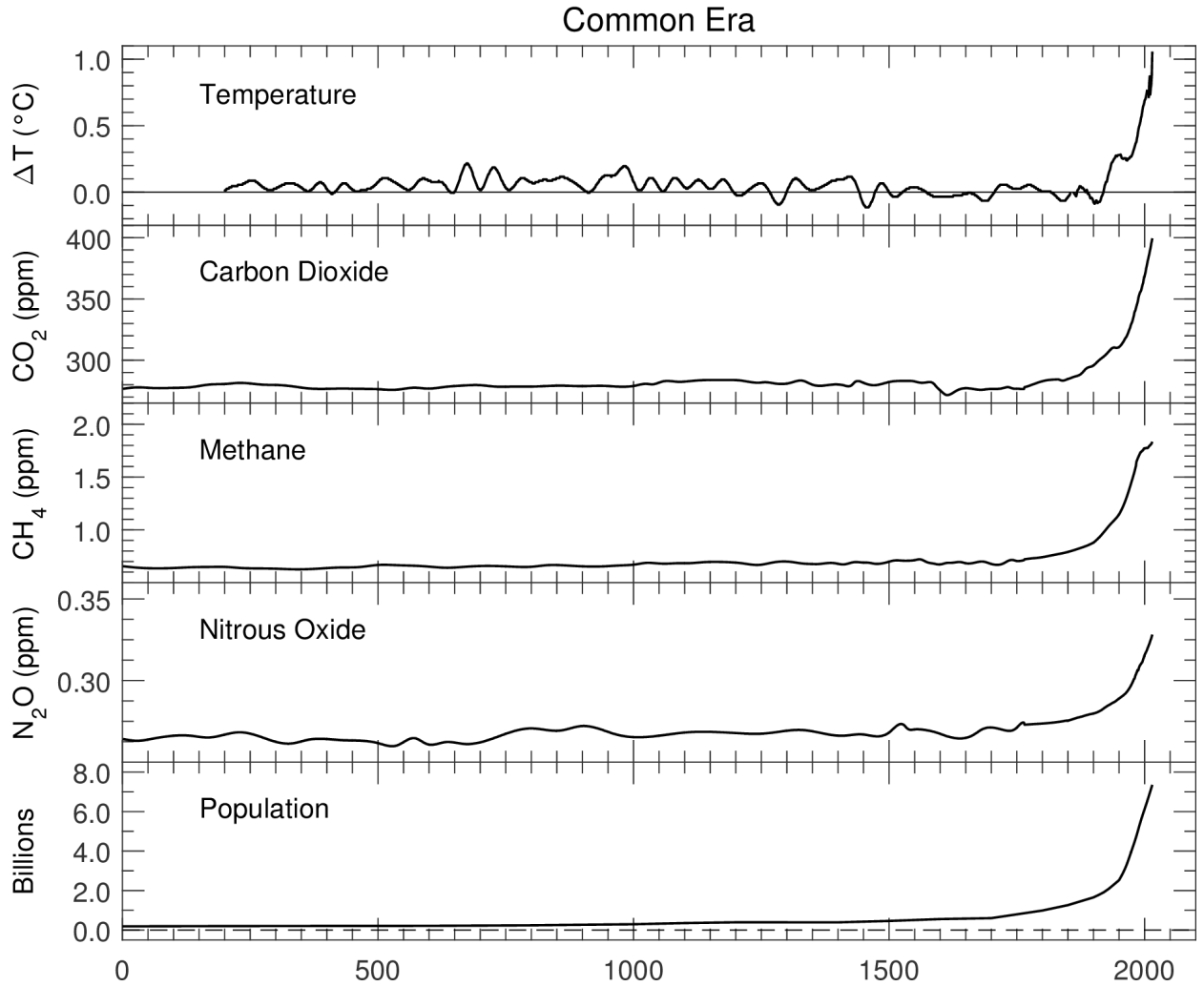
2.2 Human Fingerprints on Global Warming

Humans have only existed on Earth for a short time in the geological sense, and human society was not industrialized until a few hundred years ago. The Earth system has experienced larger temperatures swings in its past than observed over the past few hundred years. As such, it might at first seem like the thought that humans are greatly influencing the climate system is an extraordinary claim that requires extraordinary evidence. Figure 1.3 shows an incredibly strong correlation between atmospheric CO₂ and GMST – but correlation does not imply causation. It is already known how the physical properties of GHGs (§2.1) can lead to the Greenhouse Effect (§1.1.2) – but linking the rise in GHGs to human activity has not yet been thoroughly examined in this document. To properly establish this link, the next section provide multiple lines of evidence for the anthropogenic argument of global warming and evidence against any possible natural explanations for the current observed warming temperature trend.

2.2.1 The “Hockey Sticks”: Multiple Strong Recent Correlations

The assumption that humans have indeed had a strong influence on the climate system during a geologically short time on Earth begs the question of whether there is a macroscopic uniquely human quantity whose imprint is clearly seen in the climate. An obvious candidate for such a quantity would be total human population, which has remained relatively low for much of human history but has shown nearly exponential growth over the past two or three centuries. It thus remains to show a causal link between human population and increased forcing on the climate system.

Figure 2.4 – GMST, GHGs, and Population; Common Era



Reproduction of Salawitch et al. 2017 Figure 1.2, showing the comparison between temperature change since preindustrial time, the atmospheric concentrations of the big three GHG species, and total human population over the past 2000 years.

Figure 1.2 of [Salawitch *et al.*, 2017], reproduced here as figure 2.4, shows how human population, the “big three” GHGs, and GMST have changed over the Common Era. The changes over time for all five quantities, from the roughly exponential recent growth in human population to the “hockey stick” of recent GMST, famously so-coined by Michael Mann, exhibit startlingly strong visual similarity to each other. As with the discussion of Figure 1.3, correlation does not inherently imply causation. Indeed, each of the “big three” GHGs has some natural sources of variability, so they are not entirely anthropogenic in their production. However, since there are causal mechanisms linking all five quantities, the similarity across these many different quantities is unlikely to be coincidental natural variations. Importantly, the arguments for mechanisms that lead from the other quantities toward higher temperatures are stronger than the arguments suggesting that the changes in temperature force the changes in the other quantities.

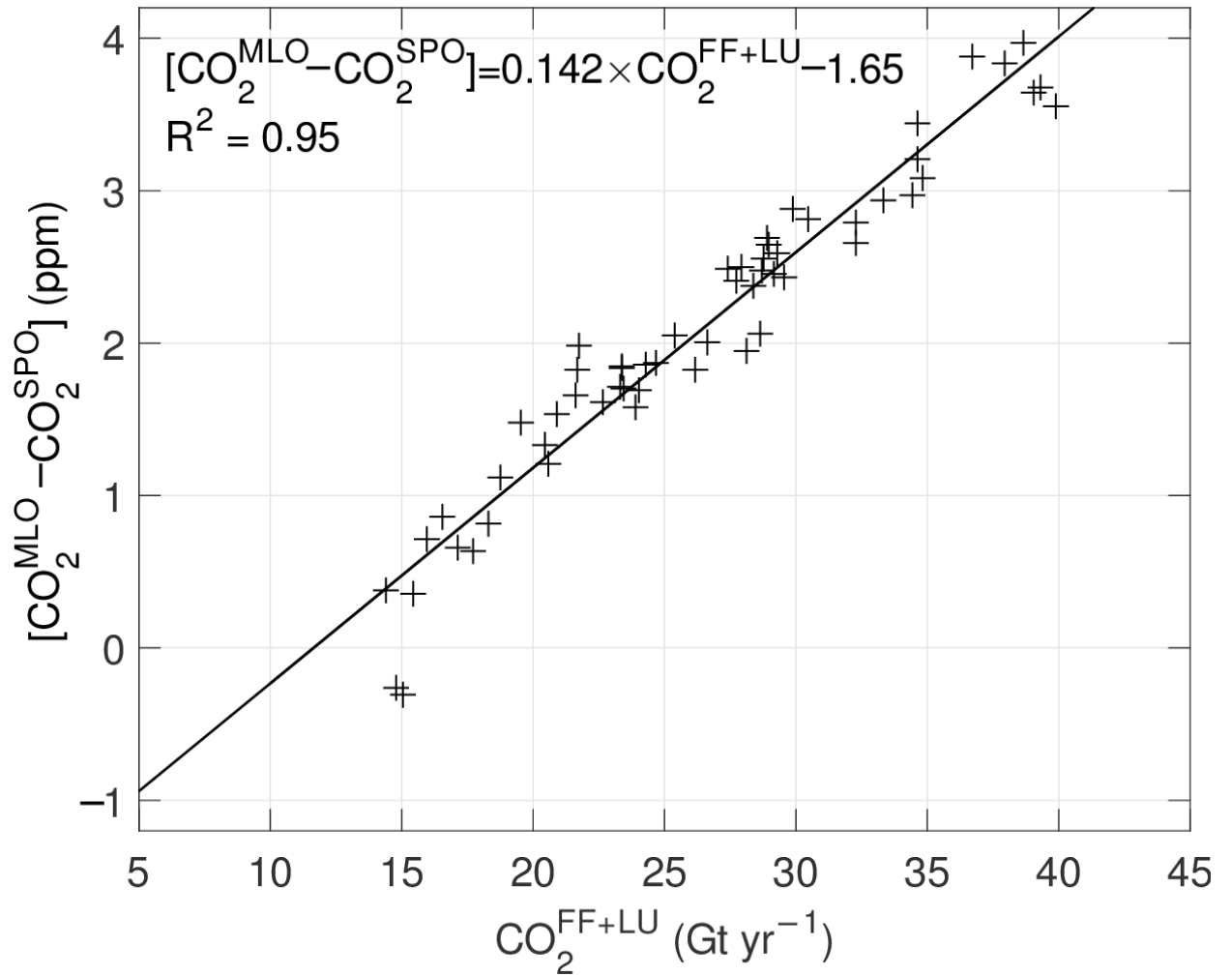
Each of the big three GHGs has a link to anthropogenic production, i.e. some aspect of either fossil fuel combustion (for electricity or for transportation) or agriculture (for both plants and animals), which will be explored in detail in the following sections. Food is a human necessity, and energy production is a key pillar of modern society – certainly for the past half-century, but also extending back to the beginnings of the Industrial Revolution and the invention of the steam engine by James Watt [Steffen *et al.*, 2015]. As such, it follows that the more people there are, the more there is a demand for food and energy. In our current society, this demand for food and energy necessitates large amounts of GHG emissions. These emissions then lead to higher GHG concentrations in the atmosphere, leading to higher RF through IR interaction and thus higher temperatures as described earlier.

2.2.2 Carbon Dioxide (CO₂)

Qualitatively, the “hockey stick” and associated mechanisms described in the preceding section already suggest the anthropogenic influence on the concentration and RF of atmospheric CO₂ (and other GHGs). In the modern instrument era, 1959 to present, direct measurements of atmospheric composition and temperature have become much more common, allowing for closer comparisons to justify the human fingerprints on climate. For CO₂, comparisons can be drawn between bottom-up annual estimates of anthropogenic CO₂ emissions from fossil fuel burning [*Boden et al.*, 2009] and land use changes [*R A Houghton et al.*, 2012] against top-down estimates of annual atmospheric CO₂ growth based on worldwide measurements of its concentration. Fairly consistently, the annual ratio between atmospheric growth and anthropogenic emissions is 40% to 50% [*Salawitch et al.*, 2017]. The ratio does fall outside this range on some years, usually on years with large positive or negative ENSO excursions, but the relatively consistency of the ratio provides a first level of quantitative reasoning to say the recent atmospheric growth of CO₂ follows directly from anthropogenic emissions. With this constant link, another explanation will be needed to explain why the atmospheric retention of CO₂ emissions is only roughly 50%. That is, while the correlation between CO₂ emission and CO₂ mixing ratio is quite high, suggesting a strong link between the two, further examination of the balance between CO₂ sources and sinks is necessary.

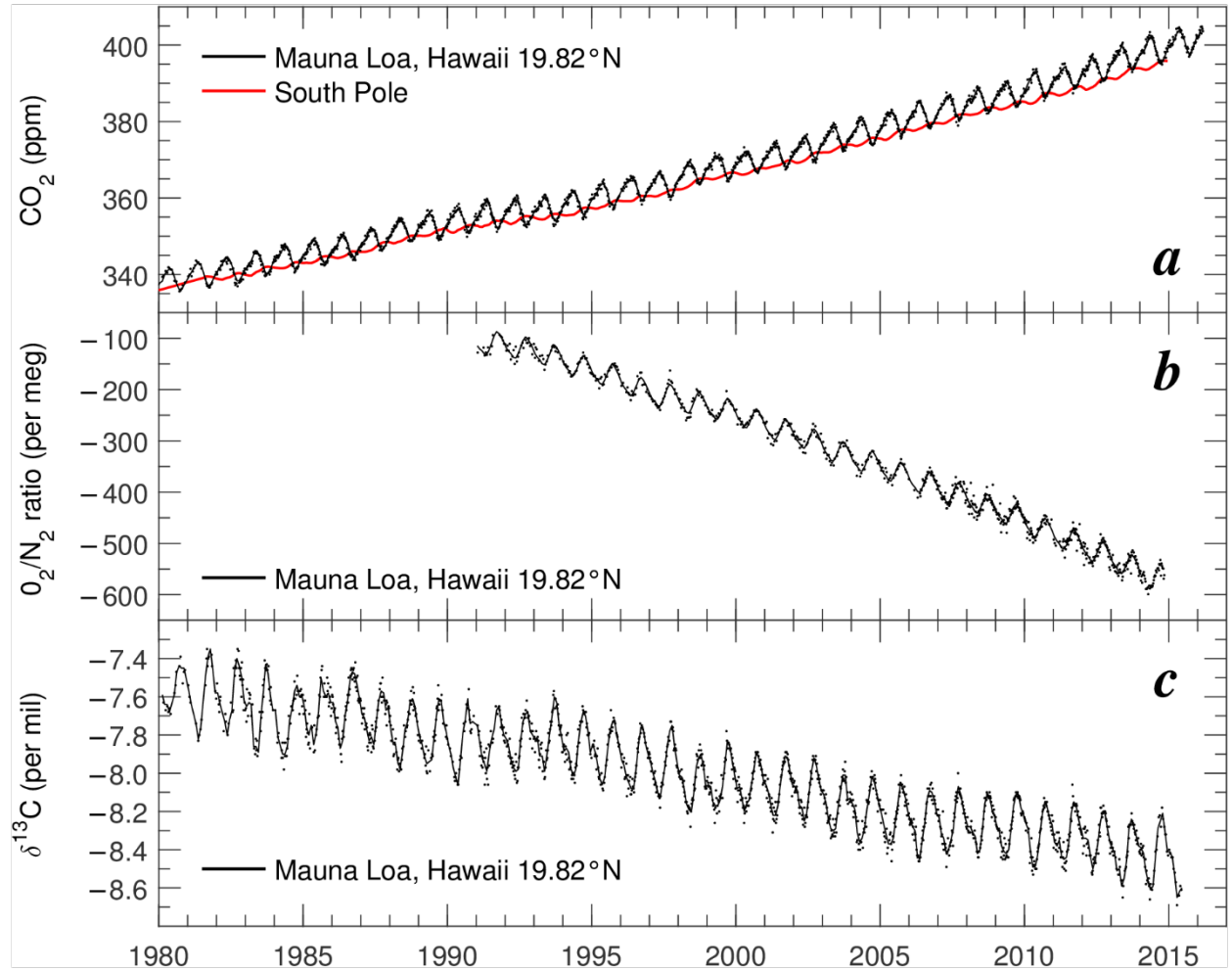
A second level of human fingerprinting on atmospheric CO₂ relies on the observed differences between hemispheres. CO₂ is considered a well-mixed GHG due to its long lifetime, hundreds of years for a majority of emitted CO₂ but several thousand years for the remaining fraction [*Archer*, 2005]. Atmospheric mixing across the equator

Figure 2.5 – CO₂ Yearly Emissions Rate vs Hemispheric Gradient



Reproduction of Salawitch et al. 2017 Figure 1.8. Horizontal axis is the annual anthropogenic emissions of CO₂; vertical axis is the difference in atmospheric CO₂ concentrations between Mauna Loa Observatory (representative of the Northern Hemisphere) and the South Pole Observatory (representative of the Southern Hemisphere). Data span 1959 to 2015.

Figure 2.6 – Atmospheric Chemistry Fingerprints of Anthropogenic Activity



Reproduction of Salawitch et al. 2017 Figure 1.7, showing three separate atmospheric chemistry trends that can be attributed to human activity, specifically the burning of fossil fuels.

takes much longer than latitudinal mixing within each hemisphere, which is a function of the strong separation of atmospheric circulation cells at the equator. Figure 1.8 of [Salawitch *et al.*, 2017], reproduced here as figure 2.5, shows the difference between northern and southern hemisphere annual CO₂ concentrations as a function of total annual emissions of CO₂. This comparison shows a strongly linear relationship. The vast majority of the world's population, and thus the majority of the world's CO₂ emissions, is based in the northern hemisphere [Fan *et al.*, 1999; Tans *et al.*, 1990]. As such, the positive linear relationship in figure 2.5 follows logically from the fact that more emissions come from the northern hemisphere, forcing higher concentrations in the north, and the lack of mixing across the equator prevents the smoothing of this excess.

The third and perhaps strongest line of evidence linking the observed rise in atmospheric CO₂ to anthropogenic emissions, particularly from fossil fuel combustion, comes from precise measurements of atmospheric composition and isotopic analysis. Figure 1.7 of [Salawitch *et al.*, 2017], reproduced here as figure 2.6, shows three panels, the first of which shows an alternate view of the hemispheric gradient in CO₂ by comparing observations over time from Hawaii (black dots) and Antarctica (red line).

The second panel of figure 2.6 examines the ratio of molecular oxygen to nitrogen in the atmosphere, which has been decreasing over the past 25 years. A strong decrease in atmospheric O₂ would suggest one of two things: the balance between respiration and photosynthesis has been shifting toward the former, or that there has been an excess of combustion globally. In either case, the net reaction is that O₂ is consumed to produce CO₂ at a rate of roughly 1 ppm of CO₂ increase for every 10 per meg decrease in the O₂/N₂ ratio [Antweiler, 2015]. Both cases are anthropogenic in nature, as a shift in

respiration versus photosynthesis means removal of green area and excess combustion means fires being set for agriculture or industry, thus suggesting that the associated rise in CO₂ is anthropogenic. Over the time period of figure 2.6b, the O₂/N₂ ratio falls between 400 and 500 per meg while the CO₂ mixing ratio grows by roughly 45 ppm, validating the ratio of *Antweiler* [2015]. It is important to note that, stoichiometrically, a 10 per meg decrease in the O₂/N₂ ratio should correspond to a 2 to 3 ppm increase in CO₂ mixing ratio, not a 1 ppm increase. However, less than half of CO₂ emissions remain in the atmosphere [*Antweiler, 2015; Canadell et al., 2007; Salawitch et al., 2017*]; the rest are taken up by land or ocean reservoirs, decreasing the expected 2 or 3 ppm of CO₂ to the 1ppm of CO₂ that remains in the atmosphere. As such, the anthropogenic production of CO₂ as evidenced by the decreasing O₂/N₂ ratio is entirely sufficient to explain the observed rise in atmospheric CO₂.

The third panel of figure 2.6 shows the decrease of heavier ¹³C in atmospheric CO₂ relative to the more common, lighter ¹²C [*Keeling et al., 2005*]. Fossil fuels are widely accepted to have biologic origin, resulting in a lighter isotopic signature than the current atmospheric reservoir [*Whiticar, 1996*]. Some generally discounted theories suggest a geologic origin for the lighter signature [*Glasby, 2006*], implying “fossil” as a signifier of biology is a misnomer, but this does not change the fact that fossil fuels are easily measured to be isotopically light. While the isotopic composition of carbon in the atmosphere does change over geologic time scales, it theoretically should remain fairly constant over the time period of modern instrument observations if only natural factors dictated changes over time. As such, the lightening of the atmospheric reservoir suggests a perturbation from an isotopically light source such as fossil fuel combustion. If one

assumes the increase in CO₂ over the time period of figure 2.6c is entirely from fossil fuel combustion, (a change in $\delta^{13}\text{C}$ of roughly -28‰), then the growth from roughly 340 ppm to roughly 400 ppm would cause the atmospheric isotope signature to fall from roughly -7.5‰ to -10.5‰ . This endpoint is noticeably lower than the -8.5‰ observed; however, we know that plants preferentially absorb $^{13}\text{CO}_2$, meaning that the lightening of the atmosphere could be lessened through increased biologic production, and we do have observations of increased biologic activity over the past five decades [*N Zeng et al.*, 2014]. Importantly at least, human activity is more than enough to explain the change in $\delta^{13}\text{C}$; any natural activity affecting this ratio must have been to counteract the anthropogenic changes occurring.

Both the oxygen ratio and the carbon isotope arguments also prove that the rise in atmospheric CO₂ is not from natural outgassing. If CO₂ were to come from the ocean, from volcanoes, or other natural sources, natural outgassing would not consume atmospheric oxygen. The only possible natural source of CO₂ would be from massive amounts of decomposition, well above and beyond the existing balanced carbon cycle, which has not been observed, nor would be considered outgassing. Volcanoes can be ruled out as well, as a lack of any active large igneous province means that human emissions of CO₂ during the industrial era simply far outstrip volcanic emissions; only on the day that Pinatubo erupted has volcanic CO₂ output has matched human output on the same day [*Gerlach, 2011*]. As such, the O₂/N₂ ratio would not be expected to fall, or change in any direction significantly, if the changing CO₂ mixing ratio was only from outgassing. Similarly, the isotopic signature of atmospheric CO₂ should not be falling significantly as observed if outgassing explained most or all of the rise in CO₂ mixing

ratio. This is because oceanic CO₂ is barely lighter than atmospheric CO₂, and geologic CO₂ is much heavier [Rizzo *et al.*, 2014]. Therefore, unless there is another natural source of CO₂ yet to be documented, the conclusion must be that the observed rise in atmospheric CO₂ is mostly, if not entirely, caused by various human activities that involve combustion along with a slight contribution from the manufacturing of cement.

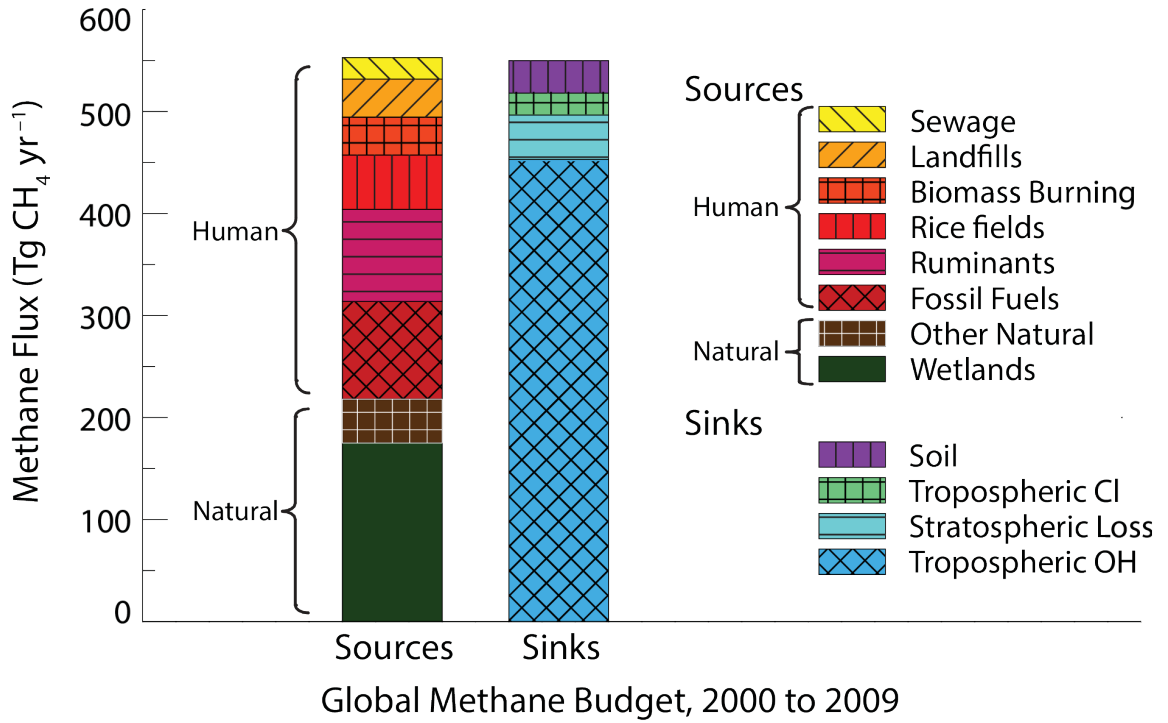
2.2.3 Other GHGs

2.2.3.1 Methane (CH₄)

The most abundant GHG after CO₂ is methane, CH₄, with a current mixing ratio of roughly 1.86 ppm. As with other major GHGs, this value is significantly higher than in even the moderately recent past, e.g. roughly 0.65 ppm over the Common Era (Figure 2.4), with the increase following the “hockey stick” that mirrors human population growth. Anthropogenic CH₄ emissions come from a wide variety of sources in roughly equal amounts, and out-emit the natural sources. Both of these facts make CH₄ a noticeably different GHG than CO₂, making the study of CH₄ a varied and complex issue (see Kirschke *et al.* [2013] and the references therein). Both the sources and sinks of CH₄, taken from 2000 to 2009, are summarized in figure 1.9 of [Salawitch *et al.*, 2017], reproduced here as figure 2.7.

The sinks for CH₄ are dominated by tropospheric chemistry. The hydroxyl radical (OH), commonly called the “detergent” of the atmosphere, scavenges many species out of the air (including CH₄) as the most common oxidizer in the troposphere. It has an incredibly short lifetime (less than one second) but is produced with enough abundance that the increase in CH₄ emissions due to humans has been nearly (but not completely) matched by an increase in the CH₄-OH reaction.

Figure 2.7 – Global Methane Budget, 2000 to 2009



Reproduction of Salawitch et al. 2017 Figure 1.9.

Understanding the balance between sources – particularly the wide variety of anthropogenic sources – and sinks is key to projecting CH₄ mixing ratio (and thus RF) into the future. The growth in atmospheric CH₄ seen over the past ten years, unfortunately, is not well understood yet [Nisbet *et al.*, 2019]. It is uncertain whether the recent increase in CH₄ is from growth of isotopically negative emissions from wetlands, ruminants, and waste, from a large increase in emissions associated with natural gas and oil production, or from a weakening in the oxidative capacity of the atmosphere – or whether the observed increase is due to something else altogether. The sheer variety of possible sources also makes the task of curbing CH₄ growth difficult, as any plan to significantly reduce CH₄ emissions would require a comprehensive strategy that covers many aspects of modern society, in contrast to the relatively simple plan for reducing CO₂ emissions by replacing fossil fuels with renewables. Complicating such a plan even further is the release of CH₄ from natural sources (such as the permafrost of undersea methyl clathrates) in response to anthropogenic warming – a feedback that was mostly theoretical until recent evidence of significant permafrost loss [Richter-Menge *et al.*, 2019; Voigt *et al.*, 2017]. This feedback process is particularly important as proper quantification of these extra emissions can noticeably affect the carbon budget [Comyn-Platt *et al.*, 2018], the amount of carbon that humanity can emit before crossing a specific warming threshold, i.e. there are different carbon budget amounts if global warming is to be limited to just 1.5°C versus being allowed to grow to 2°C.

One straightforward way to show the human fingerprint on atmospheric CH₄ is to compare the mass balance of CH₄ between the current atmosphere and the atmosphere before significant human influence, e.g. the preindustrial atmosphere. Initially, assume

that the lifetime of CH₄ has remained roughly equivalent between the two atmospheres; while the atmospheric lifetime of CH₄ is affected by the abundance of species such as OH, it is likely that the lifetime of CH₄ has not changed significantly. Atmospheric lifetime for a species is defined here as the ratio of atmospheric mass of the species (i.e. its mixing ratio m times the total atmospheric mass) divided by its removal rate. Another assumption for this calculation is that the total mass of the atmosphere (M_{atmos}) has not changed significantly since preindustrial times, as it is highly unlikely that loss of atmosphere to space has been significant over the past few centuries compared to the atmosphere's total mass. Finally, assume that removal rate (R) for each time frame is the same as emission rate (E). The last of assumptions is not explicitly true for the modern atmosphere because CH₄ is currently increasing, but the difference is small enough (Figure 2.7) that this is a good approximation. Those definitions and assumption then lead to the following algebra:

$$\begin{aligned}\tau_{\text{CH}_4} &= \frac{M_{\text{preindustrial}}}{R_{\text{preindustrial}}} = \frac{M_{\text{current}}}{R_{\text{current}}} \\ \rightarrow \frac{m_{\text{preindustrial}}M_{\text{atmos}}}{E_{\text{preindustrial}}} &= \frac{m_{\text{current}}M_{\text{atmos}}}{E_{\text{current}}} \\ \rightarrow \frac{m_{\text{preindustrial}}}{m_{\text{current}}} &= \frac{E_{\text{preindustrial}}}{E_{\text{current}}}\end{aligned}$$

Eq 2.1

If humans have been entirely responsible for the rise in atmospheric CH₄, that would mean the emission rate from natural sources has remained constant over time, and thus the last ratio in Eq 2.1 can be rewritten as $E_{\text{current-nat}} / (E_{\text{current-nat}} + E_{\text{current-hum}})$. The ratio of mixing ratios is 0.722ppm / 1.86ppm = 0.388; the ratio of emissions is 218Tg/yr / 553Tg/yr = 0.394. These two numbers agree within 2%, providing a strong

quantitative argument that the rise in atmospheric CH₄ between preindustrial times and now is entirely due to the addition of human emission sources to a world that previously only had natural sources. A more thorough argument along these lines would parse apart some of the stated assumptions, as well as account for the fact that anthropogenic CH₄ emissions in preindustrial times were actually nonzero due to the agriculture of the time, but these corrections should be minor, not significantly affecting the message of humans' influence on atmospheric CH₄.

The atmospheric lifetime of CH₄, which we leveraged above, is on the order of 10 years. The actual value is uncertain, as estimates can range from 9.1 years [Prather *et al.*, 2012] to 12.4 years [AR5], and the basic definition used above (mass divided by removal rate) gives a value of 9.7 years [Salawitch *et al.*, 2017]. Importantly, this lifetime is much shorter than the lifetime of CO₂. It could even be said that the lifetime of CH₄ in the atmosphere is on the order of a typical government term, e.g. ranging from a single two-year House of Representatives term to a typical eight-year presidential term to multiple six-year Senate terms. As such, CH₄ is an ideal target for policy aimed at short-term global warming reductions. Cuts to CH₄ emissions (along with related cuts to black carbon aerosols and the resulting drops in ozone RF) can cause a reduction in global warming of roughly 0.5°C, a reduction that is realized within ten to twenty year [Shindell *et al.*, 2012] due to CH₄'s relatively short lifetime. That is, if CH₄ emissions were drastically cut, it would only take roughly ten years for the CH₄ currently in the atmosphere to cycle out, thus greatly dropping CH₄'s RF and thus quickly backtracking its contribution to global warming. The wide variety of anthropogenic CH₄ sources make coordinating such cuts somewhat difficult, but it also potentially makes garnering support

and implementing each individual cutting effort easier, as no single entity would have to worry about a large portion of the CH₄ budget.

2.2.3.2 Nitrous Oxide (N₂O)

N₂O is often said to be the third strongest anthropogenically emitted GHG after CO₂ and CH₄, but the actual anthropogenic component to the growth in N₂O since preindustrial times is somewhat uncertain. The **AR5** best estimates for current natural and anthropogenic emission of N₂O are of similar magnitude at 34.6 Tg/yr and 21.7 Tg/yr respectively. (These values are in Tg/yr of N₂O, while Table 6.9 of **AR5** reports emissions in Tg/yr of N alone.) Using a quantitative argument similar to the one described in the previous section for CH₄ would suggest that an observed increase in atmospheric N₂O of roughly 63% could be entirely attributed to human activity. However, properly accounting for the fact that N₂O has a much longer lifetime than CH₄ (i.e. the anthropogenic emission rate of N₂O has changed noticeably during a lifetime) would somewhat reduce this fraction. Also, both estimates for current emissions are highly uncertain, with a natural emission uncertainty range from 17.0 to 61.6 Tg/yr and an anthropogenic emission range from 8.5 to 34.9 Tg/yr. These ranges could cause the attributable increase to fall as low as 14% (even before accounting for lifetime) or grow to 205% around the best estimate of 63%.

The observed growth in atmospheric N₂O from preindustrial times to the present is from 273ppb to 329ppb – an increase of 21%. If the lifetime-accounting reduction factor mentioned above is roughly a factor of two, we are comparing that observed 21% increase to calculated ratios of 7% (low end), 32% (best estimate), or 102% (high end) – suggesting that the **AR5** best estimates for current natural and anthropogenic N₂O

emission are reasonable based on observations, and thus that humans are indeed responsible for the majority of the observed increase in N₂O.

In addition, station observations of atmospheric N₂O show a hemispheric gradient with more in the northern hemisphere, as would be expected with an anthropogenic signature on global N₂O. There are also a multitude of studies (e.g. §6.3.4 of **AR5** and the references therein) documenting field measurements of strong anthropogenic sources of N₂O. These are enough to justify the notion that much of the increase in N₂O is human-driven, especially from agricultural sources, which make up roughly 60% of anthropogenic N₂O emissions.

2.2.3.3 Halogenated gases

Figure 2.2 includes anthropogenic forcing from Ozone Depleting Substances (ODS) and other F-gases in the category of well-mixed GHGs. These gases all include atoms of halogens – specifically Fluorine, Chlorine, and/or Bromine. This group of gases includes the chemical families of Chlorofluorocarbons (CFCs), haloalkanes (Haloalkanes), Hydrochlorofluorocarbons (HCFCs), Hydrofluorocarbons (HFCs), and Perfluorocarbons (PFCs), among other individual compounds. With a few rare exceptions, all these halogenated gases are entirely manmade with no natural sources. (While chloro- and bromomethane, CH₃Cl and CH₃Br, are two such halogenated gases with natural sources, they are among a handful of uncommon halogenated gases that are not included in the **AR5** data used to make figure 2.2.) As such, it is fair to consider the effect of halogenated gases on the climate system to be essentially entirely anthropogenic in origin.

Halogenated gases are incredibly rare in the atmosphere, even with the many different species of gases emitted. However, they are highly influential compounds in the

atmosphere, both chemically and radiatively. Almost all these compounds have dangerously high GWP values, starting at around 100 and going up to two orders of magnitude higher. Many ODSs and F-gases also have long lifetimes, similar to or longer than CO₂ and N₂O. The high GWP values result from the strong dipole moments formed by the halogen-carbon bonds in each molecule, as these bonds react strongly to radiation in the IR portion of the spectrum [*Ramanathan, 1975; Salawitch et al., 2017*].

Halogenated compounds, as a family, account for over 12% of all anthropogenic GHG forcing (0.36 W/m² out of 2.83 W/m² total) despite their rarity in the atmosphere – only three species register at more than 100 ppt (**AR5**).

2.2.4 Anthropogenic Aerosols

The effect of anthropogenic aerosols on the climate is simultaneously relatively easy to identify and rather hard to quantify. Aerosols are particles of liquid or solid suspended in the atmosphere, so their atmospheric lifetime is much shorter than that of GHGs. These particles either settle out of the atmosphere (dry deposition) or act as condensation nuclei to form cloud and rain droplets, leading to them being removed by precipitation (wet deposition, which can also include removal by being caught in falling rain). For any aerosols in the troposphere, both deposition processes usually occur within the time frame of a week. With such a short lifetime, aerosols generally do not become well-mixed in the atmosphere, and this heterogeneity makes it relatively easy to identify major sources of aerosols – both natural and anthropogenic. For example, persistent plumes dominated by sulfur-containing aerosols consistently rise and spread from industrialized centers of the world, while similar plumes of black, brown, and white (organic) carbon cover areas downwind of major wildfires, and large-scale wind patterns

often pick up dirt & mineral aerosols or sea salt aerosols respectively from arid regions and oceans. This means that it is easy to see where on the planet specific aerosol sources are and attribute those sources to natural or anthropogenic causes.

In practice, quantitatively meaningful attribution takes more attention to detail. While industrial fossil fuels sources that produce sulfate and nitrate aerosols (and some organic carbon) clearly are anthropogenic, some sources that outwardly appear to be natural in origin can also have human causes. Agricultural burning produces the same aerosols as wildfires, making it sometimes hard to distinguish the two. Evidence also suggests that current global warming is causing an increase in wildfire patterns above the natural baseline [*Pechony and Shindell, 2010; Running, 2006; Walker et al., 2019*] due to areas such as the US southwest and Australia becoming both drier and warmer as a result of anthropogenic climate change. That is, average conditions in those areas are becoming more prone to ignition. Similarly, discernable changes in surface patterns due to global warming can cause more mineral and sea salt to be lofted into the atmosphere, particularly in the polar regions [*McConnell et al., 2007; Struthers et al., 2011*]. Emissions/forcing scenarios intended to represent anthropogenic effects only (such as the RCP scenarios) thus include time series for all of these aerosol species [*Lamarque et al., 2011*] to represent the anthropogenic change in aerosol species that would otherwise be considered natural in origin.

Quantifying the radiative anthropogenic effect of aerosols on climate is one of the least certain areas of climate science. Excepting black carbon, most aerosols produce a neutral or negative direct effective RF (ERF) on climate with increasing concentrations. Even this is a simplification, as the difficulty in quantifying aerosol ERF causes the best

estimate for each species to change over time and sometimes depend on region.

Unsurprisingly then, the exact values for these direct ERFs are uncertain with an error on all species of at least 50% in both directions (**AR5**). For direct ERF, much of this uncertainty comes from the difficulty in measuring aerosol ERF in situ or in lab; many estimates of aerosol forcing are produced in aerosol models [*Myhre et al.*, 2013]. While the forcing due to sulfate aerosols dominates the direct aerosol effect and is comparatively certain, (with an **AR5** estimate of $-0.4 \pm 0.2 \text{ W/m}^2$), the warming effect due to black carbon continues to be studied and updated [*Bond et al.*, 2013]. While **AR5** used research from the *Bond et al.* [2013] group to increase black carbon forcing versus **AR4**, the increase was smaller than *Bond et al.* [2013] would suggest, and a following analysis from *Smith and Bond* [2014] suggest the total (primary direct and secondary indirect) RF of aerosols in 2011 is -0.75 W/m^2 , not the -0.9 W/m^2 suggested by **AR5**.

Other uncertainties come from dust aerosols, which generally reflect sunlight but can also cause warming [*Tian et al.*, 2018; *Xia et al.*, 2016], and from biomass burning, which recent analyses suggests should include less influence of cooling organic aerosols in favor of neutral-to-warming brown carbon aerosols [*Feng et al.*, 2013; *Giles et al.*, 2012; *Jo et al.*, 2016]. The exact balance between warming aerosols (i.e. black and brown carbon, plus some dust) and cooling aerosols thus can produce a wide range of values for the direct effect of anthropogenic aerosols. These values are generally negative, but the upper end of AR5's aerosol-radiation interaction estimate does give the possibility of weakly positive values, and other analyses outside of AR5 further encourage these weakly positive values.

Aerosols also affect radiative balance through several secondary effects, mostly through interactions with clouds. Clouds can both absorb outgoing longwave terrestrial radiation to be re-radiated back toward the ground (acting in a similar manner to GHGs) and reflect incoming shortwave radiation back to space (acting in a similar manner to reflective sulfate aerosols themselves). The balance between these effects depends on cloud abundance, height, and lifetime – all of which change depending on the number of available cloud condensation nuclei, i.e. the aerosol particles in the atmosphere. The aerosol semi-direct effect describes when clouds “burn off” due to tropospheric heating from warming aerosols [*Ackerman et al.*, 2000]; in **AR5**, it is included in the family of rapid adjustments to the aerosol direct effect (aerosol-radiation interactions). The cloud lifetime or Albrecht effect describes how cloud lifetime increases with increasing aerosol concentration because more condensation nuclei means smaller droplets, causing clouds to rain less frequently [*Albrecht*, 1989]; in **AR5**, this effect is included in the family of rapid adjustments to the aerosol indirect effect (aerosol-cloud interactions). The cloud albedo or Twomey effect describes the increase in cloud albedo that also follows from the increasing number and decreasing size of cloud droplets due to an increased number of condensation nuclei [*Twomey*, 1974].

Cloud microphysics are notoriously difficult to simulate in climate models due to the difference in scale, and the variety of parameterization methods between models means that different models can disagree widely on cloud properties, including the value of forcing due to aerosol-cloud interactions. While the average estimate of the aerosol indirect effect is roughly the same as the estimate of the aerosol direct effect, both stated as -0.45 W/m^2 in **AR5**, the lower end of the uncertainty estimate for the aerosol indirect

effect goes much further negative. This leads to the total effect that anthropogenic aerosols have on climate as -0.9 W/m^2 with a 5 to 95% confidence interval of -0.1 to -1.9 W/m^2 , making aerosol RF the dominant contributor to the uncertainty in the total anthropogenic RF on climate.

2.2.5 Final Comments on Anthropogenic Fingerprints and the Evolution of RF Over Time

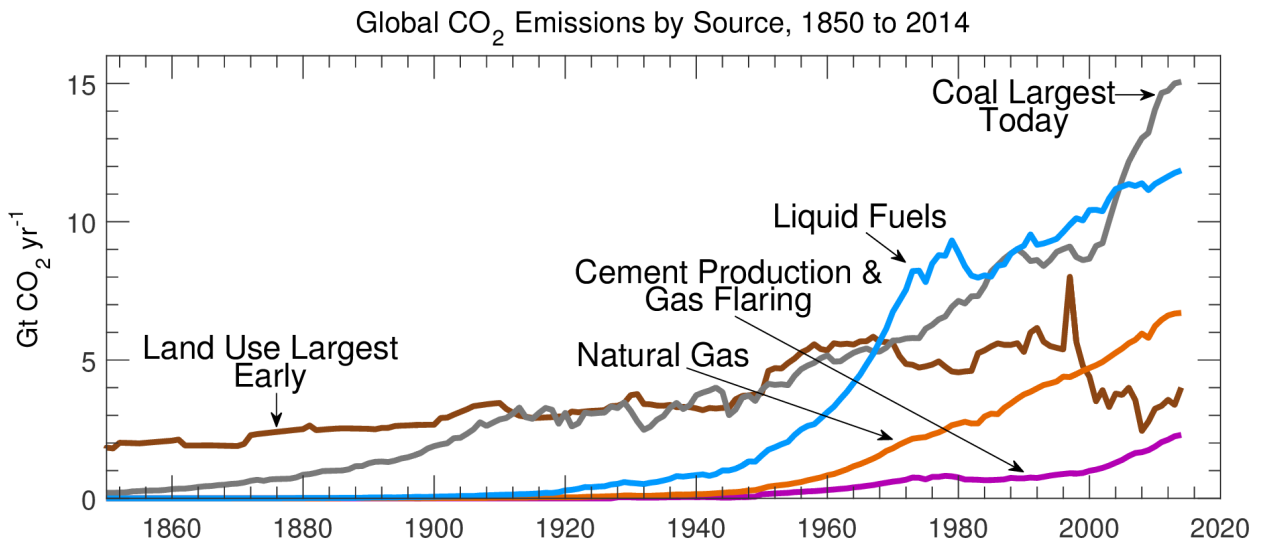
The fact that anthropogenic emissions of GHGs and aerosols have altered the composition of the atmosphere and caused an overall increase in RF is hopefully clear by now. The best estimates for these quantities are pictured in figures 2.2 and 2.3. The exact relationship between concentrations and RF is dependent on species, as mentioned during the discussion about GWP earlier in §2.1. A closer look at the evolution of RF in figure 2.3 shows some of the major changes in human activity and thus further proves the connection between humans and the current period of global warming.

The RF effect of ODSs and other F-gases shows a clear signal related to industrial production in figure 2.3. This effect does not visually appear until around 1960, and grows until around 1990, after which the rise in RF for “All GHGs” is driven entirely by the rise in the RF of the “big three”. Among ODSs and F-gases, one of the largest components is CFCs. While the first CFCs were invented in 1928, their production and use skyrocketed in the 1960s. This process did not slow (and eventually halt) until the mechanism for CFC-catalyzed O_3 depletion was discovered in 1974 and the Montreal Protocol was ratified in 1984 (and further amended multiple times between 1990 and 1999). As such, the RF pattern of CFCs and many related gases directly mirrors the industrial and political realities of the times in dealing with those substances. Even

though the gases were comparatively rare in the atmosphere, the growth from 1960 to 1990 was particularly strong because the GWP of these chemicals scales linearly with their concentration, as opposed to the logarithmic or square-root scaling rate for CO₂, CH₄, and N₂O. Their RF effect has not gone away since 1990, despite the lack of production, due to how long-lived many of these gases (and their byproducts) are in the atmosphere.

Social and economic changes in human history can also be seen in the rise of aerosol RF and its delay compared to the rise in GHG RF. While anthropogenic GHG RF rises above 0 W/m² almost immediately when data begins in figure 2.3, the overall cooling effect of aerosols does not clearly appear until the early 1800s and does not become comparable to GHG RF magnitude until several decades later. This perfectly mirrors a shift from a largely agricultural society to one that includes small-scale coal burning to the industrial-scale usage of fossil fuels. This does not imply that humans were not producing a large amount of aerosols before the industrial revolution; it does, though, show a paradigm shift from a society dominated by biomass burning (which has an RF that is weakly positive or negative, in any case near zero) to one ultimately dominated by sulfates and nitrates (which have strongly negative RF). This shift from agriculture to industry can also be seen by breaking down total CO₂ emissions over time into different time series by source, such as done in figure 4.1 from Bennett et al. [2017], reproduced here as figure 2.8. As such, the growth of aerosol RF, especially when compared to RF from co-emitted GHGs, is yet another line of evidence showing the human influence on climate.

Figure 2.8 – CO₂ Emissions by Source; Anthropocene



Reproduction of Bennett et al. 2017 Figure 4.1, showing how the relative importance of various anthropogenic CO₂ sources has changed over time. Note that the shift from agricultural burning (land use change emissions) to fossil fuel combustion (solid coal and liquid petroleum) comes with an associated shift from black and organic carbon aerosols (neutral to warming effect) to sulfate and nitrate aerosols (cooling effect).

2.3 Nonlinearity & Uncertainty of the Climate System

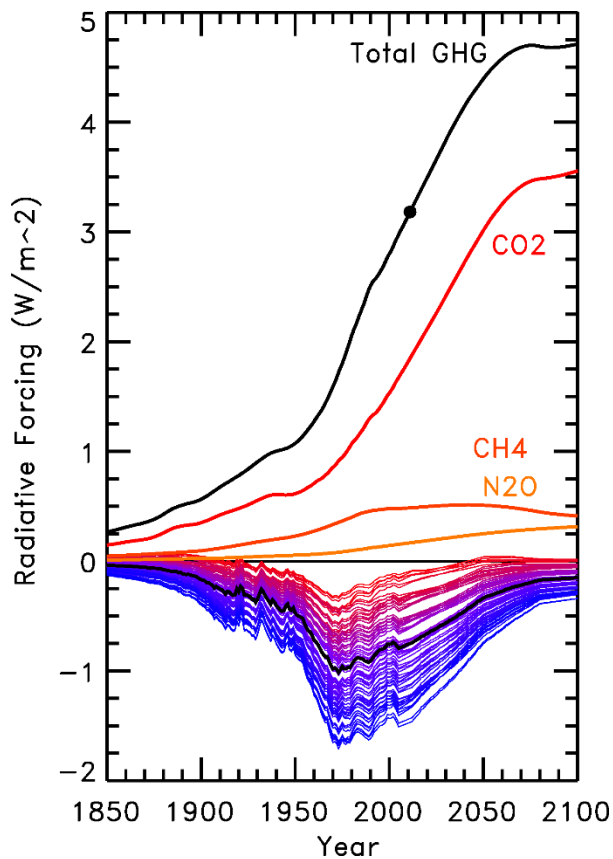
The overall evolution of aerosol RF can be clearly tied to human activity, but exact quantification of the historical growth in aerosol RF is much less certain, as shown in figure 2.2. The uncertainty in aerosol RF limits our ability to quantify a key aspect of the climate system: the ratio between a change in RF and the associated change in GMST, i.e. the constant c in Eqn. 1.3b. A basic blackbody interaction provides a zeroth-order estimate of that ratio, but Earth's climate system is complicated by many feedback processes that alter this ratio. Some climate feedback processes, such as the water vapor feedback (§2.1) and ice-albedo feedback (§2.3.1), amplify the temperature response to a change in RF, while others (such as the lapse rate feedback) reduce the response, and still others are highly uncertain, e.g. the net effect of cloud feedbacks (§1.2.1). If the net ΔRF is unknown due to uncertainty in aerosol RF, constant c from Eq. 1.3b cannot be confidently quantified, which also makes it difficult to determine the strength of each individual feedback process, even if a handful of them are well-quantified.

Uncertainty in the net climate feedback value presents another problem when attempting to project future GMST. The evolution of temperature over the next century will be driven by humans in two important ways: we continue to emit GHGs, increasing warming from GHG RF, and we are *eliminating* aerosol emissions, reducing cooling from aerosol RF. That is, no matter what the uncertainty in total RF has been to date, RF in the future will be relatively well-defined, based almost solely on GHG RF, which can be seen in figure 1.10 from Salawitch et al. [2017], *updated* here as figure 2.9. This means any uncertainty in future GMST will be driven by the current uncertainty in the total amount of climate feedback amplification, which is in turn tied to the uncertainty in

aerosol RF. If aerosol RF has been low, then total RF has been high, requiring a lower net feedback to match current historical GMST and thus leading to lower future GMST; the converse situation, high aerosol RF historically, similarly leads to extreme future warming.

A further complication is that feedback processes are not static over time. The amount of amplification or reduction they provide can change slowly over millennia (§12.5.3 of **AR5**) and can also change rapidly over short times if the climate system passes a tipping point, or nonlinearity of the system. As an example of the latter case, the ice-albedo feedback will theoretically speed up the warmer the planet because since ice melts faster under higher temperatures, but will also cease almost entirely if the polar ice caps were to melt completely because there would be no further reflective surfaces to lose. Clouds could also behave differently at higher or lower temperatures, or under alternate atmospheric aerosol loading conditions, changing the net effect of cloud feedback. Another potential tipping points could be a sudden release of GHGs from permafrost, though this is a different class of “feedbacks” because such a release is a direct change of a forcing agent itself, as opposed to a physical or chemical amplification of the forcing’s effect on temperature. All taken together, it is important to remember that Earth’s climate is a nonlinear system, which is why thorough simulations of the climate system require highly complex climate models that attempt to recreate all physical and chemical processes from small-scale to global scale. This is obviously very computationally intensive, so it is also worthwhile to attempt to reconstruct the climate system using simple, even linear, models of climate that can successfully capture the basic behavior of the climate system.

Figure 2.9 – Comparison of GHG RF vs Aerosol RF Uncertainty



Corrected version of figure 1.10 of Salawitch et al. 2017 with proper GHG RF, taken from RCP 4.5. Aerosol RF scenarios (blue-to-red time series below 0 W/m²) are constructed from Smith & Bond 2014; black line is the Smith & Bond best estimate of aerosol RF, which has a value of -0.75 W/m² in 2011, which is less extreme than the RCP best estimate of -0.9 W/m² in 2011. Black dot represents GHG RF in 2011, which we use as a comparison point to aerosol RF, whose value in 2011 is the reference point used in the EM-GC for sampling aerosol RF uncertainty.

2.3.1 Considerations for a Linear Model of a Nonlinear Climate

A simple linear model of climate can capture both first- and second-order changes in climate, even while making many assumptions and simplifications about the complex, nonlinear climate system. However, there are four key considerations that a simple model should be able to address to account for any differences between first- and higher-order temperature simulations [Marvel, 2018]. The four points are the different efficacies of forcing agents [Hansen et al., 2005; Solomon, 2007], the fact that feedback strength changes over time (§12.5.3 of AR5), the signal-to-noise interplay between internal variability and forced warming, and consideration of the energy imbalance going into the ocean and what effect that ocean heat export has on the atmosphere. While many empirical climate models do not consider some combination of these four points, the EM-GC incorporates them all aside from the changing climate feedback. These will be either implicitly or explicitly addressed to varying degrees in the next two chapters, but short explicit summaries are provided below as a group.

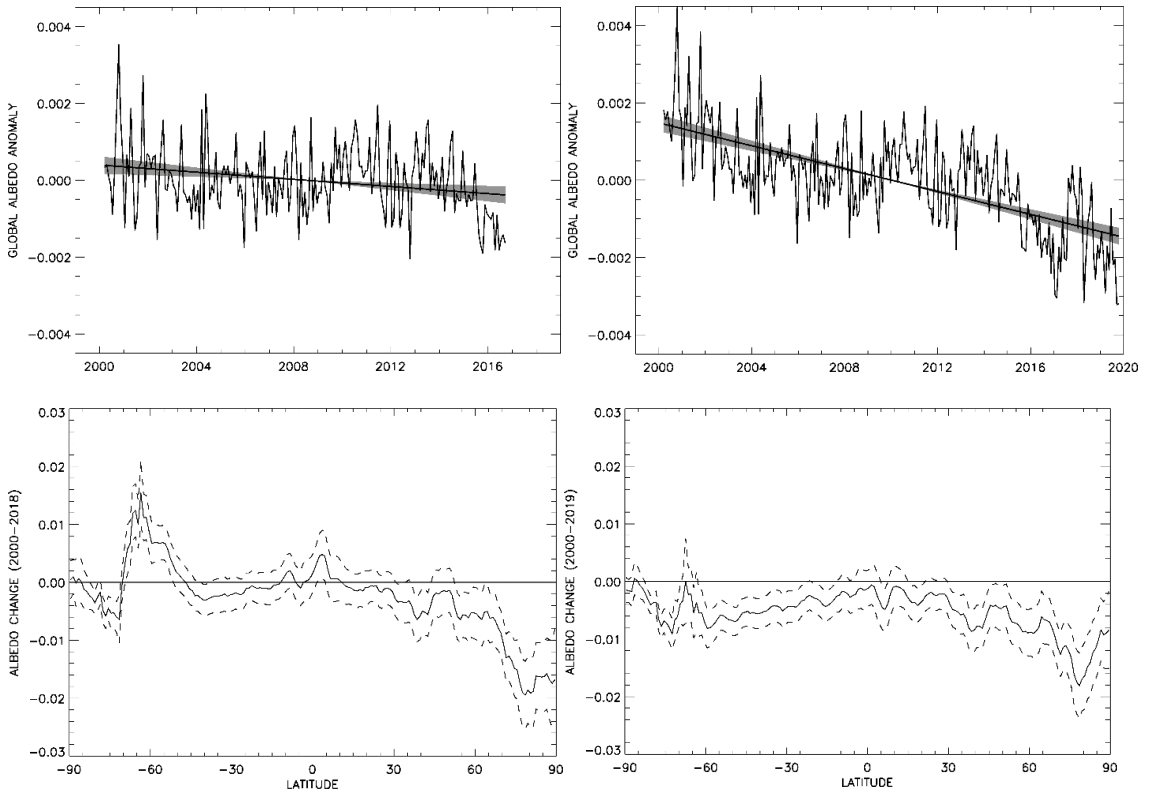
As the many different feedback processes work through multiple physical mechanisms, there is large consensus [Hansen et al., 2005; Solomon, 2007] that the climate system will respond differently to the same ΔRF when that ΔRF comes from various forcing agents. The EM-GC uses multiple linear regression (MLR) when examining the effect of natural forcing factors (e.g. solar input, stratospheric aerosol optical depth (SAOD) from volcanic eruptions, etc.), so any concerns about efficacy are folded into the regression coefficients for these model inputs. The EM-GC is not as flexible for the efficacy of different anthropogenic species since they are all grouped together before applying the climate feedback parameter, but this is not a major

drawback. The anthropogenic RF of climate is dominated by the well-mixed, long-lived GHGs (LLGHGs), which are themselves dominated by CO₂ forcing. Since efficacy is defined in relation to CO₂ RF, similar to how GWP is defined in relation to a pulse of CO₂ emissions, this means that a first-order estimate of efficacy for net anthropogenic RF is close to one. Efficacy for total anthropogenic RF would remain close to one at second order as well, as the generally greater-than-one efficacies from non-CO₂ LLGHGs and the indirect aerosol effects would be largely balanced out by generally less-than-one efficacies from ozone and direct aerosol effects respectively (see figure 2.19 of **AR4**). Also, when EM-GC's aerosol construction was updated from the *Canty et al.* [2013] formulation to the *Hope et al.* [2017] formulation, it was based on **AR5**'s use of ERF instead of RF for aerosols, so the differences in aerosol forcing efficacies are already built into the current EM-GC aerosol inputs. In an effort to be thorough, future work could include adding multiplicative constants to the individual GHG species and to the land use change (LUC) and ocean heat export (Q_{OCEAN}) terms in the EM-GC's core equation so as to test the uncertainty in the efficacy of each anthropogenic forcing. It is expected that these changes will likely have little effect on the overall future warming from the EM-GC.

The value associated with the amplification of warming due to the sum of all feedback processes generally changes slowly over the course of thousands of years [§12.5.3 of **AR5**], not considering any possible significant nonlinearities in the climate system. Many simple climate models, including the EM-GC, do not directly include a mechanism to let this feedback parameter vary over time. The EM-GC and many other MLR-based models only consider a few centuries of data at most, so the slow rate of

change in the total feedback parameter would not significantly alter warming results. To thoroughly test the assumption of constant climate feedback, it is possible to modify EM-GC output to simulate a changing feedback parameter (§4.4.1). Data from the Clouds and the Earth's Radiant Energy System (CERES) project has also been examined to see how the albedo feedback process is changing over time, if at all. While feedback processes such as the water vapor feedback and the lapse rate feedback are relatively well-quantified, the CERES data shows that the albedo feedback is more uncertain. Figure 2.10 shows that the albedo of Earth has certainly changed over time for two different versions of CERES data, edition 2.8 and edition 4.1. In the former, brightening over the equator and Southern Ocean (likely due to clouds) has offset darkening in much of the northern hemisphere (likely due to loss of ice), meaning little total change in overall albedo and a near-zero value for the sum of ice-albedo and cloud-albedo feedbacks. In the latter edition of CERES data, the brightening feature in the Southern Ocean is still clearly present, but an overall trend of darkening dominates most latitudes, meaning an overall darkening trend realizes in the whole-Earth time series for total albedo. While some of this change clearly derives from uncertainty in cloud albedo, e.g. near the equator, we can also see more ice-albedo darkening at the South Pole and *less* ice-albedo darkening at the North Pole in the newer edition of CERES data. Finally, in either case, the slope of the total albedo is roughly linear, meaning that even if the value of the albedo feedback parameter is uncertain, it is roughly constant over the time period of CERES observations. That is, over the time period of observations, linearity in the change in albedo implies a constant feedback because total anthropogenic RF has changed roughly

Figure 2.10 – The Ice-Albedo Feedback in CERES Data



Left column: CERES Edition 2.8

Right column: CERES Edition 4.1

First row: Earth total albedo anomaly as a function of time

Second row: Change in albedo by latitude over the stated time period

Earth total albedo anomaly is defined with an average of zero over the stated time period, and is weighted by latitude, i.e. the strongly negative values at the north pole in the “change by latitude” panels are reduced to roughly zero due to area weighting.

linearly over the same time period; if we had CERES-like observations since the beginning of the industrial revolution, a high correlation between anthropogenic ΔRF and change in albedo would imply a constant feedback instead.

Any MLR-based model must account for internal variability so as not to misattribute natural forcing to anthropogenic effects. In cases when natural forcings act in the same direction as anthropogenic forcing, not accounting for the internal variability causes an overestimate of human warming, e.g. see analysis of [*Foster and Rahmstorf, 2011*] in §3.3 and §4.3.2. Conversely, the global warming hiatus that occurred from 1998-2012 was a result of natural variability counteracting anthropogenic forcing, and any analysis that does not account for this variability (or does not have a sufficient number of years after 2012 included) would underestimate the human contribution to climate. This is a common criticism raised against simple climate models when they do not provide as much future warming as more complex models do [*Marvel et al., 2018*]; however, most MLR-based simple climate models (including the EM-GC) do account for multiple types of natural variability [*Chylek et al., 2016; Lean and Rind, 2008; Mascioli et al., 2012*].

I have tested multiple factors that had been proposed to explain the global warming hiatus, including the effect of minor volcanoes on SAOD [*Huber and Knutti, 2014; Santer et al., 2014; Schmidt et al., 2014*], possible changes due to SWV [*Solomon et al., 2011; Solomon et al., 2010*], undersampling of Arctic temperatures [*Cowtan and Way, 2014*], and GCM temperature data blending [*Cowtan et al., 2015*]. I discuss the latter two points in §3.4 and §4.4.1 respectively; I investigated the former two ahead of publishing *Hope et al.* [2017]. For the SAOD of minor volcanoes, their stratospheric

aerosol loading was an order of magnitude less than that associated with major volcanoes such as Pinatubo and Krakatau. Since the effect of volcanic SAOD on climate is already small – notably smaller than many GCMs suggest [*Canty et al.*, 2013; *Chylek et al.*, 2020] – the effect of minor volcanoes is not large enough to noticeably affect GMST in the way seen during the global warming hiatus. If the relationship between SAOD and its effect on GMST was nonlinear, that could provide the difference and would not be captured by models like the EM-GC; however, the physical relationship between SAOD and GMST is well-known, making a nonlinear response highly unlikely. For SWV, I ran the EM-GC with two SWV time series to examine their realization in the climate record. In both cases, the regression coefficients were near-zero. While these two independent constructions of SWV had no effect on climate, a third treatment of SWV – namely viewing it as a product of tropospheric CH₄ and thus being directly proportional to CH₄ RF – is included in the CMIP6 recommended RF time series known as the Shared Socioeconomic Pathways (SSPs). This third treatment of SWV does not provide explanation for the global warming hiatus as it enforces rather than counteracts anthropogenic RF of climate from GHGs. A combination of other natural factors already included in the EM-GC is sufficient to explain the global warming hiatus. Other suggested explanations for the hiatus include: energy transfer in the Pacific due to changing trade winds [*England et al.*, 2014], which is covered in the EM-GC by inclusion of the PDO; a recent change in ocean heat export [*Meehl et al.*, 2014a; *Meehl et al.*, 2014b], which is partially considered in the EM-GC ocean module; and a general trend toward a more La-Niña-like state [*Kosaka and Xie*, 2013], which is covered in the EM-GC by inclusion of ENSO with several indexing options. As such, even though it is

impossible to include all potential natural variations in any climate model, the EM-GC accounts for all major sources of natural variability when determining the anthropogenic effect on climate.

Lastly, simple models that do not account for the current energy imbalance in the climate system – i.e. the underlying reason for rapid warming – will not accurately represent the full anthropogenic effect on GMST. On a first-order basis, this means either directly representing the top-of-atmosphere imbalance or representing the equivalent energy sink provided by the ocean [Gregory, 2000; Schwartz *et al.*, 2014]. On a second-order basis, this means recognizing that the efficacy of ocean heat export depends on location and other factors [Rose *et al.*, 2014]. The EM-GC does include an ocean module to account for the rise in ocean heat content and its interaction with the atmosphere, addressing the first point. The model does not directly include any spatial differentiation but may still show some of the efficacy effect nonetheless, as four of the six commonly used natural regressors have associated locations driving them. Specifically, the EM-GC includes three major ocean patterns and ENSO, with the Atlantic pattern driven by deep water formation in high latitudes and the Pacific pattern and ENSO driven by ocean-atmosphere interactions in the tropics. The EM-GC generally favors the Atlantic pattern over the Pacific pattern [Canty *et al.*, 2013], implying a larger influence from high-latitude forcing, which matches the ocean heat export efficacy argument in the literature [Rose *et al.*, 2014].

2.3.2 Uncertainty in Future Projections

The underlying truth behind all projections of future GMST from various climate models is that the anthropogenic rise in GHGs traps more heat closer to Earth's surface.

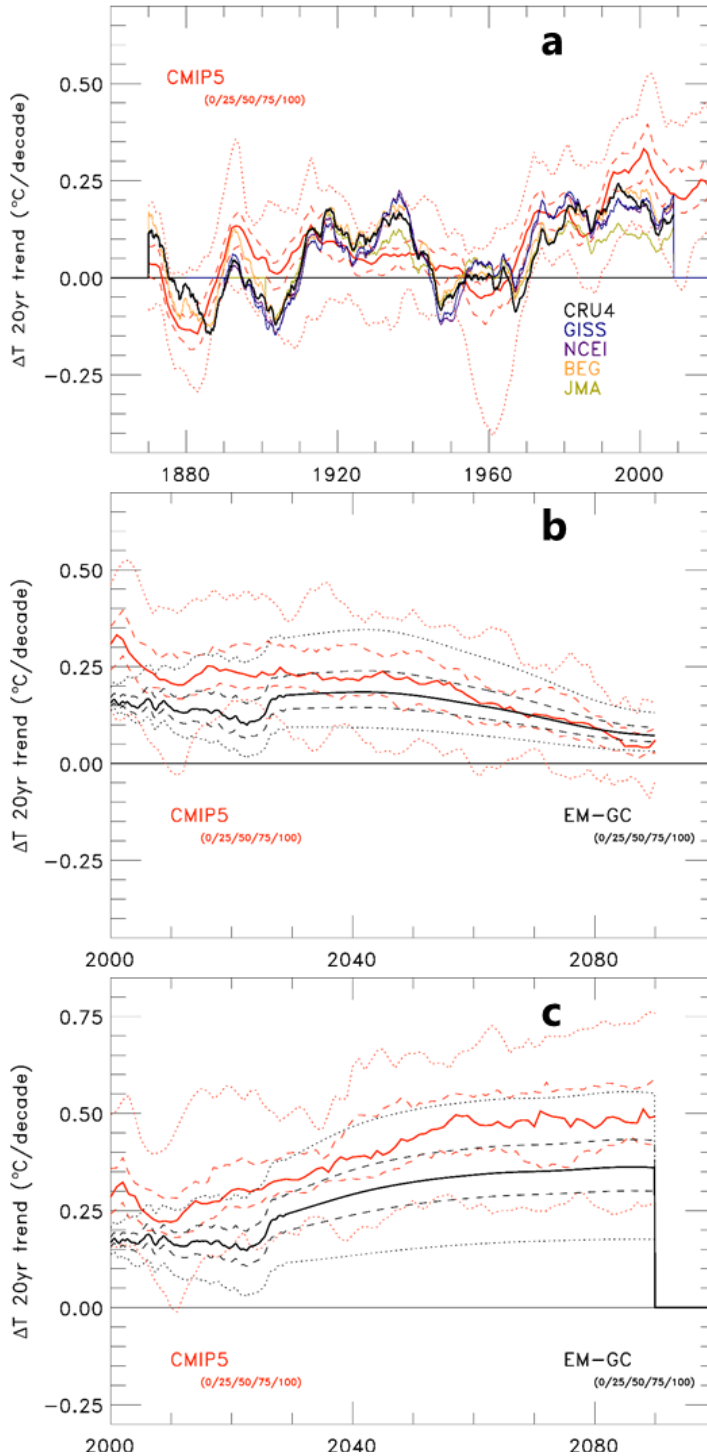
At first order, all models taken together do ultimately agree on roughly how much global warming there will be. This first-order underlying truth is one of the few components that drove early GCMs, and their projections of future GMST have proven to be fairly accurate [*Hausfather et al.*, 2020]. At second order and higher, though, uncertainties in climate modeling – aerosol forcing, cloud feedbacks, and many other model physics questions – cause noticeable spread in temperature projections (and, if left unchecked, can introduce biases in warming amount). Even when running the same RCP scenarios, the ensemble of CMIP5 GCMs often produced roughly a factor of two difference (as mentioned in §1.1.1) for end-of-century temperatures. Specifically, table SPM.2 of **AR5** states that GMST at 2100 could be 1.6 ± 0.7 °C for the low-end RCP 2.6 scenario, 2.4 ± 0.8 °C for the middle RCP 4.5 scenario, up to 4.3 ± 1.1 °C for the high-end RCP 8.5 scenario – each of those ranges spanning roughly a factor of two.

Large uncertainties present a large problem when translating the science to actionable policy measures, even if the underlying scientific message is uncompromised. Politicians (and the public) want deliverables and certainty, knowing that an action taken will achieve a given result (even if, in practice, this is rarely the case). With climate change in particular, uncertainty in the science makes some factions feel empowered to state that the message is meaningless and thus inactionable, even if this is far from the case. All models predict that continued GHG emissions result in noticeable warming, often enough warming to cause significant disruptions in how society currently functions. Nearly all climate scientists agree that swift action is necessary to prevent or at least counteract some of these warming consequences – the uncertainty in warming predictions simply affects exactly how swift and how extensive this action needs to be.

Another issue with GCM predictions of GMST is how well their predictions are realized. As mentioned before, most predictions from older GCMs have become true. However, starting with the CMIP3 models in **AR4**, the skill at predicting warming to present fell suddenly [*Hausfather et al.*, 2020]. This trend continued to the CMIP5 models in **AR5**, which particularly missed the global warming hiatus despite the hiatus beginning many years before the models were ran. It is also present in the CMIP6 models currently in use, as cloud feedback biases have pushed some models to very high equilibrium sensitivity values [*Zelinka et al.*, 2020; *Zhu et al.*, 2020] which, in turn, has led those models to overestimate observed warming [*Tokarska et al.*, 2020; *Voosen*, 2019]. Obviously, if models cannot simulate observed warming well, it makes sense that people might not trust their predictions of future warming.

The authors of chapter 11 of **AR5** recognized the discrepancy between CMIP5 GMST and observed GMST and adjusted their predictions to better reflect the observations. They made this change by selecting a more recent time period to function as the baseline for the GMST time series. While this had the effect of making short-term GMST predictions relatively certain – and cooler than the unadjusted CMIP5 prediction, which the EM-GC validates – the process of changing baselines also obfuscates several aspects of temperature comparisons. Obviously, the closer a chosen baseline is to the time period of interest, the closer any comparisons are likely to be. For global warming and the Paris Agreement in particular, temperature goals are often stated based on a preindustrial baseline; using more recent baselines to argue for the accuracy of GCMs thus also causes preindustrial temperatures to diverge, making the accuracy arguments less applicable for those policy decisions.

Figure 2.11 – Rate of Temperature Change on Different Timescales



A comparison of CMIP5 ensemble trends in GMST to observed & empirical trends in GMST for historical (a), RCP 4.5 (b), and RCP 8.5 (c) experiments. For CMIP5 and EM-GC ensembles, the lines shown are for the ensemble median, interquartile range, and extrema trend values. For each point in time, the trend value shown represents the trend in the GMST from that data set for the 20 years surrounding that time point, e.g. the CMIP5 median trend value of roughly 0.30 °C/decade at year 2000 means that the median GMST time series from the CMIP5 ensemble warmed roughly 0.6 °C from 1990-2010.

One way to circumvent baseline concerns is to instead focus on the rate of temperature change over a given time period instead of the net change in GMST over that time. Figure 2.11 shows 20-year temperature change rates for observed GMST, CMIP5 GMST, and EM-GC GMST. There are several times when CMIP5 temperature warmed more than observations, including the time period of the global warming hiatus. Even as the RCP 4.5 simulation approaches equilibrium at the end of the century, CMIP5 is consistently warming more than the EM-GC is, and the difference between CMIP5 and the EM-GC is even more noticeable in the RCP 8.5 scenario which does not approach equilibrium by the end of the century. There is overlap in their warming rate uncertainty ranges, but it shows that even the adjustment done in chapter 11 of **AR5** to correct a single temperature offset cannot explain and overall warming bias from the GCMs.

Chapter 3

3.1 Introduction

The objective of the Paris Agreement negotiated at the twenty-first session of the Conference of the Parties of the United Nations Framework Convention on Climate Change (UNFCCC) is to hold the increase in global mean surface temperature (GMST) to well below 2 °C above preindustrial levels and to pursue efforts to limit the increase to 1.5 °C above preindustrial levels. The rise in GMST relative to the preindustrial baseline, termed ΔT , is the primary focus throughout this book. We consider measurements of GMST from three data centers: CRU [*Jones et al.*, 2012]⁶, GISS [*Hansen et al.*, 2010]⁷, and NCEI [*Karl et al.*, 2015]⁸, and use the latest version of each data record available at the start of summer 2016. The values of ΔT for from these data centers are 0.828 °C, 0.890 °C, and 0.848 °C respectively⁹. The rise in GMST during the past decade is more than half way to the Paris goal to limit warming to 1.5 °C. Carbon dioxide (CO₂) is the greatest waste product of modern society and global warming caused by anthropogenic

⁶ The CRU temperature record is version HadCRUT4.4.0.0 from the Climatic Research Unit (CRU) of the University of East Anglia, in conjunction with the Hadley Centre of the U. K. Met Office: http://www.metoffice.gov.uk/hadobs/hadcrut4/data/current/time_series/HadCRUT.4.4.0.0.annual_ns_avg.txt. This data record extends back to 1850.

⁷ The GISS temperature record is version 3 of the Global Land-Ocean Temperature Index provided by the Goddard Institute for Space Studies (GISS) of the U.S. National Aeronautics and Space Administration (NASA): http://data.giss.nasa.gov/gistemp/tabledata_v3/GLB.Ts+dSST.txt. This data record extends back to 1880.

⁸ The NCEI temperature record is version 3.3 of the Global Historical Climatology Network-Monthly (GHCN-M) data set provided by the National Centers for Environmental Information (NCEI) of the U.S. National Oceanographic and Atmospheric Administration (NOAA) <http://www.ncdc.noaa.gov/monitoring-references/faq/anomalies.php>. This data record extends back to 1880.

⁹ ΔT for CRU was found relative to the 1850 to 1900 baseline using data entirely from this data record; ΔT for NCEI and GISS are also for a baseline for 1850 to 1900, computed using a blended procedure described in the Methods (§3.6) note for Figure 3.3. A decade long time period of 2006 to 2015 is used for this estimate of ΔT to remove the effect of year-to-year variability. A higher value of ΔT results if GMST from 2015 is used, but as explained later in this chapter, excess warmth in 2015 was due to a major El Niño Southern Oscillation event.

release of CO₂ is on course to break through both the Paris goal and upper limit (2.0 °C) unless the world's voracious appetite for energy from the combustion of fossil fuels is soon abated.

Forecasts of ΔT are generally based on calculations conducted by general circulation models (GCMs) that have explicit representation of many processes in Earth's atmosphere and oceans. For several decades, most models have also included a treatment of the land surface and sea-ice. More recently, models have become more sophisticated by adding treatments of tropospheric aerosols, dynamic vegetation, atmospheric chemistry, and land ice. Chapter 5 of *J. Houghton* [2009] provides a good description of how GCMs operate and the evolution of these models over time.

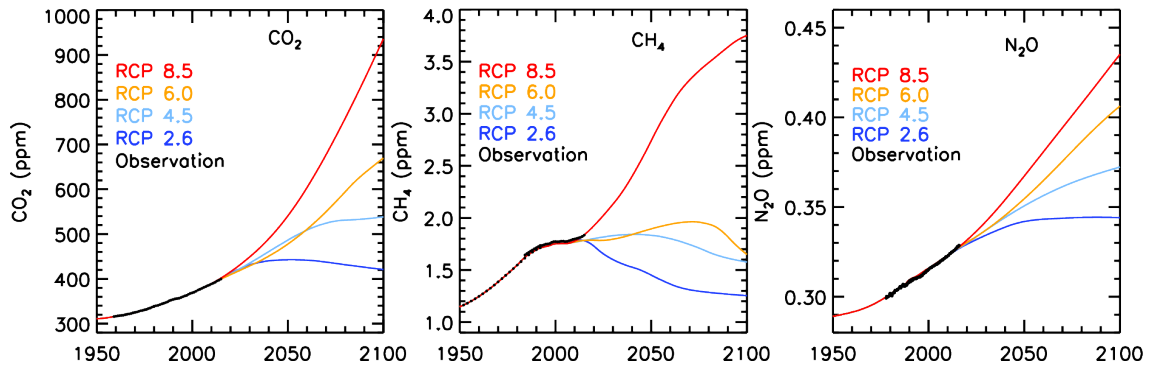
The calculations of ΔT by GCMs considered here all use specified abundances of greenhouse gases (GHGs) and precursors of tropospheric aerosols. These specifications originate from the Representative Concentration Pathway (RCP) process that resulted in 4 scenarios used throughout the fifth IPCC assessment report [*Stocker et al.*, 2013]: RCP 8.5, RCP 6.0, RCP 4.5, and RCP 2.6 [*Van Vuuren et al.*, 2011a]. The number following each scenario indicates the increase in RF of climate, in units of W/m², at the end of this century relative to 1750, due to the prescribed abundance of all anthropogenic GHGs. The GCMs use as input time series for the atmospheric abundance of GHGs as well as the industrial release of pollutants that are converted to aerosols. Each GCM projection of ΔT is guided by the calculation, internal to each model, of how atmospheric humidity, clouds, surface reflectivity, and ocean circulation responds to the change in RF of climate induced by GHGs and aerosols [*J Houghton*, 2009]. If the response to a specific process further increases RF of climate, it is called a ***positive feedback*** because it enhances the

initial perturbation. If a process decreases RF of climate, is it called a *negative feedback*. The total effect of all responses to the prescribed perturbation to RF of climate by GHGs and aerosols is called *climate feedback*, which can vary quite a bit between GCMs, mainly due to the treatment of clouds [Bony *et al.*, 2006; Vial *et al.*, 2013]. GCMs also provide estimates of the future evolution of precipitation, drought indices, sea-level rise, as well as variations in oceanic and atmospheric temperature and circulation [Stocker *et al.*, 2013].

Our focus is on analysis of projections of ΔT for the RCP 4.5 [Thomson *et al.*, 2011] and RCP 8.5 scenarios [Riahi *et al.*, 2011]. Atmospheric abundances of the three most important anthropogenic GHGs given by the RCP 4.5 and RCP 8.5 scenarios are shown in Fig. 3.1. Under RCP 8.5, the abundances of these GHGs rise to alarmingly high levels by end of century. On the other hand, for RCP 4.5, CO₂ stabilizes at 540 parts per million by volume (ppm) (~35% higher than contemporary level) and methane (CH₄) reaches 1.6 ppm (~10% lower than to-day) in 2100. The atmospheric abundance of nitrous oxide (N₂O) continues to rise under RCP 4.5, reaching 0.37 ppm by end of century (~15% higher than today).

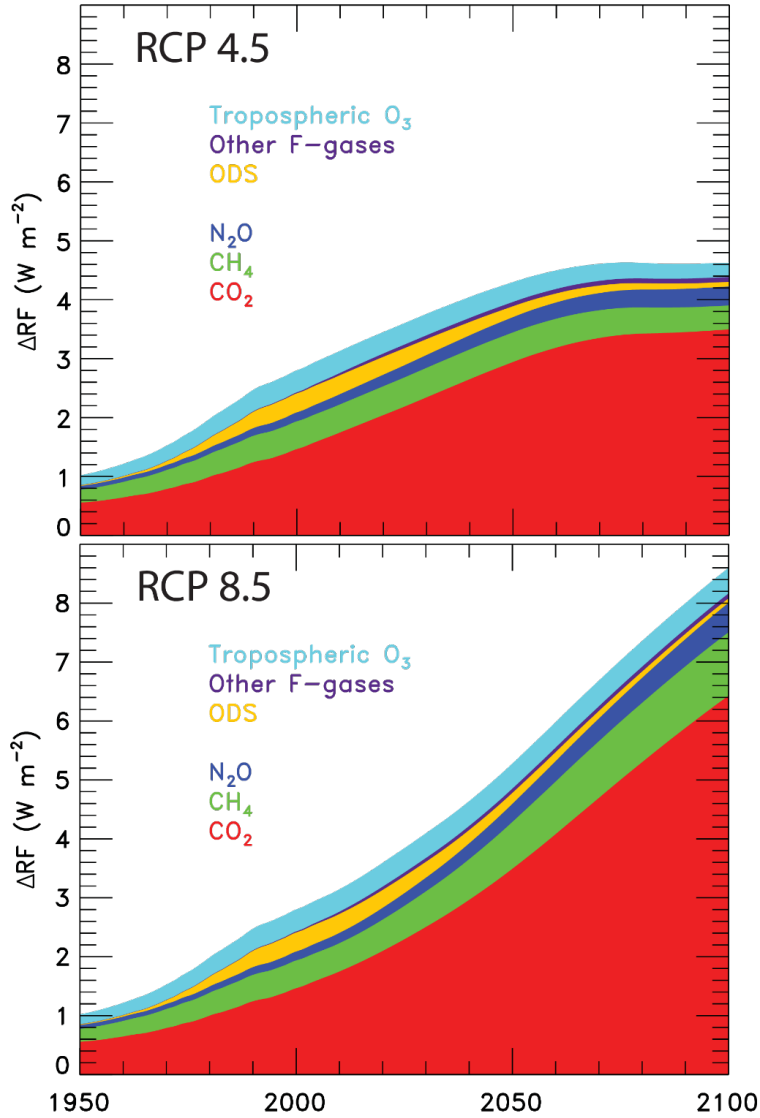
The ΔRF of climate associated with RCP 4.5 and RCP 8.5 are shown in Fig. 3.2, using the grouping of GHGs defined in Chapter 1. The contrast between these two scenarios is dramatic. For RCP 4.5, ΔRF of climate levels off at mid-century, reaching 4.5 W/m² at end-century. For RCP 8.5, ΔRF rises throughout the century, hitting 8.5 W/m² near 2100. Both behaviors are by design [Riahi *et al.*, 2011; Thomson *et al.*, 2011]. While CO₂ remains the most important anthropogenic GHG for both projections, other GHGs exert considerable influence.

Figure 3.1 – GHG abundance, 1950 to 2100



Time series of the atmospheric CO₂, CH₄, and N₂O from RCP 2.6 [van Vuuren *et al.* 2011b], RCP 4.5 [Thomson *et al.* 2011], RCP 6.0 [Masui *et al.* 2011], RCP 8.5 [Riahi *et al.* 2011], and observations (black) [Ballantyne *et al.* 2012; Dlugokencky *et al.* 2009; Montzka *et al.* 2011]. Values of GHG mixing ratios from RCP extend back to 1860, but this figure starts in 1950 since most of the rise in these GHGs has occurred since that time. See §3.6 Methods for further information.

Figure 3.2 – RF of Climate Due to GHGs, 1950 to 2100



Time series of ΔRF of climate, RCP 4.5 (top) and RCP 8.5 (bottom), due to the three dominant anthropogenic GHGs (CO_2 , CH_4 , and N_2O) plus contributions from all ozone depleting substances (ODS), other fluorine bearing compounds such as HFCs, PFCs, SF_6 , and NF_3 (Other F-gases), and tropospheric O_3 . Shaded regions represent contributions from specific gases or groups. See §3.6 Methods for further information.

The RCPs are meant to provide a mechanism whereby GCMs are able to simulate the response of climate for various prescribed ΔRF scenarios, in a manner that allows differences in model behavior to be assessed. Evaluation of GCM output has been greatly facilitated by the Climate Model Intercomparison Project Phase 5 (CMIP5) [K Taylor *et al.*, 2012], which maintains a computer archive of model output freely available following a simple registration procedure¹⁰, as well as the prior CMIP phases.

Two other scenarios, RCP 6.0 [Masui *et al.*, 2011] and RCP 2.6 [Van Vuuren *et al.*, 2011b], were considered by IPCC [Stocker *et al.*, 2013]. The mixing ratio of CO₂ peaks at about 670 ppm at end-century for RCP 6.0 (Fig. 3.1); the climate consequences for this scenario clearly lie between those of RCP 4.5 and RCP 8.5. For RCP 2.6, CO₂ peaks mid-century and slowly declines to 420 ppm at end-century¹¹. According to the authors of RCP 2.6, this scenario “is representative of the literature on mitigation scenarios aiming to limit the increase of global mean temperature to 2°C”. While this is true for literal interpretation of the output of the GCMs that contributed to the most recent IPCC report [Rogelj *et al.*, 2016], below we show these GCMs likely over-estimate the actual warming that will occur in the coming decades.

Figure 3.3 shows projections of ΔT from the CMIP5 GCMs found using RCP 4.5 and RCP 8.5. Observations of ΔT from CRU, NCEI, and GISS up to year 2012, as well as the CRU estimate of the uncertainty on ΔT , are shown. The green hatched trapezoid on Fig. 3.3 is the “indicative likely range for annual mean ΔT ” provided by Chapter 11 of IPCC [Stocker *et al.*, 2013]¹². Section 11.3.6.3 of this report states:

¹⁰ CMIP5 GCM output is at http://cmip-pcmdi.llnl.gov/cmip5/data_getting_started.html

¹¹ Globally averaged CO₂ was ~404 ppm during summer 2016. To achieve the RCP 2.6 scenario, CO₂ at the end of the century must be comparable to the present day value.

¹² The trapezoid also appears in Figure TS.14, page 87, of the IPCC (2013) Technical Summary

some CMIP5 models have a higher transient response to GHGs and a larger response to other anthropogenic forcings (dominated by the effects of aerosols) than the real world (medium confidence). These models may warm too rapidly as GHGs increase and aerosols decline

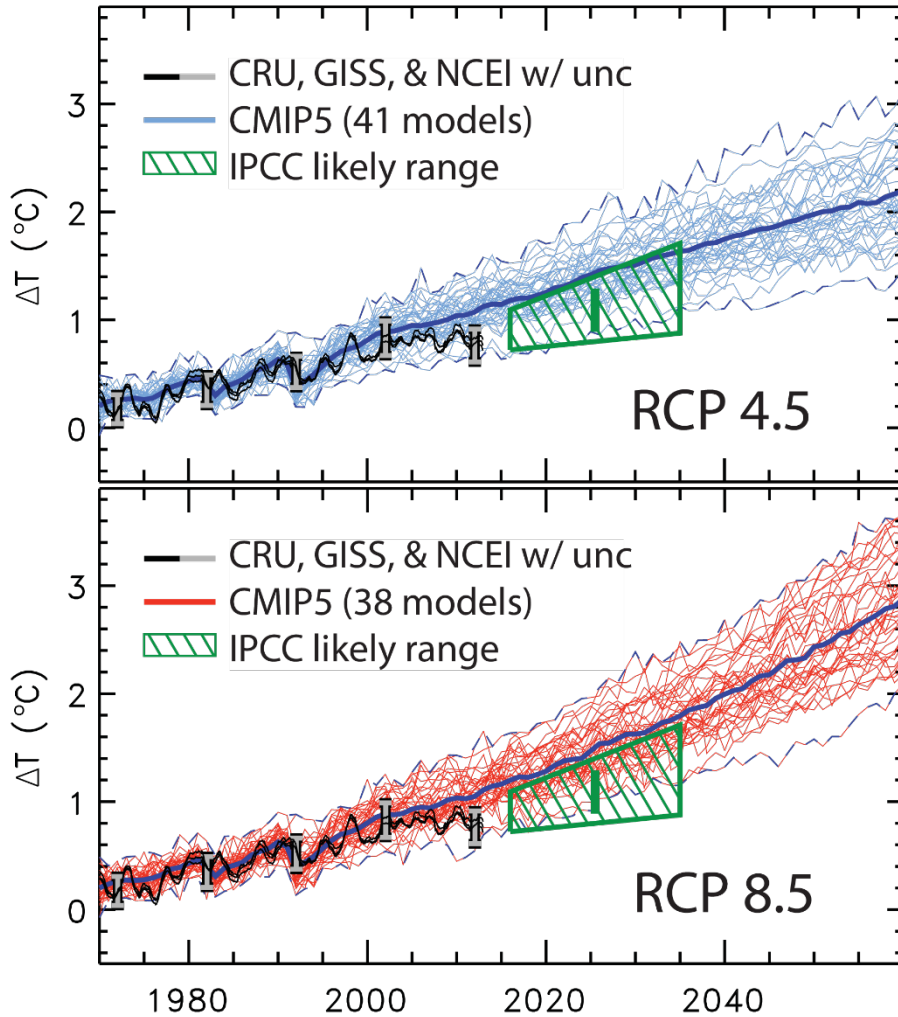
and

over the last two decades the observed rate of increase in GMST has been at the lower end of rates simulated by CMIP5 models.

In other words, the projections of ΔT by the CMIP5 GCMs tend to be too warm based on comparison of observed and modeled ΔT for prior decades [Gillett *et al.*, 2013; Stott *et al.*, 2013]. The trapezoid shown on Fig. 3.3 represents an expert judgement of the upper and lower limits for the evolution of ΔT over the next 2 decades. The vertical bar is the likely mean value of ΔT over the 2016 to 2035 time period. This projection is meant to apply to all four RCPs: i.e., it considers the full range of possible future values for CO₂, CH₄, and N₂O between present and 2035.

Our analysis of the Paris Climate Agreement will be based on the CMIP5 GCM output as well as calculations conducted using an Empirical Model of Global Climate (EM-GC) developed by our group [Canty *et al.*, 2013]. The EM-GC is described in § 2.2. While the EM-GC tool only calculates ΔT , this simple approach is computationally efficient, allowing the uncertainty on ΔT of climatically important factors such as radiative forcing by tropospheric aerosols and ocean heat content to be evaluated in a rigorous manner. We then compare estimates of how much global warming over the 1979 to 2010 time period can truly be attributed to human activity (§ 2.3). Following a brief comment on the so-called global warming hiatus (§ 2.4), we turn our attention to projections of ΔT (§ 2.5). The green trapezoid in Fig 3.3 is featured prominently in § 2.5: projections of ΔT found using the EM-GC approach are in remarkably good agreement

Figure 3.3 – Observed and GCM Simulated Global Warming, 1960 to 2060



Top: Time series of global, annually averaged ΔT relative to preindustrial baseline from 41 GCMs that submitted output to the CMIP5 archive covering both historical and future time periods, using RCP4.5 (light blue). The maximum and minimum values of CMIP5 ΔT are indicated by the dark blue dashed lines, while the multi-model-mean is denoted by the dark blue solid line. Also shown are global, annually averaged observed ΔT from CRU, GISS, and NCEI (black) along with error bars (grey) that represent the uncertainty on the CRU time series. The green trapezoid represents the indicative likely range for annual average ΔT for 2016 to 2035 (i.e., top and bottom of trapezoid are upper and lower limits, respectively) and the green bar represents the likely range for the mean value of ΔT over 2006 to 2035, both given in Chapter 11 of IPCC AR5.

Bottom: Same as top, expect for 38 GCMs that submitted output to the CMIP5 archive covering both historical and future time periods using RCP8.5 (red). After Fig. 11.25a and 11.25b of IPCC AR5.

See §3.6 Methods for further information.

with this IPCC [*Stocker et al.*, 2013] expert judgement of ΔT over the next 2 decades, lending credence to the accuracy of our empirically-based projections.

3.2 The Empirical Model of Global Climate

Earth's climate is influenced by a variety of anthropogenic and natural factors. Rising levels of greenhouse gases (GHGs) cause global warming [*Lean and Rind*, 2008; *Santer et al.*, 2013b] whereas the increased burden of tropospheric aerosols offset a portion of the GHG-induced warming [*Kiehl*, 2007; *S Smith and Bond*, 2014]. The most important natural drivers of climate during the past century have been the El Niño Southern Oscillation (ENSO), the 11 year cycle in total solar irradiance (TSI), volcanic eruptions strong enough to penetrate the tropopause as recorded by enhanced stratospheric optical depth (SOD) [*Lean and Rind*, 2008; *Santer et al.*, 2013a], and variations in the strength of the Atlantic Meridional Overturning Circulation (AMOC) [*Andronova and Schlesinger*, 2000]. Climate change is also driven by feedbacks (changes in atmospheric water vapor, lapse rate¹³, clouds, and the surface albedo in response to radiative forcing (RF) induced by GHGs and aerosols [*Bony et al.*, 2006] and transport of heat from the atmosphere to the ocean that induces a long term rise in the temperature of the world's oceans [*Levitus et al.*, 2012].

Our empirical model of global climate (EM-GC) [*Canty et al.*, 2013] uses an approach termed multiple linear regression (MLR) to simulated observed monthly variations in the global mean surface temperature anomaly (termed ΔT_i , where i is an

¹³ Lapse rate is a scientific term for the variation of temperature with respect to altitude. Over the past 50 years the upper troposphere (~10 km altitude) has warmed by a larger amount than the surface. When this type of pattern occurs, climate scientists conclude the lapse rate feedback is negative, because Earth's atmosphere is able to radiate heat into space more efficiently. The interested reader is referred to the detailed yet accessible text of Randall, D. (2012), *Atmosphere, clouds, and climate*, Princeton University Press. for more information.

index representing month) using an equation that represents the various natural and anthropogenic factors that influence ΔT_i . The EM-GC formulation represents:

- RF of climate due to anthropogenic GHGs, tropospheric aerosols, and land use change
- Exchange of heat between the atmosphere and ocean, in the tropical Pacific, regulated by ENSO
- Variations in TSI reaching Earth due to the 11 year solar cycle
- Reflection of sunlight by volcanic aerosols in the stratosphere, following major eruptions
- Exchange of heat with the ocean due to variations in the strength of AMOC
- Export of heat from the atmosphere to the ocean that causes a steady long-term rise of water

temperature throughout the world's oceans

The effects on ΔT of the Pacific Decadal Oscillation (PDO) [*Y Zhang et al.*, 1997] and the Indian Ocean Dipole (IOD) [*Saji et al.*, 1999] are also considered.

The hallmark of the MLR approach is that coefficients that represent the impact of GHGs, tropospheric aerosols, ENSO, major volcanoes, etc. on ΔT_i are found, such that the output of the EM-GC equations provide a good fit to the observed climate record. The most important model parameters are the total climate feedback parameter (designated λ) and a coefficient that represents the efficiency of the long-term export of heat from the atmosphere to the world's oceans (designated κ). Our approach is similar to many prior published studies [*Chylek et al.*, 2014; *Lean and Rind*, 2009; *T Masters*, 2014; *Stern and Kaufmann*, 2014] except ocean heat export (OHE, the transfer of heat from the atmosphere to the ocean) is explicitly considered and results are presented for a wide range of model possibilities that provide reasonably good fit to the climate record, rather than relying on a single best fit. Most of the prior studies neglect OHE and typically rely on a best fit approach.

A description of the EM-GC approach is provided in the remainder of this section. While we have limited the use of equations throughout the book, they are necessary when

providing a description of the model. We've concentrated the use of equations in the section that follows; comparisons of output from the EM-GC with results from the CMIP5 GCMs are presented in other sections with use of little or no equations.

3.2.1 Formulation

The empirical model of global climate [Canty *et al.*, 2013] provides a mathematical description of observed temperature. As noted above, temperature is influenced by a variety of human and natural factors. Our approach is to compute, from the historical climate record, numerical values of the strength of climate feedback and the efficiency of the transfer of heat from the atmosphere to the ocean. We then use these two parameters to project global warming.

Here we delve into the mathematics of the EM-GC framework. Those without an appetite for the equations are encouraged to fast forward to §2.3. There will not be a quiz at the end of this chapter.

Our simulation of observed temperature involves finding values of a series of coefficients such that the model *Cost Function*:

$$Cost\ Function = \sum_{i=1}^{N_{MONTHS}} \frac{1}{\sigma_{OBS\ i}^2} (\Delta T_{OBS\ i} - \Delta T_{EM-GC\ i})^2$$

Eq3.1

is minimized. Here, $\Delta T_{OBS\ i}$ and $\Delta T_{EM-GC\ i}$ represent time series of observed and modeled monthly, global mean surface temperature anomalies, $\sigma_{OBS\ i}$ is the 1-sigma uncertainty associated with each temperature observation, i is an index for month, and N_{MONTHS} is the total number of months. The use of $\sigma_{OBS\ i}^2$ in the denominator of Eq. 3.1 forces modeled

$\Delta T_{EM-GC i}$ to lie closest to data with smaller uncertainty, which tends to be the latter half of the $\Delta T_{OBS i}$ record.

The expression for $\Delta T_{EM-GC i}$ is:

$$\begin{aligned} \Delta T_{EM-GC i} = & \frac{1 + \gamma}{\lambda_P} (GHG \Delta RF_i + Aerosol \Delta RF_i + LUC \Delta RF_i) + C_0 + C_1 \times SOD_{i-6} \\ & + C_2 \times TSI_{i-1} + C_3 \times ENSO_{i-3} + C_4 \times AMV_i + C_5 \times PDO_i + C_6 \times IOD_i \\ & - \frac{1}{\lambda_P} Q_{OCEAN i} \end{aligned}$$

Eq3.2

where model input variables (described immediately below) are used to calculate the model output parameters C_i and γ . In Eq. 3.2 GHG ΔRF_i , Aerosol ΔRF_i , and LUC ΔRF_i represent monthly time series of the ΔRF of climate due to anthropo-genic GHGs, tropospheric aerosol, and land use change; $\lambda_P = 3.2 \text{ W/m}^2/\text{°C}$ is the response of surface temperature to a RF perturbation in the absence of climate feedback (“P” is used as a subscript because this term is called the Planck response function by the climate modeling community [Bony *et al.*, 2006]); SOD_{i-6} , TSI_{i-1} , $ENSO_{i-3}$ represent indices for stratospheric optical depth, total solar irradiance, and El Niño Southern Oscillation lagged by 6 months, 1 month, and 3 months, respectively; AMV_i , PDO_i , and IOD_i represent indices for Atlantic Multidecadal Variability (a proxy for the strength of AMOC), the Pacific Decadal Oscillation, and the Indian Ocean Dipole; and $Q_{OCEAN i} / \lambda_P$ is the Ocean Heat Export term. The use of temporal lags for SOD, TSI, and ENSO is common for MLR approaches: *Lean and Rind* [2008] use lags of 6 months, 1 month and 4 months, respectively, for these terms. These lags represent the delay between forcing of the climate system and the response of RF of climate at the tropopause, after stratospheric

adjustment. These lags are discussed at length in our model description paper [Canty *et al.*, 2013]. Finally, the AMV, PDO, and IOD terms have traditionally not been used in MLR models. Below, results are shown with and without consideration of these 3 terms. No lag is imposed for these 3 terms since the indices used to describe these processes vary slowly with respect to time.

The coefficients (C_1 to C_6) that multiply the various model terms, as well as the constant term C_0 and the variable γ , are found using multiple linear regression, which provides numerical values for each of these parameters such that the Cost Function (Eq. 2.1) has the smallest possible value. The term γ in Eq. 2.2 is the dimensionless climate sensitivity parameter. If the net response of changes in humidity, lapse rate, clouds, and surface albedo that occur in response to anthropogenic ΔRF of climate is positive, as is most often the case, then the value of γ is positive.

The estimate of Q_{OCEAN} is based on finding the value of the final model output parameter κ , the ocean heat uptake efficiency coefficient, with units of $W/m^2/^\circ C$ [Raper *et al.*, 2002], that best fits a time series of ocean heat content (OHC), where:

$$Q_{OCEAN\ i} = \kappa \frac{1 + \gamma}{\lambda_p} (GHG \Delta RF_{i-72} + Aerosol \Delta RF_{i-72} + LUC \Delta RF_{i-72})$$

Eq3.3

The subscripts $i-72$ in Eq. 2.4 represent a 6-year (or 72-month) lag between the anthropogenic ΔRF perturbation and the export of heat to the upper ocean. The numerical estimate of this lag is based on the simulations described by Schwartz [2012]; the projections of global warming found using the EM-GC framework are insensitive to any reasonable choice for the this lag. Since the model is based on matching perturbations in RF of climate to variations in temperature, the flow of heat from the atmosphere to the

ocean is modeled as a perturbation to the mean state induced by anthropogenic RF of climate (i.e., Q_{OCEAN} in Eq. 3.2 depends only on “delta” terms that represent human influence on climate). Finally, the net effect of human activity on ΔT is the sum of GHG warming, aerosol cooling, very slight cooling due to land use change, and ocean heat export:

$$\Delta T_i^{HUMAN} = \frac{1}{\lambda_p} [(1 + \gamma)(GHG \Delta RF_{i-72} + Aerosol \Delta RF_{i-72} + LUC \Delta RF_{i-72}) - Q_{OCEAN i}]$$

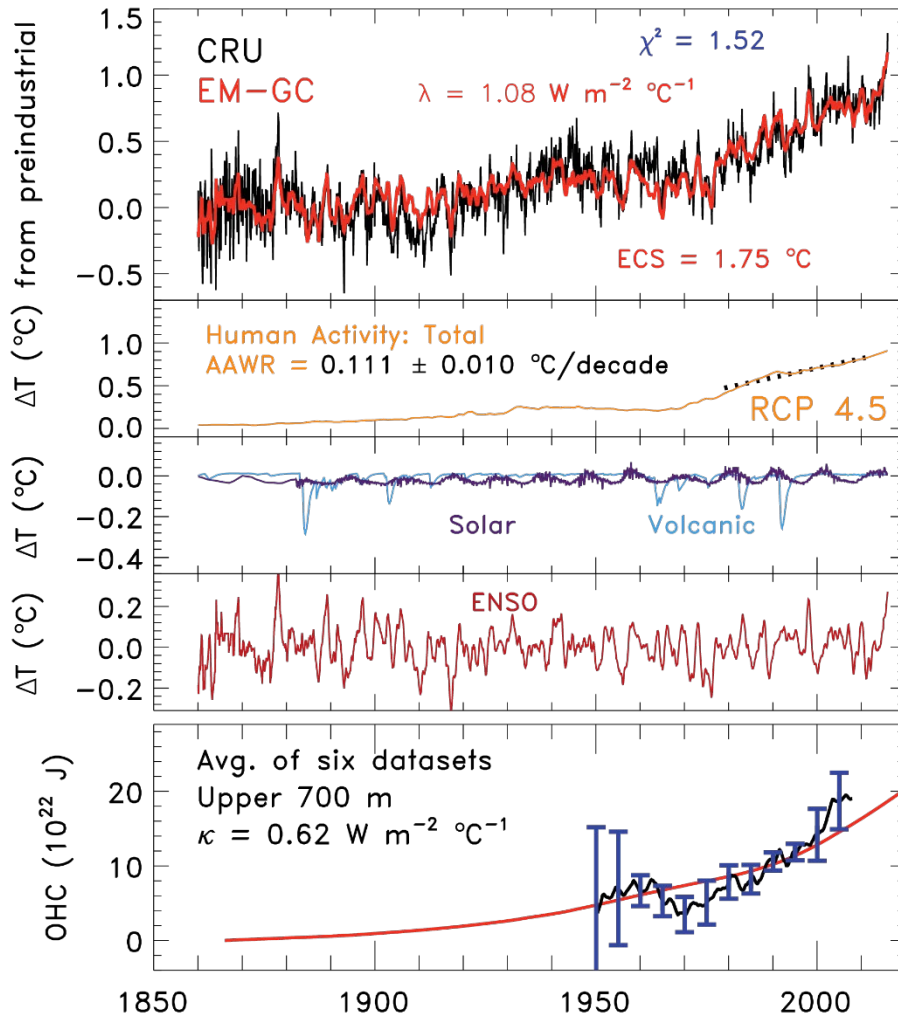
Eq3.4

Equations 3.1 to 3.4 constitute our empirical model of global climate. Of the model inputs, the aerosol ΔRF term is the most uncertain. As shown below, there is a strong relation between the value of the climate sensitivity parameter γ and the magnitude of aerosol ΔRF . This dependency is well known in the climate community, as discussed for example by *Kiehl* [2007]. Also, there is a wide variation in the value of κ , depending on which dataset is used to specify OHC.

Figures 3.4 and 3.5 provide a graphical illustration of how the model works. The simulations in these figures use estimates for GHG and aerosol ΔRF from RCP 4.5, tied to the best estimate for aerosol ΔRF in year 2011 ($AerRF_{2011}$) of -0.9 W/m^2 from IPCC [*Stocker et al.*, 2013], and a time series for OHC in the upper 700 meters of the global oceans that is an average of 6 published studies. In the interest of keeping the attention of those reading this far, we describe a few simulations prior to delving into further details about the model parameters.

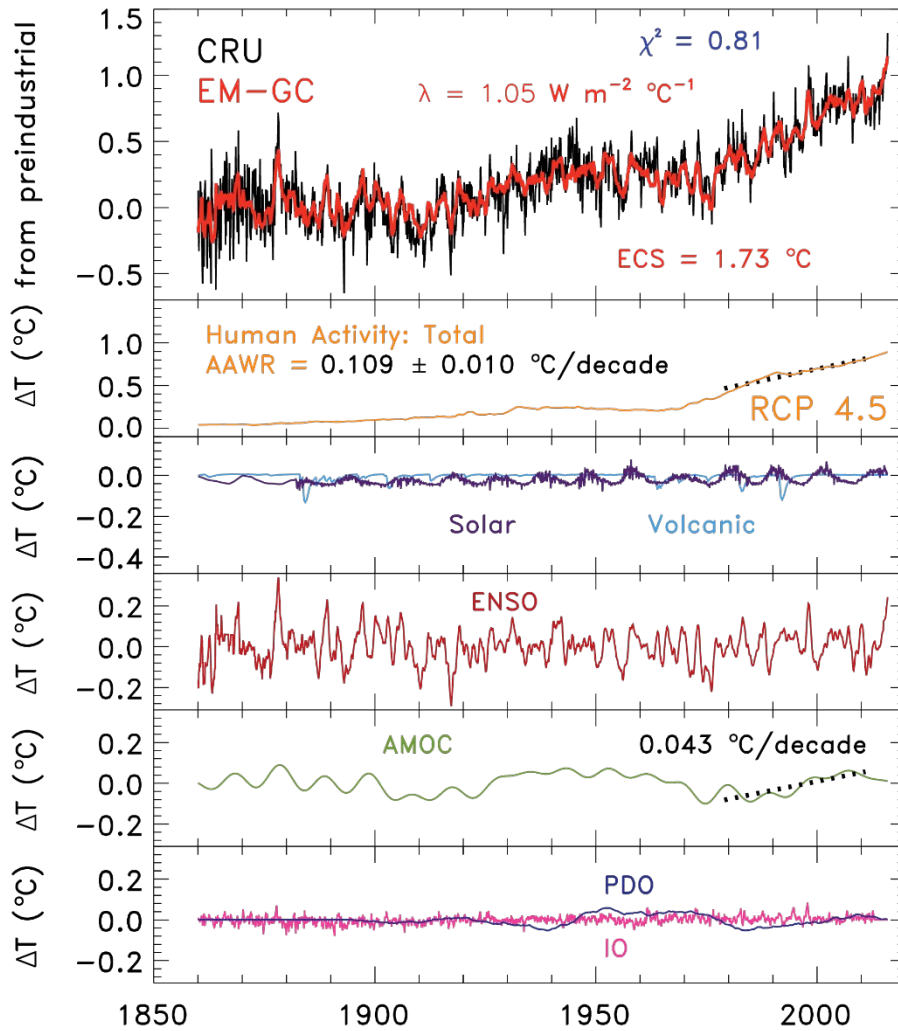
Figure 3.4 is a so-called “ladder plot” that compares a time series of observed, monthly values of ΔT (top rung) from CRU (black) to the output of the model (red). For

Figure 3.4 – Observed and EM-GC Simulated Global Warming, 1860 to 2015, Without Ocean Oscillations



Ladder plot showing CRU observed global, monthly mean ΔT from CRU (black) and as simulated by the EM-GC (red), both relative to preindustrial baseline (top rung); the contribution to ΔT from humans (orange) (2nd rung), and contributions from natural sources of climate variability due to fluctuations in the output of the sun and major volcanic eruptions (3rd rung). The final rung compares modeled and measured ocean heat content (OHC), where the data show the average (used in the model) and standard deviation of OHC from six data sets. See §3.6 Methods for further information.

Figure 3.5 – Observed and EM-GC Simulated Global Warming, 1860 to 2015, With Ocean Oscillations



Same as Fig 3.4, except the EM-GC equations have been expanded to include the effects of the Atlantic Meridional Overturning Circulation (AMOC), the Pacific Decadal Variability (PDO), and the Indian Ocean Dipole (IOD). The fifth rung of the ladder plot shows contributions to variations in ΔT from fluctuations in the strength of the AMOC; the sixth rung shows contributions from PDO and IOD. See §3.6 Methods for further information.

the simulation in Fig. 3.4, the AMV, PDO, and IOD terms have been neglected. The model provides a reasonably good description of the observed global temperature anomaly. The red curve on the top panel is the sum of the orange curve on the 2nd panel (total effect of human activity), the blue and purple curves on the 3th panel (volcanic and solar terms), and the cardinal curve on the 4th panel (ENSO), plus the regression constant C_0 (not shown). Finally, the bottom panel shows a comparison of a time series of OHC (available only from 1950 to 2007) to the modeled Q_{OCEAN} term.

Figure 3.5 is similar to Fig. 3.4, except here the model has been expanded to include the AMV, PDO, and IOD terms in Eq. 3.1. The OHC comparison is not shown in Fig. 3.5 because it looks identical to the bottom panel of Fig. 3.4. The red curve on the top panel of Fig 3.5 is the sum of the curves shown in the rest of the panels, plus the constant C_0 . The top panel of Fig. 3.5 shows remarkably good agreement between observed ΔT from CRU (black) and modeled ΔT found using the EM-GC equation (red). Consideration of these three additional ocean proxies improves the simulation of ΔT around year 1910 and in the mid-1940s (Fig. 3.5) compared to the results shown in Fig 3.4, which lacked these terms. Most of this improvement is due to the use of AMV as a proxy for variations in the strength of the Atlantic Meridional Overturning Circulation, which only recently has been recognized as having a considerable effect on global climate [Andronova and Schlesinger, 2000; Schlesinger and Ramankutty, 1994]. In our approach, the PDO [Y Zhang *et al.*, 1997] and the IOD [Saji *et al.*, 1999] have little expression on global climate, which is a common finding using MLR analysis of the ~150 year long record of ΔT [Chylek *et al.*, 2014; Rypdal, 2015]. Also, upon inclusion of the AMV proxy (Fig. 3.5), the cooling after major volcanic eruptions is diminished by

nearly a factor of two relative to a MLR analysis that neglects this term (volcanic term in Fig 3.5 compared to volcanic term in Fig. 3.4). This finding could have significant implications for the use of volcanic cooling as a proxy for the efficacy of geoengineering of climate via stratospheric sulfate injection [Canty *et al.*, 2013].

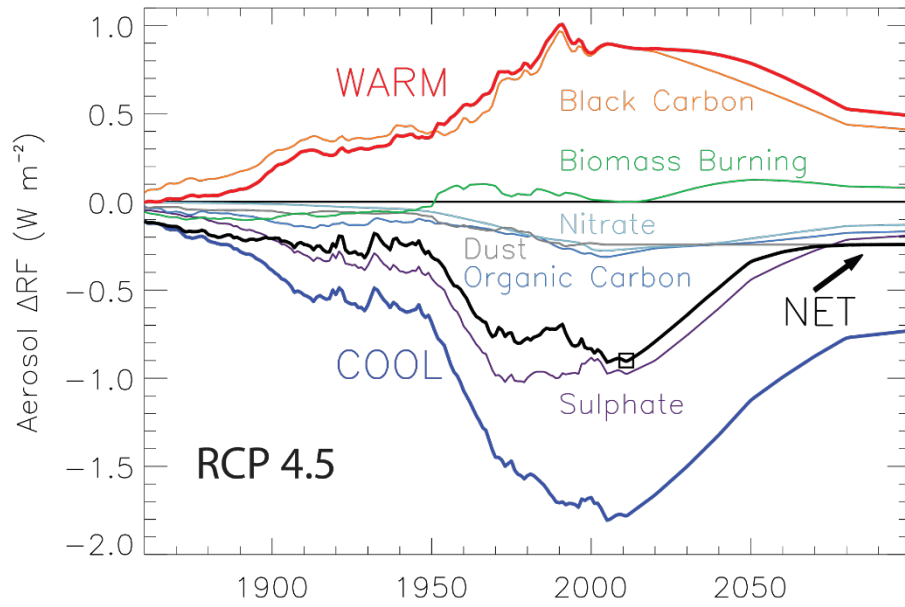
Additional detail on inputs to the empirical model of global climate is provided in §3.2.1.1. More explanation of the model outputs is given in §3.2.1.2. Both of these sections are condensed from our model description paper [Canty *et al.*, 2013], including a few updates since the original publication.

3.2.1.1 Model Inputs

The ΔRF due to GHGs is based on global, annual mean mixing ratios of CO₂, CH₄, N₂O, the class of halogenated compounds known as ozone depleting substances (ODS), HFCs, PFCs, SF₆, and NF₃ (Other F-gases) provided by the RCP 4.5 [Thomson *et al.*, 2011] and RCP 8.5 [Riahi *et al.*, 2011] scenarios. Annual abundances are interpolated to a monthly time grid, because monthly resolution is needed to resolve short-term impacts on ΔT of processes such as ENSO and volcanic eruptions. Values of ΔRF for each GHG are computed using formula originally given in Table 6.2 of IPCC (2001) except the preindustrial value of CH₄ has been adjusted to 0.722 ppm, following Table AII.1.1a of IPCC [Stocker *et al.*, 2013]. The ΔRF due to tropospheric O₃ is based on the work of Meinshausen *et al.* [2011], obtained from a file posted at the Potsdam Institute for Climate Impact Research website. The sum of ΔRF due to CO₂, CH₄, N₂O, ODS, Other F-gases, and tropospheric O₃ constitutes GHG ΔRF_i in Eq. 3.2.

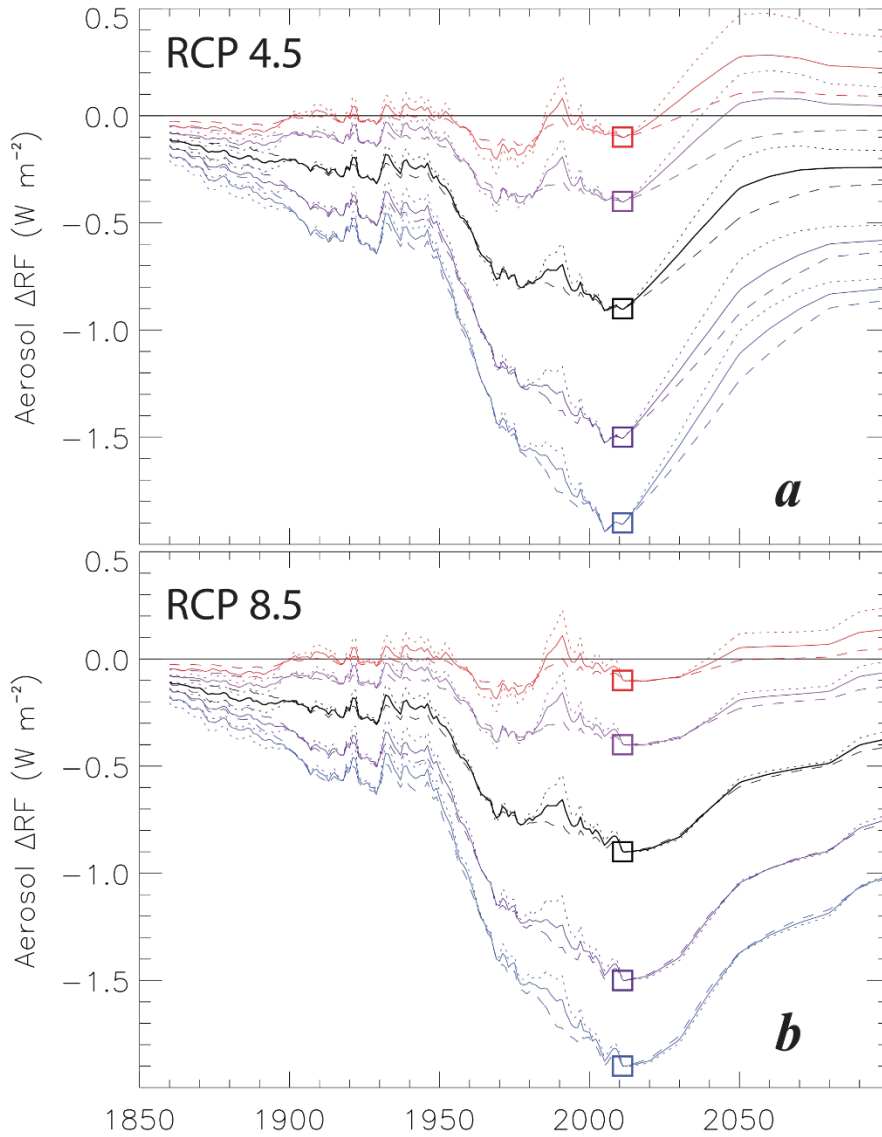
The ΔRF due to aerosols is the sum of direct and indirect effects of six types of aerosols, as described in §3.2.2 of Canty *et al.* [2013]. The six aerosol types are sulfate,

Figure 3.6 – Aerosol Δ RF Versus Time by Species, RCP 4.5, for AER RF₂₀₁₁ = -0.9 W/m²



See §3.6 Methods for further information.

Figure 3.7 – Aerosol Δ RF Versus Time, RCP 4.5 and 8.5, Various AER Δ RF₂₀₁₁ Scenarios



a) Various scenarios for AerRF₂₀₁₁ of -0.1 , -0.4 , -0.9 , -1.5 , and $-1.9\ W/m^2$ (open squares) for RCP 4.5 aerosol precursor emissions.
b) Same as **a)**, except for RCP 8.5 emission scenarios.
 See §3.6 Methods for further information.

mineral dust, ammonium nitrate, fossil fuel organic carbon, fossil fuel black carbon, and biomass burning emissions of organic and black carbon. The direct ΔRF for all aerosol types other than sulfate is also based on the work of *Meinshausen et al.* [2011], again obtained from files posted at the Potsdam Institute for Climate Impact Research website. Different estimates for RCP 4.5 and RCP 8.5 are used, since it is assumed that reduction of atmospheric release of aerosol precursors will occur more quickly in RCP 4.5, in lock-step with the decreased emission of GHGs in this scenario relative to RCP 8.5. The direct RF due to sulfate is based on the work of *Smith et al.* [2011]. Scaling parameters are used to multiply the direct ΔRF of aerosols, to account for the aerosol indirect effect, as described in §3.2.2 of *Canty et al.* [2013].

Figure 3.6 shows total ΔRF (black line) due to tropospheric aerosols that was used as EM-GC input (i.e., the term Aerosol ΔRF_i in Eq. 3.2) for the calculations shown in Figs. 3.4 and 3.5, as well as the contribution to aerosol ΔRF from the six classes of aerosols. This particular time series, based on RCP 4.5, has been designed to match the IPCC [*Stocker et al.*, 2013] best estimate of AerRF_{2011} (aerosol ΔRF in year 2011) of -0.9 W/m^2 .

As detailed in *Canty et al.* [2013], a specific value of AerRF_{2011} can be found using a variety of combinations of scaling parameters that account for the aerosol indirect effect. Figure 3.7a shows time series of aerosol ΔRF for RCP 4.5 designed to match five rather disparate estimates of AerRF_{2011} from IPCC [*Stocker et al.*, 2013]:

- -0.9 W/m^2 (best estimate)
- -0.4 W/m^2 and -1.5 W/m^2 (upper and lower limits of the likely range, denoted by the upper and lower edges of rectangle marked “Expert Judgement” in Fig. 7.19b of IPCC (2013), which are the 17th and 83d percentiles of the estimated distribution)

• -0.1 W/m^2 and -1.9 W/m^2 (upper and lower limits of the possible range, de-noted by the error bars on the “Expert Judgement” rectangle in Fig. 7.19b, which are the 5th and 95th percentiles of the estimated distribution)

Figure 3.7b shows aerosol ΔRF designed to match these same five values of AerRF_{2011} , except for the RCP 8.5 emission of aerosol precursors. Three estimates of Aerosol ΔRF are shown for each value of AerRF_{2011} , found using scaling parameters described in Methods (§3.6).

Variations in the RF of climate due to the land use change (LUC) is the final anthropogenic term considered in our EM-GC. Numerical values of $\text{LUC } \Delta\text{RF}_i$ in Eq. 3.2 are based on Table AII.1.2 of IPCC [*Stocker et al.*, 2013]. This term, which has an extremely minor effect on computed ΔT and is included for completeness, represents changes in the reflectivity of Earth’s surface caused, for example, by conversion of forest to concrete. The release of carbon and other GHGs due to LUC is not represented by this term, but rather by the $\text{GHG } \Delta\text{RF}_i$ term.

We next describe data used to define EM-GC inputs of stratospheric optical depth (SOD), total solar irradiance (TSI), El Niño Southern Oscillation (ENSO), Atlantic Multidecadal Variability (AMV), Pacific Decadal Oscillation (PDO), and the Indian Ocean Dipole (IOD). These measurements are discussed in considerable detail by *Canty et al.* [2013]; therefore, only brief descriptions are given here.

The time series for SOD_i in Eq. 3.2 is based on the global, monthly mean data set of *Sato et al.* [1993], available from 1850 to the end of 2012 (footnote ¹⁴). This time series makes use of ground-based, balloon-borne, and satellite observations, and

¹⁴ The *Sato et al.* [1993] SOD record is at:
http://data.giss.nasa.gov/modelforce/strataer/tau.line_2012.12.txt

represents perturbations to the stratospheric sulfate aerosol layer induced by volcanic eruptions that are energetic enough to penetrate the tropopause. The *Sato et al.* [1993] dataset compares reasonably well with an independent estimate of SOD provided by *Ammann et al.* [2003], which is based on a four-member ensemble simulation of volcanic eruptions by a GCM that resolves the troposphere and stratosphere and is available from 1890 to 2008 (Fig. 2.18 of IPCC AR4 [Solomon, 2007]). The value of SOD is held constant at 0.0035 for October 2012 onwards, due to unavailability of data from *Sato et al.* [1993] for more recent periods of time. The *Sato et al.* [1993] SOD record resolves the recent eruptions of Kasatochi, Sarychev and Nabro [Fromm et al., 2014; Rieger et al., 2015], but stops short of the April 2015 eruption of Calbuco that deposited sulfate into the high latitude, summer stratosphere [Solomon et al., 2016]. Since the perturbation to global SOD due to volcanic eruptions between the end of 2012 and summer 2016 is small, the use of a constant value for SOD since October 2012 has no bearing on any of our scientific conclusions. The use of $i-6$ as the subscript for SOD in Eq. 3.2 represents a 6 month delay between volcanic forcing and surface temperature response; a delay of ~ 6 months was found by the thermodynamic analyses of *Douglass and Knox* [2005] and *Thompson et al.* [2009] and a 6 month delay is used in the MLR studies of *Lean and Rind* [2008] and *Foster and Rahmstorf* [2011].

The time series of TSI_i in Eq. 3.2 is based on two time series. For years prior to 1978, TSI originates from reconstructions that make use of the number, location, and darkening of sunspots as well as various measurements from ground-based solar observatories [Lean, 2000; Wang et al., 2005]. Since 1978, TSI is based on various-spaced based measurements. The magnitude of TSI varies with the well characterized 11-

year sunspot cycle, due to distortion of magnetic field lines caused by differential rotation of the sun¹⁵. A 1 month lag for TSI_i is used in Eq. 3.2 because this yields the largest value of C_2 , the common approach for defining slight temporal offset between perturbation (solar output) and response (global temperature) in MLR-based models [Lean and Rind, 2008].

The time series of $ENSO_i$ in Eq. 3.2 is based on the Tropical Pacific Index (TPI), computed as described by Zhang *et al.* [1997]. This index represents the anomaly of sea surface temperature (SST) in the region bounded by 20°S to 20°N latitude and 160°E to 80°W longitude, relative to a long-term climatology. The SST record of HadSST3.1.1.0 [Kennedy *et al.*, 2011a; b]¹⁶ has been used to compute TPI. A 3-month lag has been applied to ENSO, because this provides the highest correlation between TPI and a simulated response of GMST to ENSO that was computed using a thermodynamic approach [Thompson *et al.*, 2009].

The time series for AMV_i in Eq. 3.2 is based on the time evolution of area weighted, monthly mean SST in the Atlantic Ocean, between the equator and 60°N [Schlesinger and Ramankutty, 1994]. Here, data from HadSST3.1.1.0 have been used (same citations and web address as for ENSO). As shown in the Supplement of Canty *et al.* [2013], nearly identical scientific results are obtained using SST from NOAA. The AMV index is a proxy for changes in the strength of the Atlantic Meridional Overturning

¹⁵ TSI for start of 2009 to 2015 is from column 3 of:

ftp://ftp.pmodwrc.ch/pub/data/irradiance/composite/DataPlots/composite_*.dat

where * is used because the name of this file changes as it is regularly updated. TSI from 1882 to end of 2008 is from column 3 of :

https://ftp.geomar.de/users/kmatthes/CMIP5/TSI_WLS_mon_1882_2008.txt

TSI prior to 1882 is from column 2 of:

ftp://ftp.ncdc.noaa.gov/pub/data/paleo/climate_forcing/solar_variability/lean2000_irradiance.txt

¹⁶ HadSST3.1.1.0 data are at:

http://hadobs.metoffice.com/hadsst3/data/HadSST.3.1.1.0/netcdf/HadSST.3.1.1.0.median_netcdf.zip

Circulation (AMOC) [*Knight et al.*, 2005; *Medhaug and Furevik*, 2011; *Stouffer et al.*, 2006; *R Zhang et al.*, 2007]. Others use Atlantic Multidecadal Oscillation (AMO) to describe this index, but we prefer AMV because whether or not the strength of the AMOC varies in a purely oscillatory manner [*Vincze and Jánosi*, 2011] is of no consequence to the use of this proxy in the EM-GC framework.

There are two important details regarding AMV_i that bear mentioning. This index represents the fact that, during times of increased strength of the AMOC, the ocean releases more heat to the atmosphere¹⁷. There is considerable debate regarding whether the strength of AMOC varies over time (e.g., Box 5.1 of IPCC AR4 [*Solomon*, 2007] and *Willis* [2010]). Our focus is on anomalies of AMOC over time; hence, the AMV_i index is detrended¹⁸. As shown in Fig. 5 of *Canty et al.* [2013], various choices for how this index is detrended have considerable effect on the shape of the resulting time series, which is important for the EM-GC approach. Here, total anthropogenic ΔRF of climate is used to detrend AMV_i , because this method appears to provide a more realistic means to infer variations in the strength of AMOC from the North Atlantic SST record than other detrending options [*Canty et al.*, 2013]. The second detail involves whether monthly data should be used for the AMV_i index, since the AMOC is sluggish and variations of North Atlantic SST on time scales of a year or less likely do not represent variations in large-scale, ocean circulation. Throughout this chapter, the AMV_i index has been filtered to

¹⁷ An illustration of the physics of the interplay between AMOC and release of heat to the atmosphere from the ocean is at http://www.whoi.edu/cms/images/oceanus/2006/11/nao-en_33957.jpg

¹⁸ The de-trending of AMV, the proxy for variations in the strength of AMOC, means that when examined over the entire 156 year record of the simulation, the slope of the panel marked AMOC in Fig 3.5 is near zero. The proxy used to represent AMOC is based on measurements of sea surface temperature, which rise over time due to the transfer of heat from the atmosphere to the ocean. Within an MLR model such as the EM-GC, the AMOC proxy should be detrended, or else a number of erroneous conclusions regarding long-term climate change could result. See §3.2.3 of *Canty et al.* [2013] for further discussion.

remove all components with temporal variations shorter than 9 years; only variations of SST on time scales of a decade or longer are preserved. The interested reader is invited to examine Figure 7 of *Canty et al.* [2013] to see the impact of various options for how AMV_i is filtered.

A major international research effort has provided new insight into temporal variations of the strength of AMOC [*Srokosz and Bryden, 2015*]. The RAPID-AMOC program, led by the Natural Environment Research Council of the United Kingdom, is designed to monitor the strength of the AMOC by deployment of an array of instruments at 26.5°N latitude, across the Atlantic Ocean, which measure temperature, salinity and ocean water velocities from the surface to ocean floor [*Duchez et al., 2014*]. Analysis of a 10-year (2004 to 2014) time series of data reveals a decline in the strength of AMOC over this decade, similar to that shown by our proxy (AMOC ladder, Fig. 3.5) over this same period of time.

The PDO represents the temporal evolution of specific patterns of sea level pressure and temperature of the Pacific Ocean poleward of 20°N [*Y Zhang et al., 1997*], which is caused by the response of the ocean to spatially coherent atmospheric forcing [*Saravanan and McWilliams, 1998; Wu and Liu, 2003*]. The PDO is of considerable interest because variations correlate with the productivity of the fishing industry in the Pacific [*Chavez et al., 2003*]. An index based on analysis of the patterns of SST conducted by the University of Washington¹⁹ is used.

¹⁹ The PDO index is at <http://research.jisao.washington.edu/pdo/PDO.latest>. This record begins in year 1900. Prior to 1900 we assume PDO_i is equal to 0.

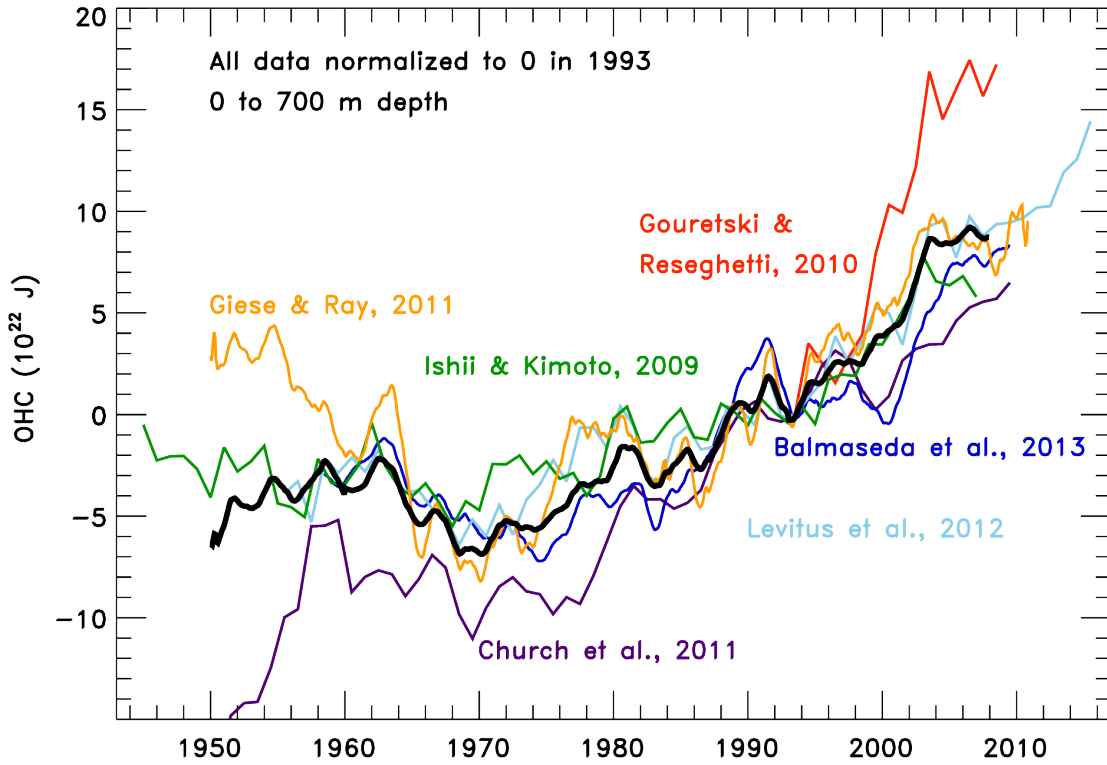
The IOD index²⁰ represents the temperature gradient between the Western and Southeastern portions of the equatorial Indian Ocean [*Saji et al.*, 1999]. The IOD index is used so that all three major ocean basins are represented. Variations in the IOD have important regional effects, including rainfall in Australia [*Cai et al.*, 2011]. However, global effects are small, most likely due to the small size of the Indian Ocean relative to the Atlantic and Pacific oceans.

The increase in the RF of climate due to human activity causes a rise in temperature of both the atmosphere or the water column of the world's oceans [*Hansen et al.*, 2011; *Raper et al.*, 2002; *Schwartz*, 2012]. The oceanographic community has used measurements of temperature throughout the water column, obtained by a variety of sensor systems and data assimilation techniques, to estimate the time variation of the heat content of the world's oceans (OHC, or Ocean Heat Content) [*Carton and Santorelli*, 2008]. Generally the focus has been on the upper 700 meters of the oceans.

Considerable uncertainty exists in OHC. Figure 3.8 shows estimates of OHC in the upper 700 meters of the world's oceans from six studies [*Balmaseda et al.*, 2013; *Carton and Giese*, 2008; *Church et al.*, 2011; *Gouretski and Reseghetti*, 2010; *Ishii and Kimoto*, 2009; *Levitus et al.*, 2012] as well as the average of the data from these six studies. Ostensibly, all of the studies make use of similar (if not the same) measurements from expendable bathythermograph (XBT) devices and the more accurate conductivity temperature depth (CTD) probes. Use of CTDs began in the 1980s, and expanded considerably in 2001 based on the deployment of thousands of drifting floats under the

²⁰ The index for IOD from 1982 to present is based on this record provided by the Observing System Monitoring Center of NOAA <http://stateoftheocean.osmc.noaa.gov/sur/data/dmi.nc>
From 1860 to 1981, IOD is based on data provided by the Japan Agency for Marine-Earth Science and Technology at http://www.jamstec.go.jp/frcgc/research/d1/iod/kaplan_sst_dmi_new.txt

Figure 3.8 – Ocean Heat Content (OHC) Versus Time



OHC from six sources (colored, as indicated). The black solid line is the average of the six measurements used in most of the EM-GC calculations. See §3.6 Methods for further information.

Argo program [Riser *et al.*, 2016]. Alas, the ocean is vast and much is not sampled. The differences in OHC shown in Fig. 3.8 published by various groups represent different methods to fill in regions not sampled by CTDs, as well as various assumptions regarding the calibration (including fall rate correction) of data returned by XBTs.

The $Q_{OCEAN\ i}$ term in Eq. 3.3 is the EM-GC representation of OHE in units of W/m^2 , i.e. OHE is heat flux. The quantity OHC represents the energy content of the upper 700 meter of the world's oceans. To relate OHC and OHE, several computational steps are necessary. First, the OHC values shown in Fig. 3.8 are multiplied by 1.42 (which equals $1/0.7$) to account for the estimate that 70% of the rise in OHC of the world's oceans occurs in the upper 700 meters (§5.2.2.1 of IPCC AR4 [Solomon, 2007]). This multiplication is carried out because ocean heat export in the model must represent the entire water column. As stated above, a 6-year lag is assumed between perturbation and response [Schwartz, 2012]. Next, OHC is divided by $3.3 \times 10^{14} m^2$, the surface area of the world's oceans. Finally, a value for κ is derived so that the change in OHC over the period of time covered by a particular data set (i.e., the average time derivative) is matched, rather than attempting to model the ups and downs of any particular OHC record. Since the ups and downs of the various records are uncorrelated, it is more likely these variations reflect measurement noise rather than true signal.

3.2.1.2 Model Outputs

In addition to the regression coefficients, two additional parameters are found by the EM-GC: the climate sensitivity parameter (γ in Eq. 3.2) and the ocean heat uptake efficiency coefficient (κ in Eq. 3.3). As described in §3.5, values of γ and κ inferred from the prior climate record are used to obtain projections of ΔT , assuming γ and κ remain

constant in time. In this section, some context for the numerical values of γ and κ is presented. Two additional model output terms, the climate feedback parameter (λ) and Equilibrium Climate Sensitivity (ECS), both of which are found from γ , are described. Finally, a metric for model performance, χ^2 , which plays an important role for the projections of ΔT , is defined.

The value of κ found using the OHC record for the upper 700 meters of the world's oceans, averaged from six studies, is $0.62 \text{ W/m}^2/\text{C}$ (bottom panel, Fig. 3.4). As stated in §3.2.1.1, the calculation of κ considers the increase in temperature for depths below 700 meter by scaling observations from the upper part of the ocean. Of the six OHC datasets, *Ishii & Kimoto* [2009] results in the smallest value for κ ($0.43 \text{ W/m}^2/\text{C}$) and *Gouretski & Reseghetti* [2010] leads to the largest value ($1.52 \text{ W/m}^2/\text{C}$). All of the values of κ found using various time series for OHC fall within the range of empirical estimates and coupled ocean-atmosphere model behavior that is shown in Fig. 2 of *Raper et al.* [2002]. As such, the representation of ocean heat export in the EM-GC framework is realistic, given the present state of knowledge. If the true value of κ changes over time, then our projections of ΔT based on an assumption of constant κ will require modification. Past measurements of OHC are too uncertain to infer, from the prior record, whether κ has changed. The nearly-factor-of-3 difference in κ inferred from various, credible estimates of OHC is certainly much larger than any reasonable change in κ that could have occurred during the time of OHC observations.

The value of γ found for the EM-GC simulation shown in Fig. 3.5 is 0.49. This means the increase in RF of climate due to GHGs, tropospheric aerosols, and land use change from 1860 to present must be increased by $\sim 50\%$ (i.e., multiplied by 1.49) to

obtain best fit to observed ΔT . In other words, the sum of all climate feedbacks must be positive. Model parameter γ represents the sensitivity of climate to all of the feedbacks that occur in response to the perturbation to RF at the tropopause induced by humans, and is related to the climate feedback parameter λ via:

$$1 + \gamma = \frac{1}{1 - \frac{\lambda}{\lambda_p}}$$

where $\lambda = \Sigma$ All Climate Feedbacks

i.e. $\lambda = \lambda_{Water\ Vapor} + \lambda_{Clouds} + \lambda_{Lapse\ Rate} + \lambda_{Surface\ Reflectivity} + etc.$

Eq3.5

This formulation for the relation between γ and λ is commonly used in the climate modeling community (see §8.6 of IPCC AR4 [Solomon, 2007]). We record λ rather than γ on all of the EM-GC ladder plots (Fig. 3.4 and 3.5) because λ is more directly comparable to GCM output, such as that in Table 9.5 of IPCC AR5 [Stocker *et al.*, 2013].

Equilibrium climate sensitivity (ECS) is also given on the top rung of the EM-GC ladder plots. This metric represents the increase in ΔT of the climate system after it has attained equilibrium, in response to a doubling of atmospheric CO_2 . In the EM-GC framework ECS is expressed as²¹:

²¹ The derivation is:

$$\begin{aligned} ECS &= \frac{1 + \gamma}{\lambda_p} \Delta RF_{CO_2} = \frac{1 + \gamma}{\lambda_p} 5.35 \text{ Wm}^{-2} \ln \frac{CO_2^{FINAL}}{CO_2^{INITIAL}} = \frac{1 + \gamma}{\lambda_p} 5.35 \text{ Wm}^{-2} \ln 2 \\ &= \frac{1 + \gamma}{\lambda_p} 5.35 \text{ Wm}^{-2} \times 0.693 = \frac{1 + \gamma}{\lambda_p} 3.71 \text{ Wm}^{-2} \end{aligned}$$

assuming, for ECS, that $CO_2^{FINAL} = 2 \times CO_2^{INITIAL}$

The expression for ΔRF_{CO_2} is from Myhre, G., E. Highwood, K. Shine, and F. Stordal (1998), New estimates of radiative forcing due to well mixed greenhouse gases, *Geophysical research letters*, 25(14), 2715-2718.

$$ECS = \frac{1 + \gamma}{\lambda_p} 3.71 \text{ Wm}^{-2}$$

Eq3.6

ECS is often used to compare and evaluate climate simulations. The EM-GC run shown in Fig. 3.5 has an ECS of 1.73°C, which means that if CO₂ were to double (i.e., reach 560 ppm, twice the pre-industrial value of 280 ppm) and if all other GHGs were to remain constant at their pre-industrial level, then ΔT would rise to a level about midway between the Paris target (1.5°C) and upper limit (2.0°C). As will soon be shown, ECS is a difficult metric to use for evaluating climate models because it depends rather sensitively on both aerosol ΔRF and ocean heat content, both of which have considerable uncertainty.

The top rung of each EM-GC ladder plot also contains a numerical value for reduced chi-squared (χ^2), a parameter that defines the goodness of fit between a series of observed and modeled quantities. In our framework, χ^2 is defined as:

$$\chi^2 = \frac{1}{(N_{YEARS} - N_{FITTING PARAMETERS} - 1)} \times \sum_{j=1}^{N_{YEARS}} \frac{1}{\langle \sigma_{OBS j} \rangle^2} (\langle \Delta T_{OBS j} \rangle - \langle \Delta T_{EM-GC j} \rangle)^2$$

Eq3.7

where $\langle \Delta T_{OBS j} \rangle$, $\langle \Delta T_{EM-GC j} \rangle$, and $\langle \sigma_{OBS j} \rangle$, represent the annually averaged observed temperature anomaly, the annually averaged modeled temperature anomaly, and the uncertainty of the annually averaged observed temperature anomaly, respectively, and $N_{FITTING PARAMETERS}$ equals 6 for the simulation shown in Fig 3.4 (4 regression coefficients plus the 2 parameters γ and κ) and equals 9 for Fig. 3.5 (3 additional regression coefficients). The formula for χ^2 is expressed in terms of annual averages,

rather than monthly values, due to the statistical behavior of the two time series that appear in the formula²².

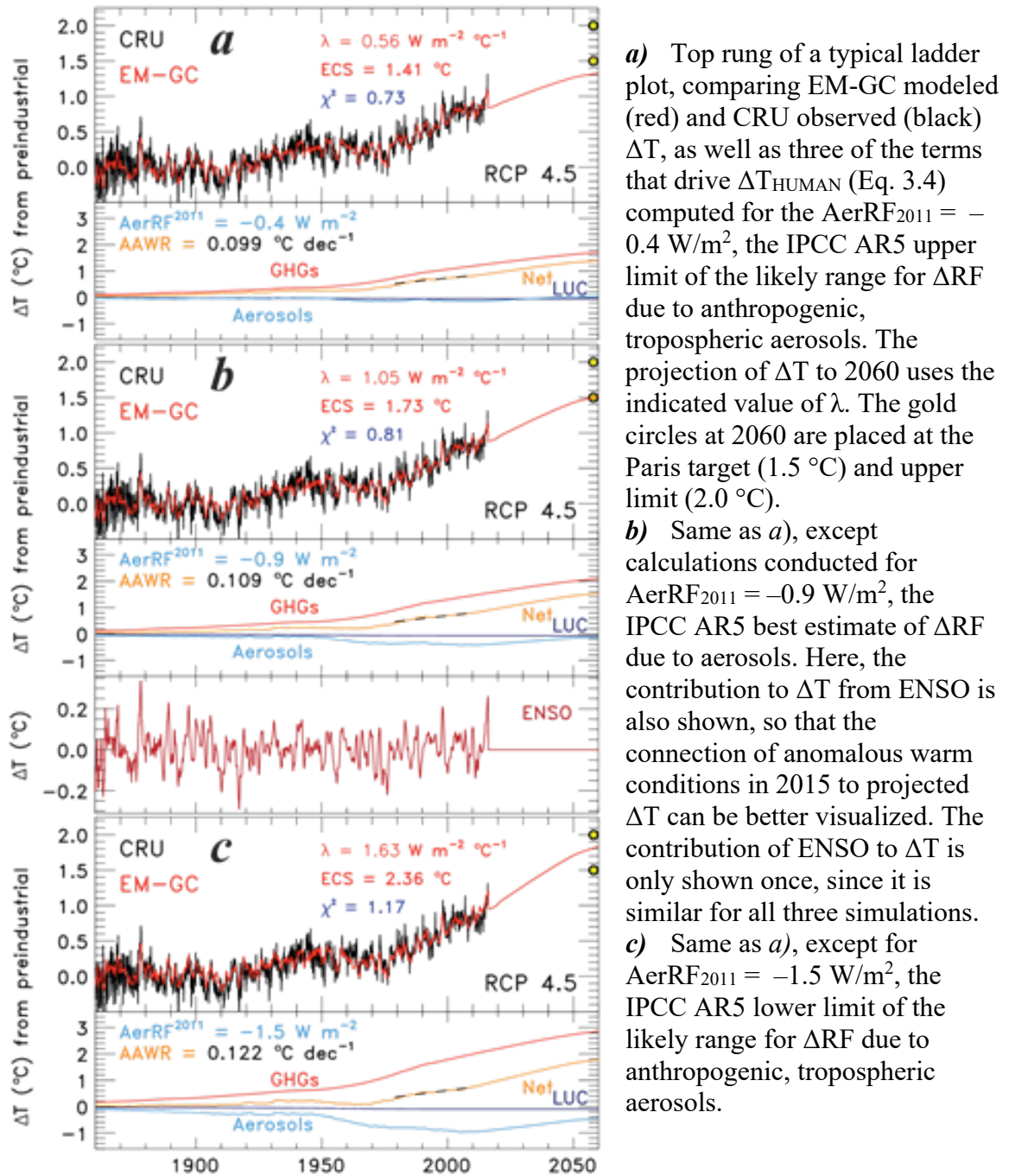
The EM-GC simulation in Fig. 3.4 has $\chi^2 = 1.52$. In the world of physics, this would be termed a reasonably good model simulation. Such an impression is also apparent based on visual inspection of the red and black curves on the top rung of Fig. 3.4. The EM-GC simulation in Fig. 3.5 has $\chi^2 = 0.81$, which is an exceptionally good simulation both in the literal interpretation of χ^2 , as well as visual inspection of Fig. 3.5. For the quantitative assessments of the amount of global warming that can be attributed to humans, as well as the projections of future global warming, EM-GC simulations are weighted by $1/\chi^2$, such that the better the goodness of fit (i.e., the smaller the value of χ^2) the larger the weight. See Chapter 7 of *Taylor* [1997] for a description of this weighting approach.

3.2.2 *The Degeneracy of Earth's Climate*

Figure 3.9 shows simulations of Earth's climate that differ only due to choice of ΔRF due to tropospheric aerosols. Figure 3.9a shows results for AerRF_{2011} of -0.4 W/m^2 (upper limit of IPCC [*Stocker et al.*, 2013] likely range), -0.9 W/m^2 (IPCC best estimate), and -1.5 W/m^2 (lower limit of IPCC likely range). For each simulation, the upper rung of a typical EM-GC ladder plot is shown, but with ΔT projected into the future. Projections use values of λ and κ associated with each simulation, together with RCP 4.5 for GHG

²² For those familiar with statistics, the auto-correlation function of modeled ΔT is compared to the auto-correlation function of the measured ΔT . As shown in the supplement to *Canty et al.* [2013], these functions differ considerably for comparison of measured and modeled monthly anomalies, indicating either the presence of a forcing in the system not resolved by the model or else considerable noise in the measurement. These auto-correlation functions are quite similar for comparison of measured and modeled annual anomalies, indicating proper physical structure of the modeled quantity and *appropriate* use of χ^2 , is applied to *annual averages* of both modeled and measured anomalies.

Figure 3.9 – Observed and EM-GC Simulated Global Warming, 1860 to 2060, for Various AER ΔRF_{2011} Scenarios



All calculations used the mean value of OHC computed from the six datasets shown in Fig. 3.8

abundances and aerosol precursor emissions. Each simulation uses the OHC record based on the average of the six studies shown in Figure 3.8. When projecting ΔT , the only term considered is ΔT_{HUMAN} (Eq. 3.4): i.e., that the future change in temperature will be based on GHG warming and aerosol cooling from RCP 4.5, climate feedback, and ocean heat export. It is also assumed that natural factors such as ENSO, solar, and volcanoes will have no influence on future temperature. The second rung of Fig. 3.9 shows ΔT_{HUMAN} as well as the contributions from individual terms (here the OHE term is not shown for clarity because it is small and nearly the same for each simulation²³). The GMST experienced in 2015 was unusually large due to the effect of ENSO, which is illustrated by inclusion of the ENSO rung for Fig. 3.9b (footnote ²⁴).

Figure 3.9 shows that the climate record can be fit nearly equally well using the EM-GC approach for two contrasting scenarios:

- 1) tropospheric aerosols have had little overall effect on prior climate due to a near balance of cooling (primarily sulfate aerosols) and heating (primarily black carbon aerosols) and the **climate feedback** (numerical value of λ) needed to fit observed ΔT_i is **small** (Fig. 3.9a)
- 2) tropospheric aerosols have offset a considerable portion of the GHG warming over the prior decades because cooling (sulfate) has dominated heating (black carbon) and the **climate feedback** needed to fit observed ΔT_i is **large** (Fig 3.9c).

If whatever value of climate feedback (model parameter λ) needed to fit the past climate record is assumed to be unchanged into the future, then projections of global warming under scenario 2 (Fig. 3.9c) far exceed those of scenario 1 (Fig 3.9a). The fundamental reason for this dichotomy is that RF of climate due to all types of tropospheric aerosols

²³ Time series of ocean heat export (OHE) appear on the next figure, which illustrates the sensitivity of the EM-GC model to choice of data set for ocean heat content (OHC).

²⁴ The ENSO rungs for Fig 3.9a and 3.9c are nearly identical to Fig 3.9b and is only shown once

will be much lower in the future than it has been in the past, due to public health legislation designed to improve air quality (Fig. 2.9). Future warming thus depends on ΔRF due to GHGs (same for both scenarios) and climate feedback (larger for scenario 2). When two different models can produce similarly good fits to a data record under contrasting assumptions, such as scenarios 1 and 2 above, physicists term the problem as being *degenerate*. Simply put, the degeneracy of Earth's climate introduces a fundamental uncertainty to projections of global warming.

The degeneracy of our present understanding of Earth's climate has important implications for policy. Figure 3.9 also contains markers, placed at year 2060, of the goal (1.5 °C warming) and upper limit (2.0 °C) of the Paris Climate Agreement. Again, all of the projections in Fig. 3.9 are based on RCP 4.5; the three simulations represent the present “likely” range of uncertainty in ΔRF of climate associated with the RCP 4.5 aerosol precursor specification. The projection of ΔT in Fig. 3.9a lies below the Paris goal for the entire time period; the projection of ΔT in Fig 3.9b hits the Paris goal right at 2060, whereas the projection of ΔT in Fig 3.9c falls between the Paris goal and upper limit in 2060. Later in this chapter we show projections out to year 2100, which is especially important since simulated temperatures are all rising at the end of the time period used for Fig. 3.9.

The calculations shown in Fig. 3.9 suggest that if the present uncertainty in ΔRF due to tropospheric aerosols could be reduced, then global warming could be projected more accurately. There is considerable effort in the climate community to reduce the uncertainty in this term. It is beyond the scope of this book to review the widespread efforts in this area; such reviews are the domain of large, community wide efforts such as

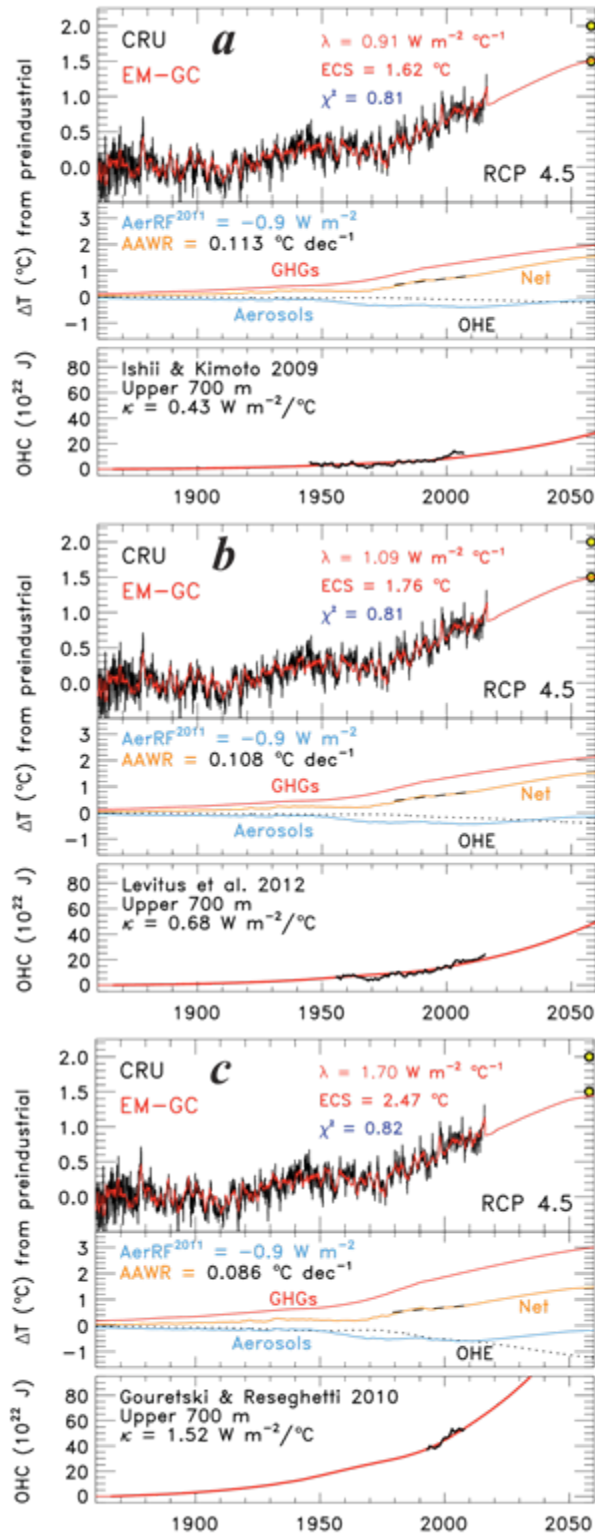
the decadal surveys of measurement needs conducted by the U.S. National Academy of Sciences (NAS)²⁵. *Bond et al.* [2013] published a detailed evaluation of the radiative effect due to black carbon (BC) aerosols and concluded the most likely value was 0.71 W/m² warming, from 1750 to 2005, which far exceeds the IPCC AR4 [*Solomon, 2007*] estimate of 0.2 W/m² warming over this same period of time. The IPCC AR5 [*Stocker et al., 2013*] best estimate of Δ RF for BC aerosols is 0.4 W/m² warming, from 1750 to 2011. If the *Bond et al.* [2013] estimate is correct, then all else being equal, the absolute value of the best estimate for AerRF₂₀₁₁ would drop, relative to the -0.9 W/m² value given by IPCC AR5 [*Stocker et al., 2013*]. Given the cantilevering between climate feedback and AerRF₂₀₁₁ (Fig. 3.9) and the sensitivity of future Δ T to climate feedback, this modification would induce a corresponding decline in the associated projection of Δ T. Much more work is needed to better quantify Δ RF due to aerosols, because of the complexity of aerosol types that affect the direct RF term [*Kahn, 2012*] as well as difficulties in assessing the effect of aerosols on clouds [*Morgan et al., 2006; Storelvmo et al., 2009*].

3.2.3 Equilibrium Climate Sensitivity

The degeneracy of the climate record also limits our ability to precisely define equilibrium climate sensitivity (ECS), the warming that occurs after climate has equilibrated with 2×preindustrial CO₂ [*Kiehl, 2007; Otto et al., 2013; Schwartz, 2012; Schwartz et al., 2014*]. The values of ECS associated with the three simulations shown in Figure 3.9 are 1.4, 1.7, and 2.4 °C, for AerRF₂₀₁₁ values of -0.4 W/m², -0.9 W/m², and

²⁵ At time of writing, the 2017 NAS Decadal Survey is underway and progress can be viewed at: <http://sites.nationalacademies.org/DEPS/ESAS2017/index.htm>

Figure 3.10 – Observed and EM-GC Simulated Global Warming, 1860 to 2060, for Various OHC Records



Top rung of a typical ladder plot, comparing EM-GC modeled (red) and CRU observed (black) ΔT , as well as three of the terms that drive ΔT_{HUMAN} (Eq. 3.4) computed for the AerRF₂₀₁₁ = -0.9 W/m², the IPCC AR5 best estimate for ΔRF due to aerosols, and comparison of modeled and measured OHC, for a simulation that derives a value for κ that provides best fit to the OHC dataset of *Ishii & Kimoto* [2009].

Same as *a*), expect for a simulation that derives a value for κ that provides best fit to the OHC dataset of *Levitus et al.* [2012].

Same as *a*), expect for a simulation that derives a value for κ that provides best fit to the OHC dataset of *Gouretski & Reseghetti* [2010]. Note how the values of Equilibrium Climate Sensitivity (ECS) given in the three panels respond to changes in OHC, whereas the transient climate responses (red curve, upper rung of each ladder plot) are nearly identical. Also, smaller values of Attributable Anthropogenic Warming Rate (AAWR) are found as OHC rises, due to interplay of the OHE and aerosol terms within ΔT_{HUMAN} .

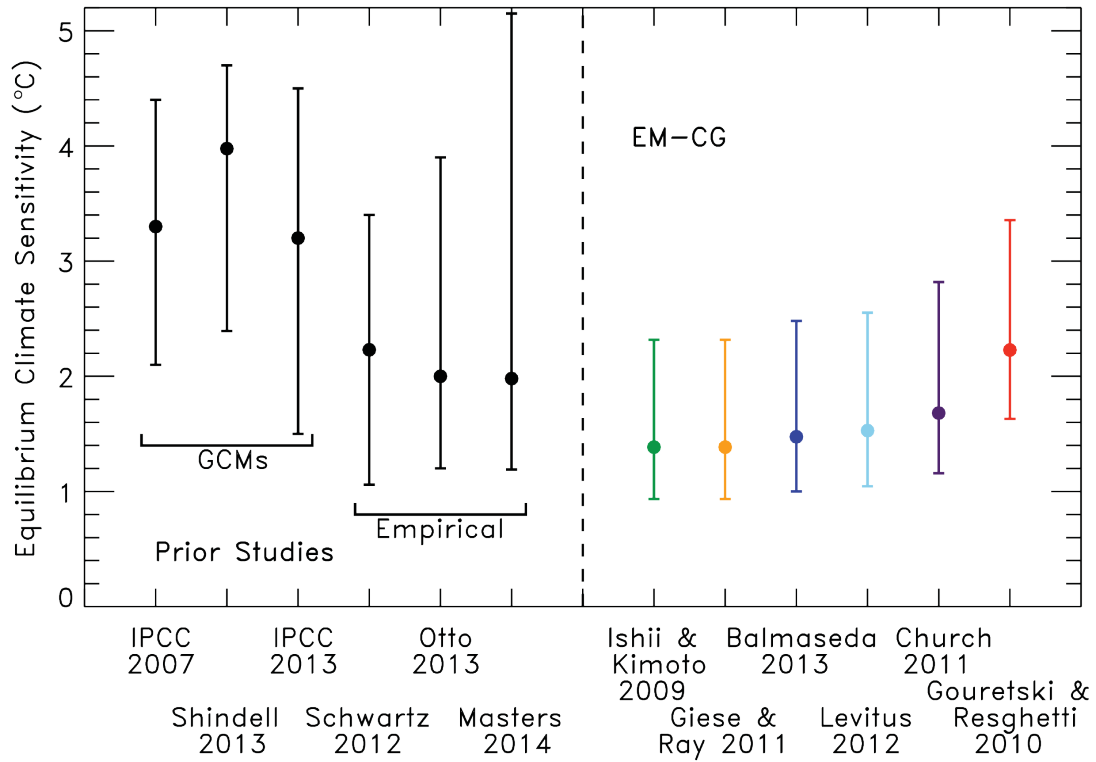
-1.5 W/m^2 , respectively. We conclude from Fig. 3.9 that if ocean heat export occurs in a manner similar to that described by the OHC determined by averaging six data records, then ECS lies between 1.4 and 2.4°C .

Alas, if only the climate system were this simple. As shown in Fig. 3.8, the OHC record is also quite uncertain. Figure 3.10 shows three additional simulations of Earth's climate, similar except for choice of OHC. All three simulations shown in Fig 3.10 use the IPCC AR5 [Stocker *et al.*, 2013] best estimate of -0.9 W/m^2 for AerRF₂₀₁₁. Fig. 3.10a utilizes the OHC record of *Ishii and Kimoto* [2009], which yields the smallest value of κ among all available datasets, $0.43 \text{ W/m}^2/^\circ\text{C}$. Fig 3.10c makes use of the OHC record of *Gouretski and Reseghetti* [2010] that yields the largest value of κ , $1.52 \text{ W/m}^2/^\circ\text{C}$. The OHC record of *Levitus et al.* [2012], which lies closest to the average of the six OHC determinations (Fig. 3.8), results in an intermediate value of κ equal to $0.68 \text{ W/m}^2/^\circ\text{C}$ (Fig 3.10b). The second rung of each ladder plot of Fig. 3.10 shows the contributions to ΔT_{HUMAN} from GHGs, tropospheric aerosols, and OHE²⁶. The value of ECS ranges from 1.6°C to 2.5°C , depending on which dataset for OHC is used. These simulations reveal a **second degeneracy** of the climate record, which further impacts our ability to define ECS. If the export of heat from the atmosphere to the oceans is truly as large as suggested by the OHC record of *Gouretski and Reseghetti* [2010], then Earth's climate exhibits considerably larger sensitivity to the doubling of atmospheric CO_2 than if the OHC record of *Ishii and Kimoto* [2009] is correct.

Despite these complexities, an important pattern emerges upon comparison of ECS inferred from observations to ECS from GCMs. Figure 3.11 shows ECS from

²⁶ The LUC term, which is always close to zero, is not shown in Fig. 2.10 for clarity

Figure 3.11 – Equilibrium Climate Sensitivity (ECS) from the Literature and EM-GC Simulations



Estimates of ECS from six previously published studies (left most points, black) and from six runs of our empirical model of global climate (right most points, colors). For the six points to the left, words below the axis are the citation for the ECS value. For the six colored points to the right, the words below the axis denote the origin of the OHC record used in the particular EM-GC simulation. See §3.6 Methods for further information.

GCMs that had been used in IPCC AR4 [Solomon, 2007], the more recent IPCC AR5 [Stocker et al., 2013] GCMs, and a subset of the IPCC AR5 GCMs that participated in an evaluation process known as the Atmospheric Chemistry and Climate Model Intercomparison Project (ACCMIP). The ACCMIP GCMs tend to have more sophisticated treatment of tropospheric aerosols than the rest of the CMIP5 GCMs [Shindell et al., 2013]. Figure 3.11 also shows three recent, independent estimates of ECS from the actual climate record: two based on analyses conceptually similar to our EM-GC approach, albeit quite different in design and implementation [T Masters, 2014; Schwartz, 2012] and a third that examined Earth's energy budget in detail over various decadal periods [Otto et al., 2013]. The righthand side of Fig. 3.11 shows ECS found using our EM-GC framework, for the six estimates of OHC that appear in Fig 3.8.

Figure 3.11 shows that published values of ECS from GCMs (average of the three best estimates is 3.5 °C) are considerably larger than estimates of ECS from the actual climate record. This pattern holds upon comparison of GCM-based ECS to values found using empirically-based estimates of ECS found by other research groups (mean value 2.1 °C) and using our EM-GC framework (mean value 1.6 °C).

These three estimates of ECS are important for policy. The mean value of ECS from GCMs (3.5 °C), taken literally and ignoring changes in other GHGs, indicates CO₂ must be kept far short of the 2×pre-industrial level to achieve the Paris upper limit of 2°C warming. The mean of the three empirically based estimates of ECS from other groups (2.1 °C) suggests the Paris upper limit can perhaps be achieved if the rise of CO₂ can be arrested before reaching the 2×pre-industrial level, whereas the mean value ECS from our EM-GC framework (1.6 °C) suggests that if society manages to keep CO₂ from reaching

2×pre-industrial level, the Paris goal might be achieved. Of course, these statements are all contingent on minimal future growth of other GHGs. Also, we stress that all of the estimates of ECS, even those from our EM-GC framework, are associated with considerable uncertainty. Nonetheless, the various ECS estimates in Fig. 3.11 suggest climate feedback within GCMs is larger than in the actual climate system²⁷, which would explain the tendency for so many CMIP5 GCM projections of ΔT to lie above the green trapezoid in Fig. 3.3.

The tendency of CMIP5 GCMs to warm too quickly, with respect to the actual human influence on ΔT , is probed further in §3.3. This shortcoming of the CMIP5 GCMs is crucial to the thesis of this book: that the Paris Climate Agreement, as presently formulated, could actually limit the growth of GMST to less than 2 °C above preindustrial.

3.3 Attributable Anthropogenic Warming Rate

The most important metric for a climate model is how well the prior rise in global mean surface temperature can be simulated. The green trapezoid used in various figures throughout this chapter is based on the recognition, by Chapter 11 of IPCC [*Stocker et al.*, 2013], that CMIP5 GCMs have warmed too aggressively compared to observations over the prior several decades. In this section, the empirical model of global climate is used to quantify the amount of global warming that can be attributed to humans, over the time period 1979 to 2010 (footnote ²⁸). These years are chosen because the rise in ΔT is nearly linear over this interval and this period has been the basis of similar examination

²⁷ Most estimates of ECS, such as Eq. 3.6, show ECS to be solely a function of climate feedback

²⁸ Specifically all analyses in this section span the start of 1979 to the end of 2010

by several other studies [*Foster and Rahmstorf, 2011; J Zhou and Tung, 2013a*]. Our analysis of ΔT is compared to simulations of this quantity provided by CMIP5 GCMs, and to other analyses of ΔT over this period of time.

First, some terminology must be defined. Chapter 10 of IPCC AR5 [*Stocker et al., 2013*] examined the amount of warming over specific time periods that can be attributed to humans, which we term Attributable Anthropogenic Warming (AAW). Figure 10.3 of IPCC AR5 shows plots of the latitudinal distribution of AAW, for time periods of 32, 50, 60, and 110 years. We prefer to divide AAW (units of $^{\circ}\text{C}$) by the length of the time period in question, to arrive at a term called Attributable Anthropogenic Warming Rate (AAWR) (units of $^{\circ}\text{C}/\text{decade}$). Consideration of AAWR, rather than AAW, provides a means to compare observed and modeled ΔT for studies that happen to examine time intervals with various lengths.

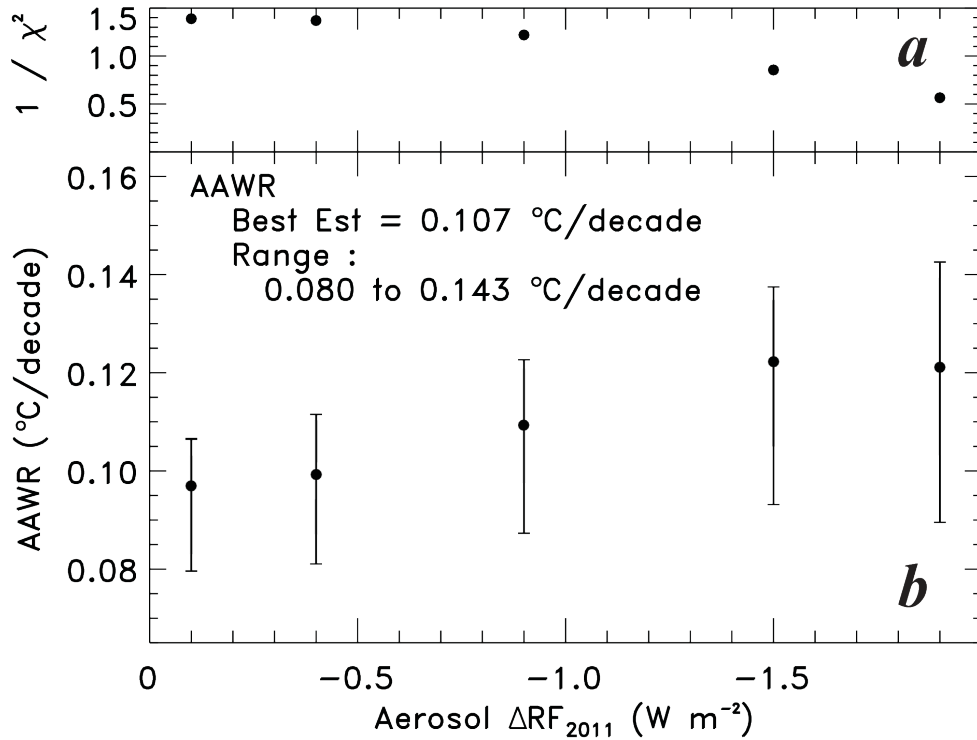
Next, the method for quantifying AAWR is described. Equation 3.4 provides a mathematical definition for $\Delta T_{\text{HUMAN } i}$ in the EM-GC framework. This equation represents the contribution to the changes in GMST due to human release of GHGs, industrial aerosols, and land use change. Central to our estimate of AAWR is quantitative representation of the climate feedback needed to match observed ΔT (parameter γ in Eq. 3.4) and transfer of heat from the atmosphere to the ocean (term Q_{OCEAN}). The slope of $\Delta T_{\text{HUMAN } i}$, found using Eq. 3.4, with respect to time, is used to define AAWR. Below, slopes are found by fitting values of $\Delta T_{\text{HUMAN } i}$ for time periods that span the start of 1979 to the end of 2010, for various runs of the EM-GC that cover the entire 1860 to 2015 period of time.

Numerical values of AAWR, from 1979 to 2010, are recorded on Figures 3.4, 3.5, 3.9, and 3.10. The uncertainty associated with each value of AAWR given on Fig. 3.4 and 3.5 is the standard error of the slope, found using linear regression²⁹. The values of AAWR on these figures span a range of 0.086 °C/decade (Fig. 3.10c) to 0.122 °C/decade (Fig 3.9c). Differences in AAWR reflect changes in the slope of $\Delta T_{\text{HUMAN } i}$ over this 32-year interval, driven by various assumptions for ΔRF due to tropospheric aerosols as well as ocean heat export.

Figure 3.12 illustrates the dependence of AAWR on how radiative forcing due to tropospheric aerosols is specified. Panel b shows estimates of AAWR as a function of AerRF_{2011} , for simulations that all utilize the average value of ocean heat content from the six datasets shown in Fig. 3.8. The uncertainty of each data point represents the range of AAWR found for various assumptions regarding the shape of ΔRF of aerosols (i.e., the three curves for a specific value of AerRF_{2011} shown in Fig. 3.7, all of which are tied to aerosol precursor emission files from RCP 4.5). Figure 3.12a shows the mean value of $1/\chi^2$ associated with the three simulations conducted for a specific value of AerRF_{2011} . The higher the value of $1/\chi^2$, the better the climate record is simulated. The best estimate for AAWR of 0.107 °C/decade is based on a weighted average of the five circles in Fig 3.12b, where $1/\chi^2$ is used as the weight for each data point. The largest and smallest values of the five error bars on Fig. 3.12b are used to determine the upper and lower limits of AAWR, respectively. We conclude that if OHC has risen in a manner described by the average of the six datasets shown in Fig. 3.8, then the best estimate of AAWR over

²⁹ Uncertainties for AAWR are omitted from Figs. 3.9 and 3.10, for clarity, but are of the same magnitude as the uncertainties given on Figs. 3.4 and 3.5.

Figure 3.12 – Sensitivity of Attributable Anthropogenic Warming Rate (AAWR) due to ΔRF of Aerosols

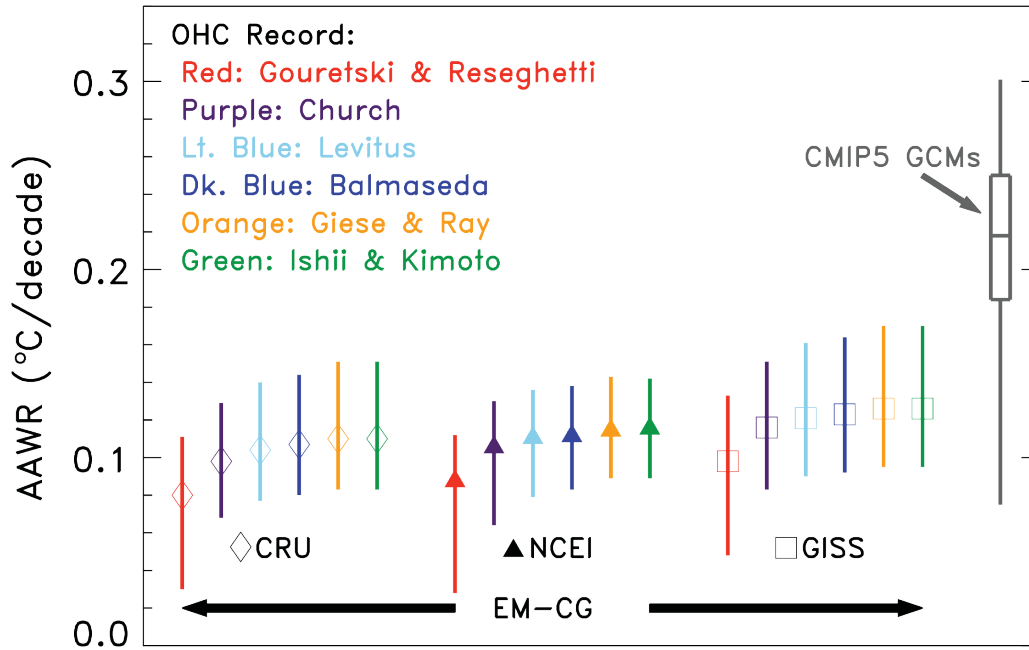


a) $1/\chi^2$ from the EM-GC simulations in the lower panel; the larger the value, the better the fit.

b) Values of AAWR for 1979 to 2010, computed as the slope of ΔT_{HUMAN} , for EM-GC simulations that use the 15 time series of aerosol ΔRF shown in Fig. 3.7a. AAWR is displayed as a function of aerosol ΔRF in year 2011 (AerRF_{2011}). All calculations used the mean value of OHC computed from the six datasets shown in Fig. 3.8. The best estimate for AAWR, found using five estimates weighted by $1/\chi^2$, as well as the lower and upper estimates for AAWR, are indicated.

See §3.6 Methods for further information.

Figure 3.13 – Comparison of AAWR from the EM-GC and CMIP5 GCMs



Diamonds, triangles, and squares show the best estimate of AAWR, 1979 to 2010, found using ΔT from the CRU [Jones *et al.* 2012], GISS [Hansen *et al.* 2010], and NCEI [Karl *et al.* 2015] data centers, for various data records of OHC denoted by color. Error bars on these points represent the upper and lower limits of AAWR computed based on consideration of 15 possible time series for ΔRF of aerosols shown in Fig. 3.7a. Values of AAWR over 1979 to 2010 from the 41 GCMs that submitted RCP 4.5 simulations to the CMIP5 archive are shown by the box and whisker (BW) symbol. The middle line of the BW symbol shows the median value of AAWR from the 41 GCMs; the boxes denote the 25th and 75th percentile of the distribution, and the whiskers show maximum and minimum values of AAWR. See §3.6 Methods for further information.

1979 to 2010 is $0.107\text{ }^{\circ}\text{C}/\text{decade}$, with 0.008 to $0.143\text{ }^{\circ}\text{C}/\text{decade}$ bounding the likely range.

The specific data record chosen for OHC has a modest effect on AAWR. This sensitivity is apparent from numerical values for AAWR recorded on Figs. 3.10a, b, and c. This dependence of AAWR on OHC is illustrated by the colored symbols on Fig. 3.13, which show the best estimate (symbols) and range of AAWR (error bars) that is found for each of the six OHC records. The three groupings of data points show AAWR found using ΔT from CRU [Jones *et al.*, 2012], GISS [Hansen *et al.*, 2010], and NCEI [Karl *et al.*, 2015]. Nearly identical values of AAWR are found, regardless of which data center record is used to define ΔT . The mean value of the 18 empirical determinations of AAWR in Fig. 2.13 is $0.109\text{ }^{\circ}\text{C}/\text{decade}$, with a low and high of 0.028 and $0.170\text{ }^{\circ}\text{C}/\text{decade}$, respectively. The notation $0.109 (0.028, 0.170)\text{ }^{\circ}\text{C}/\text{decade}$ is used to denote the mean and range of this determination of AAWR.

Figure 2.13 also contains a graphical representation of AAWR extracted from the 41 GCMs that submitted results for RCP 4.5 to the CMIP5 archive (see §3.6 Methods for details on how AAWR from GCMs is found). The GCM values of AAWR are displayed using a box and whisker symbol. The middle line represents the median value of AAWR from the GCMs; the box is bounded by the 25th and 75th percentiles, whereas the whisker (vertical line) connects the maximum and minimum values. The median value of AAWR from the CMIP5 GCMs is $0.218\text{ }^{\circ}\text{C}/\text{decade}$, about twice the observed rate of warming. The 25th percentile lies at $0.183\text{ }^{\circ}\text{C}/\text{decade}$, which exceeds the empirically determined upper limit for AAWR of $0.170\text{ }^{\circ}\text{C}/\text{decade}$ over the time period 1979 to 2010. In other words, the CMIP5 GCMs on average simulate an anthropogenically induced rate

of warming that is twice as fast as the actual climate system has warmed and three quarters of the CMIP5 GCMs exhibit warming that exceeds the highest plausible value for AAWR that we infer from the climate record. This is rather disconcerting, given the prominence of the CMIP5 GCMs in the discussion of climate policy (e.g., *Rogelj et al.* [2016] and references therein).

The most likely reason for the shortcoming of CMIP5 GCMs illustrated in Fig. 2.13 is that climate feedback within these models is too large. Although tabulations of λ from CMIP5 GCMs exist (i.e., Table 9.5 of IPCC AR5), comparison to values of λ found using the EM-GC framework is complicated by the sensitivity of λ to the ΔRF of climate due to aerosols as well as ocean heat export. Most studies of GCM output [*Andrews et al.*, 2012; *Shindell et al.*, 2012; *Vial et al.*, 2013] do not examine all three of these parameters. For meaningful comparison of GCMs to climate feedback from our simulations, it would be particularly helpful if future GCM tabulations of λ provided ΔRF due to aerosols and the ocean heat uptake efficiency coefficient [*Raper et al.*, 2002] that best describes the rise ocean heat content within each GCM simulation. While the discussion of Fig. 9.17 of AR5 emphasizes good agreement between the observed rise in ocean heat content (OHC) and the CMIP5 multi-model mean rise in OHC since the early 1960s, there is an enormous range in the actual increase of OHC among the 27 CMIP5 GCMs used in this analysis.

Cloud feedback tends to be positive in nearly all GCMs i.e., simulated changes in the properties and distribution of clouds tends to amplify ΔRF of climate due to rising GHGs [*Vial et al.*, 2013; *Zelinka et al.*, 2013; *C Zhou et al.*, 2015]³⁰. Furthermore,

³⁰ Fig 7.10 of AR5 provides a concise summary of the representation of cloud feedback within GCMs

GCMs that represent clouds in such a way that they act as a strong positive feedback tend to have larger values of ECS [Vial *et al.*, 2013]. It is quite challenging to define cloud feedback from observations because the effect of clouds on ΔRF of climate depends on cloud height, cloud thickness, and radiative effects in two distinct spectral regions³¹. To truly discern cloud feedback, the effect of anthropogenic tropospheric aerosols on clouds should be quantified and removed [Peng *et al.*, 2016]. The ephemeral nature of clouds requires either a long observing time to discern a signal from an inherently noisy process or the use of seasonal changes to deduce a relation between forcing and response [Dessler, 2010]. Nonetheless, evidence has emerged that cloud feedback in the actual atmosphere is indeed positive [Norris *et al.*, 2016; C Weaver *et al.*, 2015; C Zhou *et al.*, 2015]. However, the uncertainty in the empirical determination of cloud feedback is quite large [Dessler, 2010; C Zhou *et al.*, 2015]. Furthermore, the vast majority of satellite-based studies of cloud feedback that compare to GCM output make no attempt to quantify the effect of aerosols on clouds, which is problematic given the change in the release of aerosol precursors that has occurred in the past three decades [S Smith and Bond, 2014] combined with varied representation of the effect of aerosols on clouds within GCMs [Schmidt *et al.*, 2014]. There are major efforts underway to evaluate and improve the representation of clouds within GCMs [Webb *et al.*, 2017]. Based on the considerable existing uncertainty in the empirical determination of cloud feedback and the wide range of GCM representations of this process, cloud feedback within GCMs is

³¹ Proper determination of ΔRF due to clouds requires analysis of the impact of clouds on reflectivity and absorption of solar radiation, commonly called the cloud short wavelength (SW) effect in the literature, as well as the impact of clouds on the trapping of infrared radiation (or heat) emitted by Earth's surface, commonly called the long wavelength (LW) effect.

the leading candidate for explaining why most of the GCM-based values of AAWR exceed the empirical determination of AAWR.

Next, our determination of AAWR is compared to estimates published by other groups. All studies considered here examined the time period 1979 to 2010. Our best estimate (and range) for AAWR found using the CRU ΔT dataset is 0.107 (0.080, 0.143) $^{\circ}\text{C}/\text{decade}$. *Foster & Rahmstorf* [2011] (hereafter, FR2011) reported a value for AAWR of 0.170 $^{\circ}\text{C}/\text{decade}$ based on analysis of an earlier version of the CRU ΔT record³². They used multiple linear regression to remove the influence of ENSO, volcanoes, and total solar irradiance on observed ΔT and then examined the difference between observed ΔT and the contribution from these three exogenous factors, termed the residual, to quantify ΔT . The FR2011 estimate of AAWR exceeds our upper limit and lies closer to median GCM-based value of 0.218 $^{\circ}\text{C}/\text{decade}$ found upon our analysis of the CMIP5 archive.

The difference between our best estimate for AAWR (0.107 $^{\circ}\text{C}/\text{decade}$) and the value reported by FR2011 (0.170 $^{\circ}\text{C}/\text{decade}$), both for ΔT from CRU, is due to the two approaches used to quantify the human influence on global warming. We have applied the approach of FR2011 to the derivation of AAWR using both the older version of the CRU ΔT used in their study and the more recent version used in our analysis, and arrive at 0.166 $^{\circ}\text{C}/\text{decade}$ for the older version and 0.183 for the latest version.

The difficulty in the approach used by FR2011 is that their value of AAWR is based upon analysis of a residual found upon removal of all of the natural processes thought to influence ΔT . If an unaccounted for natural processes happens to influence ΔT over the period of time upon consideration, such as the Atlantic Meridional Overturning

³² FR2011 also reported slightly higher values of AAWR, 0.171 and 0.175 $^{\circ}\text{C}/\text{decade}$, upon use of ΔT from GISS and NCEI, respectively.

Circulation, then the value of AAWR found by examination of the residual will be biased by the magnitude of the variation in ΔT due to this process over the period of time under consideration.

Quantitative analysis of the CRU data record reveals the cause of the difference of these two apparently disparate estimates of AAWR for the 1979 to 2010 time period. The 5th rung of the Fig. 3.5 ladder plot indicates AMOC may have contributed 0.043 °C/decade to the rise of ΔT , over the time period 1979 to 2010. Upon use in our EM-GC framework of the same version of CRU ΔT that was analyzed by FR2011, we compute AAWR = 0.109 °C/decade and a slope of 0.058 °C/decade for the contribution of AMOC to ΔT over 1979 to 2010. Thus, natural variation of climate due to variations in the strength of the Atlantic Meridional Overturning Circulation accounts, nearly exactly, for the difference between the FR2011 estimate of AAWR (0.170 °C/decade) and our value (0.109 °C/decade) ³³.

There is considerable debate about whether North Atlantic SST truly provides a proxy for variations in the strength of AMOC. An independent analysis conducted using different methodology [DelSole *et al.*, 2011] supports our view that internal climate variability contributed significantly to the relative warmth of latter part of the time series examined by FR2011. Analysis of a residual to quantify a process, rather than construction and application of a model that physically represents the process, violates fundamental principles of separation of signal from noise [Silver, 2012]. The estimates of AAWR shown in Figs. 3.4 and 3.5 yield *similar values*, 0.111 °C/decade versus 0.109

³³ That is, 0.109 + 0.058 °/decade is nearly equal to 0.170 °/decade. Upon use of the same version of the CRU dataset as FR2011, we find a slope of 0.058 °/decade for 1979 to 2010, for the rung of the resulting ladder plot labeled AMOC (not shown).

°C/decade, whether or not AMOC is considered, because our determination of AAWR is built upon a *physical model for the human influence on climate* (Eq. 3.4) and does not rely on analysis of a residual.

If there is one word that best summarizes the present state of climate science in the published literature, it might be confusion. Alas, the argument put forth in the prior paragraphs, that a value for AAWR from 1979 to 2010 of ~ 0.10 °C/decade is inferred from the climate record whether or not variations in the strength of AMOC are considered in the model framework, is in direct contradiction to *Zhou & Tung* [2013] (hereafter ZT2013). ZT2013 examined version 4 of the CRU ΔT data record, using a modified residual method³⁴, and concluded AAWR is 0.169 °C/decade if temporal variation of AMOC are ignored, but drops to 0.07 °C/decade if variations in the strength of AMOC are considered. The ZT13 estimate of AAWR without consideration of AMOC is in close agreement with the value published by FR2011, and disagrees with our value for the reasons described above.

The importance of the ZT13 study is that if their value of AAWR found upon consideration of AMOC (0.07 °C/decade) is correct, one would conclude that the CMIP5 GCMs warm a factor of three more quickly than the actual climate system has responded to human influence. We are also able to reproduce the results of ZT13, but we argue their estimate of AAWR is biased low because they used a single linear function to describe ΔT_{HUMAN} over the entire 1860 to 2010 time period. As illustrated on the second rung of

³⁴ The method used by ZT13 is similar to that of FR2011, except ZT13 include a model for ΔT_{HUMAN} in their calculation of regression coefficients that are used to remove the influence of ENSO, volcanic, and solar variations from ΔT (their case 1) or remove the influence of ENSO, volcanic, solar variations, and AMOC from ΔT (their case 2). For both cases, their model of ΔT_{HUMAN} is a linear function from 1860 to 2010.

the Fig. 3.4 and 3.5 ladder plots, ΔT_{HUMAN} varied in a non-linear manner from 1860 to present. The time variation of ΔT_{HUMAN} bears a striking resemblance to the rise in population over this period of time. For the determination of AAWR, not only should a model for ΔT_{HUMAN} be used, but this model must correspond to the actual shape of the time variation of radiative forcing of climate caused by humans.

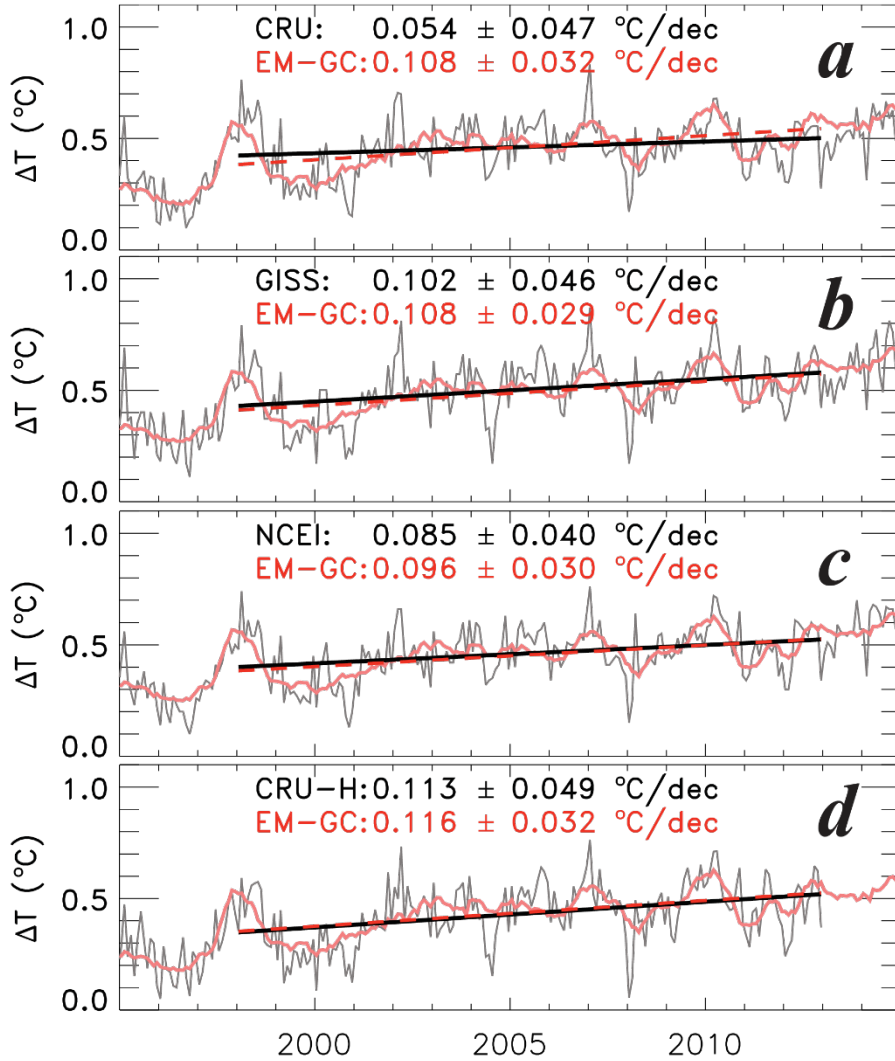
3.4 Global Warming Hiatus

The evolution of ΔT over the time period 1998 to 2012 has received enormous attention in the popular press, blogs, and scientific literature because some estimates of ΔT over this period of time had indicated little change [Trenberth and Fasullo, 2013]. Various suggestions had been put forth to explain this apparent leveling off of ΔT , including climate influence of minor volcanoes [Santer *et al.*, 2014; Schmidt *et al.*, 2014; Solomon *et al.*, 2011], changes in ocean heat uptake [Balmaseda *et al.*, 2013; Meehl *et al.*, 2011], and strengthening of trade winds in the Pacific [England *et al.*, 2014]. The major ENSO event of 1998, which led to a brief, rapid rise in ΔT due to suppression of the upwelling of cold water in the east-ern Pacific, must be factored into any analysis of the hiatus³⁵.

Karl *et al.* [2015] have questioned the existence of a hiatus. They showed an update to the NCEI record of GMST, used to define ΔT , which exhibits a steady rise from 1998 to 2012, despite the ENSO event in 1998. The main improvement was extension to present time of a method to account for biases in SST, introduced by varying techniques to record water temperature from ship-borne instruments.

³⁵ The effect of ENSO on ΔT in 1998 is readily apparent on the 4th rung of the Fig. 3.4 and 3.5 ladder plots.

Figure 3.14 – Observed and EM-GC Simulated Global Warming, 1995 to 2016



Top rung of a typical ladder plot, comparing EM-GC modeled (red) and observed (grey) ΔT . Also shown are linear fits to the modeled (red dashed) and measured (black) time series of ΔT , considering monthly values from the start of 1998 to the end of 2012. The slope and standard error of each slope are also recorded. **a)** ΔT from CRU was used [Jones *et al.* 2012] **b)** ΔT from GISS [Hansen *et al.* 2010] **c)** ΔT from NCEI [Karl *et al.* 2015] **d)** ΔT from the CRU Hybrid adjustment of Cowtan & Way [2014]. The linear fits to modeled ΔT for GISS, NCEI, and CRU-H lie right on top of the respective fits to measured ΔT .

Figure 3.14 compares measured ΔT over 1998 to 2012 to simulations of ΔT from the EM-GC. The EM-GC simulations were conducted for the entire 1860 to 2015 time period: the figure zooms in on the time period of interest. Fig. 3.14a, b, and c show results using the latest version of ΔT from CRU, GISS, and NCEI (footnotes 1 to 3 provide URLs, data versions, etc.). Each panel also includes the slopes of a linear fit to the data (black) and to modeled ΔT (red), over 1998 to 2012.

For the first time in our extensive analysis, the choice of a data center for ΔT actually matters. The observed time series of ΔT from CRU in Fig 3.14 exhibits a slope of 0.054 ± 0.05 °C/decade over this 15-year period, about a factor of two less than the modeled slope of 0.108 ± 0.03 °C/decade. These two slopes do agree within their respective uncertainties and, as is visually apparent, the ~155-year long simulation does capture the essence of the observed variations reported by CRU over the time period of the so-called hiatus. Nonetheless, the slopes disagree by a factor of 2, lending credence to the idea that some change in the climate system not picked up by the EM-GC approach could be responsible for a gap between the modeled and measured ΔT between 1998 and 2012.

Analysis of the GISS and NCEI data sets leads to a different conclusion. As shown in Fig. 3.14b and c, the observed and modeled slope of ΔT , for 1998 to 2012, agree extremely well. The GISS record of GMST is based on the same SST record used by NCEI. Earlier versions of the GISS record (not shown), released prior to the update in SST described by *Karl et al.* [2015], did support the notion that some unknown factor was suppressing the rise in ΔT from 1998 to 2012.

Cowan and Way [2014] (hereafter, CW2014) suggest the existence of a recent, cool bias in the CRU estimate of ΔT , due to closure of observing stations in the Arctic and Africa that they contend has not been handled properly in the official CRU data release. CW2014 published two alternate versions of the CRU data set, termed “kriging” and “hybrid”, to account for the impact of these station closures on ΔT . Fig 3.14d shows that, upon use of the CRU-Hybrid data set of CW2014, the observed and modeled slope of ΔT are in excellent agreement. Similarly good agreement between measured and modeled ΔT is obtained for CRU-Kriging (not shown). It remains to be seen whether CW2014 will impact future versions of ΔT from CRU. In the interim, the CW2014 analysis supports the finding, from the GISS and NCEI data sets, that there was no hiatus in the gradual, long-term rise of ΔT .

The EM-GC allows us to extract AAWR for any period of time. For the simulations shown in four panels of Fig 2.14, the values of AAWR for 1998 to 2012 are 0.1075 ± 0.0041 , 0.1186 ± 0.004 , 0.1089 ± 0.0046 , and 0.1039 ± 0.004 , respectively, all in units of $^{\circ}\text{C}/\text{decade}$. The primary factors responsible for the slightly smaller rise in ΔT (black numbers, Fig. 3.14) compared to AAWR over 1998 to 2012 is the tendency of the climate system to be in a more La Niña like state during the latter half of this period of time³⁶ [*Kosaka and Xie*, 2013] and a relatively small value of total solar irradiance during the most recent solar max cycle [*Coddington et al.*, 2016]. Our simulations, which include Kasatochi, Sarychev and Nabro, suggest these recent minor volcanic eruptions

³⁶ This is not particularly surprising given the strong ENSO of 1998. Hindsight is 20:20, but it is nonetheless remarkable how much attention has been devoted to discussion of ΔT over the 1998 to 2012 time period, including within IPCC AR5, given the unusual climatic conditions known to have occurred at the start of this time period. Apparently the global warming deniers took the lead in promulgating the notion that more than a decade had passed without a discern-able rise in ΔT , and the scientific community took that bait and devoted enormous resources to examination of GMST over this particular 15-year interval.

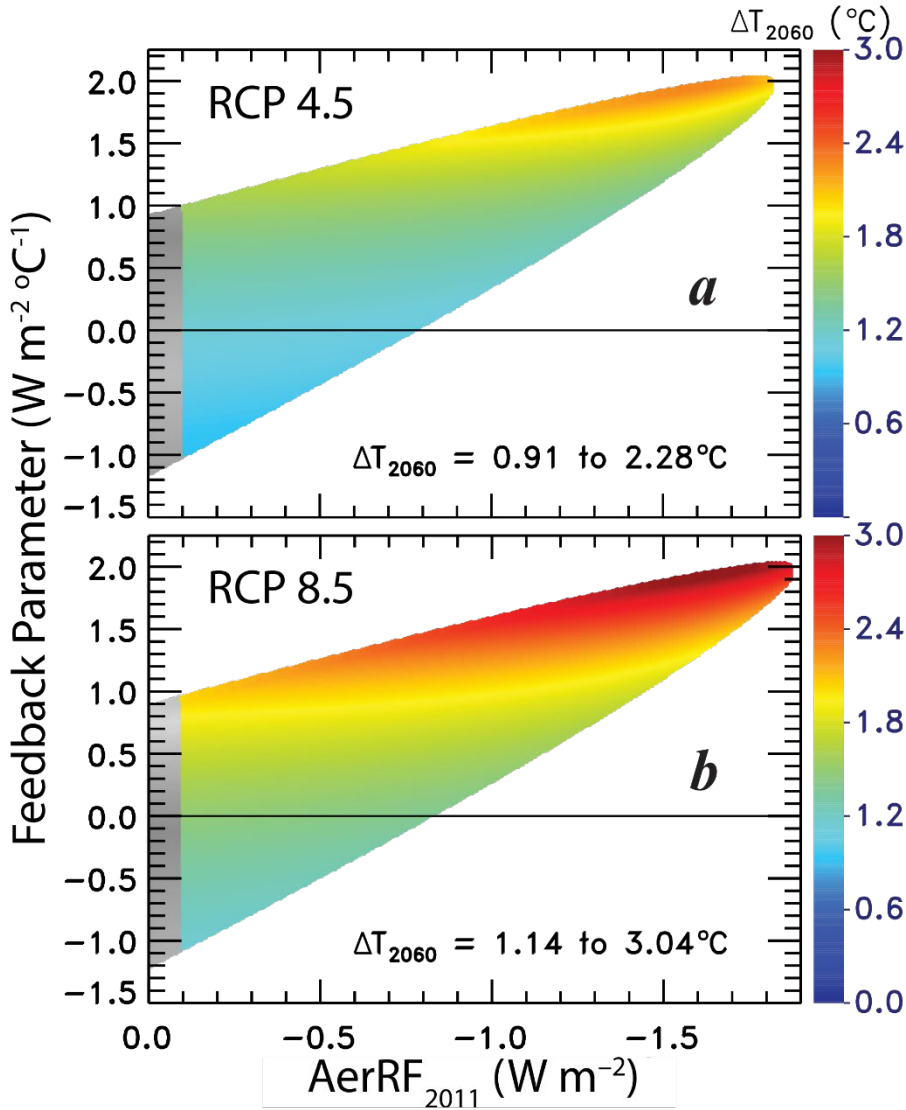
played only a miniscule role (~ 0.0018 °C/decade cooling) over this period. We conclude human activity exerted about 0.11 °C/decade warming over 1998 to 2012, and observations show a rise of ΔT that is slightly smaller in magnitude, due to natural factors that are well characterized by the empirical model of global climate.

3.5 Future Temperature Projections

Accurate projections of the rise of GMST are central for the successful implementation of the Paris Climate Agreement. As shown in §3.2.2, the degeneracy of the climate system coupled with uncertainty in ΔRF due to tropospheric aero-sols leads to considerable spread in projections of ΔT (the anomaly of GMST relative to preindustrial background). Complicating matters further, CMIP5 GCMs on average overestimate the observed rate of increase of ΔT during the past three decades by about a factor of two (§3.3). Recognition of the tendency of CMIP5 GCMs to overestimate observed ΔT led Chapter 11 of IPCC AR5 to issue a revised forecast for the rise in GMST over the next two decades, which is featured prominently below. Below, these issues are briefly reviewed in the context of the projections of ΔT relevant for evaluation of the Paris Climate Agreement. Finally, a route forward is described, based on forecasts of ΔT from the empirical model of global climate (EM-GC) [*Canty et al.*, 2013].

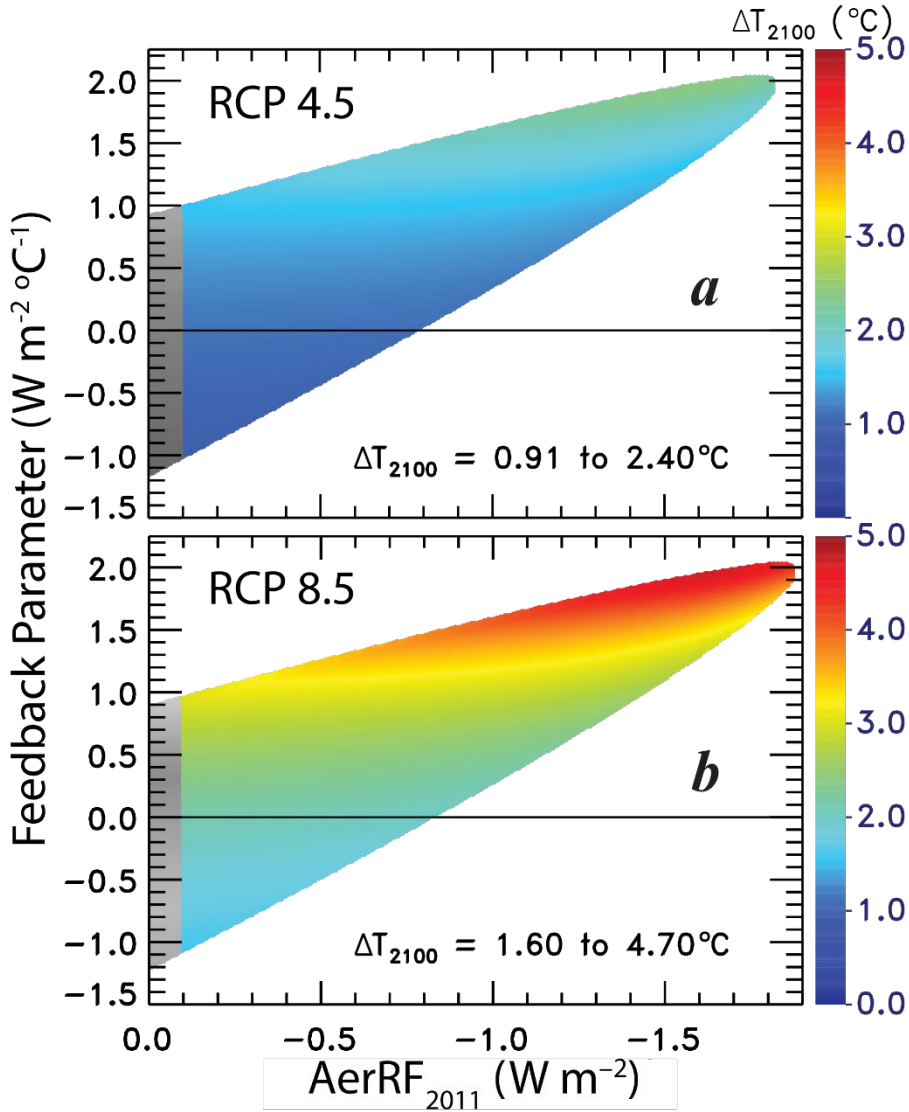
Figure 3.15 provides dramatic illustration of the impact on global warming forecasts of the degeneracy of Earth's climate system. This so-called ellipse plot shows calculations of ΔT in year 2060 (ΔT_{2060}) (various colors) computed using the EM-GC, as a function of model parameters λ (climate feedback) and $AerRF_{2011}$ (ΔRF due to tropospheric aerosols in year 2011). Values of ΔT_{2060} are shown only if a value of $\chi^2 \leq 2$ can be achieved for a particular combination of λ and $AerRF_{2011}$. In other words, the

Figure 3.15 – Projected Rise in GMST, year 2060



Values of ΔT relative to the pre-industrial baseline found using the EM-GC framework, for all combinations of model parameters λ and AerRF₂₀₁₁ that provide an acceptable fit to the climate record, defined here as yielding a value of $\chi^2 \leq 2$. Projections of ΔT are shown only for AerRF₂₀₁₁ between the IPCC AR5 limits of $-1.9 W/m^2$ and $-0.1 W/m^2$. The color bar denotes ΔT_{2060} found by considering only the ΔT_{HUMAN} term in Eq. 3.2 for the future. All simulations used OHC from the average of six data records shown in Fig 3.8 and the aerosol ΔRF time series are based on scaling parameters along the middle road of Fig 3.21. The minimum and maximum values of ΔT_{2060} are recorded on each panel.

Figure 3.16 – Projected Rise in GMST, year 2100



Same as Fig 3.15, except for EM-GC projections out to year 2100. The same color bar is used for both panels to accentuate the end of century difference between RCP 4.5 and RCP 8.5. The minimum and maximum values of ΔT_{2100} are recorded on each panel.

ellipse-like shape of ΔT_{2060} defines the range of these model parameters for which an acceptable fit to the climate record can be achieved. The EM-GC simulations in Fig 3.15a utilize forecasts of GHGs and aerosols from RCP 4.5 [Thomson *et al.*, 2011], whereas Fig 3.15b is based on RCP 8.5 [Riahi *et al.*, 2011]. As noted above, projections of ΔT consider only human influences. We limit ΔRF due to aerosols to the possible range of IPCC AR5: i.e., $AerRF_{2011}$ must lie between -0.1 W/m^2 and -1.9 W/m^2 . Even though values of $\chi^2 \leq 2$ can be achieved for values of λ and $AerRF_{2011}$ outside of this range, the corresponding portion of the ellipse is shaded grey and values of ΔT associated with this regime of parameter space are not considered. Projections of ΔT are insensitive to which OHC data record is chosen (Fig 3.10), but the location of the ellipse on analogs to Fig 3.15 varies, quite strongly in some cases, depending on which OHC data set is used. The $\chi^2 \leq 2$ ellipse-like feature upon use of OHC from Gouretski & Reseghetti [2010] is associated with larger values of λ than the ellipses that appear on Fig. 3.14; conversely, the ellipse-like feature found using OHC from Ishii & Kimoto [2009] is aligned with smaller values of λ . In both cases, the numerical values of ΔT_{2060} within the resulting ellipses are similar to those shown in Fig 3.14.

Figure 3.16 is similar to Fig. 3.15, except projections of ΔT for year 2100 (ΔT_{2100}) are shown. The range of ΔT associated with the acceptable fits is recorded on all four panels of Fig. 3.15 and 3.16. For RCP 4.5, projected ΔT lies between 0.91 to 2.28 °C in 2060 and falls within 0.91 to 2.40 °C in 2100. This large range for projections of ΔT is quite important for policy, given the Paris goal and upper limit of restricting ΔT to 1.5 °C and 2.0 °C above the preindustrial level, respectively. The large spread in ΔT is due to

the degeneracy of our present understanding of climate. In other words, the climate record can be fit nearly equally well assuming either:

- 1) small aerosol cooling (values of $AerRF_{2011}$ close to -0.4 W/m^2) and weak climate feedback, which is associated with lower values of ΔT_{2060} .
- 2) large aerosol cooling (values of $AerRF_{2011}$ close to -1.5 W/m^2) and strong climate feedback, which is associated with higher values of ΔT_{2060} .

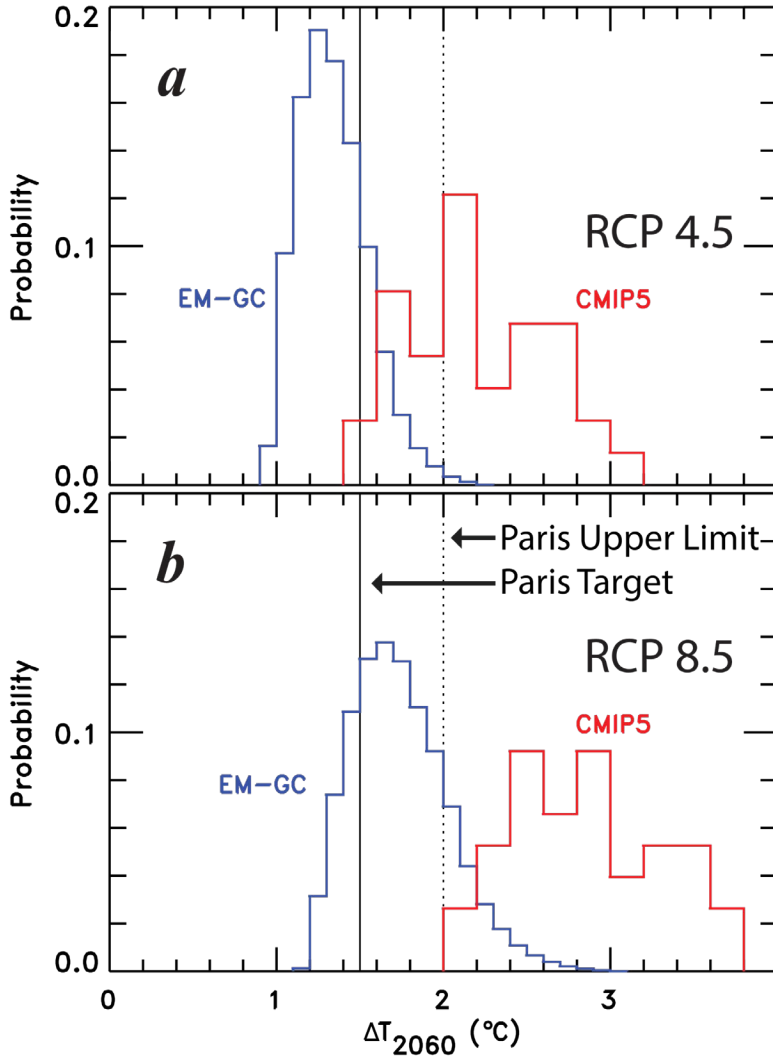
Studies of tropospheric aerosol ΔRF are unable, at present time, to definitely rule out any of these possibilities.

One clear message that emerges from Fig. 3.15 and 3.16 is that to achieve the goal of the Paris Climate Agreement, emissions of GHGs must fall significantly below those used to drive RCP 8.5. The range of ΔT_{2100} shown in Fig. 3.16b is 1.6 to 4.7 °C. Climate catastrophe (rapid rise of sea level, large shifts in patterns of drought and flooding, loss of habitat, etc.) will almost certainly occur by end of this century if the emissions of GHGs, particularly CO_2 , follow those used to drive RCP 8.5 (footnote ³⁷). The book *Six Degrees: Our Future on a Hotter Planet* [Lynas, 2008] provides an accessible discourse of the consequences of global warming, organized into 1 °C increments of future ΔT .

In the rest of this chapter, policy relevant projections of ΔT are shown, both from the EM-GC framework and CMIP5 GCMs. Figure 3.17 shows the statistical distribution of ΔT_{2060} from our EM-GC calculations. The EM-GC based projections are weighted by $1/\chi^2$ (i.e., the better the fit to the climate record, the more heavily a particular projection is weighted). The height of each histogram represents the probability that a particular range of ΔT_{2060} , defined by the width of each line segment, will occur. In other words, the most probable value of ΔT in year 2060, for the EM-GC projection that uses RCP 4.5, is 1.0 to

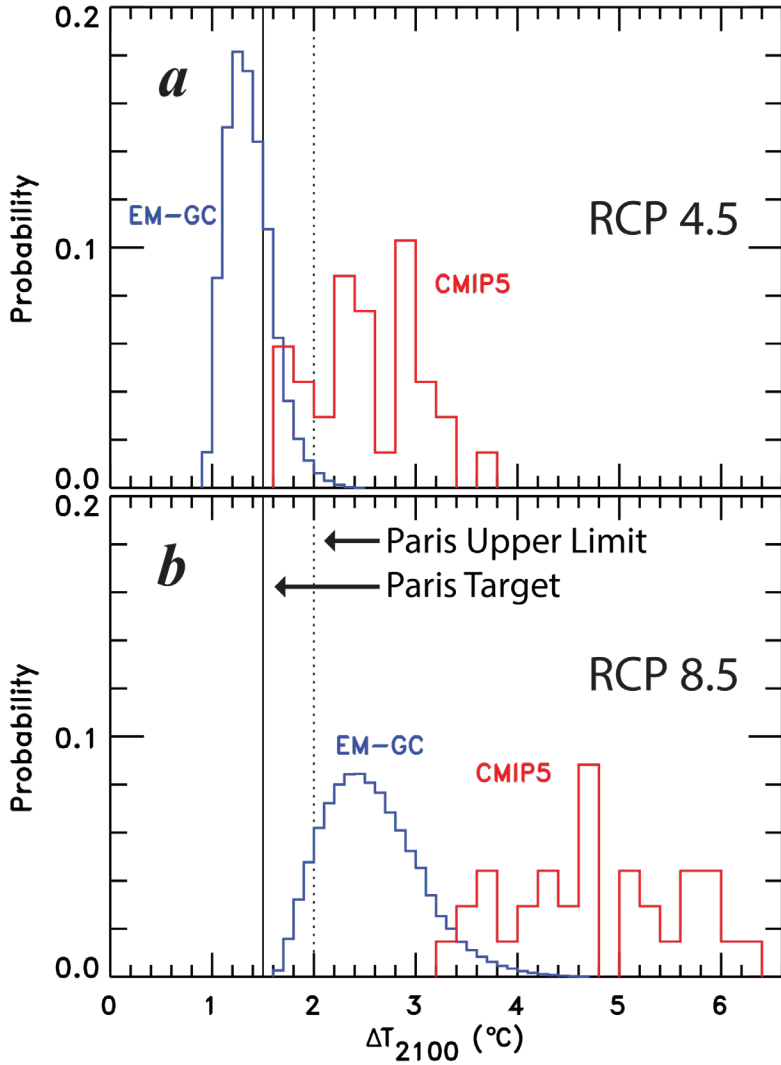
³⁷ As shown in Fig 3.1, CO_2 and CH_4 reach alarmingly high levels at end of century in the RCP 8.5 scenario.

Figure 3.17 – Probability Distribution Functions of Rise in GMST, year 2060



The line segments represent a series of histograms (narrow, vertical rectangles) for projections of ΔT in year 2060 relative to the pre-industrial baseline found using our EM-GC (blue) and CMIP5 GCMs (red). The height of each histogram represents the probability the rise of ΔT will fall within the range of ΔT that corresponds to the ends of each line segment (see main text). The Paris Climate Agreement target and upper limit of 1.5 °C and 2.0 °C warming are denoted. Projections of ΔT_{2060} found using the EM-GC consider only combinations of model parameters λ and $A_{erRF2011}$ that fall within the respective ellipse of Fig 3.17 (i.e., projections consider only acceptable fits to the climate record) and the EM-GC values of ΔT_{2060} are weighted by $1/\chi^2$, so that simulations that provide a better fit to the climate record are given more credence. Finally, the EM-GC simulations used OHC from the average of six data records shown in Fig 3.8 and the aerosol ΔRF time series based on scaling parameters along the middle road of Fig 3.21. **a)** EM-GC and CMIP5 GCM projections based on RCP 4.5; the GCM projections consider the 41 models represented in Fig 3.3a. **b)** EM-GC and CMIP5 GCM projections based on RCP 8.5; the GCM projections consider the 38 models represented in Fig 3.3b.

Figure 3.18 – Probability Distribution Functions of Rise in GMST, year 2100



Same as Fig. 3.17, except all of the projections are for year 2100.

Table 3.1 – Cumulative probability the rise in ΔT remains below a specific value, 2060 and 2100.

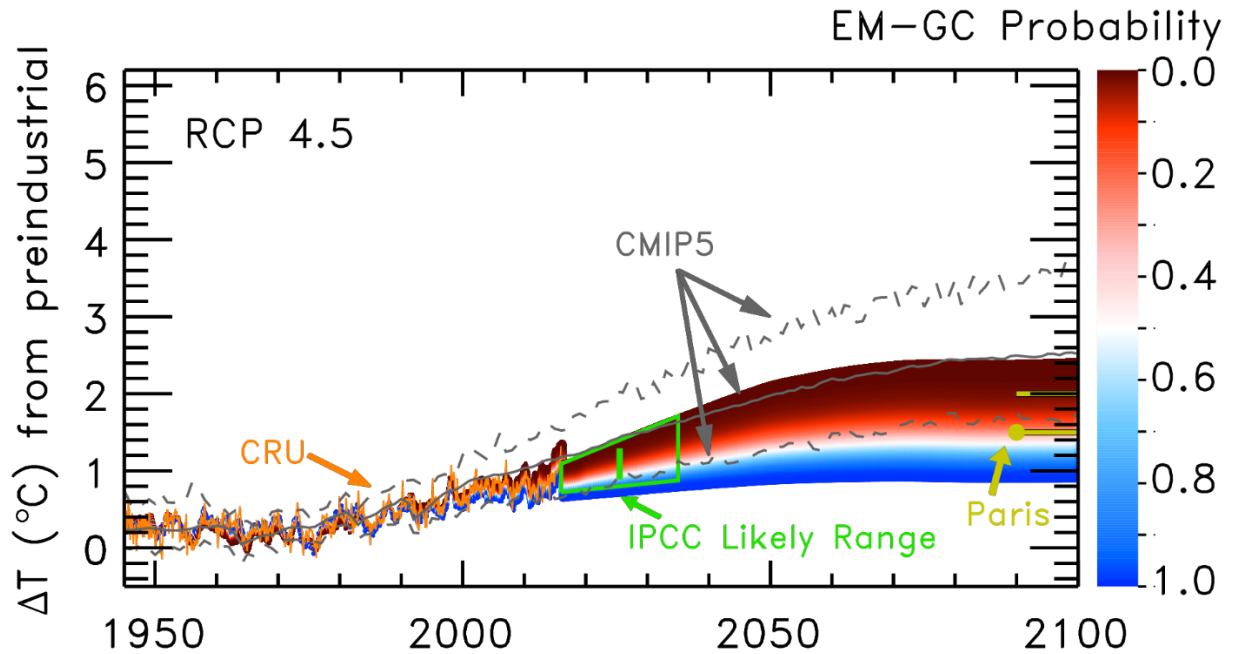
	2060		2100	
	1.5 °C	2.0 °C	1.5 °C	2.0 °C
CMIP5 GCMs RCP 4.5	0.027	0.270	0.0	0.206
CMIP5 GCMs RCP 8.5	0.0	0.026	0.0	0.0
EM-GC, RCP 4.5	0.787	0.995	0.751	0.989
EM-GC, RCP 8.5	0.215	0.816	0.0	0.098

1.1 °C above pre-industrial, and there is slightly less than 20% probability ΔT will actually fall within this range. In contrast, the CMIP5 GCMs project ΔT in 2060 will most probably be 2.0 to 2.2 °C warmer than preindustrial, with a ~12% probability ΔT will actually fall within this range. A finer spacing for ΔT is used for the EM-GC projection, since we are able to conduct many simulations in this model framework. Figure 3.18 is similar to Fig. 3.17, except the projection is for year 2100. The collection of histograms shown for any particular model (i.e., either CMIP5 GCMs or EM-GC) on a specific figure is termed the probability distribution function (PDF) for the projection of the rise in GMST (i.e., ΔT).

The PDFs shown on Figures 3.17 and 3.18 reveal stark differences in projections of ΔT based on the EM-GC framework and the CMIP5 GCMs. In all cases, ΔT from the GCMs far exceed projections using our relatively simple approach that is tightly coupled to observed ΔT , OHC, and various natural factors that influence climate. These differences are quantified in Table 3.1, which summarizes the cumulative probability that a specific Paris goal can be achieved. The cumulative probabilities shown in Table 3.1 are based on summing the height of each histogram that lies to the left of a specific temperature, on Figs. 3.17 and 3.18.

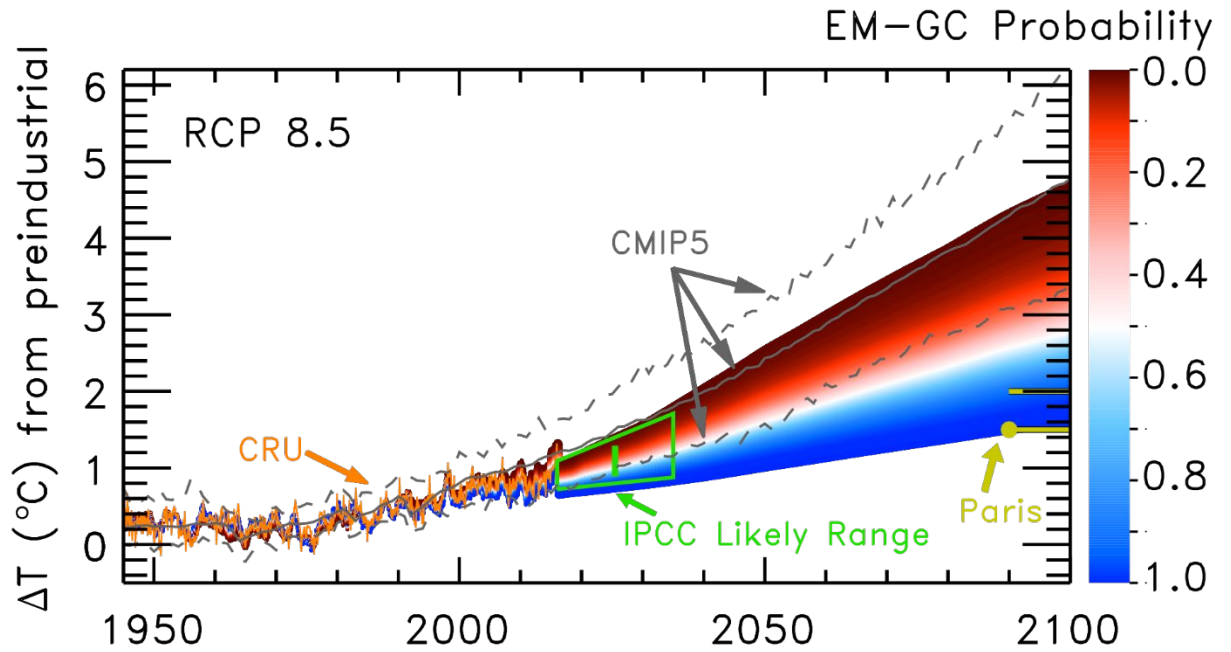
Time series of ΔT found using the CMIP5 GCM and EM-GC approaches are illustrated in Fig. 3.19 and 3.20, which show projections based on RCP 4.5 and RCP 8.5. The colors represent the probability of a particular future value of ΔT being achieved, for projections computed in the EM-GC framework weighted by $1/\chi^2$. Essentially, the red (warm), white (mid-point), and blue (cool) colors represent the visualization of a succession of histograms like those shown in Fig. 3.17 and 3.18. The GCM CMIP5

Figure 3.19 – Global Warming Projections, RCP 4.5



Global warming projections, RCP 4.5. Simulations of the GMST anomaly relative to preindustrial baseline (ΔT), found using the EM-GC (red, white, and blue colors) and from the CMIP5 GCMs (grey lines). Observed ΔT from CRU is also shown (orange). All simulations extend back to 1860; the figure shows ΔT from 1945 to 2100 so that the projections can be better visualized. The green trapezoid shows the indicative likely range of annual average ΔT for 2016 to 2035 (roof and base of trapezoid are upper and lower limits) and the green bar indicates the likely range of the mean value of ΔT over 2006 to 2035, both given in Chapter 11 of IPCC AR5. The Paris Climate Agreement target and upper limit of 1.5 and 2.0 °C warming are denoted at the end of the century. The three CMIP5 lines represent the minimum, maximum, and multi-model mean of ΔT from the 41 GCMs that submitted projections for RCP 4.5 to the CMIP5 archive. The EM-GC projections represent the probability that future value of ΔT will rise to the indicated level. As for Fig 3.17, EM-GC projections consider only acceptable fits to the climate record, are based on the average of OHC from six data records, and have been weighted by $1/\chi^2$ prior to calculation of the probabilities. The white patch of the red, white, and blue projection is the most probable future value of ΔT found using this approach.

Figure 3.20 – Global Warming Projections, RCP 8.5



Same as Fig 2.19, except for the 38 GCMs that submitted projections using RCP 8.5 to the CMIP5 archive. Note how the most probable evolution of ΔT found using the EM-GC framework passes through the middle of the IPCC AR5 trapezoid, and is matched only by the lowest projection warmings of the CMIP5 GCMs.

projections of ΔT (minimum, maximum, and multi-model mean) for RCP 4.5 and RCP 8.5 are shown by the three grey lines. These lines, identical to those shown in Fig. 3.3a (RCP 4.5) and Fig 3.3b (RCP 8.5), are based on our analysis of GCM output preserved on the CMIP5 archive. The green trapezoid, which originates from Fig 11.25b of IPCC AR5, makes a final and rather important appearance on these figures. Also, the Paris target (1.5 °C) and upper limit (2 °C) are marked on the right vertical axis of both figures.

There are resounding policy implications inherent in Figs. 3.17 to 3.20. First, most importantly, and beyond debate of any reasonable quantitative analysis of climate, if GHG emissions follow anything close to RCP 8.5, there is no chance of achieving either the goal or upper limit of the Paris climate agreement (Fig 3.20). Even though there is a small amount of overlap between the Paris targets and our EM-GC projections for year 2100 on Fig. 3.20, this is a false hope. In the highly unlikely event this realization were to actually happen, it would just be a matter of time before ΔT broke through the 2 °C barrier, with all of the attendant negative consequences [Lynas, 2008]. Plus, of course, 1.5 to 2.0 °C warming (i.e., the lead up to breaking the 2 °C barrier) could have rather severe consequences. This outcome is all but guaranteed if GHG abundances follow that of RCP 8.5.

The second policy implication is that projections of ΔT found using the EM-GC framework indicate that, if emissions of GHGs can be limited to those of RCP 4.5, then by end-century there is:

- a) a 75% probability the Paris target of 1.5°C warming above pre-industrial will be achieved
- b) a greater than 95% probability the Paris upper limit of 2°C warming will be achieved

The cumulative effect of the commitments from nations to restrict future emissions of GHGs, upon which the Paris Climate Agreement is based, have the world on course to achieve GHG emissions that fall just below those of RCP 4.5, provided: 1) both conditional and unconditional commitments are followed; 2) reductions in GHG emissions needed to achieve the Paris agreement, which generally terminate in 2030, are continually improved out to at least 2060.

The policy implication articulated above differs considerably from the consensus in the climate modeling community that emission of GHGs must follow RCP 2.6 to achieve even the 2°C upper limit of Paris [*Rogelj et al.*, 2016]. We caution those quick to dismiss the simplicity of our approach to consider the emerging view, discussed in Chapter 11 of IPCC AR5 and quantified in their Figs. 11.25 and TS.14, as well as our Fig. 3.3 and 3.13, that the CMIP5 GCMs warm much quicker than has been observed during the past three decades. In support of our approach, we emphasize that our projections of ΔT are bounded nearly exactly by the green trapezoid of IPCC AR5, which reflects the judgement of at least one group of experts as to how ΔT will evolve over the next two decades. Given our present understanding of Earth's climate system, we contend the Paris Climate Agreement is a beacon of hope because it places the world on a course of having a reasonable probability of avoiding climate catastrophe.

We conclude by cautioning against over-interpretation of the numbers in Table 3.1 or the projections in Figs. 3.19 and 3.20. Perhaps the largest source of uncertainty in the EM-GC estimates of ΔT is the assumption that whatever values of λ (climate feedback) and κ (ocean heat export coefficient) have occurred in the past will continue into the future. Should climate feedback rise, or ocean heat export fall, the future increase

of ΔT will exceed that found using our approach. On the other hand, the past climate record can be fit exceedingly well for time invariant values of λ and κ . The great difficulty is that the specific values of these two parameters are not able to be ascertained from the climate record, due to large current uncertainties in ΔRF due to aerosols and the ocean heat content record. Community-wide efforts to reduce the uncertainties in ΔRF of aerosols and ocean heat storage are vital. We urge that judgement of the veracity of the results of our EM-GC projections be based on whether other research groups are able to reproduce these projections of ΔT , based on similar types of analyses. Given these caveats, our forecasts of global warming suggest that GHG emissions of RCP 4.5 constitute a reasonable guideline for attempting to achieve the both the Paris target (1.5 °C) and upper limit (2.0 °C) for global warming, relative to the pre-industrial era.

3.6 Methods

Many of the figures use data or archives of model output from publically available sources. Here, webpage addresses of these archives, citations, and details regarding how data and model output have been processed are provided. Only those figures with “see methods for further information” in the caption are addressed below. Electronic copies of the figures are available on-line at <http://www.atmos.umd.edu/paris-beacon-of-hope>.

Figure 3.1 shows mixing ratios of CO₂, CH₄, and N₂O from RCP 2.6, RCP 4.5, RCP 6.0, and RCP 8.5, which were obtained from files:

RCP*MIDYEAR_CONCENTRATIONS.DAT

provided by the Potsdam Institute for Climate Research (PICR) at:

<http://www.pik-potsdam.de/~mmalte/rcps/data>

The figures also contain observed global, annually averaged mixing ratios for each GHG. Observed CO₂ is from data provided by NOAA Earth Science Research Laboratory (ESRL) [Ballantyne *et al.*, 2012] at:

ftp://ftp.cmdl.noaa.gov/products/trends/co2/co2_annmean_gl.txt

The CO₂ record given at the above URL starts in 1980. This record has been extended back to 1959 using annual, global average CO₂ growth rates at:

http://www.esrl.noaa.gov/gmd/ccgg/trends/global.html#global_growth

The CH₄ record for 1984 to present [Dlugokencky *et al.*, 2009] is from:

ftp://aftp.cmdl.noaa.gov/products/trends/ch4/ch4_annmean_gl.txt

For years prior to 1984, CH₄ is from a global average computed based on measurements at the Law Dome (Antarctica) and Summit (Greenland) ice cores [Etheridge *et al.*, 1998]:

http://cdiac.ornl.gov/ftp/trends/atm_meth/EthCH498B.txt

The N₂O record for 1979 to present [Montzka *et al.*, 2011] is from:

ftp://ftp.cmdl.noaa.gov/hats/n2o/combined/HATS_global_N2O.txt

Figure 3.2 shows ΔRF of climate due to GHGs, for RCP 4.5 and RCP 8.5. The GHG abundances all originate from the files provided by PICR given for Fig. 2.1. The estimates of ΔRF for each GHG other than tropospheric O₃ were found using formulae in Table 8.SM.1 of IPCC AR5, which are identical to formulae given in Table 6.2 of IPCC AR3 except the value for pre-industrial CH₄ has risen from 0.700 ppm to 0.722 ppm. These formulae use 1750 as the pre-industrial initial condition, as has been the case in all IPCC reports since 2001. Hence, ΔRF represents the increase in radiative forcing of climate since 1750. Throughout this book, we relate ΔRF computed in this manner to ΔT relative to a pre-industrial baseline of 1850 to 1900. This mismatch of baseline values for

ΔRF and ΔT is a consequence of the IPCC precedent of initializing ΔRF in 1750 combined with 1850 marking the first thermometer based estimate of GMST provided by the Climate Research Unit of East Anglia, UK [Jones *et al.*, 2012]. The rise in RF of climate between 1750 and 1900 was small, so the mismatch of baselines has no significant influence on our analysis. The ΔRF due to tropospheric O₃ is based on the work of Meinshausen *et al.* [2011], obtained from the PICR files. The grouping of GHGs into various categories on Fig 3.2 is the same as used for Fig 2.2.

Figure 2.3 shows time series of ΔT , relative to the preindustrial baseline, from CRU [Jones *et al.*, 2012], GISS [Hansen *et al.*, 2010], and NCEI [Karl *et al.*, 2015] as well as GCMs that submitted model results to the CMIP5 archive [K Taylor *et al.*, 2012] for RCP 4.5 (Fig. 3.3a) and RCP 8.5 (Fig. 3.3b). The URLs of observed ΔT are given in footnotes 3, 4, and 5. The CMIP5 URL is given in footnote 7.

All of the observed ΔT time series are normalized to a baseline for 1850 to 1900 in the following manner. The raw CRU dataset is provided for a baseline of 1961 to 1990; the raw GISS dataset is provided for a baseline of 1951 to 1980, and the raw NCEI time series for ΔT is given relative to baseline of 1901 to 2000. The CRU dataset starts in 1850; the other two time series start in 1880. To transform each time series so that ΔT is relative to 1850 to 1900, the following steps are taken:

- a) for CRU, 0.3134°C is added to each value of ΔT ; 0.3134°C is the difference between the mean of CRU ΔT during 1961 to 1990 relative to 1850 to 1900;
- b) for GISS, 0.1002°C is first added to each value of ΔT ; 0.1002°C is the difference between the mean value of GISS ΔT during 1961 to 1990 relative to 1951 to 1980. After this initial addition, the GISS data represent ΔT relative to 1961 to 1990. A second addition of 0.3134°C then occurs, to place the data on the 1850 to 1900 baseline;

c) for NCEI, 0.1202°C is first subtracted from each value of ΔT ; 0.1202°C is the difference between the mean value of NCEI ΔT during 1961 to 1990 relative to 1901 to 2000. After this initial addition, the NCEI data represent ΔT relative to 1961 to 1990. A second addition of 0.3134°C then occurs, to place the data on the 1850 to 1900 baseline.

The GCM lines in the figure are based on analysis of all of the `r*i1p1` files present on the CMIP5 archive as of early summer 2016. The 42 GCMs considered are given in Table 3.2. According to the CMIP5 nomenclature, “r” refers to realization, “i” refers to initialization method, and “p” refers to physics version, and “*” is notation for any integer. The integer that appears after the “r” in the GCM output file name is used to distinguish members of an ensemble, or realization, generated by initializing a set of GCM runs with different but equally realistic initial conditions; the “i” in the file name refers to a different method of initializing the GCM simulation; and, the “p” denotes perturbed GCM model physics. The string `i1p1` appears in the vast majority of the archived files.

For a GCM to have been used, a historical file had to have been submitted to the CMIP5 archive. The historical files contain output of gridded surface temperatures, generally for the 1850 to 2005 time period. Global mean surface temperature is computed, using cosine latitude weighting. Next, an offset such that GMST from the historical run of each GCM can be placed onto a 1961 to 1990 baseline is found and recorded. This offset is applied to all of the `r*i1p1` files from the future runs of the specific GCM, which generally cover the 2006 to 2100 time period. All GCM time series are then placed onto the 1850 to 1900 baseline by adding 0.3134°C to each value of ΔT . All of the GCMs except CCM-CESM listed in Table 3.2 submitted future runs for RCP 4.5 to the CMIP5 archive; a single line for each of the other 41 models appears in Figure

Table 3.2 – Names of the 42 CMIP5 GCMs used in Fig. 3.3.

1. ACCESS1.0	22. GFDL-ESM2M
2. ACCESS3.0	23. GISS-E2-H
3. BCC-CSM1.1	24. GISS-E2-H-CC
4. BCC-CSM1.1(m)	25. GISS-E2-R
5. BNU-CSM	26. GISS-E2-R-CC
6. CCSM4	27. HadCM3
7. CESM1(BGC)	28. HadGEM2-CC
8. CESM1(CAM5)	29. HadGEM2-ES
9. CMCC-CESM	30. INM-CM4
10. CMCC-CM	31. IPSL-CM5A-LR
11. CMCC-CMS	32. IPSL-CM5A-MR
12. CNRM-CM5	33. IPSL-CM5B-LR
13. CSIRO-Mk3.6.0	34. MIROC-ESM
14. CanCM4	35. MIROC-ESM-CHEM
15. CanESM2	36. MIROC4h
16. EC-EARTH	37. MIROC5
17. FGOALS-g2	38. MPI-EMS-LR
18. FIO-ESM	39. MPI-ESM-MR
19. GFDL-CM2.1	40. MRI-CGCM3
20. GFDL-CM3	41. NorESM1-M
21. GFDL-ESM2G	42. NorESM1-ME

Table 3.3 – AAWR from GCM RCP 4.5 Simulations in the CMIP5 Archive.

CMIP5 GCM	Modeling Center	Ensemble run	GCM-AAWR (°C/dec)	
			LIN	REG
ACCESS1.0	Bureau of Meteorology, Australia	r1ilp1	0.248	0.230
ACCESS1.3		r1ilp1	0.234	0.206
		Ctr Avg	0.241	0.218
BCC-CSM1.1	Beijing Climate Center, China Meteorological Administration	r1ilp1	0.259	0.253
BCC-CSM1.1(m)		r1ilp1	0.286	0.278
		Ctr Avg	0.273	0.265
BNU-ESM	College of Global Change and Earth System Science, Beijing Normal University, China	r1ilp1	0.320	0.301
CCSM4	National Center for Atmospheric Research (NCAR), United States	r1ilp1	0.284	0.280
		r2ilp1	0.255	0.247
		r3ilp1	0.226	0.225
		r4ilp1	0.214	0.204
		r5ilp1	0.283	0.252
		r6ilp1	0.234	0.223
		Mod Avg	0.249	0.238
CESM1(BGC)	Community Earth System Model Contributors, NCAR, United States	r1ilp1	0.249	0.223
CESM1(CAM5)		r1ilp1	0.198	0.179
		r2ilp1	0.193	0.184
		r3ilp1	0.243	0.230
		Mod Avg	0.211	0.198
		Ctr Avg	0.232	0.204
CMCC-CM	Centro Euro-Mediterraneo per I Cambiamenti Climatici, France	r1ilp1	0.228	0.235
CMCC-CMS		r1ilp1	0.227	0.250
CNRM-CM5		r1ilp1	0.242	0.221
		Ctr Avg	0.232	0.236
CSIRO-Mk3.6.0	Commonwealth Scientific and Industrial Research Organization, Australia	r1ilp1	0.172	0.170
CanCM4	Canadian Centre for Climate Modelling and Analysis	r1ilp1	0.243	0.226
		r2ilp1	0.267	0.260
		r3ilp1	0.230	0.219
		r4ilp1	0.289	0.279
		r5ilp1	0.226	0.220
		r6ilp1	0.228	0.220
		r7ilp1	0.278	0.249
		r8ilp1	0.265	0.252
		r9ilp1	0.214	0.204

CMIP5 GCM	Modeling Center	Ensemble run	GCM-AAWR (°C/dec)	
			LIN	REG
CanCM4 (cont.)	Canadian Centre for Climate Modelling and Analysis (cont.)	r10i1p1	0.195	0.191
		Mod Avg	0.244	0.232
CanESM2		r1i1p1	0.321	0.286
		r2i1p1	0.334	0.315
		r3i1p1	0.307	0.295
		r4i1p1	0.331	0.302
		r5i1p1	0.326	0.308
		Mod Avg	0.324	0.301
		Ctr Avg	0.270	0.255
EC-EARTH		r1i1p1	0.220	0.209
	r2i1p1	0.187	0.178	
	r5i1p1	0.210	0.197	
	r6i1p1	0.157	0.146	
	r8i1p1	0.204	0.203	
	r9i1p1	0.186	0.181	
	r12i1p1	0.155	0.149	
	r13i1p1	0.233	0.233	
	r14i1p1	0.188	0.160	
Mod Avg	0.193	0.184		
FGOALS-g2	Institute of Atmos. Physics, Chinese Academy of Sciences	r1i1p1	0.179	0.185
FIO-ESM	First Institute of Oceanography, State Oceanic Administration, China	r1i1p1	0.188	0.192
		r2i1p1	0.184	0.187
		r3i1p1	0.203	0.207
		Mod Avg	0.191	0.195
GFDL-CM2.1	NOAA Geophysical Fluid Dynamics Laboratory, United States	r1i1p1	0.261	0.250
		r2i1p1	0.319	0.319
		r3i1p1	0.297	0.266
		r4i1p1	0.294	0.262
		r5i1p1	0.301	0.287
		r6i1p1	0.197	0.203
		r7i1p1	0.253	0.226
		r8i1p1	0.274	0.278
		r9i1p1	0.202	0.194
		r10i1p1	0.263	0.245
		Mod Avg	0.266	0.253
GFDL-CM3		r1i1p1	0.270	0.257
GFDL-ESM2G		r1i1p1	0.275	0.253
GFDL-ESM2M		r1i1p1	0.204	0.183
		Ctr Avg	0.262	0.248

CMIP5 GCM	Modeling Center	Ensemble run	GCM-AAWR (°C/dec)		
			LIN	REG	
GISS-E2-H	NASA Goddard Institute for Space Studies, United States	r1i1p1	0.192	0.174	
		r2i1p1	0.216	0.194	
		r3i1p1	0.192	0.186	
		r4i1p1	0.207	0.192	
		r5i1p1	0.178	0.171	
		Mod Avg	0.197	0.183	
GISS-E2-H-CC		r1i1p1	0.222	0.214	
GISS-E2-R		r1i1p1	0.185	0.169	
		r2i1p1	0.189	0.177	
		r3i1p1	0.193	0.181	
		r4i1p1	0.169	0.171	
		r5i1p1	0.141	0.136	
		r6i1p1	0.229	0.204	
		Mod Avg	0.184	0.173	
GISS-E2-R-CC		r1i1p1	0.200	0.191	
		Ctr Avg	0.193	0.182	
HadCM3		Met Office Hadley Centre, United Kingdom. Additional HadGEM2-ES realizations were contributed by Instituto Nacional de Pesquisas Espaciais, Brazil.	r1i1p1	0.235	0.236
			r2i1p1	0.200	0.171
	r3i1p1		0.250	0.230	
	r4i1p1		0.208	0.192	
	r5i1p1		0.297	0.271	
	r6i1p1		0.192	0.195	
	r7i1p1		0.258	0.236	
	r8i1p1		0.257	0.214	
	r9i1p1		0.23	0.217	
	r10i1p1		0.233	0.215	
	Mod Avg		0.236	0.218	
	HadGEM2-CC		r1i1p1	0.184	0.183
	HadGEM2-ES		r1i1p1	0.289	0.277
r2i1p1		0.204	0.195		
r3i1p1		0.185	0.177		
r4i1p1		0.274	0.233		
Mod Avg		0.238	0.221		
	Ctr Avg	0.233	0.216		
INM-CM4	Institute for Numerical Mathematics, Russian Academy of Sciences	r1i1p1	0.100	0.098	
IPSL-CM5A-LR	Institut Pierre-Simon Laplace, France	r1i1p1	0.323	0.317	
		r2i1p1	0.297	0.294	
		r3i1p1	0.216	0.220	

CMIP5 GCM	Modeling Center	Ensemble run	GCM-AAWR (°C/dec)	
			LIN	REG
IPSL-CM5A-LR, cont.	Institut Pierre-Simon Laplace, France cont.	r4ilpl	0.256	0.248
		Mod Avg	0.273	0.270
		r1ilpl	0.253	0.235
		r1ilpl	0.122	0.122
IPSL-CM5A-MR				
IPSL-CM5B-LR				
		Ctr Avg	0.244	0.239
MIROC-ESM	Japan Agency for Marine-Earth Science and Technology, Atmosphere and Ocean Research Institute (Univ. of Tokyo), and National Institute for Environmental Studies	r1ilpl	0.177	0.172
MIROC-ESM-CHEM		r1ilpl	0.170	0.156
		Ctr Avg	0.174	0.164
MIROC4h	Atmosphere and Ocean Research Institute (Univ. of Tokyo), National Institute for Environmental Studies, and Japan Agency for Marine-Earth Science and Technology	r1ilpl	0.252	0.251
		r2ilpl	0.300	0.282
		r3ilpl	0.317	0.299
		Mod Avg	0.290	0.277
MIROC5		r1ilpl	0.278	0.273
		r2ilpl	0.187	0.154
		r3ilpl	0.287	0.256
		Mod Avg	0.251	0.228
		Ctr Avg	0.270	0.252
MPI-ESM-LR	Max-Planck-Institut für Meteorologie (Max Planck Institute for Meteorology), Germany	r1ilpl	0.161	0.144
		r2ilpl	0.248	0.224
		r3ilpl	0.212	0.205
		Mod Avg	0.207	0.191
MPI-ESM-MR		r1ilpl	0.272	0.256
		r2ilpl	0.199	0.184
		r3ilpl	0.239	0.225
		Mod Avg	0.237	0.222
		Ctr Avg	0.222	0.206
MRI-CGCM3	Meteorological Research Institute, Japan	r1ilpl	0.089	0.075
NorEMS1-M	Norwegian Climate Centre	r1ilpl	0.156	0.157
NorEMS1-ME		r1ilpl	0.180	0.172
		Ctr Avg	0.168	0.164

3.3a. For RCP 8.5, all of the GCMs except CanCM4, GFDL-CM2.1, HadCM3, and MIROC4h submitted output for RCP 8.5 to the CMIP5 archive; a single line for each of the other 38 models appears in Figure 3.3b. Information about the Modeling Center and Institution for these models is provided in our Table 3.3 above, for models that submitted results for RCP 4.5, and on the web at http://cmip-pcmdi.llnl.gov/cmip5/docs/CMIP5_modeling_groups.pdf.

Figure 3.3 also contains a green trapezoid and vertical bar. The coordinates of the trapezoid are (2016, 0.722 °C), (2016, 1.092 °C), (2035, 0.877 °C) and (2035, 1.710 °C) and the coordinates of the vertical bar are (2026, 0.89 °C) and (2026, 1.29 °C). Anyone concerned about the veracity of Fig. 3.3 is urged to have a look at Fig 11.25 of IPCC AR5. The right-hand side of Fig. 11.25b includes an axis labeled “Relative to 1850–1900”. Our Fig. 3.3 visually matches Fig. 11.25 of IPCC AR5 to a very high level of quantitative detail.

Figures 3.4 and 3.5 compare ΔT relative to the 1850 to 1900 baseline from CRU to values of ΔT found using the empirical model of global climate. Values of model output parameters λ , κ , ECS, and AAWR are all recorded on Figure 3.4. The simulation in Fig. 3.4 was found upon setting the regression coefficients C_4 , C_5 , and C_6 in Eq. 3.2 to zero. The simulation in Fig 3.5 made full use of all regression coefficients. The comparison of modeled and measured OHC that corresponds to the simulation shown in Fig 3.5 is nearly identical to the bottom panel of Fig 3.4, and hence has been omitted. The same value of κ was found for both of these simulations. The bottom two rungs of Fig. 3.5 show the contribution to modeled ΔT from AMOC, PDO, and IO; the slope of the AMOC contribution over 1979 to 2010 is also recorded. The top rung of each ladder plot

also records the goodness of fit parameter χ^2 (Eq. 3.7) for the two simulations. Finally, the top two rungs of each ladder plot are labeled “ ΔT from preindustrial” whereas the other rungs have labels of ΔT . The label ΔT is used for the lower rungs for compactness of notation.

Figure 3.6 shows time series for ΔRF of six classes of anthropogenic, tropospheric aerosols: four that tend to cool climate (sulfate, organic carbon from combustion of fossil fuels, dust, and nitrate) and two that warm (black carbon from combustion of fossil fuels and biomass burning, and organic carbon from biomass burning). Estimates of direct ΔRF from all but sulfate originate from values of direct radiative forcing of climate obtained from file:

RCP45_MIDYEAR_RADFORCING.DAT

provided by PICR at:

<http://www.pik-potsdam.de/~mmalte/rcps/data>

We have modified the PICR value for direct radiative forcing of sulfate, using data from [S Smith *et al.*, 2011; Stern, 2006a; b], as described in our methods paper [Canty *et al.*, 2013], because the modified time series is deemed to be more accurate than the RCP value, which was based on projections of sulfate emission reductions conducted prior to the publication of S Smith *et al.* [2011].

The estimates of direct ΔRF from the various aerosol types are then combined into two time series: one for the aerosols that cool, the other for the aerosols that heat. Next, these two time series are multiplied by scaling parameters that represent the aerosol indirect effect³⁸ for aerosols that cool and for aerosols that warm. These are the six curves

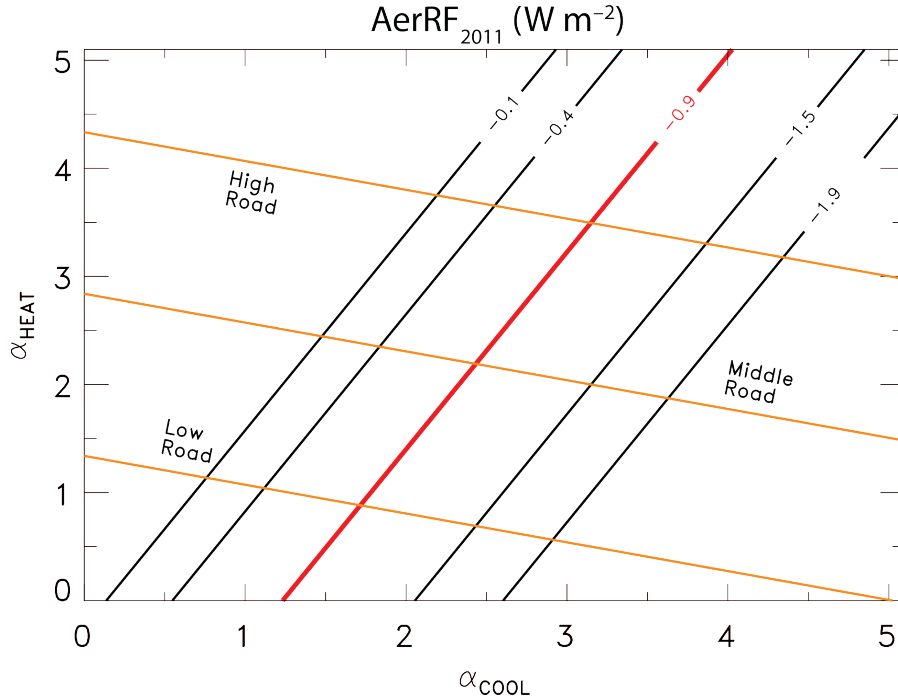
³⁸ The aerosol indirect effect is scientific nomenclature for changes in the radiative forcing of climate due to modifications to clouds caused by anthropogenic aerosols.

shown using colors that correspond to aerosol type. The total direct ΔRF of aerosols that warm, and aerosols that cool, are shown by the red and blue lines, respectively. The line labeled Net is the sum of the total warming and total cooling term, and reflects the time series of Aerosol ΔRF_i input to the EM-GC (Eq. 3.2). Finally, the black open square marks $\text{AerRF}_{2011} = -0.9 \text{ W/m}^2$ along the Net time series, which is the best estimate of total ΔRF due to anthropogenic tropospheric aerosols given by IPCC AR5.

Canty et al. [2013] relied on scaling parameters that were tied to numerical estimates of upper and lower limits of the aerosol indirect effect given by IPCC AR4 (their Fig. 4). Figure 3.21 is our new scaling parameter “road map”, updated to reflect estimates of the aerosol indirect effect by IPCC AR5. The set of scaling parameters used in Fig 3.6 are given by the intersection of “Middle Road” with the $\text{AerRF}_{2011} = -0.9 \text{ W/m}^2$ line in Fig. 3.22: i.e., $\alpha_{\text{HEAT}} = 2.19$ and $\alpha_{\text{COOL}} = 2.43$. Further details of our approach for assessing a wide range of AER RF scenarios in a manner consistent with both CMIP5 and IPCC is given in *Canty et al.* [2013].

Figure 3.7 shows time series of Aerosol ΔRF_i found using scaling parameters α_{HEAT} and α_{COOL} , combined with estimates of direct ΔRF of climate found as described above, for five values of AerRF_{2011} : -0.1 , -0.4 , -0.9 , -1.5 , and -1.9 W/m^2 (open squares). The highest and lowest values of AerRF_{2011} are the upper and lower limits of the possible range, the second highest and second lowest values are the limits of the likely range, and the middle value is the best estimate, all from IPCC AR5. Three curves are shown for each value of AerRF_{2011} : the solid curve uses values for scaling parameters α_{HEAT} and α_{COOL} along the Middle Road of Fig. 3.21, whereas the other lines use parameters along the High and Low Roads.

Figure 3.21 – Aerosol Indirect Effect Scaling Parameters



The black lines show values of total ΔRF of climate in year 2011 (AerRF_{2011}), relative to preindustrial baseline, due to anthropogenic aerosols, as a function of the parameter used to multiply the total direct ΔRF of climate from all aerosols that cool (α_{COOL}) and the parameter used to multiply the total direct ΔRF of climate from all aerosols that heat (α_{HEAT}). Parameters α_{COOL} and α_{HEAT} represent the effect of aerosols on the occurrence, distribution, and properties of clouds: the so-called aerosol indirect effects. The red line shows the most likely value of AerRF_{2011} , -0.9 W m^{-2} , from IPCC AR5. The black lines represent the IPCC AR5 upper and lower limits of the likely range (-0.4 W m^{-2} and -1.5 W m^{-2}) and the upper and lower limits of the possible range for AerRF_{2011} (-0.1 W m^{-2} and -1.9 W m^{-2}). This figure is included to indicate that various combinations of α_{COOL} and α_{HEAT} can be used to find a particular value of AerRF_{2011} . The combination of parameters along the line marked Middle Road is the most likely combination of parameters, based on detailed examination of various tables given in Chapter 7 of IPCC AR5. The high road and low road represent the ranges of plausible values of scaling parameters, again based on our analysis of IPCC AR5. Further details about this approach for representing the aerosol indirect effect in the EM-GC are given in our methods paper [Canty *et al.* 2013].

Figure 3.8 shows time series of ocean heat content for the upper 700 meters of earth's oceans from six sources, as indicated. The data have all been normalized to a common value of zero, at the start of 1993. This normalization is done for visual convenience; the EM-GC model simulates OHE, which is the time rate of change of OHC. The time rate of change is the slope of each dataset, which is unaltered upon application of an offset. The data sources are:

[*Balmaseda et al.*, 2013]:
<http://www.cgd.ucar.edu/cas/catalog/ocean/OHC700m.tar.gz>
[*Church et al.*, 2011]:
http://www.cmar.csiro.au/sealevel/TSL_OHC_20110926.html
[*Giese et al.*, 2011]:
http://dsrs.atmos.umd.edu/DATA/soda_hc2_700.nc
[*Gouretski and Reseghetti*, 2010]:
http://www1.ncdc.noaa.gov/pub/data/cmb/bams-sotc/2009/global-data-sets/OHC_viktor.txt
[*Ishii and Kimoto*, 2009]:
http://www1.ncdc.noaa.gov/pub/data/cmb/bams-sotc/2009/global-data-sets/OHC_ishii.txt
[*Levitus et al.*, 2012]:
[http://data.nodc.noaa.gov/woa/DATA_ANALYSIS/3M_HEAT_CO
NTENT/DATA/basin/yearly/h22-w0-700m.dat](http://data.nodc.noaa.gov/woa/DATA_ANALYSIS/3M_HEAT_CONTENT/DATA/basin/yearly/h22-w0-700m.dat)

As explained in the text, values of OHC shown in Figure 1.8 are multiplied by $1/0.7 = 1.42$ prior to being used in the EM-GC, to represent the estimate that 70% of the rise in OHC occurs in the upper 700 meters of the world's oceans (§5.2.2.1 of IPCC AR4).

Figure 3.11 shows twelve estimates of ECS. The six to the left are previously published values and the six to the right are values found using our EM-GC. Here, numerical estimates of the circle (best estimate), range, and brief description are given.

The ECS value from IPCC AR4 of 3.3 (2.1, 4.4) °C, given in Box 10.2, is based on GCMs that contributed to this report. Here, 2.1 and 4.4 °C are the lower and upper limits of ECS, based on < 5% and > 95% probabilities (i.e., 95% confidence interval),

respectively, as explained in Box TS.1 of IPCC AR4. The entry from *Shindell et al.* [2013] of 4.0 (2.4, 4.7) °C represents the mean and ranges (lower and upper limit) of the value of ECS from eight GCMs given in Fig. 22 of that paper. The value from IPCC AR5 of 3.2 (1.9, 4.5) °C is from Table 9.5 that provides ECS for 23 GCMs; here, the limits represents 90% confidence intervals.

The ECS value from *Schwartz* [2012] of 2.23 (1.06, 3.40) °C represents the mean and standard deviation of the nine determinations given in Table 2 of this paper. The value from *Otto et al.* [2013] of 2.0 (1.2, 3.9) °C is the most likely value and 95% confidence interval uncertainty for the first decade of this century. Finally, the ECS from *T Masters* [2014] of 1.98 (1.19, 5.15) °C is the most likely value and 90% confidence interval from an analysis that covered the past 50 years.

For the EM-GC based estimates of ECS, the error bars represent the range of uncertainty for consideration of the IPCC AR5 expert judgement of the upper limits of the full possible range of $AerRF_{2011}$ (i.e., -0.1 W/m^2 and -1.9 W/m^2) and each circle show the value of ECS found for $AerRF_{2011}$ equal to -0.9 W/m^2 , the IPCC best estimate.

Figure 3.12 shows Attributable Anthropogenic Warming Rate (AAWR) as a function of ΔRF due to aerosols. As for many of our analyses, results are shown for the five values of $AerRF_{2011}$ (-0.1 , -0.4 , -0.9 , -1.5 , and -1.9 W/m^2) which define the possible range, the likely range, and best estimate of $AERRF_{2011}$ according to IPCC AR5. For each value of $AerRF_{2011}$, model runs are conducted for the three determinations of Aerosol ΔRF shown in Fig. 3.7a. The circle represents the mean of these three runs; the error bars represent the maximum and minimum values. Precise determination of AAWR does depend on knowledge of how aerosol ΔRF has varied over the time period of

interest; uncertainty in the shape of aerosol ΔRF over 1979 to 2010 exerts considerable influence on AAWR.

Figure 3.13 shows AAWR from numerous EM-GC simulations, as detailed in the caption, and AAWR found from the 41 GCMs that submitted RCP 4.5 future runs to the CMIP5 archive. Here, a detailed explanation is provided for the determination of GCM-based AAWR.

The estimate of AAWR from GCMs is based on analysis of 112 runs of 41 GCMs, from 21 modeling centers, submitted to the CMIP5 archive. AAWR has been computed for each run using two methods: regression (REG) and linear fit (LIN). Table 3.3 details the 112 determinations of AAWR, from each method, organized first by the name of each GCM, then by modeling center. As noted earlier, we use all of the r*i1p1 runs in the CMIP5 archive that cover both the historical time period (these runs generally stop at year 2005) and the future for RCP 4.5 forcing (these runs generally start at 2006). According to CMIP5 nomenclature, “r” refers to different realizations of an ensemble simulation, all of which are initialized with different but equality realistic initial conditions; “i” refers to a completely different method for initializing a particular GCM simulation; and, “p” de-notes some perturbation to GCM model physics. The string r*i1p1 appears in the vast majority of CMIP5 files; examination of the 112 r*i1p1 runs provides a robust examination of GCM output.

The first method used to extract AAWR from each GCM run, REG, involves examination of deseasonalized, globally averaged, monthly mean values of ΔT from each run, from 1950 to 2010. Archived model output from the historical and the future run files has been combined. Both the historical and future runs were designed to use realistic

variations of total solar irradiance (TSI) and stratospheric optical depth (SOD), the climate relevant proxy for major volcanic eruptions. First, regression coefficients for TSI, SOD, and ΔT_{HUMAN} are found. For this first step, observations of TSI and SOD are used in the analysis, and ΔT_{HUMAN} is approximated as a linear function. The regression coefficient for TSI is saved. A second regression is conducted using ΔT from the GCM, for the 1979 to 2010 time period. For the second regression, the saved value for the TSI coefficient is imposed, leading to new values for the coefficients that modify SOD and ΔT_{HUMAN} . A two-step method is needed to properly determine the TSI and SOD coefficients, because the two major volcanic eruptions that took place over the period of interest, El Chichón and Mount Pinatubo, occurred at similar phases of the 11 year solar cycle. The initial regression starts in 1950 to allow coverage of enough solar cycles for extraction of the influence of solar variability on GCM-based ΔT to be found, and also because ΔT_{HUMAN} over 1950 to 2010 found using EM-GC (i.e., Human Rung on the Fig. 3.4, 3.5, 3.9, and 3.10 ladder plots) is nearly linear over this 60 year time frame. The value of AAWR using REG is the slope of ΔT_{HUMAN} , recorded for each of the 112 GCM runs in Table 3.3.

The second method used to extract AAWR from each GCM run, LIN, involves analysis of global, annual average values of ΔT from the various GCM runs. As noted above, these GCM runs were designed to simulate the short-term cooling caused by volcanic eruptions, such as El Chichón and Mount Pinatubo. The volcanic imprint from most of the GCM runs is obvious upon visual inspection: archived ΔT tends to be smaller than neighboring years in 1982, 1983, 1991, and 1992. For LIN, we find the slope of global annual average ΔT from each GCM run using linear regression, excluding

archived output for the four years noted in the prior sentence. Values of AAWR found using LIN are also recorded for each of the 112 GCM runs in Table 3.3.

We are confident AAWR has been properly extracted from the archived GCM output. Neither of our determinations attempt to discern the influence on GCM-based ΔT of natural variations such as ENSO, PDO, or AMOC. While the CMIP5 GCMs represent ENSO with some fidelity [Bellenger *et al.*, 2014], and changes in heat storage within the Pacific ocean simulated by GCMs has been linked to variability in ΔT on decadal time scales [Meehl *et al.*, 2011], these effects should appear as noise that is averaged out of the resulting signal, since our estimates of AAWR are based on analysis of 112 archived GCM runs. While GCMs might indeed have internally generated ENSO events or fluctuations in ocean heat storage that affect ΔT , the years in which these modeled events occur will bear no relation to the years these events occur in the real world (or in other models). A detailed examination of model output from four leading research centers finds little impact on ΔT of variations in the strength of AMOC within GCMs [Kavvada *et al.*, 2013]. Conversely, accurate timing of natural variations of ΔT due to solar irradiance and volcanoes is imposed on GCMs, via request that the GCMs use actual variations in TSI and SOD derived from data.

Statistical analysis supports the contention that the representation of GCM-based AAWR on Fig. 3.3 is accurate. The 112 values of AAWR in Table 3.3 found using REG compared to the 112 values found using LIN result in a correlation coefficient (r^2) of 0.953 and a ratio of 1.057 ± 0.106 , with AAWR LIN tending to exceed AAWR REG by 5.7%. Consideration of the values of AAWR associated with the 41 GCMs yields $r^2 = 0.964$ and ratio of 1.051 ± 0.101 ; again AAWR LIN is slightly larger than AAWR REG.

Finally, analysis of AAWR from the 21 modeling centers yields $r^2 = 0.977$ and ratio $= 1.052 \pm 0.103$. Values of AAWR found using REG and LIN agree to within 5% with a variance of 10%. We conclude our determination of GCM-based AAWR is accurate to $\pm 10\%$, which is much smaller than the difference between the GCM-based value of AAWR and that found using the EM-GC framework shown in Fig 3.13.

The box and whisker (BW) symbol on Fig 3.13 is based on AAWR found using the regression method (REG), for all 41 GCMs that submitted RCP 4.5 out-put to the CMIP5 archive. If a model submitted multiple runs, the resulting AAWR values are averaged, leading to a single value of AAWR for each GCM³⁹. The 41 values of AAWR upon which the BW plot is based are bold-faced on Table 3.3. The resulting BW symbol for the values of AAWR found using the linear fit (LIN) method, for the 41 GCMs in Table 3.3, is quite similar to the BW symbol shown in Fig 3.13. The primary difference is a higher median value for the LIN determination: the 25th, 75th, minimum, and maximum values are quite similar to those of the REG method. Finally, BW symbols for AAWR based on either the 112 runs or the 21 modeling centers, found using either LIN or REG, look quite similar to the GCM representation on Fig 3.13.

³⁹ Nearly identical values of AAWR are found if, rather than averaging the multiple determinations, the time series of ΔT from each GCM are averaged, and a single value of AAWR is found from the resulting, averaged time series.

Chapter 4: Examining the human influence on global climate using an empirical model

4.1 Introduction

Changes in Earth's climate on the decadal to century timescales are influenced by both anthropogenic and natural factors. Anthropogenic factors include rising concentrations of greenhouse gases (GHGs) that cause global warming [*Lean and Rind, 2008; Santer et al., 2013a*] and increased burdens of tropospheric aerosols (hereafter, aerosols) that offset a portion of the GHG-induced warming [*Bond et al., 2013; Kiehl, 2007; S Smith and Bond, 2014; Stocker et al., 2013*]. Natural factors often cited as having a significant influence on global climate include the El Niño-Southern Oscillation (ENSO), the approximately 11-year solar cycle (total solar irradiance, TSI), and increases in the stratospheric aerosol optical depth (SAOD) that are the result of powerful volcanic eruptions [*Chylek et al., 2016; Foster and Rahmstorf, 2011; Lean and Rind, 2008; Robock, 2000; Santer et al., 2013a*]. Variations in total ocean heat content (OHC), the strength of the Atlantic Meridional Overturning Circulation (AMOC), and regional oceanic patterns like the Pacific Decadal Oscillation (PDO) and the Indian Ocean Dipole (IOD) also can influence global climate, though the extent each of these effects has on climate lacks consensus [*Andronova and Schlesinger, 2000; Chylek et al., 2014; England et al., 2014; Rahmstorf et al., 2015; Rose et al., 2014; Saji et al., 1999; Steinman et al., 2015; Tokarska et al., 2019; Tung and Zhou, 2013*]. Feedbacks within the climate system driven by changes in atmospheric water vapor, lapse rate, clouds, and the surface albedo in response to radiative forcing (RF) induced by GHGs and aerosols also play a large role

in the climate system [Andrews *et al.*, 2012; Bony *et al.*, 2006; Lin *et al.*, 2019; Sherwood *et al.*, 2020; Zelinka *et al.*, 2013; C Zhou *et al.*, 2015].

Our focus is on quantification of the human influence on global climate. We examine the global monthly mean near surface air temperature anomaly relative to preindustrial (ΔT) from four data centers, collected over the past century and a half; for the purposes of this paper, we use a baseline of 1850-1900 as “preindustrial”. We quantify the human influence on ΔT , termed the Attributable Anthropogenic Warming Rate (AAWR), using an Empirical Model of Global Climate (EM-GC) [Canty *et al.*, 2013; Hope *et al.*, 2017] that represents all of the factors described above. Our determination of AAWR is motivated by Box 10.1 of IPCC’s Fifth Assessment Report, Working Group I [Stocker *et al.*, 2013] except we divide their Attributable Anthropogenic Warming (AAW, units of $^{\circ}\text{C}$) by time to arrive at warming rate (units of $^{\circ}\text{C}/\text{decade}$). We primarily examine AAWR from the start of 1979 to the end of 2010 (hereafter 1979 to 2010) because AAW is nearly linear over this 32-year interval and this time period has also been studied by several other papers [Foster and Rahmstorf, 2011; Stocker *et al.*, 2013; J Zhou and Tung, 2013a]. We also quantify AAWR from archived output of the General Circulation Models (GCMs) used throughout Stocker *et al.* [2013] – hereafter, AR5 – as part of Phase 5 of the Climate Model Intercomparison Project (CMIP5) [K Taylor *et al.*, 2012].

Another key aspect of this study is projection of the rise in ΔT to year 2100 (ΔT_{2100}). Here, we use values of key model parameters (i.e. ocean heat export efficiency and the sum of climate feedback mechanisms, defined in section 2) obtained from fitting the historical climate record to forecast how ΔT and total ocean heat content will rise

based on prescribed anthropogenic GHGs and aerosols. The projections focus solely on the anthropogenic component of ΔT so that our model results can be related to the Paris Agreement [UNFCCC, 2015]. The agreement seeks to reduce future emissions of GHGs such that the increase in ΔT is “well below 2°C” and to “pursue efforts to limit the temperature increase to 1.5°C above preindustrial” [UNFCCC, 2015]. Of course, future ΔT will also be influenced by natural variability, including TSI, ENSO, AMOC, and major volcanic eruptions [Chylek *et al.*, 2016; Kavvada *et al.*, 2013; Lean and Rind, 2009]. Although variations in TSI have been forecast and could therefore be used in our projections, TSI exerts a relatively minor influence on ΔT [Lean and Rind, 2009; Zharkova *et al.*, 2015]. Since the other natural factors cannot be reliably predicted over the coming decades, we limit our projections of ΔT to the policy-relevant human component. Finally, the projections of ΔT are also framed in terms of the cumulative amount of carbon that can be emitted to achieve either the goal (1.5°C) or upper limit (2°C) of the Paris Agreement.

4.1.1 Previous Estimates of AAWR

Multiple previous studies have examined AAWR, often focusing on 1979 to 2010 and using multiple linear regression (MLR) to quantify natural and anthropogenic influences on ΔT . Foster & Rahmstorf [2011] (hereafter FR11) suggested an AAWR of 0.170 ± 0.012 °C/decade based on analysis of version 3 of the ΔT record provided by the Climate Research Unit (HadCRUT3, hereafter CRU3) of East Anglia [Jones *et al.*, 2012]. They used MLR to remove the influence of ENSO, SAOD, and TSI on observed ΔT , and then fit the residual to quantify AAWR. Similar numerical values were reported for AAWR using ΔT from the Goddard Institute of Space Sciences (GISS, version 4)

[*Hansen et al.*, 2010] and the National Centers for Environmental Information (NCEI, blend of the Global Historical Climate Network-Monthly version 4 and the International Comprehensive Ocean-Atmosphere Data Set release 3) [*T Smith et al.*, 2008]. *Zhou & Tung* [2013a] (hereafter ZT13) examined version 4 of the CRU record (HadCRUT4, hereafter CRU4) and also used an MLR/residual method and concluded AAWR was 0.169 ± 0.019 °C/decade if temporal variations in the strength of the Atlantic Multidecadal Oscillation (AMO) are ignored. Most importantly, ZT13 stated that AAWR was 0.070 ± 0.019 °C/decade upon consideration of variations in the strength of the AMO. We highlight what we believe are shortcomings in the approaches of the FR11 and ZT13 studies in section §3.2.

Recently, *Christy & McNider* [2017], hereafter CM17, examined lower-tropospheric temperatures measured from satellite and radiosondes collected from the start of 1979 to the end of 2017. They concluded AAWR is 0.096 ± 0.023 °C/decade over this time period. This estimate covers a range of AAWR that includes the lower value of ZT13 but also suggests the value could be much higher, between the two possibilities for AAWR given by ZT13. Similar to CM17, we suggest the actual value of AAWR over 1979 to 2010 lies between the various estimates of FR11 and ZT13, though our value lies closer to the upper end of the range spanned between FR11 and ZT13.

4.1.2 Prior Projections of Future Temperature

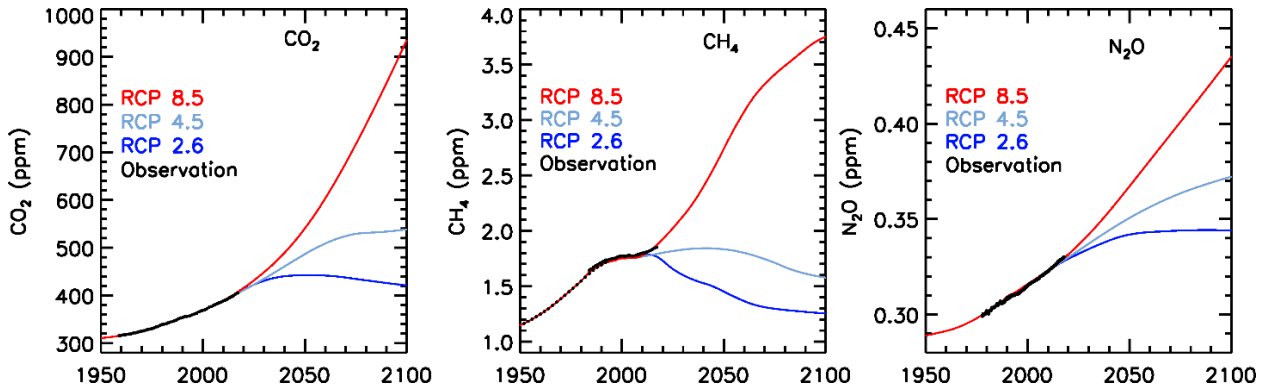
While it is certain that continued emissions of GHGs will cause a rise in ΔT , future warming is also subject to a wide range of uncertainties. One class of uncertainty, termed scenario uncertainty, is dependent on future atmospheric abundances of GHGs and aerosols. The CMIP5 community and AR5 adopted the Representative Concentration

Pathways (RCPs) [Van Vuuren *et al.*, 2011a] of GHGs and aerosols as part of an effort to address scenario uncertainty. Table SPM.2 of AR5 [IPCC, 2013] states that RCP 2.6 [Van Vuuren *et al.*, 2011b] would result in 1.6 ± 0.7 °C warming (5-95% of model range of projections) relative to preindustrial temperature by the end of the 21st century, while RCP 8.5 [Riahi *et al.*, 2011] would result in a warming of 4.3 ± 1.1 °C.

In addition to the two extreme RCP scenarios of RCP 2.6 and RCP 8.5, our study also focuses on the RCP 4.5 scenario [Thomson *et al.*, 2011]. While we have also examined RCP 6.0 [Masui *et al.*, 2011] we choose to not focus on RCP 6.0 for several reasons. First, there is significant overlap between the projections for RCP 4.5 and RCP 6.0 among the CMIP5 GCMs used by AR5: ΔT_{2100} values of 2.4 °C warming (1.7 °C to 3.2 °C, 5-95% of model range of projections) for RCP 4.5 compared to 2.8 °C warming (2.0 °C to 3.7 °C) for RCP 6.0. Second, the CMIP5 GCMs collectively ran many more simulations for RCP 4.5 than for RCP 6.0. Third, there is much more literature concerning RCP 4.5 for comparison to our results. The time evolution of atmospheric CO₂, CH₄, and N₂O for the three RCPs we consider, together with recent observed globally averaged mixing ratios, are shown in figure 4.1.

For a specific GHG scenario, such as RCP 4.5, there is a considerable range in end-of-century warming among various CMIP5 GCMs (e.g., figure SPM.7 of AR5 [IPCC, 2013]), i.e. model uncertainty. Primary drivers of these differences are uncertainties in climate feedback, the radiative forcing of climate due to aerosols, and the uptake of heat by the oceans [Forster *et al.*, 2013; Kiehl, 2007; Knutti and Hegerl, 2008]. Such model uncertainty can cause a large range of ΔT_{2100} found by different GCMs even if they use the same prescribed evolution of GHGs. Policy decisions geared towards

Figure 4.1 – Greenhouse gas abundances, 1950 to 2100, from the RCP scenarios



Each scenario's GHG abundances are portrayed in a different color: red for RCP 8.5, light blue for RCP 4.5, and dark blue for RCP 2.6 [Meinshausen *et al.*, 2011]. These mixing ratio time series are combined with those of other minor GHGs to create the GHG RF times series used in this study. With the exception of CH₄, the RCP scenarios are visually hard to distinguish from each other between their divergence in 2005 and present, though their divergence becomes clear within the next ten years. Also shown for comparison are observations (black) for each GHG (data from <https://www.esrl.noaa.gov/gmd/ccgg/trends/>).

meeting the Paris Climate Agreement must be made considering scenario and model uncertainty.

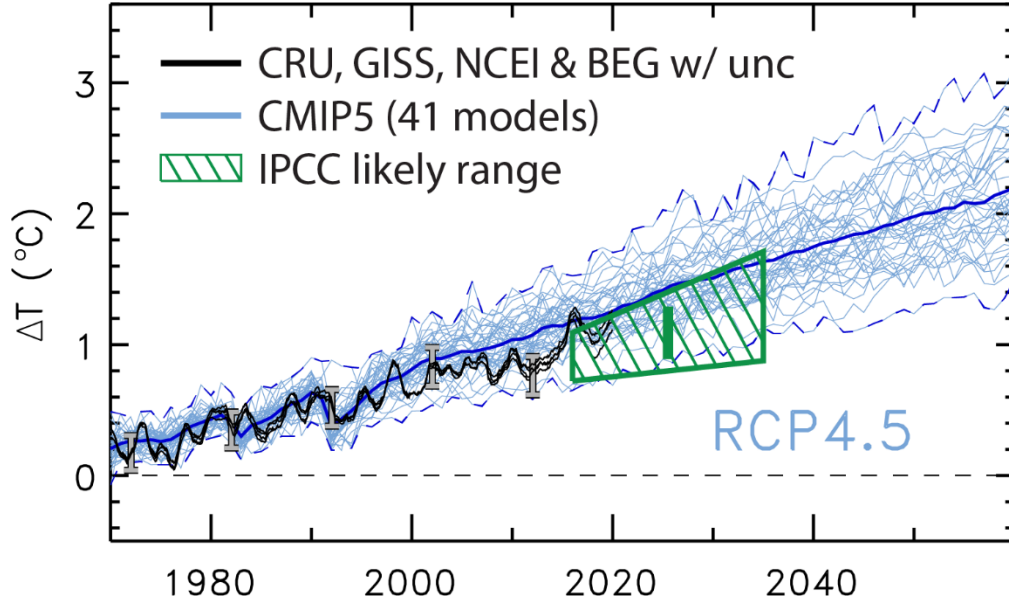
Several other approaches have been developed to forecast ΔT . Some approaches use similar regression analyses of historical records of ΔT [Chylek *et al.*, 2016; Folland *et al.*, 2018; Lean and Rind, 2009; Suckling *et al.*, 2017]. Other simple models use a small number of boxes to represent the atmosphere, ocean, and/or global carbon cycle [Meinshausen *et al.*, 2009; Schwartz, 2012]. Projections of future ΔT have also been constructed from simple calculations using emissions or mixing ratios of carbon dioxide that are from prescribed scenarios such as the RCPs or are based on forecasts of population, economic growth, and other factors [Raftery *et al.*, 2017; X Zeng and Geil, 2016].

Many of these studies reach conclusions concerning future global warming generally in agreement with the CMIP5 GCMs. Often this consensus is due to their models or analyses being driven by CMIP5 inputs and/or results. Fawcett *et al.* [2015] used a reduced complexity climate model constrained by the climate sensitivities from CMIP5 GCMs to conclude GHG emissions reductions based on the Paris Climate Agreement fall well short of the reductions needed to limit global warming to 2 °C, and suggest emissions scenarios similar to that associated with RCP 2.6 are needed. Similarly, Raftery *et al.* [2017] examined projections of population, global economic output, and the carbon intensity of the world's economies to conclude that median warming in 2100 would be 3.2 °C (likely range 2 °C to 4.9 °C) with only a 5% chance of remaining beneath 2 °C. Raftery *et al.* [2017] relied on the relationship between carbon emissions and global warming from the CMIP5 GCMs.

In slight contrast, *Chylek et al.* [2016] used a standalone regression model to project a rise in future ΔT of slightly less than 2 °C by end-of-century for RCP 4.5. This warming is somewhat less than the projected 2.5 °C multi-model mean of 42 CMIP5 GCMs. Another empirical analysis of ΔT using an energy balance model [*Mauritsen and Pincus*, 2017] examines the relationship between transient, equilibrium, and committed warming for scenarios that either omit or include the uptake of CO₂ by the world's oceans. They determined that there is a 50% chance of global warming remaining below 1.5 °C if additional future radiative forcing of climate (RF) does not exceed 1.2 W/m². This limit would be realized in year 2053 if the current rate of RF increase (+0.033 W/m²/yr) was kept constant. We reach a broadly similar conclusion based on our modeling effort with the EM-GC.

Chapter 11 of AR5 [*Kirtman et al.*, 2013] showed that the CMIP5 GCMs tend to overestimate ΔT for the early part of the 21st century, as shown in figure 4.2. This figure compares time series of ΔT from 41 CMIP5 GCMs (light blue) with the observed temperature record from the four data centers shown in figure 11.25 of AR5. Due to the tendency for observed ΔT to be overestimated by the climate models, the authors of Chapter 11 of AR5 prepared an expert judgement of the expected rise in ΔT over the next few decades (green trapezoid in Figure 4.2). Notably, these likely ranges of global warming lie below the GCM ensemble mean. This expert judgement of global warming covers a time period for which all four RCPs have similar values of RF. As will be shown in section §3, global warming forecasts by the EM-GC are in close quantitative agreement with this green trapezoid.

Figure 4.2 – Observed and GCM-Simulated Global Warming, 1970 to 2060



The observed ΔT time series are taken from four data centers (CRU4, GISS, NCEI, and a fourth option from the Berkeley Earth group notated as BEG) and are shown in black, with grey error bars representing the uncertainty from the CRU4 record every ten years. The modeled ΔT time series are taken from the output of 41 GCMs that participated in CMIP5 over the RCP historical and RCP 4.5 future experiment time periods and are shown individually in light blue. The maximum, mean, and minimum from the GCM ensemble are shown in dark blue. The green trapezoid represents the indicative likely range for annual average ΔT for the years 2016 to 2035, and the green bar represents the likely range for the mean value of ΔT for this two-decade time period, both given in Chapter 11 of AR5.

Crafting environmental policy based on such a wide range of possible futures is difficult, even if the physical link between rising GHGs and increasing temperature is well established. The Transient Climate Response to cumulative carbon Emissions (TCRE) is a metric that was developed to link global warming to future anthropogenic emissions of CO₂ [Gregory *et al.*, 2009]. As such, TCRE provides a means for policy makers to exert direct control of global warming through regulation of CO₂ emissions. Chapter 12 of AR5 [M Collins *et al.*, 2013] defines TCRE as the modeled transient increase in ΔT per 1000 GtC of CO₂ released to the atmosphere. Most climate models show that future ΔT increases in a nearly linear fashion with respect to cumulative emissions of CO₂, but this relationship is dependent on the physics and structure of the climate model, as well as assumptions regarding emissions of other GHGs and the time rate of change of emitted CO₂ (Figure 12.45 of AR5). For example, model experiments that have CO₂ concentrations increasing at the rapid rate of 1% per year find a relatively low value for TCRE compared to simulations with a slower rate of CO₂ increase (e.g. Figure SPM.10 [IPCC, 2013]) because the inertia of the climate system limits the transient temperature response relative to faster emissions. It is commonly accepted that the transient response of ΔT to rising GHGs is less than the equilibrium response because certain aspects of the climate system such as the cryosphere and the transfer of heat into the ocean occur on multi-year timescales. Chapter 12 of AR5 [M Collins *et al.*, 2013] states that TCRE likely lies between 0.8°C to 2.5°C per 1000 GtC. The CMIP5 GCMs tend to lie toward the high end of this range for TCRE, whereas projections of global warming found using our approach (§4.3) lie toward the lower end.

4.1.3 Overview of This Work

The Empirical Model of Global Climate (EM-GC) used in this study builds upon the framework first described by Canty et al. [2013]. This work also builds on *Hope et al.* [2017], who used an earlier version of the model to conduct similar analysis. The EM-GC uses MLR combined with a two-module ocean-atmosphere approach to simulate observed monthly variations in ΔT . The MLR component uses an equation that represents numerous anthropogenic and natural factors that drive variations in global climate. The version of the EM-GC used here considers several factors not present in most other MLR-based analyses, and includes several important updates since *Hope et al.* [2017], especially in the ocean module, as described in section §4.2.

Section 4.3 presents results from the EM-GC concerning AAWR and projection of ΔT out to year 2100. Differences in these quantities between the EM-GC and other works are also described in §4.3, as are analyses of these differences and how the EM-GC works. We present our conclusions and how the EM-GC results fit into the climate modeling community's knowledge of the climate system in §4.4.

4.2 Model Construction

The EM-GC provides a mathematical representation of the factors that govern the global mean surface temperature anomaly (ΔT). We compute numerical values of climate amplification (γ) and the efficiency of heat transfer from the atmosphere to the ocean (κ) based on the observed climate record. We then use these values of γ and κ to project future ΔT . While MLRs have been used to conduct similar calculations by other groups, our EM-GC includes several components not included in these other models. These differences include the long-term export of heat from the atmosphere to the ocean, a

comprehensive treatment of tropospheric aerosols, and the influence on global climate from variations in the strength of Atlantic Multidecadal Variability (AMV, which we use as a proxy for AMOC), and a new probability weighting method for the large ensemble of ΔT projections that incorporates the expert judgement of aerosol RF given in Chapter 8 of AR5 [Myhre *et al.*, 2013].

The EM-GC is an ensemble-based model whose parameter space spans a large range of possible values for both the strength of the climate feedback and the historical strength of anthropogenic aerosol forcing. The overall ensemble is filtered based on a set of model parameters that quantify a statistically acceptable fit ($\chi^2 \leq 2$, described below) between observed and modeled historical ΔT and ocean heat content (OHC). These simulations of historical ΔT and OHC are then used to create a corresponding ensemble forecasts of ΔT , which allows for a detailed statistical analysis of the impact of uncertainty in aerosol RF and climate feedback on future global warming.

In the four following sections, we describe the model equations and input data, representation of the ocean component, climate sensitivity and feedbacks, and the different modes of the EM-GC.

4.2.1 EM-GC Core Equations

The EM-GC simulation of observed ΔT uses a MLR-based analysis of the flow of energy between major components of Earth's climate system. The main equations of the EM-GC are:

$$\begin{aligned} \Delta T_{MDL i} = & \frac{1 + \gamma}{\lambda_p} \{GHG RF_i + AER RF_i + LUC RF_i - 0.671 Q_{OCEAN i}\} + C_0 \\ & + C_1 \times SAOD_{i-6} + C_2 \times TSI_{i-1} + C_3 \times ENSO_{i-2} + C_4 \times AMV_i \\ & + C_5 \times PDO_i + C_6 \times IOD_i \end{aligned} \tag{Eq4.1a}$$

$$Cost Function = \sum_{i=1}^{N_{MONTHS}} \frac{(\Delta T_{MDL i} - \Delta T_{OBS i})^2}{\sigma_{OBS i}^2} \tag{Eq4.1b}$$

$$\chi^2 = \frac{1}{(N_{YRS} - N_{DOF} - 1)} \sum_{j=1}^{N_{YRS}} \frac{(\langle \Delta T_{MDL} \rangle_j - \langle \Delta T_{OBS} \rangle_j)^2}{\langle \sigma_{OBS} \rangle_j^2} \tag{Eq4.1c}$$

where $\lambda_p = 3.2 \text{ W m}^{-2} \text{ }^\circ\text{C}^{-1}$ (Planck response), γ is the dimensionless climate amplification term, C_0 to C_6 are regression coefficients, and i is an index for month. This model representation of $\Delta T_{MDL i}$ considers four anthropogenic factors (GHGs, net anthropogenic tropospheric aerosols [AER], land use change [LUC], and ocean heat export [Q_{OCEAN}]) as well as six natural factors (SAOD, TSI, ENSO, AMV, PDO, and IOD). The data inputs for all factors aside from Q_{OCEAN} are either taken directly or modified slightly from outside sources, while Q_{OCEAN} is calculated within the EM-GC. (Section 4.2.2 below defines Q_{OCEAN} and its governing equations; the multiplication of Q_{OCEAN} by 0.671 in Equation 1a represents an area correction between Q_{OCEAN} as computed in the ocean module and its effect on the atmosphere.) The sources for all of our input data and the small changes we apply to them are fully documented in §4.2.1.1 and §4.2.1.2 below.

Each member of an EM-GC ensemble uses the same natural factors, ΔT_{OBS} record, OHC record, GHG forcing time series, and LUC forcing time series. The

ensemble members vary as each is constrained to different assumed values for AER radiative forcing and γ . The anthropogenic components for each run are fed into the OHC submodule of the EM-GC to calculate Q_{OCEAN} . The submodule produces estimates for global average sea surface temperatures (SSTs) and the human component of ΔT_{MDL} . These two temperature time series are used to recalculate Q_{OCEAN} , and the submodule iterates this process until those three quantities (i.e. SSTs, $T_{MDL-HUMAN}$, and Q_{OCEAN}) remains stable between iterations.

We then solve for the seven regression coefficients (C_i) by minimizing the cost function (Equation 4.1b), accounting for the 1σ uncertainty in each value of monthly global mean observed temperature ($\Delta T_{OBS\ i}$). The temperature records used to prescribe $\Delta T_{OBS\ i}$ are based on one of the previously mentioned CRU4, GISS, and NCEI data sets, as well as a fourth option from the Berkeley Earth group (BEG) [Rohde *et al.*, 2013]. The terms in the cost function are indexed over the total number of months (N_{MONTHS}) for which $\Delta T_{OBS\ i}$ are available, either 2040 months (Jan.1850 to Dec.2019) for CRU4 and BEG or 1680 months (Jan.1880 to Dec.2019) for GISS and NCEI.

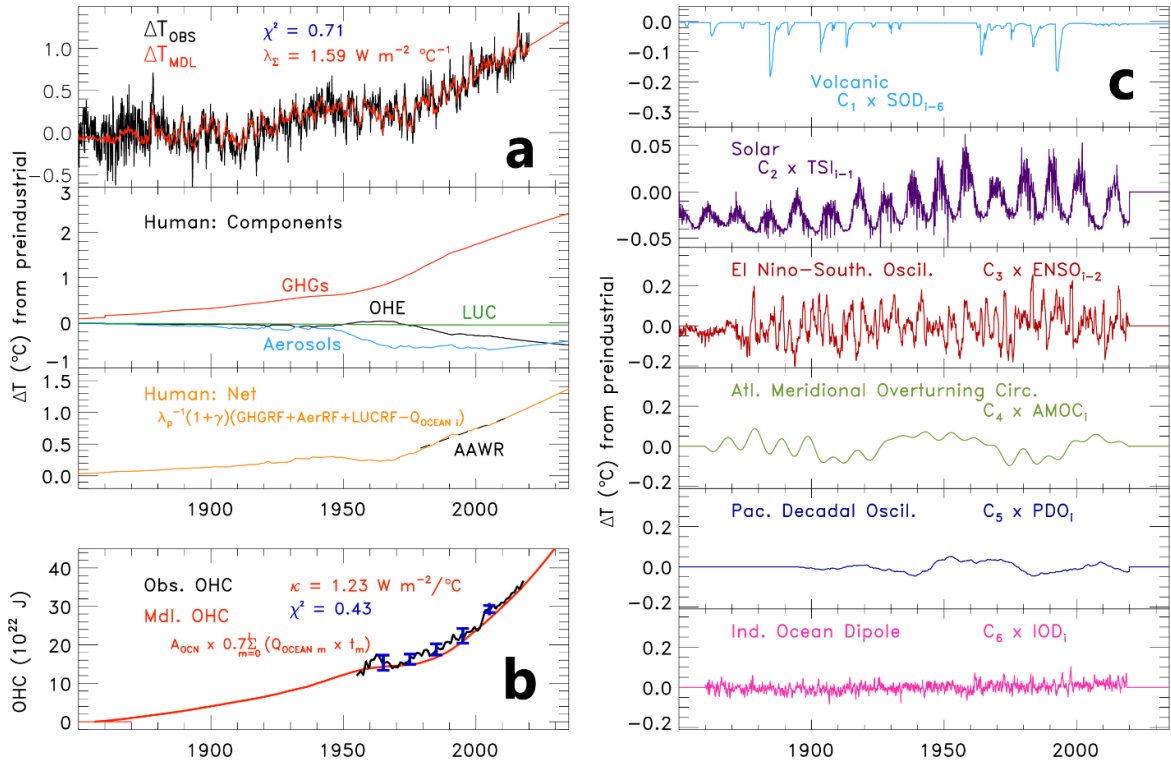
Our modeling approach also makes use of reduced chi-squared (χ^2) that defines the goodness-of-fit between observed and modeled ΔT (Equation 4.1c). In equation 4.1c, N_{YRS} represents the total number of years for which $\Delta T_{OBS\ i}$ are available (170 years for CRU4 and BEG; 140 years for GISS and NCEI) and $\langle \rangle$ denotes annual average. Unless otherwise stated, the number of degrees of freedom (N_{DOF}) in this study is nine: the climate amplification term, an ocean heat surface diffusivity parameter, and the seven regression coefficients. The EM-GC can run with any selection of our natural and anthropogenic variables included or excluded, potentially reducing N_{DOF} . The equation

for χ^2 is based on annual averages of observed and modeled ΔT because the autocorrelations of ΔT_{OBS} and ΔT_{MDL} exhibit similar shapes when examined as annual averages, but do not match on the monthly time grid [Canty *et al.*, 2013]. Therefore, the use of annual averages reduces the effect of high-frequency variations of ΔT_{OBS} that are not captured by the model. Nonetheless, the model framework is expressed in terms of monthly time series for all quantities to properly quantify the effect of factors such as major volcanic eruptions and ENSO on global climate.

We compute two other versions of χ^2 as well. While equation 1c as described above is defined for ΔT over the full time period of available observations, we additionally compute reduced chi-squared using the same framework both for OHC over the full time period of OHC and for ΔT over the most recent 80 years. As the EM-GC is designed to fit both atmospheric and oceanic observations, we do not consider simulations with acceptable fits to ΔT_{OBS} if they do not also provide an acceptable fit between OHC_{MDL} and OHC_{OBS} . We then consider χ^2 for ΔT over the past 80 years because a combination of factors makes it possible to achieve an acceptable fit (i.e., $\chi^2 \leq 2$) for the full time series of ΔT_{OBS} while significantly over- or under-estimating warming during the last 30 to 50 years. Since the most recent several decades are a focus of our study, a lack of fit of ΔT_{OBS} over this period would confound meaningful analysis. We choose a length of 80 years to assure that all semi-oscillatory natural forcing factors experience at least one full cycle within the years of consideration (PDO and AMV vary on time scales of up to 60 or 70 years).

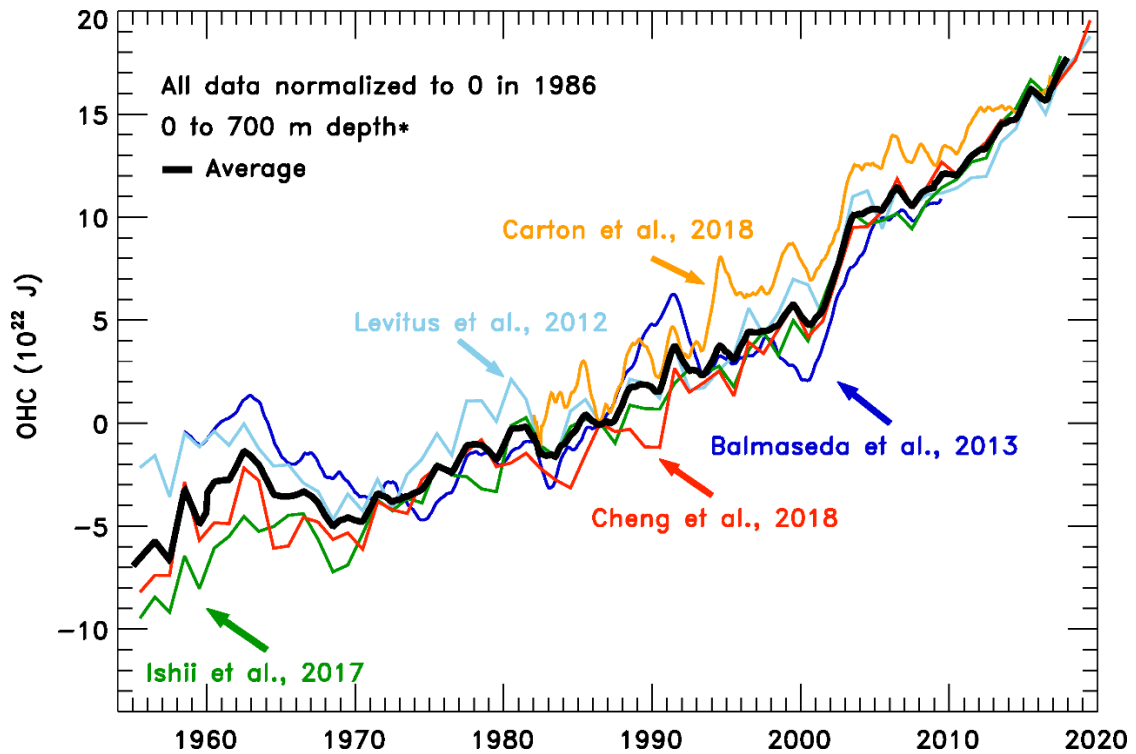
Figure 4.3 provides a visual representation of our model (i.e. Equations 4.1a-c) by showing a single run from an EM-GC ensemble with the best fits to ΔT_{OBS} when using a

Figure 4.3 – Observed and EM-GC-Modeled ΔT , 1850 to 2019



Ladder plots showing observed ΔT from CRU4 (top rung of Figure 3a, black line), the EM-GC simulation of ΔT from CRU4 (top rung, red line), ΔT_{HUMAN} (third rung of Figure 3a, gold line) and its components (second rung of 3a), AAWR (third rung of 3a, dashed black line), and contributions to ΔT from various natural factors (TSI, second rung of 3c, purple line; SAOD, first rung of 3c, light blue line; ENSO as measured by the Multivariate ENSO Index version 2, third rung of 3c, crimson line; AMV with 9-year Fourier filtering as our AMOC proxy, fourth rung on 3c, green line; PDO with 10-year smoothing, fifth rung of 3c, indigo line; IOD, sixth rung of 3c, pink line). Figure 3b shows the model-simulated rise in OHC (red line) from the top 700 m compared to the average of five OHC data sets (black line; blue error bars show the 1σ standard deviation of these data about mean OHC).

Figure 4.4 – Ocean Heat Content (OHC) Records



The five OHC_{OBS} are shown in color and are normalized to 0 in 1986. The average of the five OHC_{OBS} records is shown with a thick black line. The average is calculated for any year when at least three of the five OHC_{OBS} records are present. 1986 was chosen as the normalization year as the midpoint year of the time period for which the calculated average exists.

time series for aerosol radiative forcing (AER RF) that matches the IPCC most-likely value of AER RF in 2011. We refer to this depiction of the EM-GC's components as a "ladder plot". The top rung of figure 4.3a shows model input ($\Delta T_{OBS\ i}$, black) and output ($\Delta T_{MDL\ i}$, red). The second and third rungs of Figure 4.3a show the anthropogenic components of ΔT_{MDL} , both separated (second rung) and combined (third rung). GHG RF in this run is based on the RCP 4.5 time series for CO₂, CH₄, N₂O, and other GHGs [Meinshausen *et al.*, 2011; Thomson *et al.*, 2011]. Nearly identical results are found upon use of RCP 8.5 or RCP 2.6, because the RCP scenarios use the same historical data for all species until 2005 (Figure 1). The time series for AER RF used in figure 4.3a is based upon our analysis of direct RF due to six aerosol types provided by RCP [Lamarque *et al.*, 2011], combined and expanded to include the indirect aerosol effect as well, as described in §4.2.1.2. LUC RF is taken from Table AII.1.2 of AR5. Our Q_{OCEAN} , the export of heat from the atmosphere to the ocean, is found by simulating the long-term observed rise in OHC, as described in §4.2.2. The net human time series in the third rung (gold line) serves as the basis for calculating AAWR and is further discussed in §4.2.3.

The lower-left rung of the ladder plot (Figure 3b) depicts the modeled increase in OHC (red curve, proportional to the summation of Q_{OCEAN} via equation 2) and the observed rise in OHC (black line). In figure 3b, the observed OHC is based upon the average of five data sets [Balmaseda *et al.*, 2013; Carton *et al.*, 2018; Cheng *et al.*, 2016; Ishii *et al.*, 2017; Levitus *et al.*, 2012] such that the average is taken for each year when at least three of the five data sets provide an annual value (see figure 4.4). The modeled increase in OHC is related to Q_{OCEAN} as follows:

$$OHC_{MDL i} = A_{OCEAN} \times 0.7 \sum_{m=0}^i [Q_{OCEAN m} \times t_m]$$

Eq4.2

In equation 4.2, A_{OCEAN} is $3.3 \times 10^{14} \text{ m}^2$ [Domingues *et al.*, 2008], and t_m is the time length for month m in seconds, with $m=0$ representing the first month of a model run (e.g. January 1850 for runs using CRU4). The factor of 0.7 is used to account for the fact that the OHC data sets we use represent only the top 700 m of the oceans, which hold roughly 70% of the total heat content of the ocean (Sect. 5.2.2.1 of AR4). We verified this value of roughly 70% by comparing the OHC time series for the upper 700 m to the time series for the upper 2000 m or full ocean for the three data sources that provided time series for multiple depths [Balmaseda *et al.*, 2013; Carton *et al.*, 2018; Levitus *et al.*, 2012].

The influences on ΔT of solar irradiance, volcanoes, ENSO, AMOC, PDO, and IOD are shown on the six rungs on figure 4.3c. The sum of the variations in ΔT due to the six natural factors (figure 4.3c) and the four anthropogenic factors (third rung of figure 4.3a) plus the regression constant (C_0) equal ΔT_{MDL} . The overall agreement between the black and red lines in figure 4.3a demonstrates the ability of the EM-GC to capture much of the variability and rise in global mean surface temperature over the past century and a half.

4.2.1.1 Model Input, Natural Factors

In this section, we describe the data used to define model inputs for stratospheric optical depth (SAOD), total solar irradiance (TSI), the El Niño-Southern Oscillation (ENSO), the Atlantic Multidecadal Variability (AMV), Pacific Decadal Oscillation (PDO), and the Indian Ocean Dipole (IOD). Table 4.1 provides URLs of the websites that host these data records.

Table 4.1 – Natural Factor Input Sources

Variable	Data Name	Years	Location
SAOD	CMIP6	1850-2014	https://esgf-node.llnl.gov/search/input4mips/
	GloSSACv2	1979-2018	https://opendap.larc.nasa.gov/opendap/GloSSAC/contents.html
	CALIPSO	2019	https://opendap.larc.nasa.gov/opendap/CALIPSO/contents.html
TSI	CMIP6	1850-2014	https://esgf-node.llnl.gov/search/input4mips/
	SORCE	2003-2019	https://lasp.colorado.edu/home/sorce/data/tsi-data/
ENSO ^a	MEIv2	1979-2019	https://psl.noaa.gov/enso/mei/data/meiv2.data
	MEI-ext	1871-2005	https://psl.noaa.gov/enso/mei.ext/table.ext.html
AMOC ^b	AMV	1850-2019	https://crudata.uea.ac.uk/cru/data/temperature/HadSST.3.1.1.0.median.nc
PDO		1900-2018	http://research.jisao.washington.edu/pdo/PDO.latest.txt
IOD		1870-2019	http://www.jamstec.go.jp/frcgc/research/d1/iod/iod/dipole_mode_index.html
		1850-1870	http://www.jamstec.go.jp/frcgc/research/d1/iod/kaplan_sst_dmi_new.txt

^a1850-1870 ENSO constructed as an area SST average over the Nino3.4 region using

<https://crudata.uea.ac.uk/cru/data/temperature/HadSST.3.1.1.0.median.nc>

^bAMV calculated as an area average of Atlantic SSTs; multiple detrending and Fourier filtering options can be applied

The time series for SAOD is a combination of two data sources. The first source is the recommended input for Phase 6 of the Climate Model Intercomparison Project (CMIP6). This CMIP6 SAOD time series is a combination of the Volcanic Model Intercomparison Project [Zanchettin *et al.*, 2016] for enhanced values of SAOD before the satellite era, Arfeuille *et al.* [2014] for background values before the satellite era, and the GloSSAC data set [Thomason *et al.*, 2016] for all values during the satellite era. GloSSAC has since been extended past the last year of CMIP6 [Thomason *et al.*, 2018]. We then use the Cloud-Aerosol Lidar and Infrared Pathfinder Satellite Observations (CALIPSO) data [Vaughan *et al.*, 2004] for year 2019 as our second source since the GloSSAC record available at time of paper submission ends in Dec 2018. The GloSSAC and CALIPSO data are available as SAOD values by latitude; we create SAOD values by latitude for years before 1979 by taking extinction coefficients and integrating them from the tropopause to the top of the atmosphere. We then weight each latitude band by area to reach a near-global SAOD time series (80°S to 80°N). The three data sets, as presently available, match very closely during their respective time periods of overlap, though we do apply a small adjustment to bring CALIPSO in line with GloSSAC. We treat SAOD after 2019 in the same way that we treat all of our natural factors from 2020 onward: we flatline the data at a value near zero representative of the current, non-volcanic background. As SAOD has a small background value, it is the only natural time series in the EM-GC that uses a nonzero value into the future (specifically, the December 2019 value of SAOD from CALIPSO). The final SAOD time series is then lagged by six months in equation 4.1a to match the delay between surface forcing and the thermodynamic response to major volcanic eruptions found by Thompson *et al.* [2009]

which is the same time lag that has been used in other MLR studies [*Foster and Rahmstorf, 2011; Lean and Rind, 2008*].

The time series of TSI used in the EM-GC is constructed from two data sets. TSI data up to 2014 are an average of two solar models, one empirical and one semi-empirical [*Matthes et al., 2017*]; TSI data after 2014 are from satellite-based solar radiance measurements [*Dudok de Wit et al., 2017*]. These two data sets agree well at the point of merging. The EM-GC can propagate the underlying 11-year solar cycle past 2019, but in this analysis we flatline TSI in the future. We make this choice so that future projections of ΔT are based solely on anthropogenic forcing. A one-month lag for TSI is used in equation 1a, because this lag yields the largest value of C_2 . Lagging TSI is a common approach for quantifying the slight temporal offset of ΔT in response to variations in total solar output [*Lean and Rind, 2008*].

The proxy for variations in the strength of the El Niño-Southern Oscillation used here is built around the Multivariate ENSO Index version 2 (MEIv2) [*Wolter and Timlin, 1993; H Zhang et al., 2019*]. The MEI time series, regularly updated, consists of a principle component analysis of five physical quantities (sea level pressure, sea surface temperature, surface zonal winds, surface meridional winds, and outgoing longwave radiation) that represent the state of the tropical ocean-atmosphere system. The MEIv2 record begins in 1979. To provide data back to 1870, we prepend the MEI-extended record [*Wolter and Timlin, 2011*], which uses a weighted combination of two components (SSTs and the Southern Oscillation time series); the MEI-extended was created as an extension of the original MEI record [*Wolter and Timlin, 1993*] that uses six physical quantities instead of five. To extend the MEI-based data record from 1869 back to 1850,

we manually compute the SST average over the ocean surface area considered in the MEI records. To prevent data shock, we increase the MEIv2 values by a constant offset so that its average from 1979 to 2005 matches the average of the MEI-extended over the same time period (which is the extent of their overlap). A two-month lag has been applied to the ENSO index in equation 1a, because this lag provides the highest correlation with the simulated response of ΔT to ENSO found using a thermodynamic approach [Thompson *et al.*, 2009]. The process used to determine this lag from ENSO is described in Canty *et al.* [2013]; this two-month lag is the same as used in other MLR studies (e.g. Lean & Rind [2008] and FR11). The EM-GC is capable of using five other ENSO data sets: the original MEI-based record (i.e. not MEIv2-based) as used in previous iterations of the EM-GC [Canty *et al.*, 2013; Hope *et al.*, 2017], the Tropical Pacific Index [Y Zhang *et al.*, 1997], the Niño 3.4 index [Trenberth, 1997], the Cold Tongue Index [Deser and Wallace, 1990], and the thermodynamic index of Thompson *et al.* [2009]. Our scientific conclusions are entirely insensitive to which ENSO index is used. Here we choose to focus on the MEIv2 as its multiple-component construction leads to a robust time series with less noise than other ENSO time series, particularly those that are based only on SST averages.

Our AMV index is based on the area weighted, monthly mean SST in the Atlantic Ocean, between the equator and 60°N [Schlesinger and Ramankutty, 1994]. We detrend the AMV index using the RF anomaly due to human activity over the century-and-a-half time period of analysis, as described in section §3.2.3 of Canty *et al.* [2013]. This detrending process removes the influence of long-term global warming on the AMV time series; without this external influence, the detrended index can serve as a proxy for

variations in the strength of the Atlantic Meridional Overturning Circulation (AMOC) [Knight *et al.*, 2005; Medhaug and Furevik, 2011; Stouffer *et al.*, 2006]. Since AMOC is slowly varying, if it affects the climate with AMV as a proxy, then high-frequency components of the AMV would be indicative of influence from non-AMOC factors (such as ENSO) or noise. As such, our AMV index is also Fourier-filtered to remove all components with temporal variations shorter than nine years, as described in Canty *et al.* [2013]. The resulting index represents anomalies in the north Atlantic SST that vary on time scales of a decade or longer and are decoupled from human influence.

For the Atlantic signal, we have also tested the LOWESS filtering of ZT13, the “Atlantic Water Variability index” of Pausata *et al.* [2015], and the “Atlantic gyre index” of Rahmstorf *et al.* [2015], and two other levels of Fourier filtering of the AMV. Our main results concerning AAWR are insensitive to the proxy used for AMOC, though the water variability index and gyre index both have little to no expression in the climate record (i.e. the EM-GC returns near-zero values for regression coefficient C_4). As such, we favor using the AMV with nine-year filtering and anthropogenic detrending as the AMOC proxy in our regressions. Including AMV produces relatively low values for χ^2 , allowing our ensembles to include more members without biasing either AAWR or γ (which determines the trend of future temperatures). We have not yet tested the North Atlantic Variability Index (NAVI), an alternative to AMV [Haustein *et al.*, 2019]. However, near-zero values for C_4 are found for several other proxies for AMOC and the resulting values of AAWR and ΔT_{2100} are similar to those shown when AMV is used in the regression. We expect the NAVI [Haustein *et al.*, 2019] to be inconsequential for our general scientific conclusions (§4.3.1) because values of AAWR and ΔT_{2100} found in our

model framework are insensitive to various other proposed proxies for AMOC, as well as the omission of a proxy for AMOC from our regression.

Directly measuring the AMOC, namely its overall rate and volume of flow, is inherently difficult and has not been done over a long enough time period to be used in the EM-GC. However, observations of AMOC have been made in recent years. An analysis of a 14 year (April 2004 to September 2018) time series of data from the RAPID-AMOC program [*Duchez et al.*, 2014] reveals a decline in the strength of AMOC over this time period [*Smeed et al.*, 2017; *Srokosz and Bryden*, 2015], similar to that shown by the AMV over these same years (Figure 4.3c).

The PDO represents the temporal evolution of temperature and sea level pressure of the Pacific Ocean poleward of 20°N [*Y Zhang et al.*, 1997]. The PDO index, which begins in 1900 and extends to present, represents the response of circulation in the Pacific Ocean to atmospheric forcing [*Saravanan and McWilliams*, 1998; *Wu and Liu*, 2003]. This index is regularly updated by the University of Washington. The EM-GC also has the capability to use the Interdecadal Pacific Oscillation (IPO) index to represent the influence of the Pacific Ocean on global climate, rather than the PDO. For comparison to our decadal-filtered Atlantic signal, we use a 10-year running mean of PDO (or IPO) in our analysis, a method reflected in other studies that attempt to link the Pacific signal to global temperature patterns [*England et al.*, 2014]. In this paper, we use the 10-year average of the PDO; using the IPO or using different smoothing times does not change our results. We have also attempted to take the integral of the PDO to address the idea that the sign of PDO affects the trend of ΔT , but taking the integral of PDO produces a time series with an uncharacteristically large peak in the middle of the time series and

few other features relating to ΔT_{OBS} , leading to very small values for C_5 . As detailed in *Canty et al.* [2013], variations in ΔT are more strongly influenced by the Atlantic Ocean than the Pacific, regardless of the treatment of PDO. That said, the Pacific signal is stronger than the Atlantic signal in some select ensemble members with strong aerosol forcing or with Atlantic proxies that exhibit inherently weak fits to the ΔT_{OBS} record.

A proxy for variations in the circulation of the Indian Ocean is also used, so that all three major ocean basins are represented. We use the Indian Ocean Dipole (IOD) index as defined *Saji et al.* [1999], which represents the temperature gradient between the Western and Southeastern portions of the equatorial Indian Ocean. The IOD time series we use is made with SSTs from the Centennial in situ Observation-Based Estimate record [*Ishii et al.*, 2005]. We find that influence of the Indian Ocean on ΔT is small, likely due to the size of this ocean basin relative to those of the Atlantic and Pacific.

4.2.1.2 Model Inputs, Anthropogenic Factors

The anthropogenic inputs included in the EM-GC are greenhouse gases, tropospheric aerosols, land use change, and the long-term export of heat into the ocean in response to anthropogenic atmospheric warming. All data mentioned below can be found online, with source websites and other comments listed in table 4.2.

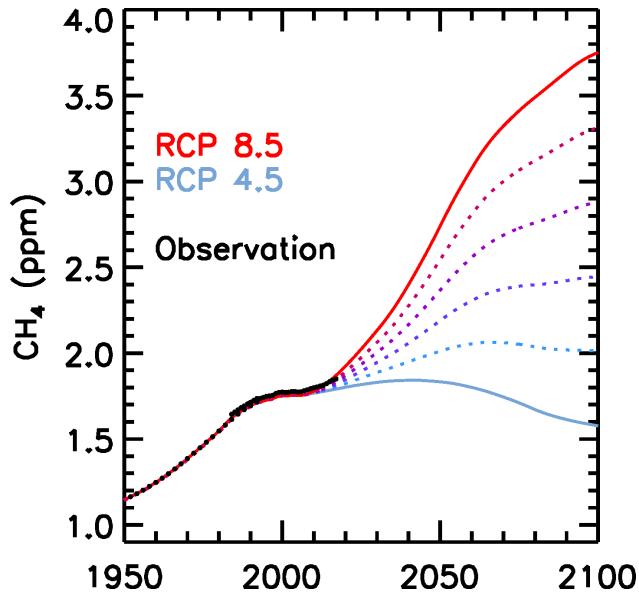
Atmospheric abundances of the main drivers of the anthropogenic RF of climate – the well-mixed greenhouse gases CO_2 , CH_4 , and N_2O – are taken directly from the RCP scenarios [*Meinshausen et al.*, 2011]. For these and other GHGs referenced to *Meinshausen et al.* [2011], we specifically use data from files provided by the Potsdam Institute for Climate Research (PICR, URL in Table 4.2). Annual mixing ratios for each gas are converted to radiative forcing, using the equations from Myhre [1998] and initial

Table 4.2 – Anthropogenic Factor Input Sources

Variable	Data Name	Years	Location
GHG RF	RCPs	1850-2099	http://www.pik-potsdam.de/~mmalte/rcps/
AER RF ^c	Sulfates	1850-2005	http://www.sterndavidi.com/datasite.html http://ciera-air.org/sites/default/files/Total SO2.xls
	Levitus	1955-2019	http://data.nodc.noaa.gov/woa/DATA_ANALYSIS/3M_HEAT_CONTENT/DATA/basin/yearly/h22-w0-700m.dat
OHC	Balmaseda	1958-2017	http://www.cgd.ucar.edu/cas/catalog/ocean/OHC700m.tar.gz
	Cheng	1955-2019	http://159.226.119.60/cheng/
	Ishii	1955-2017	http://159.226.119.60/cheng/
	Carton	1982-2017	https://www.atmos.umd.edu/~ocean/index_files/soda3_readme.htm

^cThe six time series of AER RF for each of the six types of aerosol species considered were combined as described in section §4.2.1.2

Figure 4.5 – Blended Methane Scenarios



Same as the middle panel of Figure 1 except replacing RCP 2.6 methane with the four linear combinations of methane scenarios between RCP 8.5 and RCP 4.5 used in this study.

values from table AII.1.1a in AR5. The RF values are interpolated onto the EM-GC's monthly time grid, with annual RF treated as midyear conditions. The projected mixing ratio of CH₄ in year 2100 is dramatically higher in RCP 8.5 (3.48 ppm) compared to RCP 4.5 (1.54 ppm) (Figure 4.1). To quantify the sensitivity of global warming to CH₄, we have defined four new hybrid scenarios for CH₄ that are linear combinations of RCP 4.5 and RCP 8.5 (Figure 4.5). The RF of CH₄ for the RCPs used here differs slightly from values of RF for CH₄ archived at PICR, due to the update for the preindustrial value for CH₄ given in table AII.1.1a of AR5.

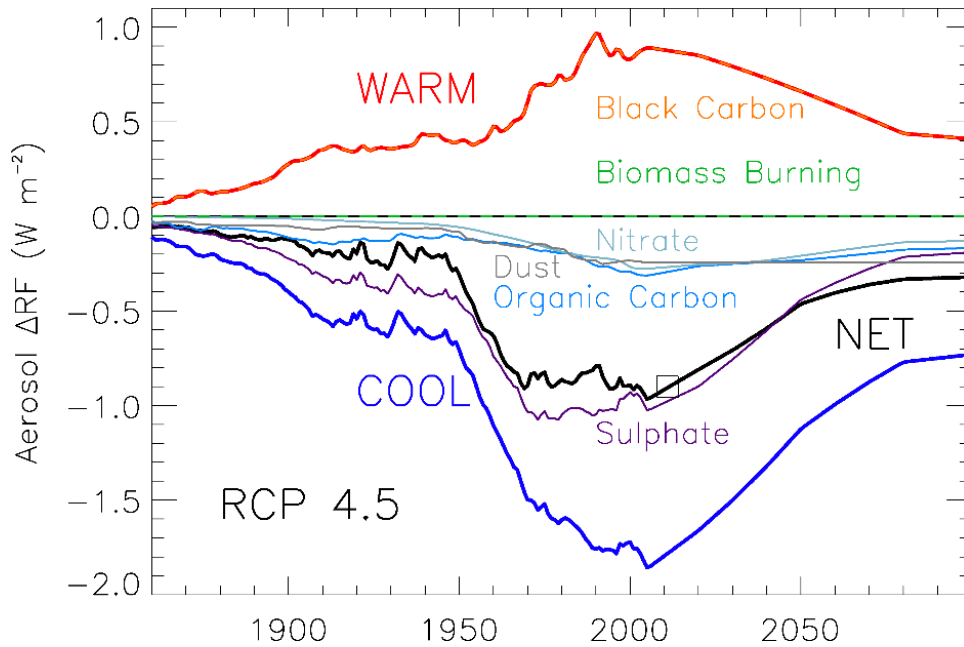
Other greenhouse gases include tropospheric ozone (O₃), stratospheric-ozone-depleting substances (CFCs, HCFCs, CCl₄, CH₃Cl, CH₃Br, etc.), and other F-gases (HFCs, PFCs, and SF₆). Prior and future RF of climate due to tropospheric O₃ is taken directly from *Meinshausen et al.* [2011] for each RCP scenario. The increase in RF of climate due to tropospheric O₃ between 1750 and 2011 is nearly equal to that of CH₄, albeit with much larger uncertainty. The various RCPs project different future RFs due to tropospheric O₃, with RCP 8.5 being the largest. The RF of climate due to ozone-depleting substances (ODS), HFCs, PFCs, and SF₆ are all also taken directly from the RCPs, via PICR.

We consider numerous anthropogenic aerosol scenarios that represent a wide range of total (direct and indirect) RF of climate due to the aerosols. This wide range is essential for consideration because the historical effect of aerosols on climate is not well-known [*Myhre et al.*, 2013], whereas future AER RF is projected to decline due to air quality regulations [*S Smith and Bond*, 2014]. The climate record can be well-simulated by an aerosol scenario for which the RF of climate due to GHGs has been considerably

offset by aerosol cooling: in this case, large values for the sum of climate feedback mechanisms (§4.2.3) are needed to match the observed rise in ΔT . The climate record can be fit just as well by a scenario for which RF due to GHGs has barely been offset by aerosol cooling, in which case small values for the sum of climate feedback mechanisms are required to match ΔT . If we assume that the feedback inferred from the prior climate record will persist into the future, the strong aerosol cooling case will lead to much larger future warming than the weaker cooling case [Knutti and Hegerl, 2008]. The need to consider this relation between AER RF and feedback drives the wide range of scenarios for AER RF described below. We will often refer to a given AER RF time series by the value in year 2011 (AER RF₂₀₁₁) in order to relate our results to estimates of AER RF₂₀₁₁ given in chapter 8 of AR5 [Myhre *et al.*, 2013].

We construct our AER RF scenarios based on forcing data from the RCP database. First, the direct RF for six types of aerosols (sulfate, black carbon, nitrate, dust, organic carbon, and biomass burning products) are obtained from PICR for each RCP scenario [Lamarque *et al.*, 2011]. These direct RF estimates were tied to the state of knowledge that guided the fourth IPCC assessment report [Solomon, 2007]. As was done in Canty *et al.* (2013), we use direct RF as given by PICR for five of the six aerosol species; for sulfate, Smith *et al.* [2011] is used instead because the PICR sulfate data do not reflect sulfate emissions well. In our study, the direct RF time series for each component has been scaled to match values of direct RF in 2011 given by chapter 8 of AR5 [Myhre *et al.*, 2013], as noted in the caption of figure 4.6. This matching process includes eliminating the effect of biomass burning on RF of climate, as AR5 chapter 8 estimated that the RF due to biomass burning in 2011 was zero. Physically, biomass

Figure 4.6 – Example Time Series of Total Aerosol ΔRF by Species



Total aerosol ΔRF for the six species considered by IPCC AR4, as used in this analysis to create the “middle road” time series that achieves AER RF₂₀₁₁ of -0.9 W/m^2 . Black box shows the value of -0.9 W/m^2 in 2011. Original direct ΔRF time series [*Canty et al.*, 2013; *Lamarque et al.*, 2011; *Thomson et al.*, 2011] have been slightly altered so their ΔRF values in 2011 match those stated in AR5. The six species are grouped into four aerosols that cool (sum – thick blue line) and two that warm (sum – thick red line) and then are multiplied by scaling factors to account for indirect ΔRF and create the AER RF time series (thick black line).

burning can conceivably provide no RF impact as a result of cancellation between the warming due to black carbon and the cooling due to organic aerosols products (sections 7.5.2.2 and 8.3.4.2 of AR5). Our scientific conclusions would be unaffected had we used the RCP AER RF time series directly, as archived by PICR. Nonetheless, we scale to AR5 values of direct RF in 2011 so that our study is consistent with the consensus of the scientific community at the time of paper submission.

We perform a second scaling on the aerosol direct RF time series to mathematically simulate the aerosol indirect effect, e.g. cloud-aerosol interactions, with the goal of reaching the AR5 best estimate for total aerosol forcing of -0.9 W/m^2 in 2011. First we separate the direct RF time series into a cooling group – sulfates, mineral dust, primary and secondary organic aerosols, and nitrates – and a warming “group” of black carbon; as biomass burning products were zeroed earlier, they do not factor into the remainder of this analysis. Second, we take the ratio of the sulfate total RF to the sulfate direct RF based on *Smith et al.* [2011] and *Stern* [2006b] as described in *Canty et al.* [2013], a scaling of 2.432. We apply this ratio to the cooling group overall as the scaling factor to change the direct RF time series of the cooling group to the respective total RF time series. We term the value used to scale direct-to-total RF for the cooling group as α_{COOL} . Next, we find the respective direct-to-total ratio for the heating group – α_{HEAT} , in this case 2.188 – needed to make the total cooling RF times series and total heating RF time series add together such that the value in 2011 is -0.9 W/m^2 , which is AR5’s best estimate of effective AER RF₂₀₁₁.

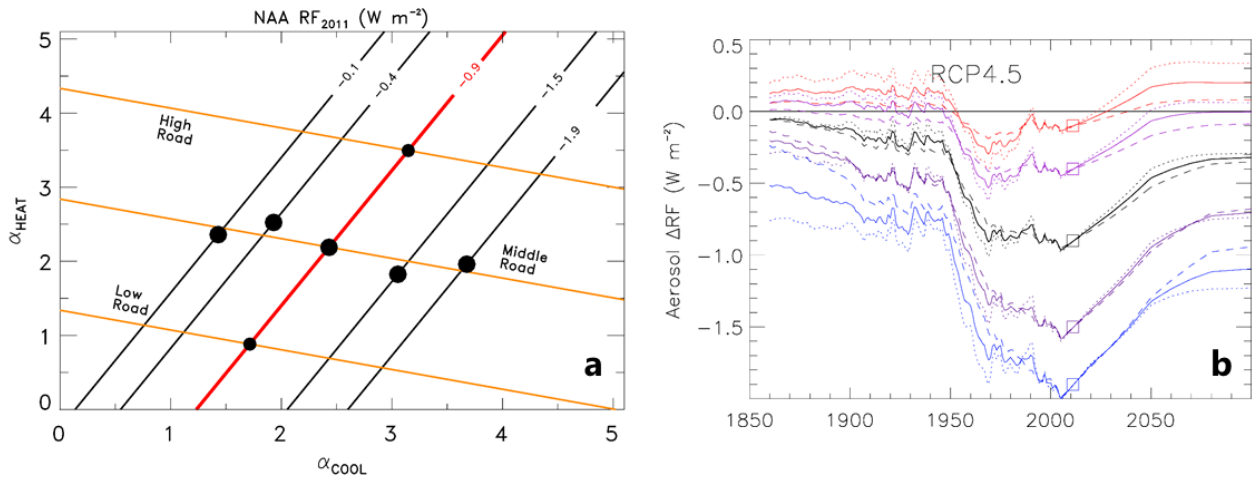
To simulate the uncertainty in historical AER RF, we create other AER RF time series by varying α_{COOL} and α_{HEAT} . In doing so, we can create a potentially infinite

number of AER RF times series of different shapes and strengths. For each ensemble run of the EM-GC, we constrain our AER RF times series to those constructed using a finite length of a cross-section through this α -space, which we term “roads”, shown visually in figure 4.7a. The “middle road” of aerosol scenarios is anchored by the α -space point obtained by attaining the best-estimate AER RF₂₀₁₁ (-0.9 W/m^2) as described in the previous paragraph. The slope of the middle road is found by determining four other statistical combinations of the six aerosol direct RF time series that produce values of total AER RF₂₀₁₁ corresponding to the AR5 confidence intervals (-0.4 W/m^2 to -1.5 W/m^2 , likely range, and -0.1 W/m^2 to -1.9 W/m^2 , 5 to 95% confidence range). The “low road” and “high road” are then anchored by points in α -space that also have an AER RF₂₀₁₁ value of -0.9 W/m^2 . Figure 4.7b then shows the fifteen resulting AER RF time series that correspond to the intersections of the three roads and five forcing isopleths.

Variations in the composition of Earth’s surface due to deforestation and other human activities can also exert a change in the radiative forcing of climate. The ΔRF effect of anthropogenic land use change (LUC) is taken directly from table AII.1.2 of AR5, with the annual values linearly interpolated to the EM-GC’s monthly time grid. We assume the annual values are centered at midyear in the interpolation. The release of GHGs from land-use-change activities such as deforestation or concrete laying are factored into the GHG term itself, as the LUC term only represents surface reflectivity.

We consider the rise in OHC as an anthropogenic signal because increases in the RF of climate due to human activity cause a rise in temperature of both the atmosphere and the oceans [*Hansen et al.*, 2011; *Raper et al.*, 2002; *Schwartz*, 2012]. The focus of many OHC studies has been the top 700 m or top 2 km of the world’s oceans, and our

Figure 4.7 – Aerosol “Roads” Scaling Procedure



a) Aerosol indirect effect scaling parameters. The black and red lines show values of total ΔRF of climate in year 2011 (AER RF₂₀₁₁), relative to preindustrial baseline, due to anthropogenic aerosols, with the AR5 best estimate highlighted in red. The large and small black dots represent the combined scaling factors used to define the three “Roads” (gold lines), which were used to create complete AER RF time series from the base aerosols. The “High Road” and “Low Road” anchor points are found by changing the scaling representing the indirect effect for cooling aerosols by half, with the scaling for indirect heating changed accordingly to remain on the -0.9 W/m^2 isopleth. That is, the best-estimate α_{COOL} of 2.432 implies in indirect effect that is $1.432\times$ the direct RF magnitude, so we increase or decrease that factor of 1.432 by half (0.716 or 2.148) to create the new indirect effect estimate, leading α_{COOL} to be either 1.716 or 3.148. The low and high road take a slope parallel to the middle road through their respective anchor points.

b) The resulting time series of the high, middle, and low “road” combinations of adjusted RCP 4.5 aerosols [Lamarque *et al.*, 2011]. Solid lines represent the middle road time series for each target value of AER RF₂₀₁₁, with the dotted and dashed lines representing the low and high roads respectively. The solid black line in figure 4.7b is the same solid black line as in figure 4.6.

work considers data from five such studies [Balmaseda et al., 2013; Carton et al., 2018; Cheng et al., 2016; Ishii et al., 2017; Levitus et al., 2012]; three of these five studies consider both depths. For proper comparison, the five data sets are normalized to a common value of 0 in 1986 (the midpoint year for the range of time where three or more of the five OHC records are provided) before being averaged together. The magnitude of an input OHC data set at any given point in time is not important in our model framework, because we rely upon change in OHC over time. In this study, we focus on EM-GC runs that use 700 m OHC data, in which case we multiply the OHC values by 1.429 (1/0.7) before the model computes κ , the ocean heat diffusivity term, so as to scale the OHC from the upper 700 m to a value that approximates OHC for the full ocean.

4.2.2 EM-GC Ocean Components

The formulation for Q_{OCEAN} is based on finding the value of κ that best fits observed OHC data. Raper, Gregory, & Stouffer [2002] define κ as the ratio between the atmosphere-to-ocean temperature difference and the heat lost to the ocean. We assume Q_{OCEAN} is anthropogenically driven and we define the monthly values of $Q_{OCEAN i}$ as:

$$\begin{aligned}
 Q_{OCEAN i} &= \kappa(\Delta T_{ATM,HUMAN i} - \Delta T_{OCN,HUMAN i}) \\
 &= \kappa \left(\left[\frac{1 + \gamma}{\lambda_p} \{GHG RF_i + AER RF_i + LUC RF_i\} \right] - \Delta T_{OCN,HUMAN i} \right)
 \end{aligned}$$

Eq4.3

We calculate k , the diffusivity of heat across the atmosphere-ocean surface, as:

$$\kappa = \frac{\Delta OHC \div A_{OCEAN}}{\int_{t_{START}}^{t_{END}} (\Delta T_{ATM,HUMAN} - \Delta T_{OCN,HUMAN})_{i-72} dt}$$

$$= \frac{OHE \times \Delta t}{\int_{t_{START}}^{t_{END}} \left(\left[\frac{1+\gamma}{\lambda_p} \{GHG RF_{i-72} + AER RF_{i-72} + LUC RF_{i-72}\} \right] - [f_0 \sum_0^{i-144} Q_{OCEAN} + f_1 \sum_{i-144}^{i-72} Q_{OCEAN}] \right) dt}$$

Eq4.4a

$$f_0 = f_p \frac{t_{month}}{dc_p \rho} ; f_1 = \left(\frac{1-f_p}{2} \right) \frac{t_{month}}{dc_p \rho}$$

Eq4.4b

The main improvement from *Hope et al.* [2017] is the inclusion of $\Delta T_{OCN,HUMAN}$, which represents the temperature response of the well-mixed upper 100 m of the ocean due to the total rise in OHC. In the previous version of the EM-GC, heat exited the atmosphere without any modulation from an ocean response (i.e. $T_{OCN,HUMAN,i} = 0$ for all i) allowing the ocean to function as an infinite sink. By allowing the model ocean to warm in response to the increase in atmospheric temperature, the amount of heat lost to the ocean per month is reduced over time due to the smaller difference in temperatures between the ocean surface and overlying air, providing a more realistic description of the climate system than earlier versions of our model. The new interactive ocean module provides a reduction in Q_{OCEAN} over time compared to the earlier version of the model, resulting in a slight rise in total anthropogenic RF and in computed future global mean surface temperature relative to that found using a static ocean. This new model formulation thus also introduces a mechanism for the climate system to continue warming even after total anthropogenic RF plateaus, as it does in both RCP 4.5 and RCP 2.6.

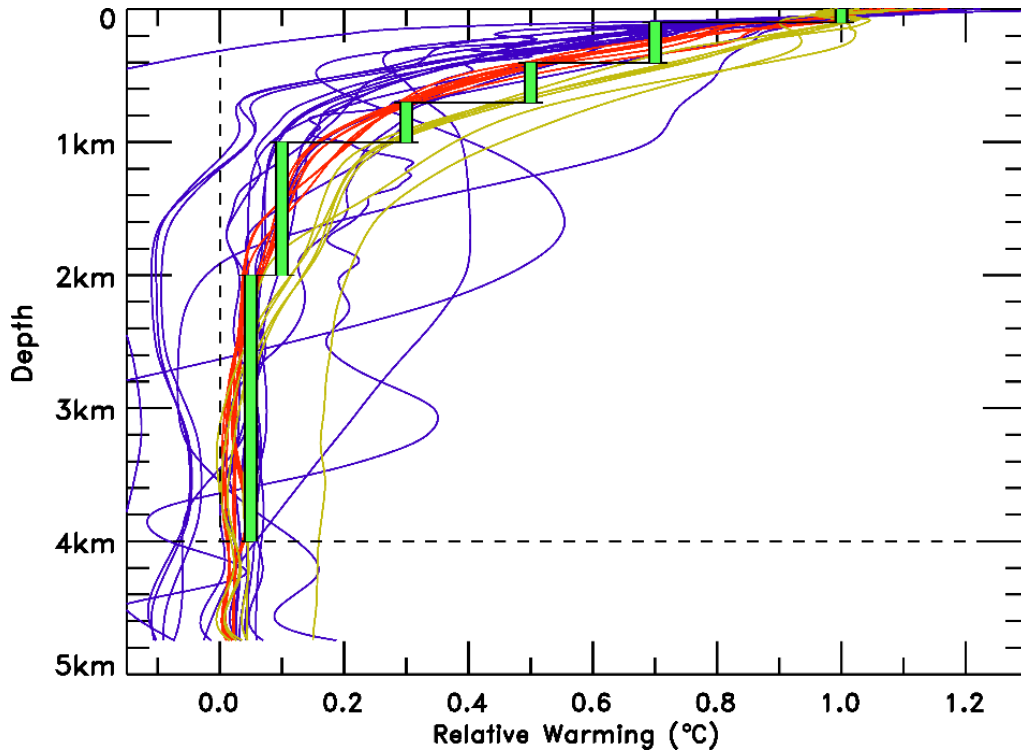
The integral in the denominator and the delta time in the numerator of equation 4.4 are both taken over the entire time extent of the OHC record being considered, i.e. t_{START} and t_{END} are the first and last months corresponding to the years of the OHC record being used. Ocean Heat Export (OHE) is an average over area and time of the export of heat from the atmosphere to the ocean, obtained by estimating the total rise in OHC over time with a linear fit [Canty *et al.*, 2013]. We apply a six-year (72 month) lag to account for the time needed for a given amount of heat leaving the atmosphere to penetrate to depth [Schwartz, 2012]. Other studies [Lean and Rind, 2008; Suckling *et al.*, 2017] infer or apply a ten-year lag; key model outputs such as AAWR are insensitive to choices for the time delay between atmospheric perturbation and mean oceanic response (equation 4.4) for any timescales ranging from annual to multidecadal. The new formulation for Q_{OCEAN} allows the model parameter κ to be directly compared to literature values derived from GCMs [Raper *et al.*, 2002].

The terms f_0 and f_i in equation 4.4 represents a combination of the heat capacity of ocean water (c_p), the fraction of ocean volume in the surface layer (d, ρ) of interest, and the fraction of total Q_{OCEAN} that warms the surface layer (f_p) per month (t_{month}). To calculate f_p , decadal ocean warming as a function of depth was extracted from a selection of CMIP5 models' output, smoothed, and then normalized to the warming in the layer from 0-100 m. A simplified warming profile was then selected for the remaining depth of the ocean down to 4 km, (green segments of Figure 4.8) favoring the group of warming profiles from RCP 4.5 and RCP 8.5. This stratified warming profile was used in combination with the ocean depth profile to determine the percentage of ocean heat export that warmed the 0-100 m layer, producing $\Delta T_{\text{OCN,HUMAN}}$. This 100 m top layer is

used as the section of ocean that interacts directly with the atmosphere, because it is well-mixed. We represent the ocean as being 1 km deep for 10% of the ocean area (representing the continental shelves) and 4 km deep for the remaining 90%. This simplified depth profile approximates the average depth of the real ocean to within 3%, 3.7 km compared to 3.682-3.814 km [Charette and Smith, 2010]; using the ocean surface area estimate of $3.3 \times 10^8 \text{ km}^2$ from [Domingues et al., 2008], our simplified ocean also approximates the total volume of the real ocean to within 10%, $1.221 \times 10^9 \text{ km}^3$ compared to $1.33\text{-}1.37 \times 10^9 \text{ km}^3$. Taken together, this CMIP5-based warming profile with depth implies that 13.7% of the rise in total OHC occurs in the well mixed, upper 100 m of the ocean, resulting in the $\Delta T_{\text{OCN,HUMAN}}$ term in equations 4.3 and 4.4. As a result, the value of f_o in equation 4.4 is $8.76 \times 10^{-5} \text{ }^\circ\text{Cm}^2/\text{W}$.

Output from the ocean module, Q_{OCEAN} , is area corrected to scale the average forcing applied to the atmosphere by the ocean before this quantity is used in the MLR. The ocean module is based upon the total surface area of the world's oceans, but the inputs to the atmospheric module are applied to the entire surface area of the Earth. As such, we scale Q_{OCEAN} in the model atmosphere by the ratio of ocean surface area to Earth's total surface area, (i.e. the multiplier 0.671 in equation 4.1a,) to ensure that the total amount of energy leaving the atmosphere is the same as the total amount of energy entering the oceans.

Figure 4.8 – Ocean Warming Profiles, CMIP5 (normalized) vs EM-GC (simplified)



CMIP5 experiment results (selected models) represent historical (blue), RCP 4.5 (yellow), and RCP 8.5 (red) model runs with spline smoothing. The EM-GC approximation to the overall CMIP5 warming profile is shown in green. The values for each warming profile are expressed as a fraction of the warming-per-decade seen in the 0-100 m layer. The approximate warming profile (green) is then applied to a simple ocean depth profile with 90% of the EM-GC ocean being 4 km deep while the remaining 10% is 1 km deep. With this warming profile and depth profile, the fraction of total warming in the upper 100 m is caused by 13.70% of total ocean heating, as follows: $(100 \text{ m} \times 1^\circ\text{C} \times 100\%) / [(100 \text{ m} \times 1^\circ\text{C} \times 100\%) + (300 \text{ m} \times 0.7^\circ\text{C} \times 100\%) + (300 \text{ m} \times 0.5^\circ\text{C} \times 100\%) + (300 \text{ m} \times 0.3^\circ\text{C} \times 100\%) + (1000 \text{ m} \times 0.1^\circ\text{C} \times 90\%) + (2000 \text{ m} \times 0.05^\circ\text{C} \times 90\%)] = 100 \text{ m}^\circ\text{C} / 730 \text{ m}^\circ\text{C} = 13.70\%$.

Table 4.3 – Comparison of Simulated Ocean Warming Profiles

Profile name	Profile warming description	% of heating in the upper 100 m		"Central" run		
				AAWR, °C/dec	λ_s , W/m ² /°C	T_{2100} , °C
Upper	Linear warming profile through upper 1km of ocean and no warming deeper than 1km, i.e. 900m-1km layer warms 10% as quickly as 0-100m layer	18.18%	(1/5.5)	0.152 °C/dec	1.62 W/m ² /°C	1.95 °C
CMIP5	Stratified approximation of CMIP5 output warming profiles	13.70%	(1/7.3)	0.146 °C/dec	1.59 W/m ² /°C	1.79 °C
Middle	Approximate average between CMIP5 profile and Linear profile	9.50%	(~1/10.5)	0.142 °C/dec	1.54 W/m ² /°C	1.63 °C
Linear	Linear warming profile through entire 4km of ocean, i.e. 400m-500m layer warms 90% as quickly as 0-100m layer and 3.9km-4km warms 2.5% as quickly	5.17%	(1/19.3375)	0.142 °C/dec	1.52 W/m ² /°C	1.51 °C
Constant	Entire 4km of ocean warms as quickly as 0-100m layer	2.70%	(1/37)	0.141 °C/dec	1.50 W/m ² /°C	1.45 °C

Each profile provides a different value for the percentage of the increase in OHC that remains in the top 100m layer, which determines $T_{OCN,HUMAN}$. Fractions in parentheses represent the exact ratio calculated for the profile described in a simple ocean that is 4 km deep for 90% of its area and 1 km deep for the remaining 10%. (This is why, for example, the ratio for the Constant profile is one part in 37 instead of one part in 40, and why the ratio for the Linear profile looks excessively precise.) Key quantities from our model are also shown for simulations identical to that shown in figure 4.3 except for changing the fraction of heat that remains in the top 100 m ocean surface layer.

Four alternate values for the fraction of OHC in the upper 100 m were also considered to test the sensitivity of future atmospheric temperatures to the ocean's response to global warming. At one extreme, warming due to the rise in OHC is distributed linearly in just the upper 1 km of the ocean with no warming deeper, putting 18.2% of the rise in OHC into the top 100 m of the global ocean. At the other extreme, a warming profile that assumes a constant warming rate throughout the entire ocean has only 2.7% of the rise in OHC going into the upper 100 m. Both scenarios are physically unrealistic but provide bounds for the range of how much $\Delta T_{\text{OCN,HUMAN}}$ can change for a given OHC record. All five warming profiles with depth and their associated top 100 m fractions are summarized in table 4.3. Choice of ocean warming profile does not affect our results for AAWR significantly, as the interplay between $\Delta T_{\text{OCN,HUMAN}}$ and κ means that Q_{OCEAN} is largely driven by the choice of OHC_{OBS} , but this choice could affect ΔT_{2100} if the true warming profile is significantly different from the CMIP5 simulations.

4.2.3 Climate Feedback and Sensitivity

Climate feedback processes and overall climate sensitivity define how changes in RF, particularly the rise in anthropogenic RF, drive ΔT . In the EM-GC, the sum of RF due to GHGs, aerosols, LUC, and OHE is multiplied by $(1+\gamma)/\lambda_P$, where λ_P is the Planck response parameter ($3.2 \text{ W m}^{-2} \text{ }^\circ\text{C}^{-1}$) and γ is the dimensionless climate amplification term, to determine ΔT (equation 4.1a). If the net response of changes in humidity, lapse rate, clouds, and surface albedo that occur in response to anthropogenic RF of climate is positive, as is the case for the vast majority of simulations conducted for this study, then the numerical value of γ is positive. This model framework is based on that described in *Bony et al.* [2006] and §8.6 of the previous IPCC report [*Solomon, 2007*]. The EM-GC's

variable for the sum of climate feedback mechanisms, λ_{Σ} , has units of $\text{W m}^{-2} \text{ }^{\circ}\text{C}^{-1}$ and is related to γ and λ_P via:

$$1 + \gamma = \frac{1}{1 - \frac{\lambda_{\Sigma}}{\lambda_P}} = \frac{\lambda_P}{\lambda_P - \lambda_{\Sigma}}$$

Eq4.5

This relation between γ and λ_{Σ} is commonly used in the climate modeling community (§8.6 of AR4). We can also relate λ_{Σ} to the traditional climate feedback parameter λ [Bony *et al.*, 2006; Gregory, 2000; Schwartz, 2012; Sherwood *et al.*, 2020] by reducing equation 4.1a to just the anthropogenic terms to produce the relations:

$$\Delta T_{Human\ i} = \frac{1 + \gamma}{\lambda_P} \{GHG\ RF_i + AER\ RF_i + LUC\ RF_i - Q_{OCEAN\ i}\}$$

Eq4.6a

$$\Delta T_{Human} = \frac{1 + \gamma}{\lambda_P} \Delta F_{Human}$$

Eq4.6b

$$\lambda^{-1} = \frac{1 + \gamma}{\lambda_P} \rightarrow \lambda = \lambda_P - \lambda_{\Sigma}$$

Eq4.6c

We choose to focus on λ_{Σ} instead of λ for the majority of this paper. This choice allows for an intuitive comparison between λ_{Σ} , γ , and ΔT – as one quantity rises, so do the others. This intuitive relationship highlights how uncertainty in various climate feedback mechanisms (i.e. aside from the blackbody response) can be the driving force in future ΔT uncertainty. We assume a constant value for λ_{Σ} (and λ) for each ensemble member in most of the results shown below, as this assumption provides a multitude of

simulations of ΔT with χ^2 values less than 1, well below our acceptable fitting limit of 2. We view this as a reasonable approximation because §12.5.3 of AR5 and references therein suggest λ changes slowly over millennia; any changes in λ over a few centuries should be unnoticeable unless gradual changes force the climate system past a significant tipping point. For completeness, we also examine the effect on EM-GC ΔT of a slowly- or moderately-varying λ in section §4.3.4 of this paper.

4.3 Results and Analysis

Our results focus mainly on Attributable Anthropogenic Warming Rate (AAWR) and projections of the global mean surface temperature anomaly relative to preindustrial (ΔT). We first present here a summary of the probabilistic distribution of these two quantities for our best representative ensemble of EM-GC simulations, and next describe how these distributions compare to CMIP5 and other studies. Then, in each subsection to follow, we delve further into our results for AAWR and ΔT_{2100} , providing a detailed description of their sensitivities as well as comparisons to other published results. The first three subsections present discussion of AAWR, in which we describe our approach, possible shortcomings in prior efforts used to evaluate AAWR, and the uncertainties involved in proper quantification of AAWR. The last five subsections present results for ΔT , including quantification of the sensitivity to uncertainty in future emissions of CH_4 and relating our projections of future warming to cumulative, anthropogenic emissions of CO_2 .

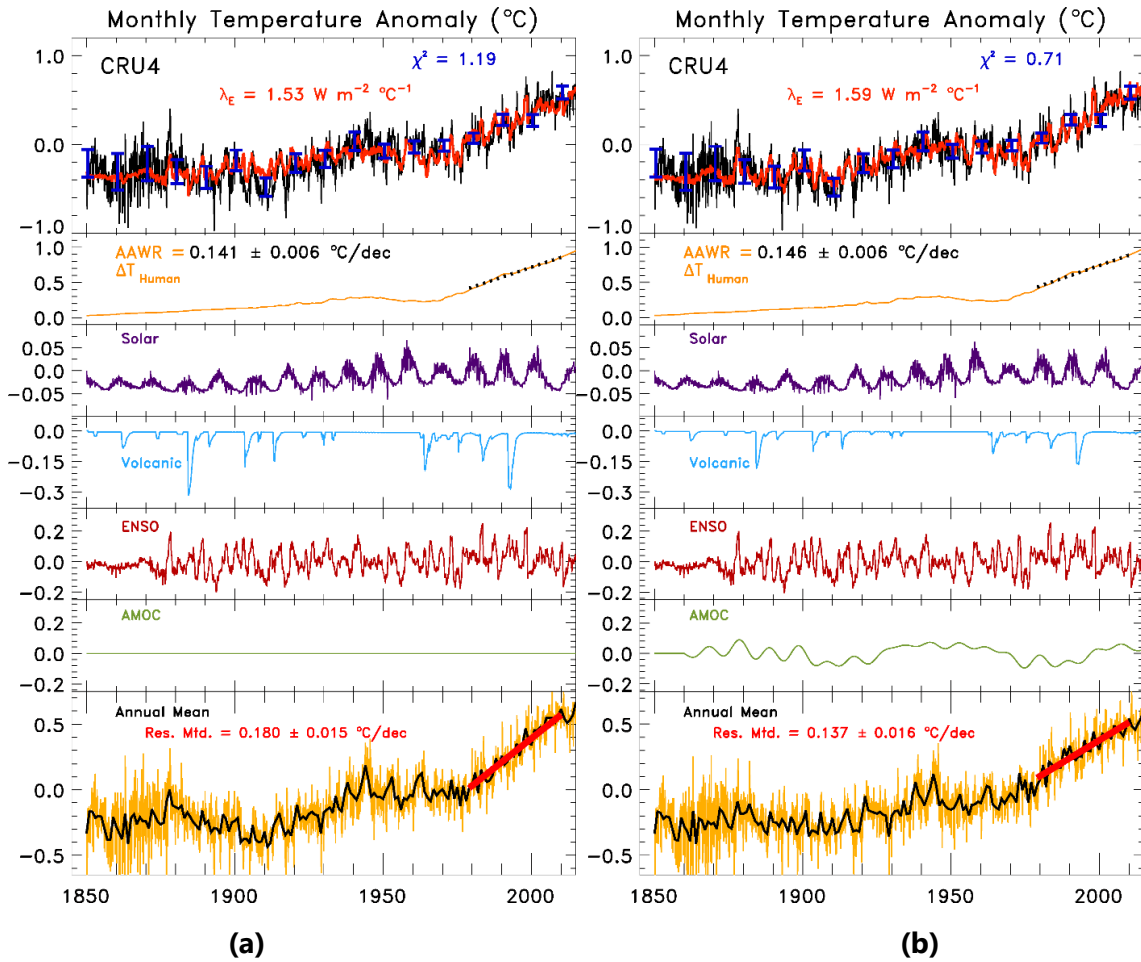
Overall, our numerical estimates of AAWR for 1979 to 2100 fall between prior estimates. Our best estimate of AAWR is $\sim 0.14^\circ\text{C}/\text{decade}$, which is noticeably lower than the value for AAWR from CMIP5 GCMs ($\sim 0.22^\circ\text{C}/\text{decade}$). Our value for AAWR

falls between estimates of AAWR from FR11 (0.170 ± 0.012) and the AMOC-based AAWR from ZT13 (0.070 ± 0.019). Below, we describe the sensitivity of AAWR to various estimates of radiative forcing by aerosols, the sum of climate feedback mechanisms, and multiple records for ΔT_{OBS} . Notably, AAWR in our model is largely insensitive to whether AMOC is included (see §2.1.1 and figure 4.9a,b).

Our ensemble median value for global warming at the end of this century, ΔT_{2100} , is consistently cooler than the CMIP5 ensemble median value for ΔT_{2100} . Indeed, our ensemble median of ΔT_{2100} often lies close to the CMIP5 ensemble minimum warming. The EM-CG framework, with its tendency for cooler results, assigns each RCP scenario a higher probability of fulfilling the Paris Agreement warming limitations, compared to the CMIP5 GCMs. The near-term warming found by our EM-GC also closely matches the expert assessment of CMIP5 results shown in chapter 11 of AR5, represented by the green trapezoid in figure 4.2.

Figure 4.10 shows AAWR and ΔT_{2100} for the same ensemble run of the EM-GC and depicts the weighting function we use to create probabilistic summaries of our results. Each simulation in this ensemble has the same set of inputs except for varying λ_{Σ} and varying the shape and strength of anthropogenic aerosol forcing, pinned to the value of AER RF in 2011. Computed values of AAWR are sensitive to AER RF and λ_{Σ} because of differences in the shape of the aerosol term (blue line, figure 4.3a) that is subtracted from the GHG term (red line, figure 4.3a), for various members of the ensemble. Values of ΔT_{2100} are particularly sensitive to climate feedback, because by end of century the RF due to aerosols is expected to be considerably smaller than contemporary values [*S Smith and Bond, 2014*]. The EM-GC ensemble shown in figure 4.10 is based on RCP 4.5 GHGs

Figure 4.9 – Measured and modeled global temperature anomaly: fallacy of the residual method



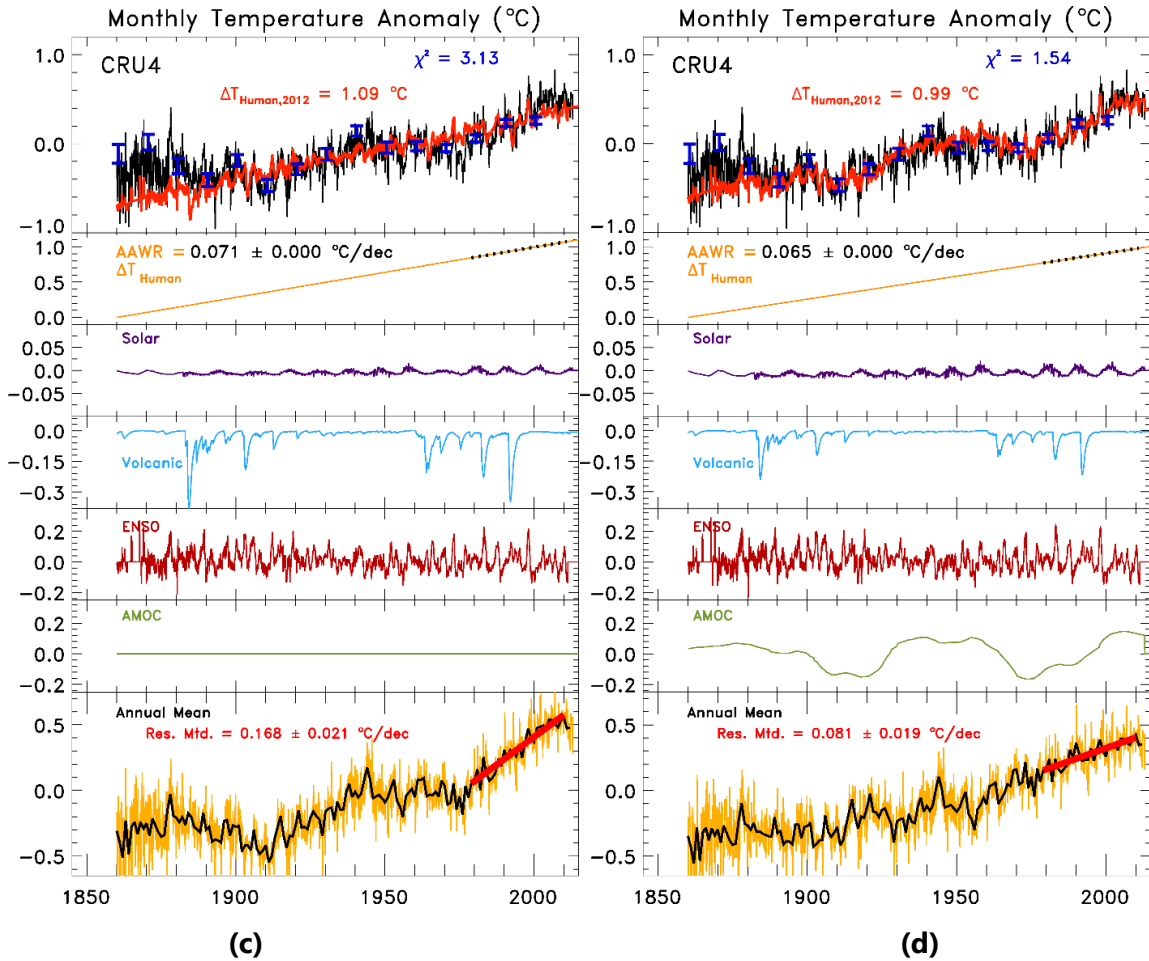
Ladder plots shown are similar to those in Figure 4, though no model runs in this figure include PDO or IOD, and CTI is used in place of MEI for the ENSO signal. In addition, the last rung on each ladder shows the difference between the measured and modeled temperature time series of the first rung added to ΔT_{HUMAN} from the second rung, as this general practice is what was used by both FR11 and ZT13; the first and last rungs are shown with a temperature baseline of 1961-1990, as was done by ZT13. Here, we specifically show the effect of including an AMOC signal in this practice, as well as display the error made by ZT13 in their first guess of ΔT_{HUMAN} .

a) uses the RCP estimate of ΔT_{HUMAN} and no AMOC

b) same as (a) except for using the Fourier-filtered AMV as the AMOC signal, i.e. same model simulation as figure 4.3.

[cont'd next page]

Figure 4.9 cont.

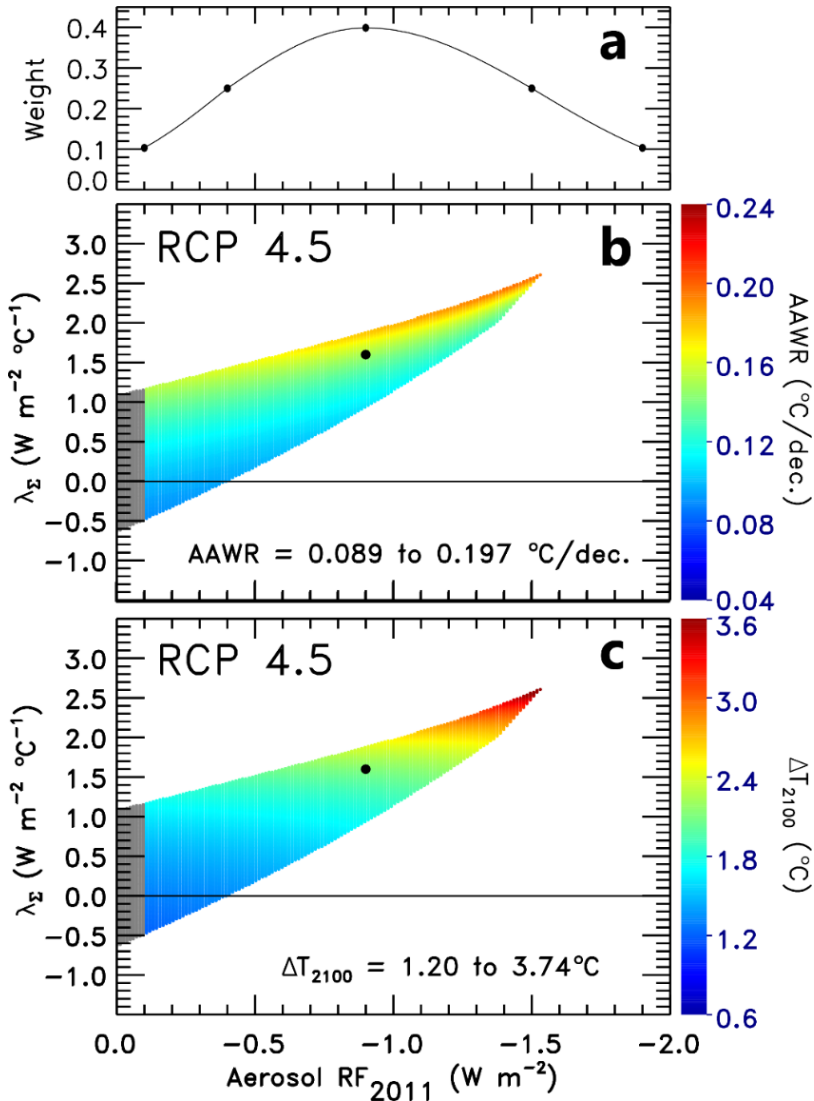


c) same as (a) except with a linear guess for ΔT_{HUMAN} over the entire time period of the model run, as was done by ZT13

d) same as c) except with the ZT13 LOWESS-filtered AMV as the AMOC signal.

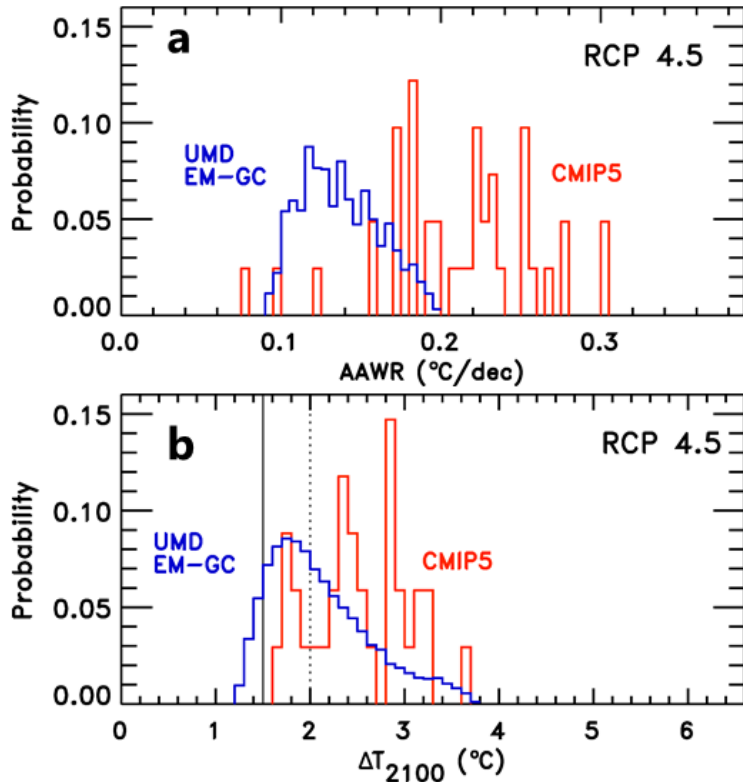
In (c) and (d), we capture essentially the same result of ZT13, with their residual-method version of AAWR producing $0.168 \text{ } ^\circ\text{C/decade}$ without AMOC (match within 1%) and $0.081 \text{ } ^\circ\text{C/decade}$ with AMOC (close match). However, we see both visually and through chi-squared that the fit to the observed record in (c)+(d) is much poorer than in (a)+(b). The residual method differences are highly sensitive to the initial linear guess for ΔT_{HUMAN} , as the result in (a)+(b) only causes a drop from $0.180 \text{ } ^\circ\text{C/decade}$ to $0.137 \text{ } ^\circ\text{C/decade}$, despite the fact that in both cases the direct ΔT_{HUMAN} signal changes very little whether AMOC is considered or not. ZT13 claim that using the RCP-based initial guess for ΔT_{HUMAN} causes the difference between observed and modeled ΔT to have noticeable positive, then negative, trends; we do not observe this in (b).

Figure 4.10 – AAWR and ΔT_{2100} as a function of AER RF₂₀₁₁ and λ_{Σ}



AAWR and ΔT_{2100} as a function of AER RF₂₀₁₁ and λ_{Σ} over a single EM-GC ensemble (panels b and c) and the AER RF₂₀₁₁-based weighting function used to aggregate our ensemble statistics (panel a). Values of AAWR are for 1979 to 2010 and values of ΔT_{2100} are relative to the preindustrial baseline. We show all simulations for which $\chi^2 \leq 2$ for all three fitting comparisons, (i.e. fitting ΔT for the full time period, fitting ΔT for the most recent 80 years, and fitting OHC over its time period,) though any model results that for AER RF₂₀₁₁ outside of the range -0.1 to -1.9 W m⁻², the 5% and 95% confidence intervals given in AR5, are covered using the color grey. All runs in this ensemble use RCP 4.5 GHG RF and RCP 4.5-based AER RF scenarios along the middle road of figure 4.7 to simulate the CRU4 ΔT_{OBS} record. The black dot in panels b and c represents the single run from the ensemble with the lowest χ^2 over the full ΔT record among simulations forced with the AER RF times series that gives -0.9 W/m² in 2011, the best estimate for AER RF₂₀₁₁ stated in AR5. Results from this single simulation, broken into component time series, are shown in figure 4.3.

Figure 4.11 – Probability Density Functions of AAWR and ΔT_{2100} , RCP 4.5



Probability density functions (PDFs) of the EM-GC computations of AAWR and ΔT_{2100} for RCP 4.5 shown in figures 4.10b and 4.10c, weighted by the associated value of AER RF₂₀₁₁ using the weighting function shown in figure 4.10a (blue lines). PDFs of AAWR and ΔT_{2100} from CMIP5 GCMs, also for RCP 4.5, are also shown (red lines). The height for each bin (0.1°C width for ΔT_{2100} , 0.05°C/decade width for AAWR) for the UMD EM-GC PDFs represents the probability of a run with that value being randomly selected from the respective model output shown by non-grey colors in figure 4.10b and 4.10c, when each model run is weighted by the AER RF₂₀₁₁-based weighting function shown in figure 4.10a. Similar probabilities can be taken from the CMIP5 ensemble giving results from each GCM equal weighting (red). For panel b, the Paris Agreement goal of 1.5°C warming and upper limit of 2°C warming are shown by the vertical solid and dotted lines, respectively.

and constrained by the CRU4 record for ΔT_{OBS} from 1850 to 2019. The values of AAWR and ΔT_{2100} shown in figure 4.10 are for those members of the ensemble for which all three χ^2 filters yield a value less than or equal to 2: i.e., those sets of model results able to provide a “good fit” to ΔT_{OBS} from 1850 to 2019, from 1940 to 2019, and to OHC averaged among five data centers from 1955 to 2018. We also eliminate any simulations for which AER RF₂₀₁₁ does not lie between -1.9 and -0.1 W m^{-2} , the 5% and 95% confidence intervals for RF due to anthropogenic aerosols given in AR5, which is why model results shown on the left side of Figure 4.10b and 4.10c are shown in grey.

Figure 4.11 then aggregates these results into probability density functions (PDFs) of AAWR and ΔT_{2100} from the EM-GC (blue) using a weighting method, described in section §3.1, that is based on the AR5 likelihoods for the values of AER RF₂₀₁₁ (figure 4.10a). Similar PDFs based on results from 41 CMIP5 GCMs (without any weighting, red) are also shown in figure 4.11.

4.3.1 AAWR from the EM-GC

We base our estimate of AAWR on the slope of ΔT_{HUMAN} over the years 1979 to 2010. To calculate AAWR, our empirical model is first run over a chosen time period to produce the ΔT_{HUMAN} series; then a linear fit is calculated from this series over the years 1979 to 2010. Except when otherwise stated, the chosen time period for the model run is the entire available ΔT record, which for the CRU4 record used in figure 4.3 is January 1850 to December 2019. To choose which ensemble member from figure 4.10 would be shown in figure 4.3, we selected the run with the best estimate of AER RF₂₀₁₁ from AR5 (-0.9 W/m^2) that had the lowest value of χ^2 for fitting the full ΔT_{OBS} record. This selected run gives a value for AAWR of $0.146 \text{ }^\circ\text{C/decade}$.

To aggregate the EM-GC ensemble results from Figure 4.10b, we assign probabilities to each ~150 long time series for the RF due to aerosols, tied to the value of AER RF₂₀₁₁ for each time series. We create an approximate Gaussian distribution of AER RF₂₀₁₁ based upon AR5 estimates of this quantity (figure 4.10a). This weighting function peaks at -0.9 W/m^2 (AR5 best estimate of AER RF₂₀₁₁) and the cumulative probability of AER RF₂₀₁₁ values between -0.4 and -1.5 W/m^2 is set at 66.7%. Similarly, the cumulative probability of the weighting function between -0.1 and -1.9 W/m^2 is 90%, which corresponds to the AR5 specification of -0.1 and -1.9 W/m^2 being the 5% and 95% confidence intervals for this quantity [Myhre *et al.*, 2013]. We then take all runs shown as non-grey colors for AAWR in figure 4.10b (i.e. all runs for which a good fit to ΔT for the full time period, ΔT for the most recent 80 years, and OHC from 1955 to 2018 can be obtained), bin by AER RF₂₀₁₁, and find the probability distribution for AAWR within each of these bins. The PDFs for AAWR within each bin are then aggregated using the IPCC-based weightings for each value of AER RF₂₀₁₁ (figure 4.10a) to create the final PDF shown as a blue line in figure 4.11a. We use this superposition of PDFs weighting method to account for the fact that the EM-GC finds many more acceptable fits to the climate record (i.e. $\chi^2 \leq 2$) for combinations of λ_Σ and AER RF₂₀₁₁ associated with less-negative values of AER RF₂₀₁₁, whereas AR5 suggests that -1.5 W/m^2 is as likely as -0.4 W/m^2 for the RF of climate in 2011 due to aerosols. This weighting method gives model runs with stronger aerosol cooling the same weight as runs with weaker aerosol cooling. For the AAWR ensemble shown in figure 4.10b, this weighting process produces a median of $0.135 \text{ }^\circ\text{C/decade}$, with a full range of $0.089 \text{ }^\circ\text{C/decade}$ to $0.197 \text{ }^\circ\text{C/decade}$. Through most of the ensemble, the resulting time series for ΔT_{HUMAN} and the

resulting values of AAWR agree well with another recent estimate found using a similar approach [Chylek *et al.*, 2014].

Our estimate of AAWR is sensitive to which aerosol forcing time series is used, especially in relation to λ_{Σ} , and is partially sensitive to ΔT_{OBS} , but insensitive to the inclusion of terms for AMV, the PDO, and the IOD in the model framework. The insensitivity of AAWR to AMV extends to all of the other proxies for variations in the strength of the AMOC we have considered. The modeled strength of the PDO varies noticeably depending on the proxies and filtering methods chosen for both this climate signal and as well as AMV and RF due to aerosols. Specifically, the contribution of the PDO to ΔT_{MDL} increases in magnitude with stronger-cooling aerosol scenarios – but these model results do not show any strong effect on AAWR. We can also run the EM-GC with specific single records for OHC instead of using the average of five OHC data records; varying the input OHC time series does not produce any noticeable variation in AAWR.

One EM-GC simplification that deserves mention is the lack of spatial variability in the effect of the oceans. *Rose et al.* [2014] showed that the climatic effect of ocean heat uptake is weaker if heat export from the atmosphere is concentrated in the tropics and stronger if heat export is concentrated in high latitudes. While the EM-GC cannot directly separate the locality of ocean heat export, it corroborates the *Rose et al.* [2014] result in the sense that almost all runs show a stronger climatic signal from the AMOC (driven by high-latitude deep water formation) and a weaker signal from the PDO (an expression of comparatively shallow-water heat storage in the tropics [England *et al.*, 2014]; see §4.2.1.1 for a summary of the various AMOC and PDO proxies tested). While

various other MLR studies [Chylek *et al.*, 2016; J Zhou and Tung, 2013a] focus on the AMOC as the main oceanic driver of the climate system, other literature suggests the PDO has a stronger influence on global temperature, either overall or specifically for the last few decades [England *et al.*, 2014; Steinman *et al.*, 2015; Tokarska *et al.*, 2019]. Due to the structure of MLR models, finding regression coefficients for time spans less than the multidecadal characteristic time of known natural variability is not practical, nor is attempting to define climate drivers using fewer total years than this characteristic time scale. Some research suggests that the sign of the PDO is what drives trends in ΔT [England *et al.*, 2014], meaning an integral of the original PDO time series might be a stronger regressor. However, using a time series calculated as such did not produce lower values of χ^2 or higher values of the PDO regression coefficient than found using the raw PDO signal, further suggesting that AMOC is likely the stronger driver of variations in ΔT .

Our method of determining AAWR is also relatively insensitive to the choice of beginning and end years (table 4.4). For example, using the EM-GC simulation shown in Figure 4.3, AAWR only varies from 0.130 to 0.156 °C/decade when we vary both the initial year (1975 to 1985) and final year (2006 to 2016) around the default AAWR time range of 1979 to 2010. This insensitivity derives from the fact that ΔT_{HUMAN} follows from the known rise in CO₂, CH₄, and N₂O that leads to a RF of climate due to GHGs that rises in a roughly linear manner over the past four to five decades. Our calculation of AAWR is thus robust and, as detailed in the following section, does a better job of isolating the underlying anthropogenic climate trend than methods that rely on analysis of ΔT using the residual method.

4.3.2 Comparison to previous AAWR estimates

We assert that the slope of ΔT_{HUMAN} provides a more accurate method for quantifying AAWR than the use of a residual method. As described in section §4.3.1, our median estimate of AAWR with RCP 4.5 GHGs and “middle road” aerosols is 0.135 °C/decade, with range of possible values extending from 0.089 °C/decade to 0.197 °C/decade based on uncertainty in RF due to aerosols and climate feedback. The best estimate of AAWR given by FR11 for 1979 to 2010, upon analysis of ΔT from CRU3, is 0.170 °C/decade. The residual method used by FR11 involves finding the slope of observed ΔT after the contributions from solar irradiance, volcanoes, and ENSO have been removed. By not including AMV (green curve in figure 4.3c) and by focusing their analysis solely on a 31 year period of time, FR11 do not account for the significant warming trend that occurred from 1979 to 2010 that our analysis suggests is due to natural variability and instead attributed this component of the rise in ΔT to anthropogenic warming. Although the precise magnitude of the AMV influence is sensitive to how North Atlantic SST is detrended [*Canty et al.*, 2013] and smoothed, an independent analysis of SST using spectral methods [*DelSole et al.*, 2011] supports our suggestion that internal climate variability contributed significantly to the relative warming over our default time period for AAWR.

We note that *Haustein et al.* [2019] emphatically state “we argue that AMV must not be used as a regressor” because “AMV is found to be primarily controlled by external forcing”. *Booth et al.* [2012] implicate tropospheric aerosols due to pollution and stratospheric sulfate aerosols due to major volcanic eruptions of the primary driver of

Table 4.4 – Variation of AAWR Based on Start and End Year

AAWR (°C/dec)	1975	1977	1979	1981	1983	1985
2006	0.156±0.0075	0.153±0.0082	0.148±0.0084	0.144±0.0090	0.138±0.0089	0.130±0.0078
2008	0.153±0.0069	0.151±0.0074	0.146±0.0075	0.142±0.0078	0.137±0.0076	0.130±0.0065
2010	0.151±0.0062	0.150±0.0066	0.146±0.0065	0.142±0.0067	0.137±0.0065	0.132±0.0057
2012	0.152±0.0055	0.150±0.0058	0.146±0.0058	0.143±0.0060	0.139±0.0060	0.135±0.0054
2014	0.152±0.0050	0.150±0.0052	0.147±0.0052	0.145±0.0054	0.142±0.0054	0.138±0.0053
2016	0.153±0.0045	0.151±0.0048	0.149±0.0048	0.147±0.0050	0.144±0.0052	0.142±0.0054

Default time period used in the paper is 1979 to 2010 (AAWR value bolded). The ΔT_{HUMAN} time series used remains the same for all combinations of start and end year, taken from the single EM-GC simulation used in figure 4.3.

SST variability in the North Atlantic. There are numerous other studies making similar claims [*Knight et al.*, 2005; *Medhaug and Furevik*, 2011; *Meehl et al.*, 2011; *Stouffer et al.*, 2006], including a study of paloeurrent speed that extends over a time period of 230 years [*Boessenkool et al.*, 2007], that suggests our AMV proxy does represent interval variability of the climate record. Regardless, we find nearly identical values of AAWR based on the slope of ΔT_{HUMAN} , with or without the use of AMV as a term in the regression model (Figure 4.9a vs 4.9b). We are therefore confident FR11 have overestimated the true value AAWR, either because there is a component of natural variability present in the residual they have computed, or because their analysis is restricted to such a short period of time. In contrast, our computation of AAWR for 1979 to 2010 is found using a physical model that provides consistent treatment of RF due to GHGs, aerosols, and natural factors such as ENSO, TSI, and SAOD, over a century and a half period, which mitigates a host of potential complications present when one examines a residual [*Silver*, 2012].

Other studies suggest the PDO or changes in SAOD from minor volcanic eruptions could have also played a role in driving variations of ΔT over this time period (e.g. *Tokarska* [2019] and the references therein). Our estimates of AAWR include all of these factors and based on analysis of data collected over a ~ 150 year time period; in our model framework the most important natural drivers of ΔT over the past four to five decades are ENSO, major volcanic eruptions, and AMV. If temperature is affected by a natural process not represented by the exogenous factors used to compute the residual, then quantification of AAWR will be unduly influenced (Figure 4.9). In particular, the difference between our best estimate of AAWR and that given by FR11 is nearly

completely explained by the proper attribution of the signal from variations in the strength of AMOC⁴⁰.

Conversely, the estimate of AAWR over 1979 to 2010 provided by ZT13 upon consideration of the variations in the strength of AMOC is likely biased low. They suggest AAWR drops from 0.170 °C/decade in a regression without AMV to 0.070 °C/decade with AMV included. Even though they considered AMV as a proxy for variations in the strength of AMOC, they used a linear function to describe ΔT_{HUMAN} over the entire 1860 to 2010 time period as an input to their MLR. We are able to closely reproduce their estimate of AAWR if we replace our formulation of ΔT_{HUMAN} with a linear function spanning 1860 to 2010 (Figure 4.9c,d). However, it is well known that anthropogenic RF of climate, which drives ΔT_{HUMAN} , has varied in a non-linear manner that generally follows human population over the past century and a half. While ZT13 state that the use of an RCP-shaped anthropogenic forcing causes trends in their computed residual between ΔT_{OBS} and ΔT_{MDL} , we cannot reproduce this result. With our use of RCP-based anthropogenic forcing that underlies the CMIP5 GCMs, for the entire historical record (1850-present) and our method of calculating AAWR, we find that both

⁴⁰ FR11 determined that their equivalent of AAWR was 0.170 °C/decade using the CRU3 ΔT record. There are several differences between the FR11 regression model and the EM-GC aside from the fact they fit a trend to their residual to get their equivalent of AAWR instead of fitting a direct signal. When the EM-GC is used to simulate their analysis, (running 1979 to 2010 instead of 1850 to 2019, no ocean signals aside from ENSO, and a linear function for ΔT_{HUMAN}), the resulting AAWR is 0.166 °C/decade – sufficiently similar to trust that the EM-GC captures the essence of FR11’s analysis. When the AAWR is run as in Figure 4.3 except with CRU3 instead of CRU4, AAWR falls to 0.109 °C/decade while the AMOC signal contributes 0.058°C/decade (the 1979-2010 trends in PDO and IOD are an order of magnitude smaller than the AMOC trend and opposite in sign). Whether using CRU3 (0.109+0.058=0.167 °C/decade) or CRU4 (0.146+0.040=0.186 °C/decade), the difference between the EM-GC AAWR (~0.14 °C/decade) and FR11’s AAWR (0.170 °C/decade, or 0.166 °C/decade by our simulation) can be largely explained by the proper attribution of the signal from AMOC.

ΔT_{HUMAN} and AAWR are insensitive to the inclusion or exclusion of a proxy for AMOC in the regression analysis.

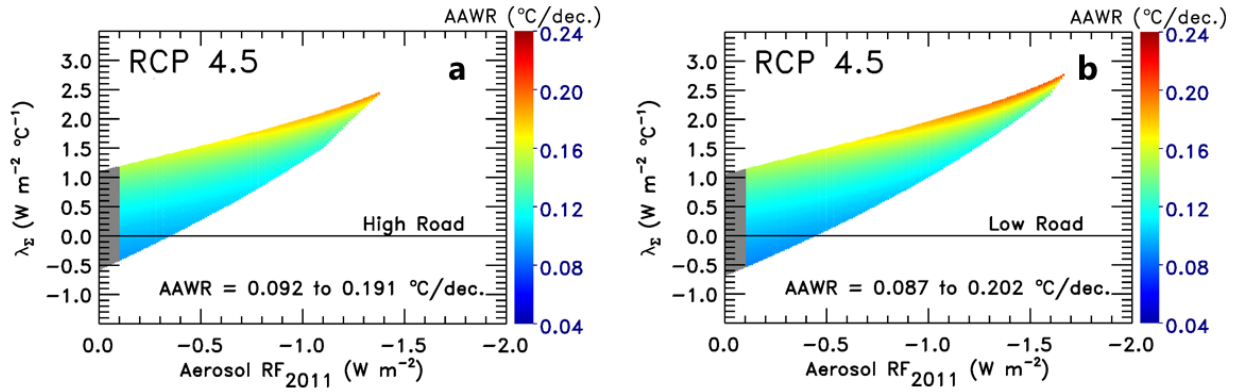
The uncertainty in AAWR is likely much higher than the small values suggested by FR11 and ZT13. As detailed in section §4.3.3, our estimate of AAWR based on the full uncertainty in AER RF and analysis of ΔT_{OBS} from multiple data centers spans the range 0.08 °C/decade to 0.20 °C/decade. FR11 state that the computation of AAWR upon use of ΔT_{OBS} from various data centers provides a range of 0.158 °C/decade to 0.187 °C/decade (these values are the 1σ lower and upper uncertainties of the standard error of their regression). The final estimate of AAWR given by ZT13 is 0.05 °C/decade to 0.09 °C/decade based solely on the mathematical uncertainty from calculating a linear fit to their ΔT_{HUMAN} . In our model framework, uncertainties in the strength and temporal shape of AER RF over the past four decades cause ΔT_{HUMAN} to vary much more than allowed by uncertainties from any linear fit to ΔT_{HUMAN} . The variation of AER RF used in our study results in a range for AAWR of 0.089 to 0.197 °C/decade for a single ensemble (Figure 4.10); this range extends slightly further to 0.084 to 0.202 °C/decade when considering all ensembles. Figure 4.10 and figure 4.12 show that EM-GC runs with small amounts of aerosol cooling tend to have both lower values of χ^2 (i.e good fits to the climate record span a wider range of values for λ_{Σ}) and lower values of AAWR than model runs constrained by larger aerosol cooling.

Individual runs demonstrating the effect AER RF has on ΔT_{HUMAN} and χ^2 are highlighted in figure 4.13. As AER RF cooling was largest in the 1970s and decreased in past decade [S Smith and Bond, 2014], larger aerosol cooling implies higher values of AAWR due to the nature of the definition of ΔT_{HUMAN} (equation 4.6a). This relationship explains why

figure 4.13a, with a relatively weak AER RF₂₀₁₁ value of -0.4 W/m^2 , has a relatively low AAWR value of $0.128 \text{ }^\circ\text{C/decade}$; conversely, the simulation in figure 4.13c with strong aerosol cooling (AER RF₂₀₁₁ of -1.4 W/m^2) results in a relatively high AAWR value of $0.169 \text{ }^\circ\text{C/decade}$. If the global warming due to black carbon aerosols and co-emitted species over the industrial era were as large as the best-estimate of *Bond et al.* [2013], this term would place the actual value of AER RF₂₀₁₁ close to -0.4 W/m^2 rather than the AR5 best estimate of -0.9 W/m^2 , rendering AAWR well below the best estimate of $0.170 \text{ }^\circ\text{C/decade}$ given by FR11. On the other hand, if the cooling of climate due to anthropogenic aerosols was as large as suggested by the recent study of *Shen et al.* [2020], this finding would likely place AER RF₂₀₁₁ close to -1.4 W/m^2 , leading to a value of AAWR similar to the $0.170 \text{ }^\circ\text{C/decade}$ estimate of FR11. FR11 do not address the quite large uncertainty in AAWR due to imprecise knowledge of the RF of climate by tropospheric aerosols.

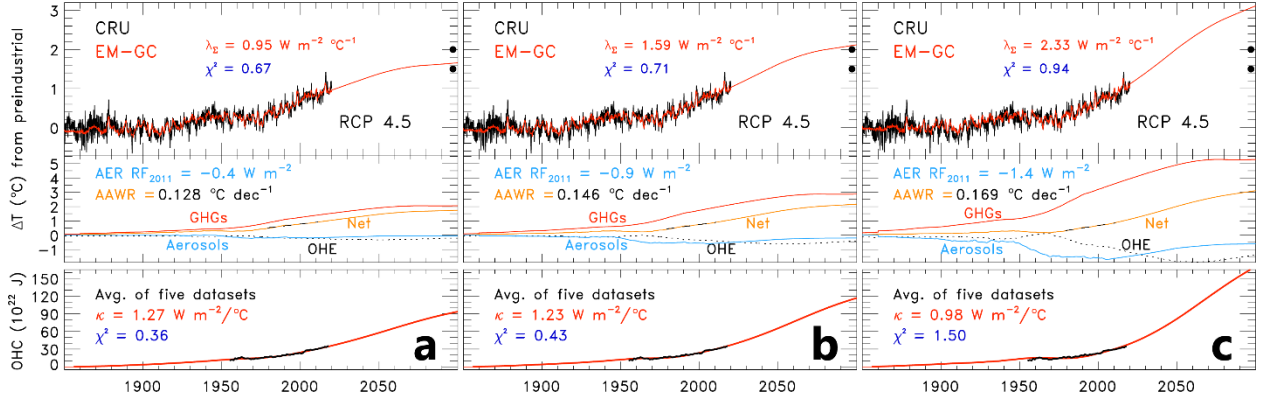
There remains an important distinction to be made when comparing values of AAWR based on specific estimates of AER RF₂₀₁₁. While figure 4.13b shows that using an AER RF time series with the AR5 best estimate for AER RF₂₀₁₁ (-0.9 W/m^2) gives an AAWR of $0.146 \text{ }^\circ\text{C/decade}$, whereas our weighted ensemble median value of AAWR is $0.135 \text{ }^\circ\text{C/decade}$. The lower value for the ensemble median follows from how our χ^2 strength-of-fit filters eliminate more runs with stronger aerosol cooling than runs with weaker aerosol cooling. Runs that use weaker aerosol cooling have lower resulting values for AAWR, so even though our ensemble weighting method theoretically assigns equal

Figure 4.12 – AAWR as a Function of AER RF₂₀₁₁, λ_{Σ} , and AER “Road”



Same as figure 4.10b except using the “low road” and “high road” AER RF constructions instead of the “middle road”.

Figure 4.13 – Observed and Modeled ΔT , 1850 to 2100, Varying AER ΔRF_{2011}



The model runs pictured are identical to the run in figure 4.3, except 4.13a and 4.13c use alternate middle road constructions of AER RF. We show a run with AER RF_{2011} of -1.4 W m^{-2} instead of -1.5 W m^{-2} because the simulation with -1.5 W m^{-2} exists at the far edge of acceptable χ^2 values, producing unrealistic individual anthropogenic components and OHC_{2100} . (AER RF_{2011} of -0.4 W m^{-2} to -1.5 W m^{-2} would match the upper and lower limits respectively of AR5’s likely range of anthropogenic, tropospheric forcing values in 2011 relative to preindustrial values). The upper rung of each abbreviated ladder plot here is the same format as those in figure 3a. The second rungs show the anthropogenic effect on the climate in gold as well as three of its four components: the temperature rise from GHG forcing (red), the temperature fall from aerosol cooling (light blue), and the temperature fall from OHE (dashed black). For clarity, the LUC component is not shown as its value is consistently near-zero compared to the other components.

weighting to runs with -0.1 W/m^2 and -1.9 W/m^2 , the relative lack of high values of AAWR corresponding to stronger aerosol cooling that pass this filter causes the weighted median AAWR to be slightly lower than $0.146 \text{ }^\circ\text{C/decade}$.

We state our estimate of AAWR for 1979 to 2010 as $0.14 \pm 0.06 \text{ }^\circ\text{C/decade}$, where the uncertainty covers the full range of model runs that yield a good fit to ΔT_{OBS} from CRU4. Our estimate of AAWR is larger than the trend in lower tropospheric temperature of $0.096 \pm 0.012 \text{ }^\circ\text{C/decade}$ reported by CM17. Their estimate is based upon analysis of satellite and radiosonde measurements of temperature throughout the global lower troposphere (GLT, the atmospheric layer from the surface to approximately 300 hPa) over the time period Jan. 1979 to June 2017. Similar to FR11, CM17 do not address the contribution of imprecise knowledge of AER RF to their estimate of AAWR, which leads to their small uncertainty for AAWR compared to our uncertainty. We reach similar results, though, when comparing the drop seen between the trend in observed ΔT and the trend after removing natural components of ΔT . They report a significant difference between the temperature trend for raw data ($0.155 \text{ }^\circ\text{C/decade}$) and the trend after the data have been adjusted to account for natural influences due to major volcanoes and ENSO ($0.095 \text{ }^\circ\text{C/decade}$). Our best estimate of AAWR for the Jan. 1979 to June 2017 time period, based on a linear fit to ΔT_{HUMAN} shown in figure 3a, remains $\sim 0.14 \text{ }^\circ\text{C/decade}$, compared to the trend in ΔT_{OBS} of $\sim 0.18 \text{ }^\circ\text{C/decade}$ for this time period. As such, we compute the drop from the trend in ΔT_{OBS} to trend in ΔT_{HUMAN} to be about two-thirds of the corresponding drop reported by CM17. Given the presence of two major volcanic eruptions in the first half of this time period and a major ENSO event in 2015-16, the drop in value from the observed trend to the anthropogenic trend should be expected. We

caution that precise determination of the effect of major volcanic eruptions for analysis of GLT data collected during the satellite era is affected by whether or not one includes the effect of AMV in the analysis (§4.5 of *Canty et al.* [2013]), which may explain the difference between our drop and the drop from CM17. Finally, and most importantly, CM17 emphasize (i.e. their figure 2) that CMIP5 GCM simulations of GLT result in considerably more rapid warming than is discerned from their adjusted observations. We reach a similar conclusion based on our analysis of ΔT , as described in the following section.

4.3.3 Comparison to AAWR from GCMs

In this section, we conduct a comparison of estimates of AAWR found using our EM-GC to AAWR inferred from CMIP5 GCMs. First, we further characterize uncertainties in AAWR.

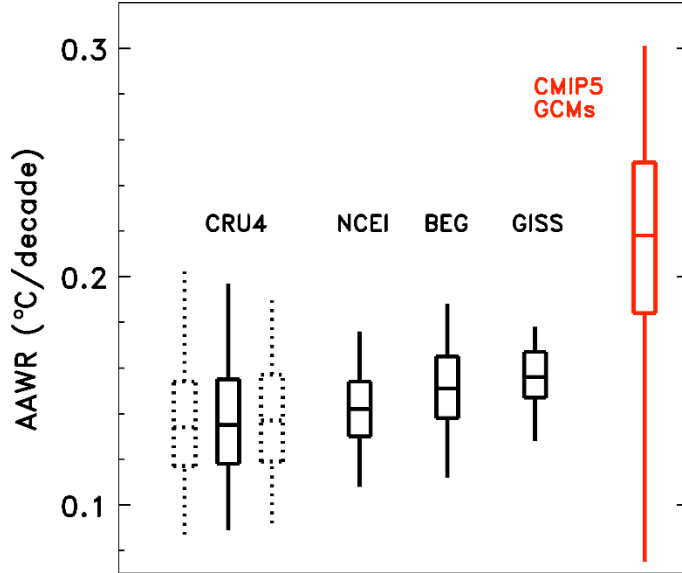
Figure 4.14 shows the sensitivity of AAWR to AER RF and the choice of data record for ΔT_{OBS} . The middle of box and whicker (BW) plot under the label CRU4 summarizes the weighted median (0.135 °C/decade), weighted interquartile range (IQR), and extrema of AAWR for the EM-GC determined PDF shown in figure 4.11a.

The EM-GC ensembles shown thus far relied only on time series of AER RF found using scaling factors for aerosol cooling (α_{COOL}) and heating (α_{HEAT}) along the “middle road” of figure 4.7 (section §4.2.1.2). The shape of the AER RF time series varies by choosing values for α_{COOL} and α_{HEAT} along either the “low” or “high” road of figure 4.7. The dashed BW plots surrounding the solid BW labeled CRU4 show the AAWR ensemble changes by a small amount, upon modification of the shape of the input AER RF time series. Scatter plots of AAWR versus AER RF₂₀₁₁ and λ_{Σ} as well as ladder

plots documenting the computation of ΔT_{HUMAN} and AAWR for the AR5 best estimate of AER RF₂₀₁₁, for these “high” and “low” road simulations, are shown in Figures 4.12 and 4.15. The value of AAWR exhibits only a small sensitivity to variation of the shape of AER RF. We include this comparison for the CRU4 record of ΔT_{OBS} because the various time series for AER RF that underlie the model inputs for these simulations cover a large range of possibilities, similar to that shown in figure 4 of Smith & Bond [2014].

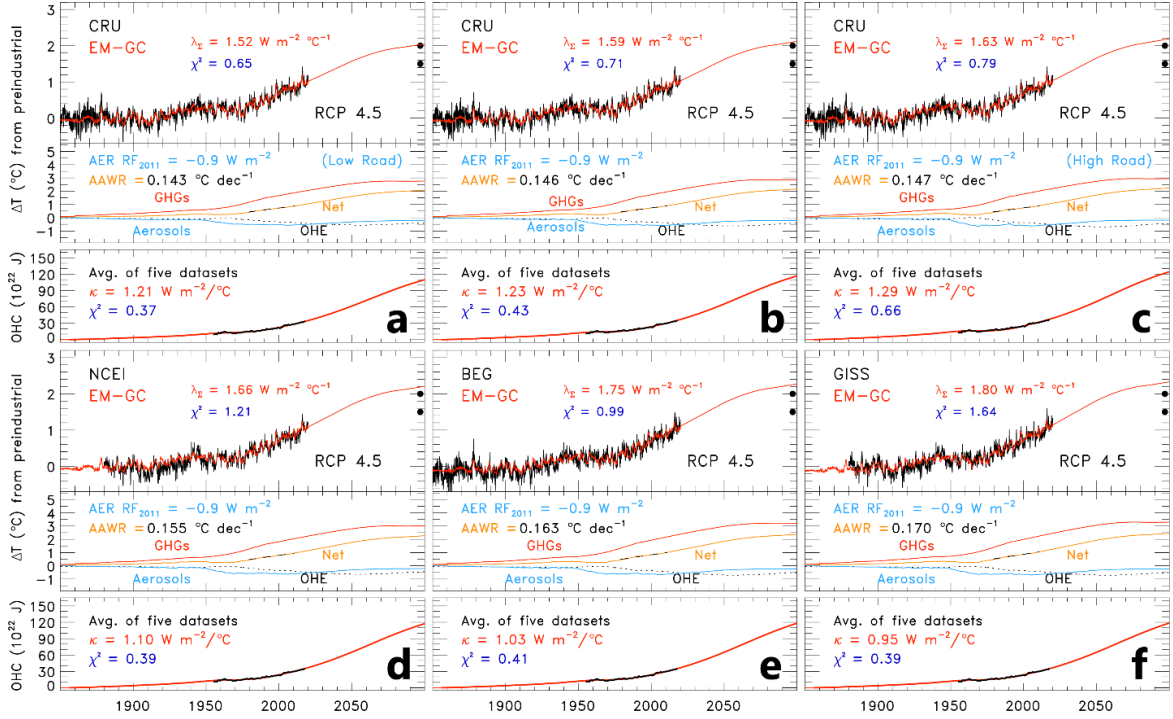
The choice of data center for the ΔT_{OBS} record contributes another small uncertainty to AAWR. Figure 4.14 shows BW plots for ΔT_{OBS} from other data centers. The median values of AAWR for AER RF computed with α_{COOL} and α_{HEAT} along the “middle road” of figure 4.7 are 0.142, 0.151, and 0.156 °C/decade for the use of temperature data from NCEI, BEG, and GISS, respectively. The choice of data center exerts a difference of 0.021 °C/decade between the largest and smallest median values, which is quite a bit larger than the value of 0.005 °C/decade difference reported by FR11 for selection of data between CRU3, NCDC (this dataset is now termed NCEI), and GISS. We find the largest value of AAWR upon use of ΔT_{OBS} from GISS and the smallest value upon use of data from CRU4. We have featured data from CRU4 throughout our paper, as well as in our earlier studies [*Canty et al.*, 2013; *Hope et al.*, 2017] because so many other published papers over the prior decade have used CRU temperature records as their baseline dataset. The 0.021 °C/decade difference in AAWR that arises between our use of ΔT from CRU4 compared to GISS is much smaller than the difference between any AAWR from the EM-GC and the Coupled Model Intercomparison Project (CMIP5) [*K Taylor et al.*, 2012] GCM multi-model mean value of AAWR.

Figure 4.14 – Comparison of Values of AAWR, EM-GC vs CMIP5 GCMs



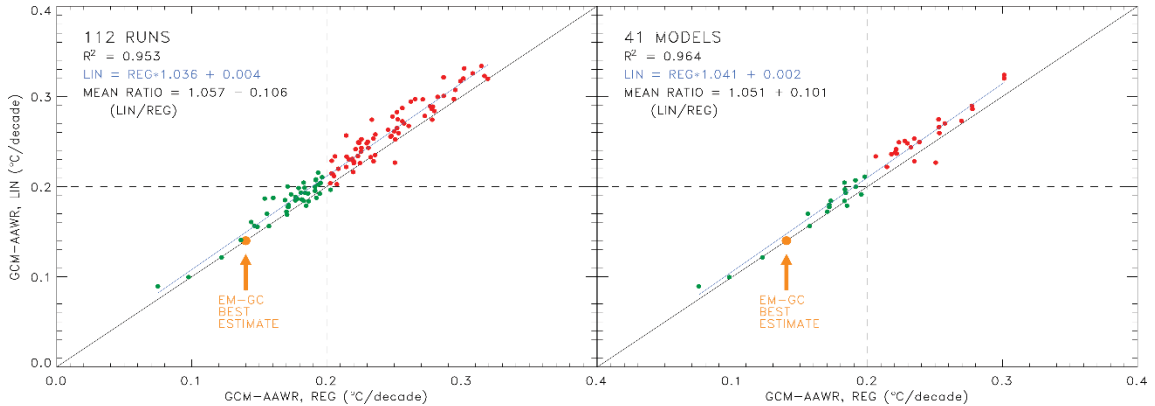
Each black box-and-whisker plot shows the weighted median, weighted IQR, and extrema from PDFs for AAWR found using the EM-GC, as shown in figure 4.11. The solid black box-and-whisker plots represent EM-GC ensembles fit to records of ΔT_{OBS} from various data centers (as indicated), found using RF from RCP 4.5 with the middle road construction of AER RF as shown in figure 4.7. The dashed box-and-whisker plots show AAWR for ΔT_{OBS} from CRU4, found using the low (left) and high (right) road constructions for AER RF (section §4.2.1.2); for simplicity, this comparison is not shown for the other temperature records. Among all of the EM-GC results, the maximum value of AAWR is 0.202 °C/decade and minimum is 0.084 °C/decade. The red box and whisker plot at the right shows AAWR found using the regression method described in section §4.2.4, using archived output of ΔT from 112 individual CMIP5 GCM runs, all constrained by RCP 4.5.

Figure 4.15 – Observed and Modeled ΔT , 1850 to 2100, Varying AER “Road” and ΔT_{OBS}



Similar to figure 4.13, except instead of varying the value of AER RF_{2011} , here we vary the “road” of the aerosol time series (panels a-c) or the ΔT_{OBS} time series (panels d-f). For reference, figure 4.15b is identical to figure 4.13b.

Figure 4.16 – AAWR from GCMs, Found Using Linear Fit and Regression

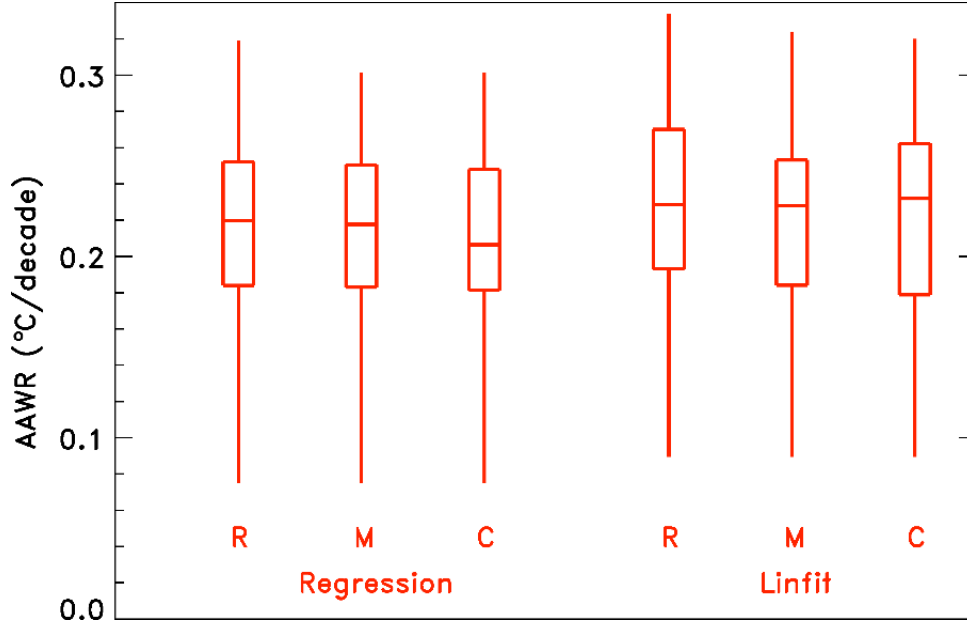


Scatter plots of GCM-AAWR found using a linear fit to ΔT from 1979 to 2010, neglecting years with strong volcanic influence (GCM-AAWR, LIN), versus GCM-AAWR found using regression versus ΔT_{HUMAN} (assumed to be linear over 1979 to 2010), solar irradiance, and stratospheric optical depth (proxy for volcanic influence) (GCM-AAWR, REG).

- a)** determinations of GCM-AAWR, LIN and GCM-AAWR, REG from 112 CMIP5 GCM runs
- b)** same as (a) but for the 41 GCMs; each data point represents the mean value of GCM-AAWR, LIN and GCM-AAWR, REG from the various runs from a specific GCM, if more than one run was archived.

Each panel shows the 1 to 1 line, the correlation coefficient, the best fit line and equation of this line (blue), and the mean and 2σ standard deviation of the quotient of GCM-AAWR, LIN divided GCM-AAWR, REG. Each panel also shows our best estimate of AAWR from the climate record (orange circle) and the upper limit of AAWR (dashed lines).

Figure 4.17 – Box-and-Whisker Plots of AAWR from GCMs



AAWR from GCMs found using regression (left) and linear fit (right), for GCM-AAWR grouped according to runs (R), mean per each GCM (“model”, M), and mean for each of the 21 modeling centers (C) that participated in the RCP 4.5 CMIP5 experiment. The middle line of each box-and-whisker plot shows median GCM-AAWR; the boxes show the 25th and 75th percentiles of the distribution of GCM-AAWR and the whiskers show the maximum and minimum GCM-AAWR.

The far-right red BW plot in figure 4.14 shows AAWR from the CMIP5 GCMs used by AR5. Archived output from the CMIP5 [K Taylor *et al.*, 2012] for 112 runs of 41 GCMs driven by RCP 4.5 [Thomson *et al.*, 2011] has been used to estimate AAWR from these GCM results (see §4.3.3.1 for details). We find good agreement between values of AAWR from these 112 runs found using two analysis methods, termed linear fit (LIN) and regression (REG) (figure 4.16, figure 4.17, and table 3.3). For the AAWR found using LIN, we perform a linear least squares regression to archived output of global mean two-meter air temperature (TAS) or years 1979 to 2010, ignoring years with obvious major volcanic eruptions (1982, 1983, 1991, and 1992). The rationale behind this method is natural variability in TAS due to internally model generated ENSO events will be randomly distributed in time; the influence of variations in the strength of AMOC on TAS tend to be small within these GCMs [Kavvada *et al.*, 2013]. For AAWR found using REG, we perform a multiple linear regression of TAS versus TSI and SAOD in a two-step process, as described in §4.3.3.1. Values of AAWR found using both methods are also given in table 3.3 for each GCM. Comparing AAWR from LIN versus REG shows the two methods result in values of AAWR with a high correlation coefficient ($r^2 \geq 0.95$) and a mean ratio close to 1, providing confidence that AAWR has been computed accurately from the CMIP5 GCMs.

All of the CMIP5 GCM output used here are global, two-meter air temperature (TAS) data. According to Cowtan *et al.* [2015], the blending of TAS (over land) with GCM output of sea surface temperature (SST, termed TOS in the CMIP5 archive) provides a more appropriate manner for sampling GCM output than use of global TAS, since datasets such as CRU4-based ΔT are a combination of near surface air temperature

over land and SST over water. *Cowtan et al.* [2015] state the use of blended temperature rather than air temperature accounts for 25% of the difference between the GCM-based and observed variations in global temperature over 2009–2013 and 38% of this difference over 1975–2014. Our own analysis using TAS-TOS blended temperature from CMIP5 GCMs results in a reduction of AAWR by roughly 2–5%, depending on which GCM is considered. This 2–5% reduction in GCM-AAWR translates to explaining 6–14% of the difference between median GCM-based and median EMGC-based values of AAWR, as well as 11–28% of the difference between GCM-based AAWR and the observed CRU4 slope of 0.18 °C/decade over the AAWR time period. While our use of blended temperature from a handful of CMIP5 GCMs rather than TAS does lead to a reduction in GCM-based values of AAWR, we find this effect is small (i.e. 2 to 5 %). A similar conclusion was reached by *Tokarska et al.* [2020]. Therefore, other than this paragraph, our paper focuses entirely on TAS from the GCMs because the use of blended temperature introduces a modest effect that does not alter any of our major conclusions, plus the information needed to produce blended temperature is no longer available on the CMIP5 archive for enough GCMs to complete an ensemble similar in size to our initial the GCM ensemble shown in figures 4.10 and 4.11.

The median value of the CMIP5 GCM-based AAWR found with the regression method 0.22 °C/decade. This value for AAWR is slightly more than 50% larger than our best empirical estimate of 0.14 °C/decade. The IQR for AAWR inferred from CMIP5 GCMs is 0.184 to 0.250 °C/decade, and the extrema are 0.075 and 0.301 °C/decade. More than two-thirds of the 112 archived CMIP5 GCM runs (Table 3.3) exhibit a value for AAWR larger than our upper limit of 0.202 °C/decade, and there is no overlap

between the CMIP5 IQR and any IQR from the EM-GC – the 25th percentile of the CMIP5 ensemble is 0.184 °C/decade, while the highest 75th percentile from an EM-GC ensemble is 0.167 °C/decade (figure 4.14, GISS). Also, only 3 of the 41 CMIP5 GCMs exhibit a value of AAWR less than 0.14 °C/decade: INM-CM4 [Volodin *et al.*, 2010], IPSL-CM5B-LR [Hourdin *et al.*, 2013], and MRI-CGCM3 [Yukimoto *et al.*, 2012] (table 3.3). We conclude therefore that the large majority of the CMIP5 GCMs exhibit anthropogenically induced warming that is considerably more rapid than what has actually occurred over the time period 1979 to 2010. This finding is not closely tied to the chosen time period for AAWR: whereas AAWR does exhibit some dependence on start and end year (table 4.4), the median value of CMIP5 GCM-based AAWR exceeds these empirical values by about the same amount for any similar time period. The tendency of most GCMs to overestimate empirical AAWR is evident in plots of time series of archived ΔT shown in AR5 (i.e. figure 11.25a) and persists whether the GCM output is examined in terms of individual runs, various GCMs, or specific modeling centers (figure 4.17, table 3.3). A similar tendency of GCM-based warming rates to lie considerably above empirical estimates has been noted by multiple recent, complementary studies [Christy and McNider, 2017; Chylek *et al.*, 2014; Fyfe *et al.*, 2013; Millar *et al.*, 2017; Tokarska *et al.*, 2020].

A GCM retrospective paper by Hausfather *et al.* [2020] shows that many past GCMs have predicted the observed rise in ΔT quite well. By comparing older GCM predictions of ΔT to the rise in ΔT_{OBS} since those predictions were made, Hausfather *et al.* [2020] show that the skill in predicting $\Delta T/\Delta t$ up to 2017 increased through the first three IPCC assessment reports. This ability to predictively match $\Delta T/\Delta t$ with the realized

ΔT_{OBS} is quantified with unitless skill values, which increase from 0.63 to 0.73 to 0.81 for the first three assessment reports. However, the predictions of ΔT_{OBS} for GCMs used in the fourth IPCC assessment report overestimated observed $\Delta T/\Delta t$ from 2007-2017, resulting in an overall skill value of 0.56 despite being a short-term prediction using the most advanced GCMs available at the time. While this excess warming in the GCMs that underlie the fourth report is argued to be due to overestimated scenario RF, excess warming continued into the AR5 GCMs with CMIP5, as documented here and in figure 11.25b of AR5. Early indications are that the tendency for GCMs to warm more quickly than the actual climate system extends into the CMIP6 GCMs being used as the backbone of the sixth assessment report [Belcher *et al.*, 2019; Tokarska *et al.*, 2020; Voosen, 2019]. While the increase in GCM complexity over the years certainly provides many benefits, it appears that such complexity has had the unintended consequence of providing a noticeable warming bias compared to older GCMs.

It is possible that some of the differences between AAWR found using our EM-GC and that inferred from CMIP5 GCMs are due to unaccounted internal variability in the observed temperature record. In particular, common explanations for the inability of models to match the lack of warming from 1998-2012 include shifts in the PDO and the strength of SAOD from minor volcanic eruptions [England *et al.*, 2014; Tokarska *et al.*, 2019], as well as variations in transport of heat to the deep ocean [Meehl *et al.*, 2011] that we have attempted to simulate using AMV as a proxy for the strength of AMOC. Some members of the EM-GC ensemble produce results consistent with a climatically important role for the PDO: as mentioned in sections §4.2.1.1 and §4.3.1, simulations with high values of AER RF₂₀₁₁ show relatively stronger influence of the PDO and

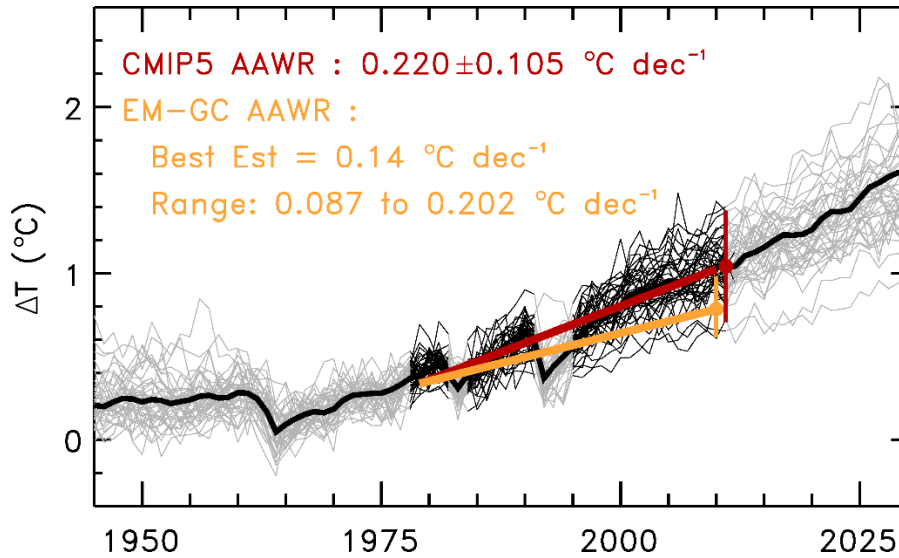
relatively weaker influence of AMOC compared to the results shown in figure 4.3. These ensemble members also result in an increase in the climatic importance of SAOD following major volcanic eruptions [*Canty et al.*, 2013]. However, consistent with the conclusion of *Chylek et al.* [2020], we find enhancements of SAOD due to recent minor eruptions to have a negligible effect on ΔT for all members of our EM-GC ensemble. The very low values of globally averaged SAOD following minor eruptions in the past decade will not noticeably affect ΔT , unless the climate response to SAOD is highly nonlinear.

4.3.3.1 Extracting AAWR from GCMs

AAWR from GCM output was computed using two methods that yield similar results. Monthly, global mean values of temperature were obtained for 112 simulations from 41 models and 21 modeling centers in the CMIP5 archive. These estimates are based on analysis of monthly mean global temperature from historical run files (which extend to year 2005) and the RCP 4.5 run files (which start in year 2005). We have used RCP 4.5 [*Thomson et al.*, 2011] to cover this latter time period due to its wide use in other studies and because, in *Hope et al.* [2017] the adherence to RCP 4.5 kept ΔT from rising past 2°C above preindustrial with high confidence, though in this study the probability has dropped to 50%. Similar analyses have been done for the other three RCP scenarios as well; the difference in AAWR from CGMs does not strongly depend on the RCP scenario used as the RCPs do not differ significantly between 2005 and 2010. The analysis uses all of the ensemble members that cover both the historical and RCP 4.5 time periods that were present on the CMIP5 archive as of 24 June 2014; some CMIP5 data has left the archive since then.

The first method we use to find GCM-AAWR, termed REG (regression), involves examination of de-seasonalized global, monthly mean values of ΔT from the various GCM runs. We determine regression coefficients for the contribution of total solar irradiance, stratospheric optical depth, and humans on ΔT by carrying out a regression using the proxies for TSI and SAOD given in *Canty et al.* [2013] and a linear function for ΔT_{HUMAN} , saving the coefficient for TSI. The regression analysis is repeated for only the 1979 to 2010 time period, using the saved value for the TSI coefficient and finding new values for the SAOD and human coefficients. A two-step process is needed to properly determine the TSI coefficient because the two major volcanic eruptions since 1979, El Chichón and Mount Pinatubo, occurred at similar phases of the ~ 11 year solar cycle. The second method of calculating GCM-AAWR, termed LIN (linear fit), involves examination of global, annual average values of ΔT from the various GCM runs, from 1979 to 2010 (figure 4.18). These GCM runs were designed to simulate the climatic effect of the eruptions of El Chichón and Mount Pinatubo on climate. This volcanic effect is obvious upon visual inspection of time series of annual average ΔT from the GCM archive. For LIN, we find the slope of ΔT versus time using a linear fit to the annual average GCM output of ΔT for years 1979 to 2010, excluding the years of strong volcanic influence (1982, 1983, 1991-94).

Figure 4.18 – AAWR from 41 GCMs (RCP 4.5) compared to empirical AAWR



Time series of the global, annual average ΔT relative to the preindustrial baseline, for the GCMs that have archived r*11p1 runs in the CMIP5 archive using RCP4.5. If a particular GCM submitted more than one run, ΔT has been averaged to obtain a single time series for that GCM. The 41 grey lines show ΔT from 1945 to 2030 from the 41 GCMs, the thick black line shows the multi-model mean of ΔT , and the 41 thin black lines show ΔT from 1979 to 2010 excluding years with strong volcanic influence (1982, 1983, and 1991 to 1994). The figure legend shows the mean and 2σ standard deviation of GCM-AAWR found using linear fits to the 41 time series of ΔT from 1979 to 2010 (excluding years with strong volcanic influence). The thick crimson line has a slope of $0.22^\circ\text{C}/\text{decade}$, the mean of GCM-AAWR, and starts at the multi model mean value of ΔT in 1979; the error bar at the end of the thick crimson line represents the 2σ standard deviation of GCM-AAWR. The crimson error bar is displaced by a year to not overlap with the respective orange symbols. The orange depicts the empirical best estimate and range of AAWR, overlapping the crimson line in 1979 and rising with a slope of $0.14^\circ\text{C}/\text{decade}$. The orange error bars represent the upper and lower limit for AAWR discussed throughout the main paper.

The values of GCM-AAWR from the 112 RCP 4.5 runs found using REG and LIN are presented in table 3.3. Scatter plots of LIN versus REG determinations of GCM-AAWR for each of these 112 runs are shown in figure 4.16a. The two determinations of GCM-AAWR exhibit a strong correlation ($r^2 = 0.95$) and AAWR found using REG is ~6% less than found using LIN. The box-and-whisker plot in figure 4.14 for GCM-AAWR is based solely on the REG determination since we view the REG method as being more thorough as well as lessening the appearance of the CMIP5 GCMs warming too much. This implies a CMIP5 median AAWR of 0.22 °C, with 61% of models showing an AAWR outside our empirical upper limit of 0.202 °C/decade. Had we instead chosen the values from the LIN method, the median value of GCM-AAWR would rise to 0.23 °C/decade and we would have concluded 73% of the determinations of GCM-AAWR from the 112 CMIP5 runs lie outside our empirical upper limit. Figure 4.17 show box-and-whisker plots of GCM-AAWR found using both REG and LIN, grouped according to all 112 runs, the 41 models, and the 21 modeling centers. These 6 box-and-whisker plots show that the tendency of the median value of GCM-AAWR to exceed our ~0.14 °C/decade best estimate by about 50% is a robust result. The tendency for between two-thirds and three-quarters of the values of GCM-AAWR to exceed our upper limit of 0.202 °C/decade is similarly robust. Both results persist regardless of how GCM-AAWR is calculated or how the model runs are grouped.

4.3.4 The effects of aerosols and climate feedback on future ΔT

We turn our attention to the effects of the radiative forcing due to AER RF and λ_{Σ} on future projections of ΔT . Figure 4.13, in addition to showing the effect on AAWR of varying the input model time series for AER RF, also shows how these three simulations

differ in ΔT out to year 2100 (ΔT_{2100}). The projection of ΔT is produced by applying the solutions for λ_{Σ} and κ that best fit the historical record to the prescribed GHG forcing pathways of RCP 4.5 out to the end of this century. Natural variations of all climatically important factors are assumed to be zero in the future to highlight only the rise in human driven rise in the global mean surface temperature anomaly (ΔT_{HUMAN}). We focus on projecting the underlying trend of future warming due to anthropogenic GHGs, as opposed to attempting to predict year-to-year variations in temperatures.

The full historical time series for ΔT can be fit reasonably well ($\chi^2 \leq 2$) for many combinations of time series of AER RF (indexed by their value in 2011) and value of λ_{Σ} . As a result, there exist a wide range of possible future temperature projections assuming the value for the sum of climate feedback mechanisms needed to simulate prior warming will persist into the future. This ability to fit the historical global temperature record with a wide range of possible climate feedback values is the main source of the resulting uncertainty in our estimate of ΔT_{2100} . If aerosol cooling to date has been low, then aerosols have counteracted only a small amount of the GHG forcing that warms the atmosphere, necessitating a low value of λ_{Σ} , resulting in modest future warming. By the same logic, a high amount of aerosol cooling to date leads to a large amount of future warming [Goodwin *et al.*, 2018; Kiehl, 2007; Knutti and Hegerl, 2008].

Figure 4.13a shows a value for ΔT_{2100} of just 1.7°C for weak aerosol cooling (AER RF₂₀₁₁ of -0.4 W/m²) offsetting the warming from RCP 4.5 GHGs. Conversely, if aerosol cooling has been large (AER RF₂₀₁₁ of -1.4 W/m²), global warming will be much more intense: Figure 4.13c shows a ΔT_{2100} slightly above 3.1°C. Warming can reach over 4°C by 2100, still with RCP 4.5 GHGs, for the upper range of aerosol cooling scenarios

stated in AR5 (i.e. AER RF₂₀₁₁ from -1.6 W/m^2 to -1.9 W/m^2). However, under these strong aerosol cooling scenarios, it is not possible in our modeling framework to obtain values of χ^2 below 2 for the full historical ΔT fit and particularly for the OHC fit, which is why the largest aerosol cooling case shown in figure 4.13c is for AER RF₂₀₁₁ of -1.4 W/m^2 . The individual simulations pictured in figure 4.13 were chosen by finding the value of λ_Σ that minimizes χ^2 over the entire CRU4 record of ΔT (equation 4.1c), for each value of AER RF₂₀₁₁. This difference in ΔT_{2100} results from the fact that aerosol concentrations, and thus aerosol forcings, are set to return to near-zero values in the future as an effect of air quality regulations that arise from human health concerns [Smith and Bond, 2014]. As such, all simulations approach the same net human RF by 2100 but have different values of λ_Σ based on the amount of GHG RF that was offset by anthropogenic aerosols over the historical record.

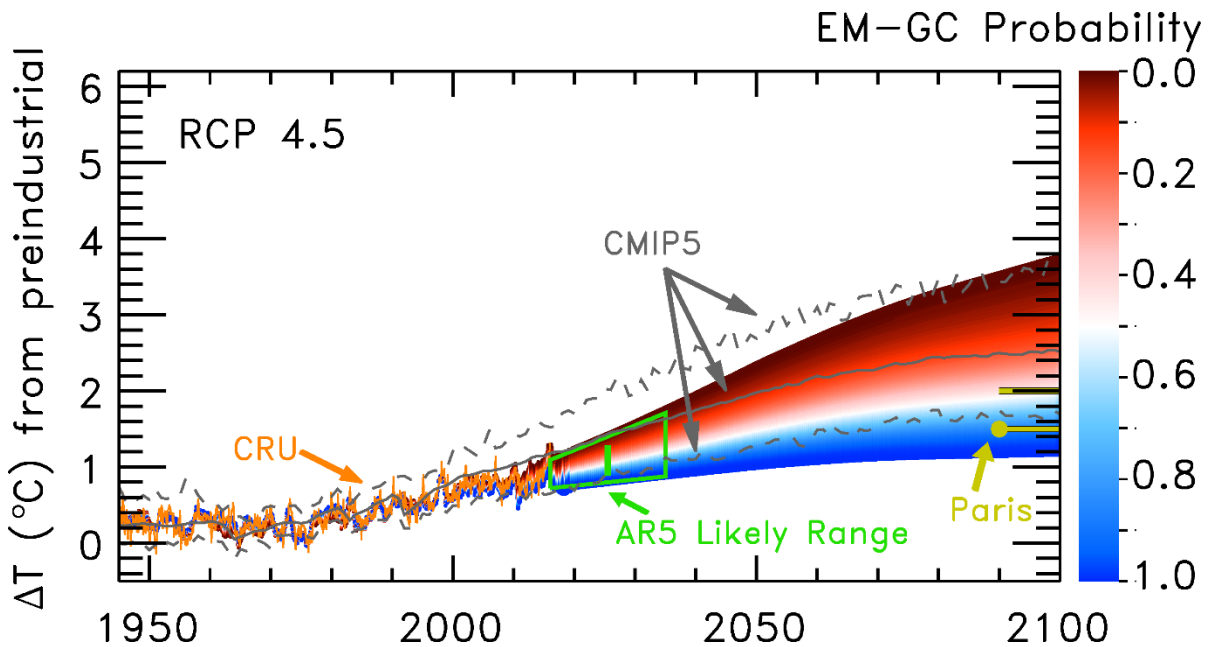
Figure 4.10c shows ΔT_{2100} as a function of λ_Σ and AER RF₂₀₁₁ for RCP 4.5. Figure 4.11b shows a PDF of ΔT_{2100} for the ensemble members shown in figure 4.10c, computed using the weighting method based on the AR5 likelihoods for the values of AER RF₂₀₁₁ (figure 4.10a) described in section §4.3.1. Figures 4.10c and 4.11b illustrate a vitally important aspect of the climate system: the present uncertainty in the amount of GHG warming offset by aerosols causes a large spread in future warming, for a single future GHG abundance scenario, in this case RCP 4.5. If warming due to black carbon aerosols and co-emitted species were as large as the best-estimate of Bond *et al.* [2013], this term would place the actual value of AER RF₂₀₁₁ close to -0.4 W/m^2 , resulting in values of ΔT_{2100} in our model framework close to the low end (i.e. $1.20 \text{ }^\circ\text{C}$) of this forecast. On the other hand, if the climate cooling due to aerosols was as large as

suggested by *Shen et al.* [2020], values of ΔT_{2100} would lie towards the high close on end (i.e. 3.74 °C) of our forecast. A reduction in the uncertainty of the amount of warming offset by tropospheric aerosols for the contemporary atmosphere, which requires obtaining consensus on the role of black carbon [*Bond et al.*, 2013] as well as various aerosol indirect effects [*Chen and Penner*, 2005; *Gryspeerd et al.*, 2020], would enable more accurate forecasts of end of century warming.

A PDF of ΔT_{2100} for the output from 41 GCMs is also shown in figure 4.11b. For GCMs that have submitted multiple runs using RCP 4.5 to the CMIP5 archive, ΔT in year 2100 is first averaged for these runs, such that the PDF consists of the distribution of ΔT_{2100} for the 41 GCMs shown in table 3.3. The median warming of T_{2100} from our EM-GC simulations for RCP 4.5 is 2.00 °C, with lower and upper limits of 1.20 and 3.74 °C, respectively. The median ΔT_{2100} from the 41 GCMs is 2.52 °C, with lower and upper limits of 1.69 and 3.64 °C. Only 7 of the 41 CMIP5 GCMs exhibit a value for ΔT_{2100} less than the EM-GC median of 2 °C.

Figure 4.19 shows a probabilistic forecast of the future rise in ΔT from our EM-GC for RCP 4.5. Colors denote the probability of reaching at least that temperature by each year. The figure also contains the CMIP5 GCM ensemble minimum, multi-model mean, and maximum values of ΔT (gray lines) as well as the likely range of warming (green trapezoid) from figure 11.25b of AR5 [*Kirtman et al.*, 2013]. Temperature projections from our EM-GC agree well with the expert judgement of the near-future rise ΔT provided by Chapter 11 of AR5. The white color in figure 4.19 for EM-GC probability is the median warming projection in our model framework. Similar to the comparison shown in §4.3.3 for AAWR, projections of warming from the CMIP5 GCMs

Figure 4.19 – Global Warming Projections for RCP 4.5, 1950 to 2100



The EM-GC ensemble is shown with red-to-blue envelope and the CMIP5 GCM ensemble is shown with grey lines. Color at any given point within the EM-GC envelope represents the chance of ΔT reaching at least that temperature at that time. The three CMIP5 lines represent the minimum, multi-model mean, and maximum of ΔT from the GCMs that submitted projections of each RCP scenario respectively to the CMIP5 archive (grey lines). One set of observed temperatures to date (CRU4, orange line), the expert judgement from Figure 11.25 of AR5 (green trapezoid and vertical bar), and the targets of the Paris Agreement (gold spikes at right) are also shown for comparison.

tend, on average, to be larger than the warming projection from our empirical model of global climate. Notably from a policy perspective, our most likely outcome for ΔT lies slightly above the CMIP5 GCM multi-model minimum, with both the EM-GC-based median and the GCM-based minimum lying below the Paris Climate upper limit of 2 °C. As explored further in §4.3.7, carbon emissions consistent with the CO₂ trajectory of RCP 4.5 provide a more likely chance of limiting global warming to either the Paris goal (1.5 °C) or upper limit (2 °C) than is projected by CMIP5 GCMs constrained by RCP 4.5. Most notably, observed ΔT over the years ~2005 to 2020 lies between the CMIP5 GCM multi-model minimum and mean, which of course was the driving factor behind the formulation of the green trapezoid in figure 4.19 by the authors of Chapter 11 of AR5 [Kirtman *et al.*, 2013].

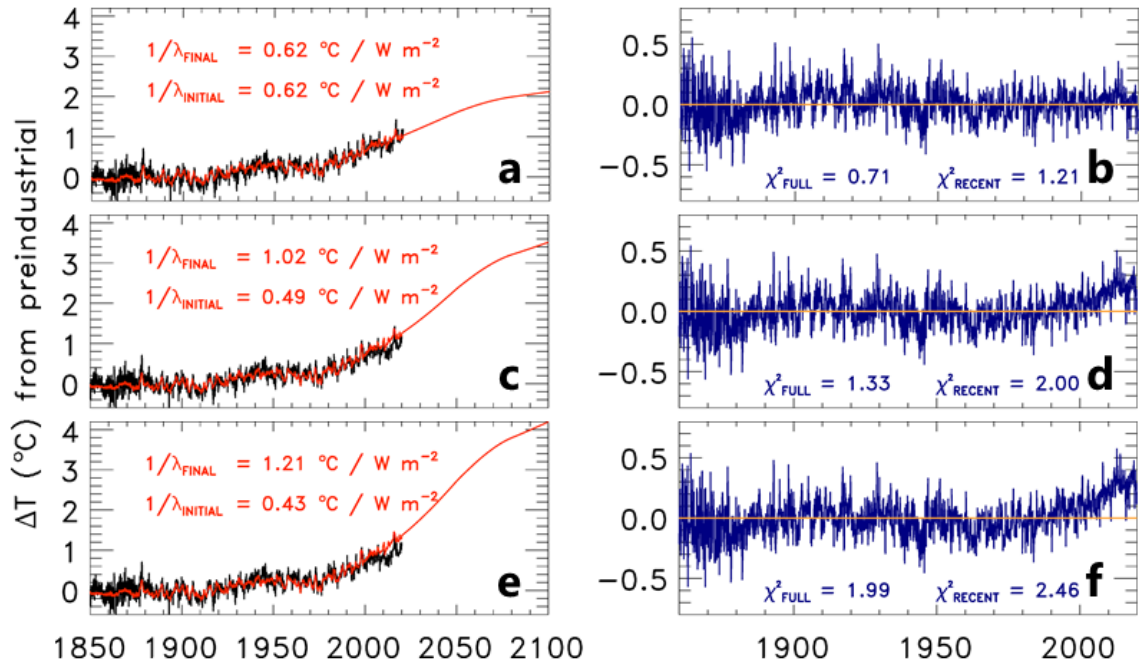
The values of λ_{Σ} for the EM-GC-based projections shown above suggest less future warming than similar values provided by most CMIP5 GCMs. Table 9.5 of AR5 [Flato *et al.*, 2013] suggests model mean values for λ_{Σ} of 1.6, 2.04, or 2.15 W/m²/°C depending on which quantities are used to infer λ_{Σ} ; specifically, the first value is the sum of the average value of the four individual feedbacks, the second value is based upon their estimate of ECS and the RF associated with 2×CO₂, and the third value is based upon the values for the climate sensitivity parameter and climate feedback parameter given. Table 1 of Sherwood *et al.* [2020] gives a value for λ_{Σ} of 1.9 W/m²/°C, with a 66% confidence range of 1.46 to 2.34 W/m²/°C. Although tabulations of λ_{Σ} from CMIP5 models exist [Andrews *et al.*, 2012; Forster *et al.*, 2013; Vial *et al.*, 2013], particularly Table 9.5 of AR5 [Flato *et al.*, 2013] and Table 1 and Figure 4 of Sherwood *et al.* [2020], comparison to our values is complicated by the sensitivity of λ_{Σ} to AER RF for good fits

to the climate record (figure 4.10). In general, our λ_{Σ} (and thus λ) suggest less future warming than those from the CMIP5 GCMs.

An important assumption for our quantification of both AAWR and ΔT_{2100} using the EM-GC is that λ_{Σ} (and thus λ) has remained constant over time. However, we can also simulate time dependent climate feedback to address the possibility that λ_{Σ} may change over time (section 12.5.3 of AR5 and references therein; also *Rose et al.* [2014], *Shindell* [2014], and *Marvel et al.* [2018]). Recall that $1/\lambda = (1 + \gamma)/\lambda_p = 1/(\lambda_p - \lambda_{\Sigma})$ from equations 4.5 and 4.6; we have used λ_{Σ} up to this point as simulations with higher values of λ_{Σ} have higher future ΔT . For this reason, we prefer to examine a time dependent λ in terms of its inverse, $1/\lambda$, also known as the climate sensitivity parameter, because this quantity also has a positive correlation with ΔT . Figure 4.20 and table 4.5 summarize how ΔT_{2100} changes if we allow $1/\lambda$ to vary over time while still keeping the strength of fit between ΔT_{OBS} and ΔT_{MDL} at acceptable levels ($\chi^2 \leq 2$) for either the full historical time period or the most recent 80 years.

For four different cases of aerosol forcing, we find that allowing $1/\lambda$ to scale with anthropogenic forcing while still keeping $\chi^2 \leq 2$ over the full historical time period results in roughly doubling of ΔT_{2100} compared to the constant feedback case (table 4.5). This scenario with time-varying feedback, which results in our maximum warming, implies an increase in $1/\lambda$ by nearly a factor of three over two and a half centuries (figure 4.20e). This rise in $1/\lambda$ is much more rapid than expected. Even one of the most extreme estimates from recent work [*Marvel et al.*, 2018] suggests an increase in median estimated equilibrium climate sensitivity (ECS) from 1.8°C (for simulations constrained to match data acquired over 1979-2005) to a long-term (end of century) value of 3.1°C,

Figure 4.20 – EM-GC Temperature Comparisons for Time-Varying $1/\lambda$



Historical and modeled temperatures (left column) and the residuals between them (right column) for different treatments of the climate feedback parameter. Each row corresponds to the respective row of table 4.5. All results shown here are for runs with the aerosol scenario of $\text{AER RF}_{2011} = -0.9 \text{ W/m}^2$ as used through much of this paper.

Table 4.5 – ΔT_{2100} and $1/\lambda_{\text{FINAL}}$ as $1/\lambda$ Varies

λ treatment	AER RF ₂₀₁₁ value			
	-0.1 W/m ²	-0.4 W/m ²	-0.9 W/m ²	-1.5 W/m ²
Constant $1/\lambda$	1.6°C	1.7°C	2.1°C	3.5°C
	0.38°C/W/m ²	0.44°C/W/m ²	0.62°C/W/m ²	1.43°C/W/m ²
Varying $1/\lambda$, recent fit	2.2°C	2.6°C	3.5°C	7.6°C
	0.54°C/W/m ²	0.65°C/W/m ²	1.02°C/W/m ²	3.14°C/W/m ²
Varying $1/\lambda$, full record fit	2.6°C	3.0°C	4.2°C	8.4°C
	0.62°C/W/m ²	0.76°C/W/m ²	1.21°C/W/m ²	3.46°C/W/m ²

End-of-century temperatures and the values of $1/\lambda_{\text{FINAL}}$ for different treatments of the climate feedback parameter across four aerosol forcing scenarios (as built from [Lamarque *et al.*, 2011] with “middle road” construction). The first row corresponds to runs as used throughout the main body of the paper, with $1/\lambda$ remaining constant over time (i.e. $1/\lambda = 1/\lambda_{\text{INITIAL}} = 1/\lambda_{\text{FINAL}}$). The next two rows of the table take the runs from the first row and, keeping everything else identical, modify the ΔT_{HUMAN} component of the original EM-GC simulations to represent $1/\lambda$ that varies. The climate feedback in these cases takes the same shape as total RCP 4.5 RF, scaled and shifted so that the new $1/\lambda$ time series maintains an average value over the time of the ΔT_{OBS} record identical to the original unaltered λ value. This produces a “tilt” in the residual between modeled and observed temperatures, causing χ^2 to increase as the scaling versus RCP 4.5 increases. The third row is the result from the maximum scaling that can be applied to climate feedback over time while keeping $\chi^2 \leq 2$, as defined over the entire ΔT_{OBS} record. This scenario produces a noticeable gap between observed and modeled temperatures over the most recent decades, so the second row is the result of the maximum scaling that can be applied to climate feedback over time while keeping $\chi^2 \leq 2$ except just over the recent decades.

which corresponds to a 72% increase. This rise in ECS postulated by Marvel et al. (2018) is predicated on the assumption that current atmospheric and oceanic conditions are truly exceptional. The validity of preliminary results for a handful of CMIP6 models suggesting even higher ECS [Belcher et al., 2019; Gettelman et al., 2019; Zelinka et al., 2020] has been questioned by numerous recent papers based upon analysis of paleoclimate data as well as climatic conditions over the past several decades [Forster et al., 2020; Nijssen et al., 2020; Sherwood et al., 2020; Voosen, 2019; Zhu et al., 2020]. Such scenarios that greatly increase $1/\lambda$ by the end of the century also produces a time dependent drift in the residual between observed and modeled over the historical record in our model framework (figure 4.20f). Coincidentally, the comparison between modeled and measured ΔT in figure 4.20f looks similar to the comparison of the CMIP5 GCM multi-model mean and ΔT_{OBS} shown in figure 4.2. This time dependent drift between ΔT_{OBS} and our modeled ΔT , combined with the large temporal change in λ that underlies this simulation, suggests this might be an unreasonable scenario for use in CO₂ emission mitigation strategies.

We also calculate a medium-varying feedback case by considering a $\chi^2 \leq 2$ strength-of-fit restriction that focuses only on the most recent 80 years of the ΔT_{OBS} record (figure 4.20c,d) instead of $\chi^2 \leq 2$ over the full ΔT_{OBS} time series. This scenario results in a simulation of ΔT that appears more reasonable upon inspection of the residuals and the smaller rise in $1/\lambda$. However, depending on the strength of AER RF, the increase in $1/\lambda$ can still range from roughly 50% to more than a factor of two (table 4.5). Changes in $1/\lambda$ of this magnitude over two and a half centuries are faster than the millennia-order timescale changes usually referenced (e.g. section 12.5.3 of AR5 and

references therein) when discussing noticeable changes in λ , ECS, and other related quantities such as transient climate sensitivity (TCS). While a factor of two or more rise in $1/\lambda$ does not match literature, an increase of roughly 50% falls in line with a 50% increase in TCS [Shindell, 2014] and neatly between the 28% increase (1.8 °C to 2.3 °C) and the 72% increase (1.8 °C to 3.1 °C) [Marvel *et al.*, 2018] seen in other re-analyses of historical forcing results from GCMs. As there is no strong evidence from the climate record for a noticeable rise in $1/\lambda$ on the multidecadal time scale consistent with the simulations shown in figure 4.20, we assert that the assumption of constant feedback within the EM-GC framework seems to be a reasonable assumption for the next few decades. There also certainly exists the possibility that by end of century, the rise in ΔT could be a few tenths of a degree warmer than our current best estimates assuming constant λ_{Σ} due to a slow rise in $1/\lambda$.

We also assume for our computation of Q_{OCEAN} that κ is constant over time. This assumption follows from the fact that, like λ , the rate of change of κ is most likely small enough to not have a significant effect on the time scale of our calculations of ΔT [Raper *et al.*, 2002]. Our application of κ requires a monotonic increase in the magnitude of this term, we solve for Q_{OCEAN} based on $\Delta T_{\text{ATM,HUMAN}}$ instead of total ΔT_{MDL} because the latter displays strong natural variability and thus is not monotonically increasing. The anthropogenically-forced temperature itself is not strictly monotonic either, especially for AER RF time series corresponding to more negative values of AER RF₂₀₁₁, but the short, small, instances of cooling in those scenarios are relatively insignificant. Also, those cooling instances are pre-1950, and the OHC record we fit does not extend earlier than 1950. As such, the few instances when ΔT_{HUMAN} includes short, small cooling periods

should not affect the overall approximation of κ as a constant. As with λ and fitting ΔT_{OBS} , a constant value of κ results in modeled OHC that fits the observed OHC quite well (figure 4.3b and figure 4.13).

Model treatment of aerosols and clouds are two possible explanations for why λ from the EM-GC differs from CMIP5 models. About half of the CMIP5 GCMs do not include aerosol indirect effects [*Schmidt et al.*, 2014]. A lack of the indirect effect in our EM-GC would result in cooler projections of future ΔT , as less total AER RF over the historical record would favor lower values of λ_{Σ} and thus lower ΔT_{2100} . Such a relationship between ΔT_{2100} and the presence of the indirect effect does seem to appear in CMIP5 results as well: models without the indirect aerosol effect consistently warm less from 2014 to 2100 than models that do include it [*Chylek et al.*, 2016]. Considering that the CMIP5 GCMs tend to warm more than the EM-GC in terms of both AAWR (§4.3.3) and ΔT_{2100} (§4.3.5), a lack of the indirect effect in some GCMs does not explain the excess warming in GCMs, meaning it seems more likely that the difference between the EM-GC and CMIP5 GCMs lies in cloud feedback. (This should not eliminate considerations of aerosols and their complex interactions, however, especially given that aerosol indirect effects and cloud feedback processes are related.) It is widely known that uncertainty in the cloud feedback is much larger than that of other major feedbacks and this uncertainty is a main driver for the spread between CMIP5 models [*Dolinar et al.*, 2015; *Stocker et al.*, 2013; *C Zhou et al.*, 2015]. While the fourth IPCC report [*Solomon*, 2007] suggested a cloud response spread centered around zero feedback within the CMIP3 GCMs, AR5 suggests a largely positive cloud feedback, in line with some recent observations [*Dolinar et al.*, 2015; *C Zhou et al.*, 2015]. However, there is considerable

spread in the determination of cloud feedback from observations, including the possibility of a neutral or even negative feedback [Ceppi *et al.*, 2017; Vial *et al.*, 2013; Zelinka *et al.*, 2016]. While some recent studies suggest that cloud feedback and overall ECS interpreted from observation are higher than those from modeling studies based solely on observations since 2000 [Dessler, 2013; Sherwood *et al.*, 2020], other observational studies offer lower ECS values than those found in modeling studies [Lewis and Curry, 2018; T Masters, 2014; Otto *et al.*, 2013; Schwartz, 2012]. If the actual cloud feedback is less positive than the models currently suggest, that could also be a factor in the high bias of GCMs for AAWR, ECS, and ΔT_{2100} [Hope *et al.*, 2017; Tokarska *et al.*, 2020; C J Weaver *et al.*, 2020; Zelinka *et al.*, 2020].

4.3.5 Other RCPs and comparisons to projections from GCMs

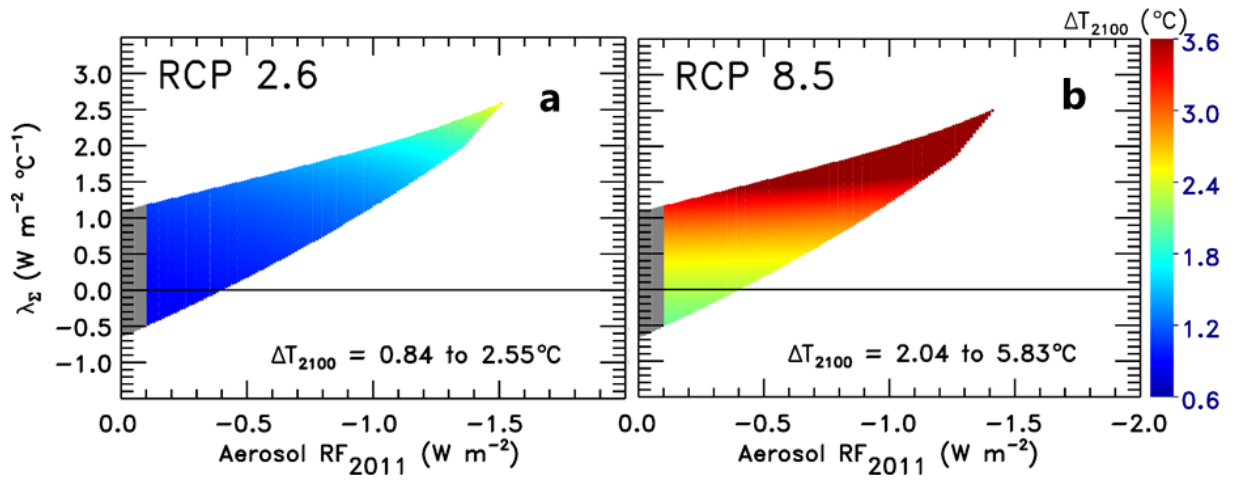
One advantage of simple models such as the EM-GC is the ability to perform sensitivity testing by completing many more runs of the model with less computing power. For example, each ensemble represented in figure 4.14, originally consisting of 160,000 simulations, takes roughly two hours to complete. All those ensembles focus on ΔT_{HUMAN} driven by RF from GHG abundances from RCP 4.5, and a full treatment of the effects of uncertainty in RF due to aerosols. Figures 4.21a and 4.22a, driven by RCP 2.6, and figures 4.21b and 4.22b, driven by RCP 8.5, show the results of EM-GC ensembles constrained by low and high ends of RF tested in CMIP5, respectively. The panels of figure 21 and figure 22 are the same as figure 4.10b and figure 4.11b, respectively, except for the different RCP scenario driving the ensembles. As the RCP scenarios are identical up to 2005 and do not differ greatly until after 2020, the shape of the model output shown in figure 4.10b and figure 4.21 are nearly identical, because the three χ^2 calculations (fits

to total ΔT , recent ΔT , and OHC) used to select good fits to the climate record consider only historical data. The difference in end-of-century RF drives the differences in ΔT_{2100} , shown both in the colors of the model output and the positions of the PDFs in figure 4.11b, figure 4.22a, and figure 4.22b. The probabilities of the rise in ΔT_{2100} staying beneath 2°C are 92%, 50%, and 0% for RCP 2.6, 4.5, and 8.5 respectively; probabilities for ΔT_{2100} remaining below 1.5°C fall to 67%, 10%, and 0%. For RCP 6.0, (not pictured,) the probability of staying beneath 2°C is 20%, which falls to 0.1% for 1.5°C .

Figure 4.22c and 4.22d also compare ΔT_{2100} from the EM-GC to temperatures at the end of the century presented in *Sherwood et al.* [2020]. The probabilistic estimate of end of century warming given in *Sherwood et al.* [2020] is based upon their expert evaluation of climate sensitivity combined with the assumption of a linear relation between the transient climate response and radiative forcing. They estimate that by end of century warming will be less than 2°C relative to pre-industrial are 83%, 17%, and 0% for RCP 2.6, 4.5, and 8.5, respectively. The probabilistic estimate of the upper end of warming given by *Sherwood et al.* [2020] is considerably less than indicated by the CMIP5 GCMs (green versus red lines in figure 4.22). They also compute a lower probability for the low end of the distribution of ΔT_{2100} than we find using our EM-GC, which is traceable to their judgement that the most likely value of total cloud feedback is positive [*Klein et al.*, 2017].

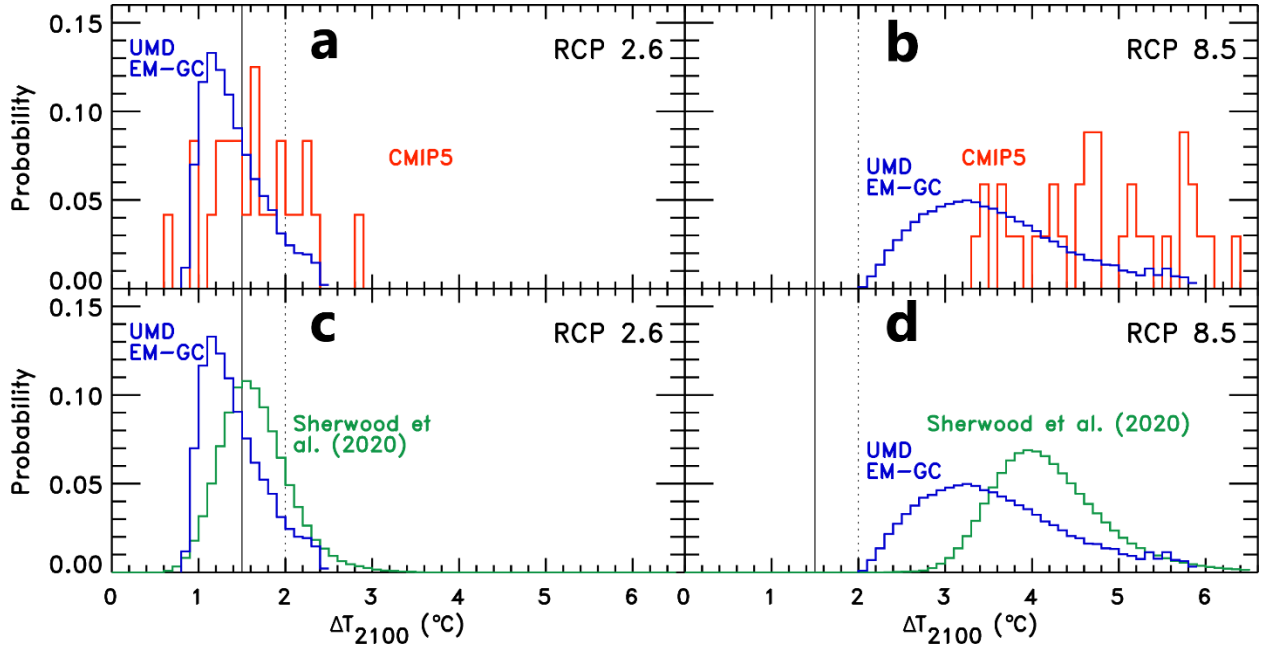
There are three clear takeaways from figures 4.11b and 4.22. First, earth's climate allows for a wide range of future temperatures, even when a model such as our EM-GC is sufficiently trained with historical data due to uncertainty in quantities such as AER RF_{2011} . Second, consistent with the expert assessment of temperature projections from

Figure 4.21 – ΔT_{2100} as a function of AER RF₂₀₁₁ and λ_{Σ} , RCP 2.6 and 8.5



Same as figure 4.10c except for ensembles using RCP 2.6 and RCP 8.5 anthropogenic forcing instead of RCP 4.5.

Figure 4.22 – Probability Density Functions of ΔT_{2100} , RCP 2.6 and 8.5



Panels a and b are the same as figure 4.11b except for ensembles using RCP 2.6 and RCP 8.5 anthropogenic forcing instead of RCP 4.5. Panels c and d then exchange CMIP5 data for data taken from figure 23 of *Sherwood et al.* [2020], binned to match the structure presented in the previous PDFs of this study.

CMIP5 GCMs given in Chapter 11 of AR5 [Kirtman *et al.*, 2013], our EM-GC projects smaller future increases in ΔT than provided by most of the CMIP5 GCMs. Third, while temperature projections from our EM-GC agree with CMIP5 GCM results in that society must avoid a GHG pathway consistent with RCP 8.5 to achieve the goals of the Paris Climate Agreement, our model simulations show that RCP 4.5 and particularly RCP 2.6 are GHG pathways more likely to achieve limited warming than indicated by GCM results within the CMIP5 archive. Our model projections suggest that adhering to the RCP 4.5 pathway is as likely as not (=50%) to give Earth a future that limits global warming to 2°C above preindustrial; placing GHGs on the RCP 2.6 pathway is highly likely (>90%) to limit global warming to 2°C and likely (>66.7%) to stay beneath 1.5°C.

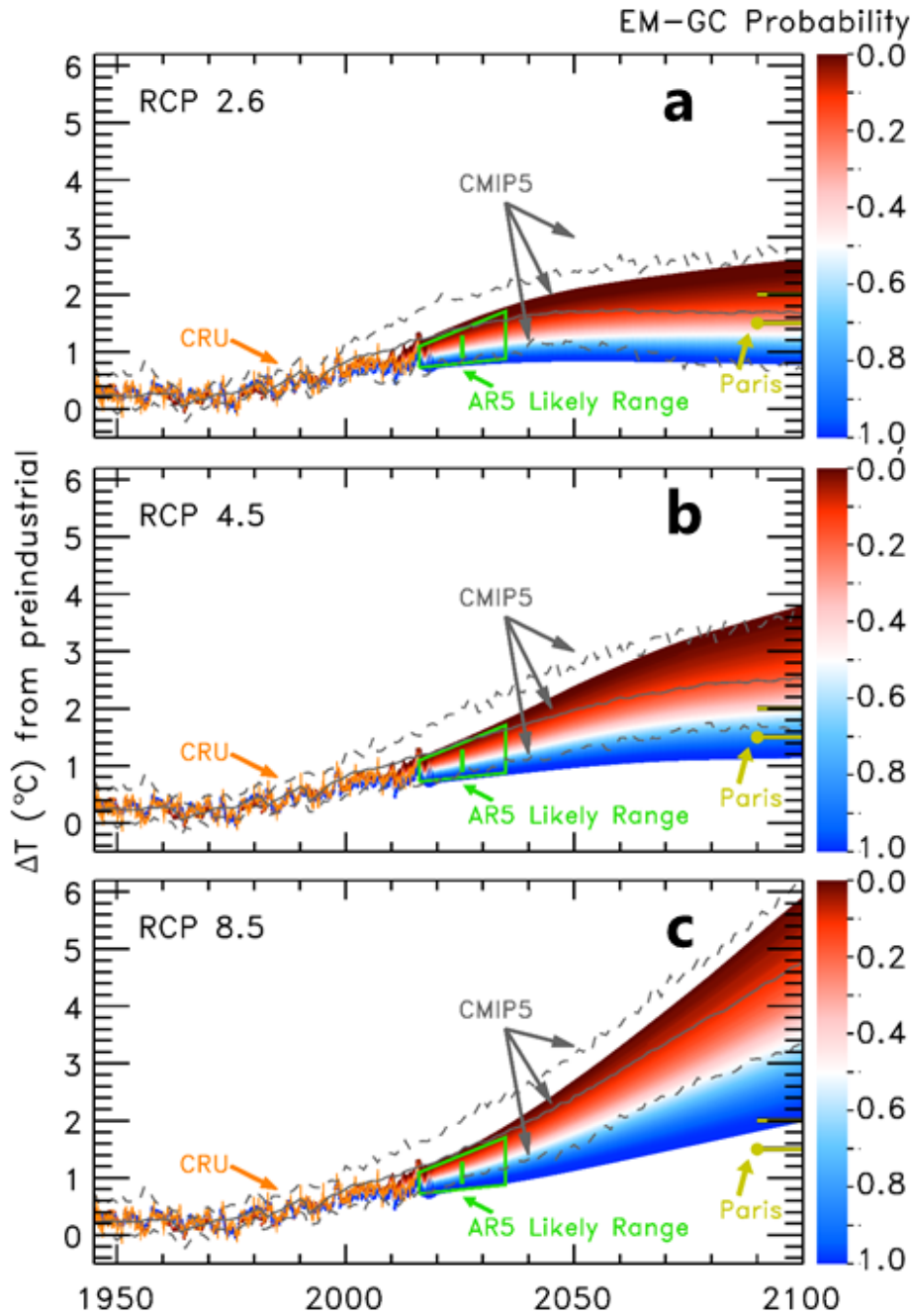
Our probabilistic temperature projections disagree somewhat with AR5.

According to CMIP5 GCM results as presented in AR5, RCP 2.6 is likely but not highly likely (that is, >66.7% but not >90%) to keep global temperatures beneath 2°C. AR5 also says RCP 4.5 is more likely than not (>50%) to *exceed* 2°C. The power of RCP 2.6 to keep us beneath 2°C of warming appeared in another recent study [Goodwin *et al.*, 2018] that determined staying beneath 2°C to be highly likely, much closer to our result than to those of CMIP5.

Figure 4.23 shows probabilistic projections of global warming for RCP 2.6, 4.5, and 8.5. This figure is the same as figure 4.19 (that showed results for RCP 4.5), using the same vertical axis for all three ensembles. This figure demonstrates a fourth key takeaway from our modeled projections of future temperature. Projections of global warming computed using our EM-GC agree well with the expert judgement of near-future ΔT from AR5 of Chapter 11 [Kirtman *et al.*, 2013], shown as a trapezoid on each

panel of figure 4.23. The colored envelope for each panel of figure 4.23 is based upon a representative sample of the runs from each respective RCP ensemble (figure 4.10b and figure 4.21) and displays the rise in ΔT out to the end of the century. At each time along this envelope, the color represents the probability within the ensemble of reaching at least that temperature. Whatever RCP scenario we examine, the EM-GC results match the near-future projections (trapezoid) based on the expert judgement of AR5's Chapter 11 authors. Our projections of warming using a physically based model tied to observations of ocean heat content, natural as well as anthropogenic drivers of variations in ΔT , and the consideration of uncertainty in AER RF are thus remarkably similar to the expert assessment of the CMIP5-GCM-based future rise in ΔT sketched out in figure 11.25b of AR5 [*Kirtman et al.*, 2013].

Figure 4.23 – Global Warming Projections for Various RCPs, 1950 to 2100



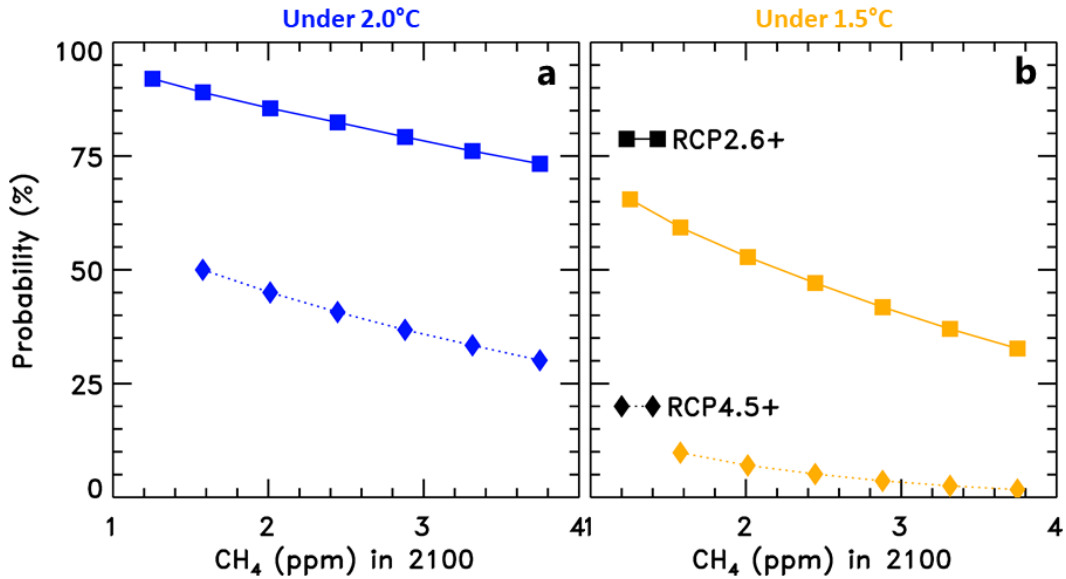
Global warming projections for RCP 2.6, RCP 4.5, and RCP 8.5 relative to the preindustrial baseline. Figure 4.23b is the same as figure 4.19; all three panels are of similar construction. Color at any given point within the EM-GC envelope represents the chance of ΔT reaching at least that temperature at that time.

4.3.6 The Effect of Increased Future Emissions of CH₄

As many countries around the world transition from coal to natural gas as a primary fossil fuel for electricity production, assumptions about future methane scenarios must shift to account for faster growth [Molnár, 2018; Sauniois et al., 2020]. The RCP 4.5 scenario has future CH₄ leveling off by midcentury at near-current atmospheric mixing ratios, then decreasing until the end of the 21st century (Figure 4.1b). The RCP 2.6 scenario has even more drastic and immediate reductions in atmospheric CH₄. This leveling off may be difficult for society to achieve due to natural gas becoming a primary source of energy for the foreseeable future [R B Jackson et al., 2018]. This energy shift would imply more leakage of CH₄ from extraction and utility infrastructure as demand increases [Sauniois et al., 2020] which would lead to increases in RF instead of decreases, though this could be offset with significant improvements to leakage rates [Alvarez et al., 2012]. The atmospheric mixing ratio might also rise through anthropogenically-induced releases of natural CH₄ reservoirs, such as permafrost melting, or increased biogenic activity [Comyn-Platt et al., 2018; Voigt et al., 2017]. Finally, the observed abundance of atmospheric CH₄ has already been rising faster in the past few years than in the previous two decades [Nisbet et al., 2019; Sauniois et al., 2020], exceeding the RCP 4.5 projection and mapping closer to the most intense RCP 8.5 scenario. These factors taken together suggest that we should expect that the abundance of CH₄ in the atmosphere may increase over time, and not level off as suggested in the RCP 4.5 scenario [Sauniois et al., 2016]. Therefore, we have created blended CH₄ scenarios, noted in section §4.2.1.2 and shown in Figure 4.5, to test the sensitivity of warming computed using our EM-GC to various future for atmospheric CH₄.

Figure 4.24 shows the probability of achieving the Paris Climate Agreement goals as a function of the atmospheric abundance of CH₄ in 2100. Each symbol in figure 4.24 shows ΔT_{2100} for an ensemble of EM-GC runs where the only change between the ensembles is the input time series of CH₄. Starting from either the RCP 2.6 (squares) and RCP 4.5 (diamonds) as scenario for all GHGs other than CH₄, the time series for each ensemble calculation is based upon either RCP 2.6, RCP 4.5, RCP 8.5, or one of four linear combinations of CH₄ versus time between RCP4.5 and RCP 8.5 shown in Figure 4.5. Otherwise the ensembles are identical to those in figures 4.22a and 4.22b for RCP 2.6 and RCP 4.5 respectively. In RCP 4.5, the abundance of CH₄ in 2100 is 1578 ppb; in the ensemble driven by RCP 4.5 with no changes to CH₄, we compute a 50% probability of ΔT_{2100} remaining beneath 2°C and a 10% chance of remaining beneath 1.5°C. These probabilities correspond to the leftmost diamonds in each panel of figure 4.24. As the CH₄ time series approaches the RCP 8.5 pathway, which has a CH₄ mixing ratio of 3748 ppb in 2100, the probabilities of future warming remaining beneath 2°C and 1.5°C fall to 30% and 2%, respectively (rightmost diamonds). Similarly, switching from RCP 2.6 for all GHGs to a combined scenario that uses CH₄ from RCP 8.5 causes the probability of ΔT_{2100} staying below 2°C to decrease from 92% to 73% and the likelihood of staying below 1.5°C warming to decrease from 66% to 33% (left- and rightmost squares). This analysis indicates that failure to limit methane to the RCP 2.6 trajectory will have a large impact on the achievement of the 1.5°C goal of the Paris Climate Agreement.

Figure 4.24 – Impact of CH₄ on EM-GC Projections



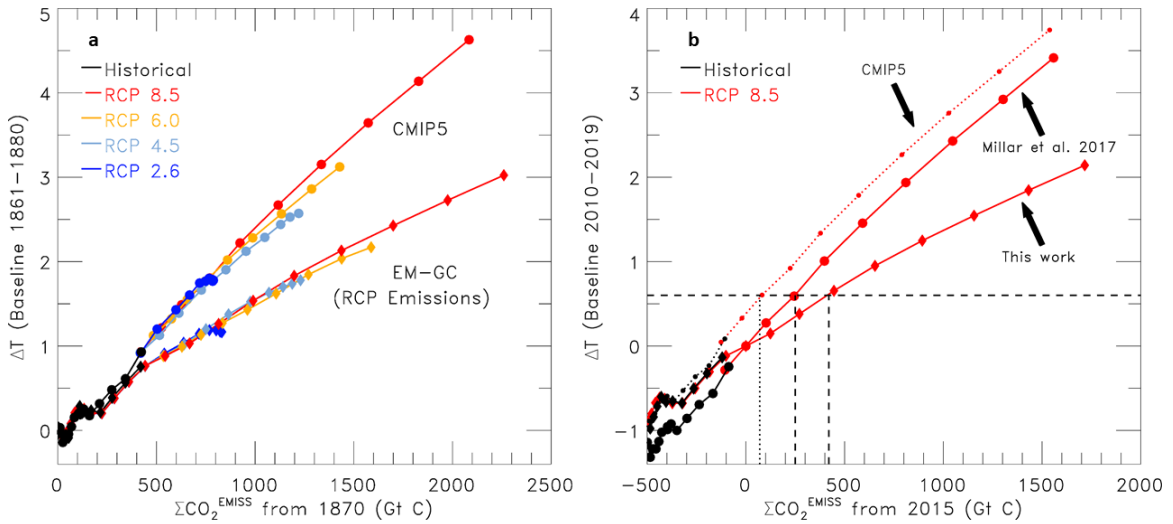
Shown are the probabilities that ΔT_{2100} remains below 2°C (4.24a, blue) or below 1.5°C (4.24b, gold) for both the RCP 2.6-based ensembles (squares, solid lines) and RCP 4.5-based ensembles (diamonds, dotted lines) relative to preindustrial. Each ensemble based on RCP 4.5 uses all GHG and aerosol forcing inputs from RCP 4.5 except replacing the RCP 4.5 CH₄ time series with one of six linear combinations between the RCP 4.5 CH₄ scenario and the RCP 8.5 CH₄ scenario, inclusive. Likewise, each ensemble based on RCP 2.6 uses all forcing inputs from RCP 2.6 except substituting the RCP 2.6 CH₄ with one of the six linear combinations (save for the seventh ensemble, far left, which is purely RCP 2.6). Ensembles are placed in this figure based on the CH₄ mixing ratio in 2100 (i.e. end values of figure 4.5).

4.3.7 Response to cumulative emissions

The Transient Climate Response to cumulative carbon Emissions (TCRE), which relates ΔT to accumulated anthropogenic emissions of CO₂, is an important policy metric [Gregory *et al.*, 2009; Millar *et al.*, 2017]. As the EM-GC projects generally less future warming than most of the CMIP5 GCMs, it follows that TCRE derived from the EM-GC falls on the low side of the range for TCRE given in AR5 (0.8 to 2.5°C per 1,000 GtC). Figure 4.25 shows the results of the ensemble median EM-GC simulations for the four RCP pathways. All four EM-GC ensemble medians suggest a TCRE of roughly 1.4°C per 1,000 GtC. The other four lines on figure 4.25a show the multi-model mean projections from the CMIP5 GCMs for the four RCP scenarios, taken from figure SPM.10 of AR5. TCRE from the CMIP5 GCMs in this figure has a value of 2.3°C per 1,000 GtC, which lies well above the EM-GC estimate and in the high end of the assessed range given by AR5. Following AR5 and Millar *et al.* [2017], future cumulative emissions of CO₂ in figure 4.25a are based on the rise since 1870, with ΔT shown relative to the two-decade average for 1861-1880. The emissions along the horizontal axis represent global, atmospheric release of CO₂ due to combustion of fossil fuels, flaring, cement production, and LUC from the RCP database.

Figure 4.25b shows an adjustment of the RCP 8.5 lines from figure 4.25a that are set to zero for the most recent decade (2010 to 2019), as done in Millar *et al.* [2017]. This adjustment clarifies the allowable remaining carbon budget for limiting future warming to remain beneath a given amount. Millar *et al.* [2017] presented this adjustment as one manner of accounting for the overestimate of ΔT_{MDL} provided by CMIP5 GCMs

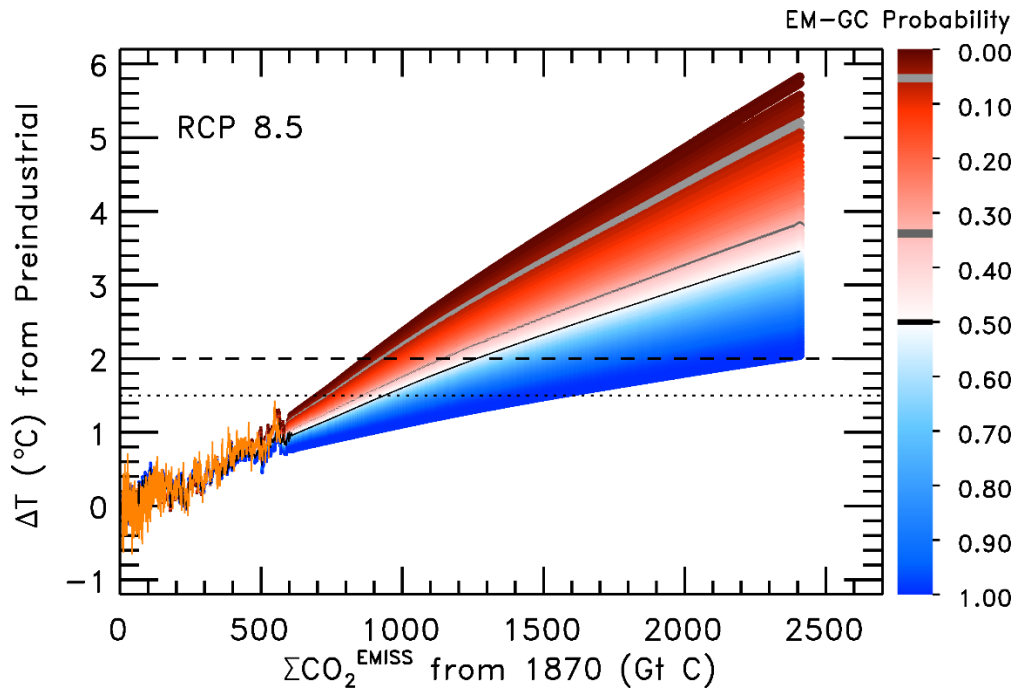
Figure 4.25 – ΔT as a Function of CO₂ Emissions, Ensemble Medians



a) Transient climate response to cumulative CO₂ emissions, in units of GtC. Average ΔT from CMIP5 GCMs, as taken from figure SPM.10 of AR5, is plotted against the average cumulative emissions since 1870 modeled to meet RCP prescribed concentrations (circles). EM-GC results show ΔT from a single EM-GC simulation for each RCP scenario representing the median of the ensemble; CO₂ emissions for each RCP ensemble are taken directly from the RCP database.

b) TCRE for different studies of RCP 8.5, illustrated using the same axes as *Millar et al.* [2017]. Both the EM-GC projection and the *Millar et al.* [2017] projection from CMIP5 are plotted such that the point representing the decade of the 2010s (centered on 2015) is set to the origin, based on current ΔT and estimated cumulative emission to date. For comparison, the CMIP5 projection is also shown such that it matches the EM-GC results for roughly the first century of the simulation, as done in panel a, i.e. instead of matching in the 2010s, so as to demonstrate the effective shift that *Millar et al.* [2017] applied to the CMIP5 projection. Vertical dotted and dashed lines indicate the remaining amount of CO₂ that can be released prior to having ΔT rise 1.5°C above preindustrial (i.e., 0.6°C above the observed 0.9°C rise in ΔT for the 2010s) according to the three studies.

Figure 4.26 – ΔT as a Function of CO₂ Emissions, RCP 8.5



Full EM-GC projection of transient climate response to cumulative CO₂ emissions for RCP 8.5. Colors and structure mirror those of figure 4.23c. The three grey lines of varying darkness provide a visual guide to highlight the lines of 50%, 66%, and 95% probability for keeping temperatures cooler than those temperatures, while the black horizontal lines are a visual guide to the two Paris Climate Agreement target ΔT values. As such, the intersection of a grey line with a black line determines the maximum amount of cumulative emissions that would be allowed while remaining cooler than one of the Paris Climate Agreement targets with the given probability.

Table 4.6 – Carbon Budget Comparisons

Source & reference emissions	Threshold Budget for 1.5°C			Threshold Budget for 2.0°C		
	50% prob.	65% prob.	90/95% prob.	50% prob.	65% prob.	90/95% prob.
Millar et al. (2017) - 545 GtC, 2014	768 GtC	749 GtC	709 GtC (90%)	961 GtC	940 GtC	875 GtC (90%)
Tokarsak & Gillet (2018) - 555 GtC, 2015	763 GtC	685 GtC	*	*	*	*
Rogelj et al. (2018) – 605 GtC 2017	158 GtC	114 GtC	*	*	*	*
Goodwin et al. (2018) - 572 GtC, 2016	*	767-777 GtC	*	*	967-1027 GtC	*
This study - 532 GtC, 2014 ; 590 GtC, 2019	930 GtC	850 GtC	710 GtC (95%)	1250 GtC	1140 GtC	900 GtC (95%)

compared to ΔT_{OBS} ; setting the ΔT baseline to recent years is also the process behind the expert judgement of *Kirtman et al.* [2013] that produced the AR5-based trapezoid shown in previous figures. The central finding of *Millar et al.* [2017] is that the best estimate of the remaining carbon budget needed to limit future warming to 0.6°C relative to 2015 (which translates to 1.5°C relative to preindustrial) is higher than the best estimate suggested by AR5. They later issued a public clarification saying their estimate for future temperature (and thus their carbon budget) still lies within the AR5 uncertainty [*Allen and Millar, 2017*], albeit with their carbon budget on the high extreme of the AR5 range. As shown in figure 4.25 and further discussed below, our EM-GC projection of ΔT_{MDL} indicates the remaining carbon budget is even larger than the values given by AR5 and *Millar et al.* [2017].

We can also use full ensemble simulations within the EM-GC to compute probabilistic forecasts of emissions thresholds for the Paris Agreement targets. Figure 4.26 displays ΔT with respect to cumulative emissions of CO_2 , using the same color scheme adopted for figures 4.19 and 4.23. The colors represent the probability that a particular future value of ΔT will reach at least that temperature for the specified cumulative emission of CO_2 . Figure 4.26 is based on the RCP 8.5 scenario for GHGs, to cover the widest range of future anthropogenic emissions of CO_2 .

Figure 4.26 shows that according to calculations conducted in our model framework, if society can keep cumulative carbon emissions below 900 GtC, then we will have a 95% chance of preventing global warming from exceeding 2°C relative to preindustrial. Cumulative emissions of 1140 GtC or 1250 GtC would lower the chance of ΔT remaining below 2°C to 66% or 50%, respectively. Likewise, the 95%, 66%, or 50%

probabilities for ΔT remaining below 1.5°C correspond to cumulative CO₂ emissions of 710 GtC, 850 GtC, or 930 GtC, respectively. For comparison, these emission numbers are listed in table 4.6, alongside comparable numbers from other studies [*Goodwin et al.*, 2018; *Millar et al.*, 2017; *Tokarska and Gillett*, 2018]. Similar quantities from Chapter 2 of the IPCC 1.5 C Special Report are also included, and show lower allowable carbon emission budgets driven by two intermediate-complexity climate models, FAIR and MAGICC, that are constrained to approximate climate sensitivity from the CMIP5 GCMs [*Rogelj et al.*, 2018].

For reference, while *Millar et al.* [2017] suggest that human activity has emitted roughly 545 GtC from 1870 to 2014, leading to a rise in ΔT of 0.9 °C for that time [*Millar et al.*, 2017]. Improvements in the understanding of LUC emission and five more years of emitting CO₂ suggest these values increase to 635 GtC [*Friedlingstein et al.*, 2019; *Le Quéré et al.*, 2018] and 1.0 °C respectively for 1870 to 2019. Using only emissions prescribed by the RCP scenarios, the carbon budget values are 532 GtC to 2014 and 590 GtC to 2019, but similar to the 545 GtC value from *Millar et al.* [2017], these numbers do not reflect updated understanding of past emissions from LUC. Society has been emitting 11.0 ± 0.8 GtC per year over the past decade, a rate that has also been increasing over previous decades, with a current annual value of nearly 12 GtC per year [*Friedlingstein et al.*, 2019].

Table 4.7 shows the remaining, post end of 2019 carbon budget for limiting warming to either 1.5°C or 2.0°C in our model framework. For all entries in table 4.7 we assume at the end of 2019 that cumulative carbon emissions are 590 GtC. We tie this cumulative carbon emission estimate to the time series used to drive the global carbon

Table 4.7 – Metrics for Future Carbon Budgets Leading to Crossing the Pairs Thresholds

Warming Targets		Future Budget to Threshold Budget ^a	Future Budget as % of Past Budget ^a	Range of Years to Meet Threshold Budget ^b
1.5 °C	95%	120 GtC	20%	2028-2029
	66%	260 GtC	44%	2037-2041
	50%	340 GtC	58%	2042-2048
2.0 °C	95%	310 GtC	53%	2040-2045
	66%	550 GtC	93%	2052-2065
	50%	660 GtC	112%	2057-2074

^aFuture Budget = Threshold Budget – Past Budget, with threshold and past budgets taken from the final row of Table 4.6 (2019 reference year).

^bFirst year of range is taken from RCP 8.5 prescribed emissions; last year of range assumes the current rate of emissions of roughly 12GtC continues into the future.

cycle model that underlies the RCP 8.5 specification of atmosphere CO₂. The current annual rate of global carbon emission of nearly 12 GtC would imply surpassing 710 GtC, our RCP-based threshold for staying below 1.5 °C with 95% confidence, in 2029 and surpassing the 2.0 °C, 95% confidence threshold of 900 GtC in 2045. These dates of passing the 95% confidence intervals for the target and upper limit of the Paris Agreement fall to 2028 and 2040, respectively, if we allow total carbon emissions to rise at the rate that underlies RCP 8.5. Similarly, year ranges for passing the 66% confidence interval for 1.5°C and 2.0°C warming are 2037-2041 and 2052-2065, respectively (table 4.7). The 50% confidence interval estimates for these thresholds rise to 2042-2048 and 2057-2074. We emphasize that even though our EM-GC exhibits slower warming than the CMIP5 GCMs, the Paris Climate Agreement target of limiting warming to 1.5°C cannot be achieved unless society begins a near immediate transition to a low carbon future, and at the same time slows or eliminates the rise in atmospheric CH₄ (section §4.3.6).

4.4 Conclusions

The value of the anthropogenic contribution to global warming over the past three decades, termed attributable anthropogenic warming rate (AAWR), has been analyzed in detail using both an empirical model of global climate (EM-GC) and output from CMIP5 GCMs. We find AAWR to be as 0.14 ± 0.06 °C/decade (full range of possible values) for 1979 to 2010 using our EM-GC, where the uncertainty covers the full range of model runs that yield a good fit to ΔT_{OBS} from CRU4. The CMIP5 GCMs exhibit values of AAWR of 0.22 ± 0.10 °C/decade (standard deviation among AAWR values from the CMIP5 GCMs), considerably larger than inferred from the climate record using our EM-GC. More than two-thirds of the 112 archived CMIP5 GCM runs exhibit a value for

AAWR larger than our upper limit of 0.20 °C/decade. The uncertainty in the EM-GC based derivation of AAWR is driven by imprecise knowledge of the radiative forcing of climate due to tropospheric aerosols, whereas the largest source of spread in the GCM simulation of GMST is due to uncertainty in cloud feedback [Ceppi *et al.*, 2017; Vial *et al.*, 2013; Zelinka *et al.*, 2016]. Our finding that the CMIP5 GCMS exhibit a considerably faster rise in GMST than observed is consistent with finding of Chapter 11 of AR5 (Kirtman *et al.*, 2013). Attempts to improve the understanding of aerosol species is an active area of current research, but large uncertainties persist [Bond *et al.*, 2013; W J Collins *et al.*, 2017; Pincus *et al.*, 2016; Shen *et al.*, 2020; S Smith *et al.*, 2011; S Smith and Bond, 2014; Thornhill *et al.*, 2020]. Similarly, while some recent studies suggest total cloud feedback is positive [Klein *et al.*, 2017; Sherwood *et al.*, 2020], a recent analysis of a 40 year satellite record shows no trend in cloud reflectivity [C J Weaver *et al.*, 2020], which is thought to be the largest driver of this positive trend.

While it is beyond the scope of this study to thoroughly assess the possible shortcomings of the CMIP5 GCM simulations over the past three decades, we suggest that high values for the sum of climate feedback mechanisms (λ_{Σ}), in particular the various cloud feedback processes, could be responsible for the apparent warm bias of the CMIP5 GCMs. Indeed, a recent analysis of CMIP6 shows that the next generation of GCMs displays high correlation between high ECS (i.e. high λ_{Σ} in the EM-GC) and a poor fit to observed AAWR from 1981 to 2014/17 [Tokarska *et al.*, 2020], and these high-ECS models have strongly positive cloud feedbacks [Zelinka *et al.*, 2020]. If the actual cloud feedback is less positive than currently exhibited by CMIP5 and CMIP6 GCMs, this could explain the apparent warm bias of these models.

Accurate projections of ΔT are critical to the successful implementation of the Paris Agreement. However, the wide span of possible futures even in our EM-GC framework confounds policy-making efforts and confidence in achieving the desired warming limits. While our model projections show a wide range of possible warming by end of century for the same GHG scenario, our forecasts produce a more optimistic likelihood for achieving the goals of the Paris Agreement than is provided by the CMIP5 GCMs. The temperature forecasts given by our EM-GC tend to lie among the lower half of the projections provided by the CMIP5 GCMs, with our maximum forecast warming tending to lie near the CMIP5 multi-model mean. Most importantly, the projections of ΔT from our EM-GC agree extremely well with the “indicative likely range for annual mean ΔT ” from Chapter 11 of AR5 [Kirtman *et al.*, 2013] – lending important computational support for this expert assessment of the CMIP5 GCMs driven by the fact many of the GCM-based values of ΔT have exceeded ΔT_{OBS} over the past few decades (Figure 4.2 here and figure 11.25b of Kirtman *et al.* [2013]).

Projections of ΔT versus cumulative emissions provides a policy relevant framework for achieving the goals of the Paris Climate Agreement. From 1870 to date, humans have emitted roughly 600 GtC, and are currently emitting nearly 12 GtC per year. If society is to achieve the Paris Agreement by keeping the rise in ΔT below 2°C with 95% probability by 2100, then only 20 to 25 years of cumulative carbon emissions remain in the allowable budget (table 4.7). However, in reality society has less than 20 to 25 years when considering practical complications. Since it is unreasonable to assume that annual emissions can drop from 12 GtC to zero instantaneously, the reduction in emission rate must begin earlier to reach the same cumulative emissions total. While the

20 to 25 year limit found in our model framework suggests society has more time to act than indicated by the CMIP5 GCMs, we emphasize that the goal of the Paris Climate Agreement can only be achieved by near immediate reductions in global carbon emissions.

Methane, a potent GHG, also needs to be a large part of policy considerations when considering how cumulative emissions compare to global warming projections. As the United States and other major coal-burning nations switch to natural gas, the risk of significant CH₄ leakage into the atmosphere increases, potentially negating the climate benefit of switching to the less carbon intensive fossil fuel source [R B Jackson *et al.*, 2018; Saunio *et al.*, 2020]. Carbon cycle feedbacks, such as higher activity in natural or agricultural wetland methane production or leakage from previously locked natural reservoirs, could further increase the atmospheric abundance of CH₄ [Comyn-Platt *et al.*, 2018; Voigt *et al.*, 2017]. It is probably not reasonable to expect CH₄ to follow the peak-and-decline component pattern of RCP 4.5; on the other hand, the aggressive methane growth of RCP 8.5 also seems unreasonable (figure 4.1). A projection of methane mid-range between RCP 4.5 and RCP 8.5 is a more likely scenario, implying a value for atmospheric methane between 2 and 3 ppm by 2100. Placing all GHGs other than methane along the RCP 2.6 trajectory would place us on a trajectory for having a reasonably favorable probability of limiting warming to 2°C, irrespective of the future methane scenario (figure 4.24). However, even for RCP 2.6, achievement of the ambitious Paris Climate Agreement target of 1.5°C drops noticeably as future atmospheric methane intensifies. Quite simply, limiting warming to 1.5°C will require aggressive future controls on atmospheric release of both CO₂ and CH₄.

Chapter 5: Conclusion and Future Research Opportunities

5.1 Summary of Work Presented

In this thesis research, I have analyzed past and future GMST using a simple energy balance model of climate that includes MLR. With this model, my group has determined the relative importance of various forcing agents of climate and used these analyses to create probabilistic projections of future temperature. Most notably, we have shown that keeping GMST below the goals set by the Paris Agreement with significantly higher than a 50% likelihood requires a future GHG emissions scenario notably more ambitious than RCP 4.5. We also have performed a large amount of sensitivity testing to determine our confidence in our results, such as quantifying the dependence of ECS on choice of OHC record and evaluating the effect of future atmospheric CH₄ on ΔT_{2100} in a manner based upon interpolation of the RCP scenarios. Many of the improvements I have added to the EM-GC since *Canty et al.* [2013] have had the effect of raising λ_{Σ} and ΔT_{2100} , bringing the predictions of the EM-GC somewhat closer to those from CMIP5. The EM-GC still produces cooler temperature projections than are provided by the CMIP5 GCMs, suggesting society has a bit more time to act to alleviate dire effects of climate change than one would infer from literal interpretation of GCM output. Nonetheless, society must still implement rapid and strong reductions in the emissions of CO₂ and CH₄ to slow and potentially reverse current global warming.

Our work shows that attributable anthropogenic warming rate (AAWR) from 1979 to 2010 is lower than that inferred from GCM output, particularly as the latter does a poor job of matching observed temperatures from 1998 to 2012, though this comparison between the EM-GC and the CMIP5 GCMs is not very sensitive to the exact start and end

years for each comparative time period. At the same time, AAWR from the EM-GC is comparable to or higher than AAWR from other empirical studies [*Christy and McNider, 2017; Foster and Rahmstorf, 2011; J Zhou and Tung, 2013a*]. Due to updates made over the course of this project, AAWR determined through the EM-GC has increased from roughly 0.12 °C/decade to roughly 0.14 °C/decade; this falls between values for AAWR below 0.10 °C/decade from *Zhou & Tung [2013a]* and *Christy & McNider [2017]* and values above 0.18 °C/decade for over 75% of CMIP5 GCMs.

Similar to the resulting increase in AAWR, my updates to the EM-GC drove our projections for ΔT_{2100} with the RCP 4.5 scenario toward more warming, from a median of roughly 1.39 °C (range 0.91 to 2.40) to a median of 2.00 °C (range 1.20 to 3.74). This significant increase in ΔT_{2100} is largely driven by the addition of a responsive ocean with an explicit application of climate feedbacks, allowing what was previously an infinite heat sink to also begin warming in tandem with the atmosphere. In turn, the responsive ocean allows the atmosphere to warm towards a true equilibrium slowly as opposed to rapidly reaching a cooler false equilibrium. This large increase does not bring the EM-GC projection for RCP 4.5 to fully agree with the CMIP5 median and range of 2.52 °C (1.69 to 3.64); the EM-GC median and minimum are still noticeably lower than the respective values from the CMIP5 GCMs. Similar comparisons happen with RCP 2.6 (median and maximum are cooler than those from the GCMs) and RCP 8.5 (minimum, median, and maximum). While consideration such as growth in CH₄ and a potential increase in λ_{Σ} can further warm the EM-GC projections, cooler projections than those in **AR5** suggest that society has a bit more time and a larger carbon budget, than suggested by GCM results, to reach goals such as those articulated in the Paris Climate Agreement.

5.2 Potential Future Work

There are numerous research opportunities that we could address with updates to the EM-GC, both in the structure of the model and in the data we analyze. The EM-GC currently runs with global average time series on a monthly grid. Changing our input data sets and model equations to a regional scale could allow for a more thorough examination of temperature attribution and a reduction in uncertainty by comparing a larger number of experiments. Such changes could allow for examination of climate-relevant quantities other than temperature (such as precipitation) especially if examined on seasonal or yearly time scales.

Future comparisons to GCMs will also include newer models than those used in CMIP5. While CMIP5 produced enough data to provide many more analyses, GCMs are continuously updated, and new emissions scenarios are produced as well. The current generation of GCMs participate in CMIP6 [Eyring *et al.*, 2016] and its component experiments such as ScenarioMIP [O'Neill *et al.*, 2016], using the Shared Socioeconomic Pathways (SSPs) [O'Neill *et al.*, 2017; O'Neill *et al.*, 2014] in place of the RCPs. These scenarios closely tie social and political changes to GHG atmospheric mixing ratios through dozens of possible futures, ideally giving a more tangible outline of potential global warming. They also include updates to the science underlying the projections, such as a 15% increase in the RF of CH₄ due to the associated production of SWV [Myhre *et al.*, 2007]. An increase in the strength of past GHG RF would imply a weaker climate feedback (§4.2.1.2); a change in the shape of the time series of past GHG RF (due to an increase in just one of its components) would also change the strength-of-fit between ΔT_{MDL} from the EM-GC and ΔT_{OBS} , potentially growing or shrinking the size of the EM-

GC ensemble with allowable fits (§4.3.3). Use of the SSPs within the EM-GC and comparison to CMIP6 output is thus a logical continuation of the work presented here. We have taken a first step in this regard, with submission of a paper to *Earth System Dynamics* led by University of Maryland chemistry graduate student Laura McBride, on which I am a co-author [McBride *et al.*, 2020]. The results of this paper will appear as a chapter in her doctoral dissertation.

5.2.1 Altering the Spatial and Temporal Resolution of the EM-GC

One of the largest simplifications of the EM-GC is its global resolution. While treating the whole Earth as a single unit is highly appropriate for a first-principles energy balance analysis, it limits the analysis to GMST and hinders the ability to make policy decisions on regional, national, and local scales. As such, altering the EM-GC to run on smaller spatial scales is a major opportunity for increasing our scientific capabilities.

To run the EM-GC on regional and smaller scales, all appropriate data sets would require according updates. For example, temperature and aerosol RF depend on the area being examined and TSI varies with season for all regions outside the tropics, while GHG RF would not have such a dependence due to most GHGs being well-mixed in the atmosphere; teleconnection forcings such as ENSO would also not need a regional update. In addition to data set regionalization, the core model equations would require extra terms to account for the fact that each experiment would now have spatial boundaries within the atmosphere (and, depending on region, within the ocean as well) through which other forcing to the region of interest could be applied. Our treatment of Q_{OCEAN} would also require new consideration for any region that is purely continental, as the lack of ocean surface in such regions would prevent direct OHE; the effect of Q_{OCEAN}

on the atmospheric surface temperatures of that region would necessarily have to be incorporated into the atmospheric boundary conditions of such an experiment instead.

An alternate or concurrent version of regionalization that could be added to the model is the addition of parameterizations to account for circulation pattern differences in both the atmosphere and ocean. In the atmosphere, these patterns are largely determined by latitude, with the most basic pattern being the six circulation cells (north and south polar, Hadley, and Ferrel cells). Of Earth's regions, the poles are warming significantly faster than other areas, so a division or parameterization of atmospheric temperatures to represent the latitudinal differences and interactions could provide extra enlightenment and accuracy. In the ocean, these patterns depend both on latitude and on the physical shape and limitations of the various ocean basins. The background ocean temperature profile and depth of the mixed layer varies greatly with latitude, meaning the average ocean warming profile interpreted from CMIP5 output may not be an accurate simplification for calculating $T_{\text{OCEAN,HUMAN}}$. Importantly, mixed layer depth and warming rate are generally inversely correlated. As such, adding in parameterizations for horizontal heat transport in the ocean and a dependence on mixed layer depth could be an alternate or additional option during regionalization.

Regionalization of the EM-GC also opens the possibility of considering other regressors that don't significantly affect global scale temperatures but do have effects on smaller scales, especially by affecting weather patterns. Like previous considerations of SWV for the global warming hiatus period (§2.3.1), we could add forcings to the EM-GC such as the Arctic Oscillation, the Pacific-North American pattern, or the Quasi-biennial Oscillation to look at temperatures or other climate indicators on the continental or

country scale. Adding extra regressors makes overfitting of the climate record a concern, so as part of such an analysis, determining which regressors explain the most variation in the climate record and which regressors do not significantly improve the fit (as done in *Chylek et al.* [2016]) should be a larger part of the project than currently in this thesis. Of course, the addition of new regressor variables also has to be based on a physical mechanism linking the process under consideration to variations in regional temperature.

In addition to adding alternate spatial scales to the EM-GC, we can expand the model's capabilities by adding options for alternate temporal scales as well. While the EM-GC currently operates on a monthly time grid, the strength-of-fit calculations already leverage an annual time scale to account for autocorrelation of the GMST anomaly [*Canty et al.*, 2013]. Directly running on an annual time grid would bypass this slight mixing of time scales, and it would involve more use of combining existing data (averaging monthly time series such as ENSO or TSI to the yearly scale) in favor of inferring data (interpolating annual data such as GHG emissions or AER RF to the monthly scale). The ability to run the EM-GC on seasonal time scales – whether as four time steps per year or by selectively examining a single season through successive years – could also provide information on temperature-dependent nonlinearity in the climate system, e.g. whether temperature or other factors react more to the same amount of forcing depending on season.

5.2.1.1 Other Ocean Temporal and Spatial Issues to Examine

Several aspects of ocean physics not currently accounted for in our simple ocean module could potentially affect our atmospheric temperature analysis. The properties range from the aforementioned regional differences in mixed layer depth and temperature

to the vertical diffusion of heat between ocean layers to the two-way interactions between ocean circulation patterns. Some of these properties act on timescales far longer than our model simulations, but others act on the order of centuries, potentially providing a drifting effect over the length of our simulation, and some have a timescale of several decades, putting them in the same category as our AMV and PDO signals. As such, any efforts we make to improve the model should at least consider these changes to the ocean in addition to our atmospheric advances.

In addition to creating a parameterization of the horizontal transfer of heat mentioned in the previous section, we could also write a parameterization to better represent the vertical diffusion of heat between layers of the ocean. For the length scale of the “surface layer” our simple ocean module considers, the time scale for internal diffusion of heat is on the order of a few decades. In theory, the sample warming profile used in our ocean module could equilibrate over time, within the span of our simulations, with a smaller percentage of heat remaining in the surface layer, thus increasing the value of Q_{OCEAN} and lowering our atmospheric temperatures. However, as our CMIP5-based warming profile appears similar to the existing average temperature profile of the oceans, I expect this result would have only a small effect on our warming projections. On the other hand, the differences between CMIP5 experiments in figure 4.8 and the quantities in table 4.3 suggest experiment scenario design could be important, as the historical, RCP 8.5, and RCP 4.5 experiments appear like they may map onto the “shallow”, “CMIP5”, and “middle” warming profiles when separated – these experiments differ by how close the scenario is to equilibrium at the beginning and end of each experiment. A parametrization to represent downward diffusion would not be too difficult to include, as

we could program f_p to decrease slowly over the course of a simulation; the difficulty would be deciding what rate of decrease would be most appropriate, and would likely require sensitivity testing. A future student could look into simple, zonal mean 2D models of MOC [Ferrari *et al.*, 2014; Jansen and Nadeau, 2019] and attempt to pull simple relations out from their results to construct both the horizontal and vertical parameterizations.

The interplay between ocean circulation patterns and climate change also should be taken into account. One consideration is the ability of the oceans to continue to function as a heat sink. Heat that enters the MOC and travels through the deep oceans requires multiple centuries to millennia to fully cycle [UCAR SCIED]. In theory, heat that entered the ocean during the early stages of the Industrial Revolution (mid-1700s) could be completing the cycle and returning to warm the surface now, or at least by the end of this century; more likely, though, is that it takes longer, and would be a minor effect compared to the accelerated warming that has occurred since the mid-1900s. Nonetheless, other more regional circulation patterns operate on shorter timescales, providing more noticeable effects on our simulations. The AMV, which we use as a proxy for AMOC, is the most notable of these, and not only does it have a large effect on our simulations of climate [DelSole *et al.*, 2011], but it also stands to change significantly under the effects of climate change [Rahmstorf *et al.*, 2015; Stocker *et al.*, 2013; Willis, 2010]. The deep water that drives MOC forms as cold, salty ocean water sinks. Global warming suggests not only a warmer surface layer, but a fresher one as well as ice melts and extra precipitation falls. These changes could greatly alter the character of AMOC, directly affecting the regression component of our model and potentially changing the

rate at which we can send heat from the atmosphere into the ocean. While our model is not able to resolve circulation patterns by design, we could certainly alter input time series to represent the effect of major changes to AMOC and/or our Q_{OCEAN} mechanism. On top of that, future work that includes full regionalization of the EM-GC should be constructed such that we can examine the evolution of AMOC more precisely with the regional coupling between the atmosphere and ocean, which should hopefully do better than a linear model at capturing nonlinearities.

Of course, with any of these potential additions, we must assess and sample the uncertainty in the data or parameter space we might consider. Similarly, we must remain cognizant of the uncertainty in existing portions of our ocean module. In the current framework, we attempt to fit various OHC records based on observations by calculating the average rate of OHC increase, with the value for that rate driving the ocean module in the model. We do not span this range for the average rate of OHC increase or test values outside the reasonable range in a continuous manner similar to the process for examining aerosol forcing or climate feedback. In future updates to the model, we could add the capability to feed any value in for the rate of OHC increase to thoroughly test the sensitivity of our results to this quantity. That said, doing so would remove the meaning of our χ^2 fitting parameter for the oceans, so we would need to find a new way to evaluate whether our modeled OHC shows a reasonable increase over time. Also, the OHC records we do consider already span a large range for this value without seeing a large sensitivity to OHC in our results, so I do not anticipate such sensitivity testing producing any significant changes to our conclusions.

5.2.2 *Climate Relationships to Examine*

The ability to run the EM-GC at multiple spatial and temporal scales would provide the opportunity to test hypotheses that could not be done with a single, global-scale experiment. The strength of many individual feedback processes will vary by locality depending on things such as aridity and surface type, meaning that the range and best estimate of overall feedback values found by the EM-GC ensembles will likely vary by region. Also, the strength of aerosol radiative forcing will also vary by a very large amount, as developing agricultural regions will likely be dominated by biomass burning while heavily industrial regions will be dominated by sulfate and nitrate emissions, with temporal variations that must consider various emission controls. These facts together could provide significant insight on which feedback processes are important in various locations as well as provide weighted statistics for the global averages of λ_{Σ} and AER RF to hopefully reduce the overall uncertainty in these terms.

Regionalization could also allow us to begin bridging the weather-climate gap by making annual and seasonal projections on topics such as precipitation. While the EM-GC would of course not be able to make daily weather predictions for specific cities, seasonal predictions of basin-scale rainfall would be incredibly useful for agriculture, municipal water management, and flood preparation and mitigation efforts. As examples of such relationships we could expect to see when examining precipitation, ENSO is well known for causing precipitation shifts across the USA [Lindsey, 2017], the IOD affects the Asian monsoon [Ashok et al., 2001] and precipitation from east Africa to Australia [Hirons and Turner, 2018; Ummenhofer et al., 2009], and the Arctic Oscillation greatly alters storm tracks from the northeastern USA to Europe [Nie et al., 2008].

Understanding how these multi-annual patterns then interact with anthropogenic global warming would be one potential goal of regionalizing the EM-GC.

As we make all the input data updates necessary for regionalization, we could also begin directly incorporating GCM output data as inputs. By training the EM-GC with output of ΔT from GCM historical experiments instead of with ΔT_{OBS} , we could then determine whether the discrepancy in future ΔT is driven solely by the GCMs' inability to match ΔT_{OBS} over the past few decades, whether it is due to some more fundamental, persistent difference in physics, or some combination of the two. This exercise could provide some potential validation of GCM projections of future warming and the associated carbon budgets, and would at least give insight into what aspect of GCM simulations are driving their warm bias based on the fit we would provide to their historical data. I am co-author of a paper that describes this possibility, currently under review at *Geoscientific Model Development* [Nicholls *et al.*, 2020].

5.2.3 Public Modeling

One last potential line for future development would be outreach rather than research. Our group has previously discussed is creating a web version of the EM-GC for public use. Due to the relatively simplicity of the EM-GC and how rapidly it runs, it is possible for a user to make a handful of simple choices for inputs and have the EM-GC return a single simulation of climate with those inputs in a matter of minutes, with minimal stress on the server hosting the web-based model. Most input choices with the EM-GC had to be made with hard coding when I began my project, so I created an exhaustive text-based user interface to run the EM-GC. It would not be too difficult to make an effectively similar GUI of model inputs for a potential web version of the model.

Climate modeling research is a political topic in modern society, a fact that is not helped by how abstract climate models are to most people. Providing a way for people to work with a climate model in a hands-on fashion could help bridge this gap, and at the very least help children become interested in science and coding. Also, if we retain access to the model output that members of the public produce through this web version of the model, this “crowdsourcing” could also bring to light potential relationships we have not yet seen in our own ensembles, providing another new avenue for potential research.

5.3 Final Comment

The EM-GC is ripe with potential for future work, ranging from inclusion of new data sets to extra atmospheric and oceanic parameterizations for fully coupled regionalization. The simplicity of this model makes it an incredible tool for interacting with the public, and no matter how much more complexity is added, it will be useful to also maintain the version of this model described in Chapter 4. The primary version of the model provides a cautionary counterpoint to GCMs; the future warming forecast by our model is somewhat uncertain, as some considerations (time-varying λ_S , increasing CH₄ emission scenarios) suggest warming closer to GCM results while others (increases in the best estimate of AER RF₂₀₁₁, downward diffusion of heat in the ocean) suggest less warming than found by GCMs. Currently, it appears that the upward trajectory of anthropogenic global warming is not quite as drastic as seen in GCM output. Either way, it is still clear and imperative that society, as the main source on equilibrium-disturbing GHG emissions, has to undertake considerable actions for reducing future warming, and maybe even reversing warming if technology advances quickly enough. Hopefully future work with the EM-GC can continue to examine these advances.

Bibliography

- Ackerman, A. S., O. B. Toon, J. P. Taylor, D. W. Johnson, P. V. Hobbs, and R. J. Ferek (2000), Effects of aerosols on cloud albedo: Evaluation of Twomey's parameterization of cloud susceptibility using measurements of ship tracks, *Journal of the Atmospheric Sciences*, 57(16), 2684-2695.
- Albrecht, B. A. (1989), Aerosols, cloud microphysics, and fractional cloudiness, *Science*, 245(4923), 1227-1230.
- Allen, M., and R. Millar (2017), Clarification on recent press coverage of our '1.5 degrees' paper in Nature Geoscience, in *Opinion*, edited, Oxford Martin School, <https://www.oxfordmartin.ox.ac.uk/opinion/view/379>.
- Alvarez, R. A., S. W. Pacala, J. J. Winebrake, W. L. Chameides, and S. P. Hamburg (2012), Greater focus needed on methane leakage from natural gas infrastructure, *Proceedings of the National Academy of Sciences*, 109(17), 6435-6440.
- Ammann, C., G. Meehl, W. Washington, and C. Zender (2003), A monthly and latitudinally varying volcanic forcing dataset in simulations of 20th century climate, *Geophysical Research Letters*, 30(12).
- Andrews, T., J. Gregory, M. Webb, and K. Taylor (2012), Forcing, feedbacks and climate sensitivity in CMIP5 coupled atmosphere-ocean climate models, *Geophysical Research Letters*, 39, doi:10.1029/2012GL051607.
- Andronova, N., and M. Schlesinger (2000), Causes of global temperature changes during the 19th and 20th centuries, *Geophysical Research Letters*, 27(14), 2137-2140, doi:10.1029/2000GL006109.
- Antweiler, W. (2015), Fossil fuels and declining oxygen in our atmosphere, edited.
- Archer, D. (2005), Fate of fossil fuel CO₂ in geologic time, *Journal of geophysical research: Oceans*, 110(C9).
- Arfeuille, F., D. Weisenstein, H. Mack, E. Rozanov, T. Peter, and S. Brönnimann (2014), Volcanic forcing for climate modeling: a new microphysics-based data set covering years 1600–present, *Climate of the Past*, 10(1), 359-375.
- Ashok, K., Z. Guan, and T. Yamagata (2001), Impact of the Indian Ocean dipole on the relationship between the Indian monsoon rainfall and ENSO, *Geophysical Research Letters*, 28(23), 4499-4502.
- Ballantyne, A., C. Alden, J. Miller, P. Tans, and J. White (2012), Increase in observed net carbon dioxide uptake by land and oceans during the past 50 years, *Nature*, 488(7409), 70-72.
- Balmaseda, M., K. Trenberth, and E. Kallen (2013), Distinctive climate signals in reanalysis of global ocean heat content, *Geophysical Research Letters*, 40(9), 1754-1759, doi:10.1002/grl.50382.
- Belcher, S., O. Boucher, and R. Sutton (2019), Why results from the next generation of climate models matter, in *Carbon Brief*, edited, <https://www.carbonbrief.org/guest-post-why-results-from-the-next-generation-of-climate-models-matter>.
- Bellenger, H., É. Guilyardi, J. Leloup, M. Lengaigne, and J. Vialard (2014), ENSO representation in climate models: From CMIP3 to CMIP5, *Climate Dynamics*, 42(7-8), 1999-2018.

- Bennett, B. F., A. P. Hope, R. J. Salawitch, W. R. Tribett, and T. P. Canty (2017), Implementation, in *Paris Climate Agreement: Beacon of Hope*, edited, pp. 147-181, Springer.
- Boden, T. A., G. Marland, and R. J. Andres (2009), Global, regional, and national fossil-fuel CO₂ emissions, *Carbon dioxide information analysis center, Oak ridge national laboratory, US department of energy, Oak Ridge, Tenn., USA doi, 10*.
- Boessenkool, K. P., I. R. Hall, H. Elderfield, and I. Yashayaev (2007), North Atlantic climate and deep-ocean flow speed changes during the last 230 years, *Geophysical Research Letters*, *34*(13).
- Bond, T., et al. (2013), Bounding the role of black carbon in the climate system: A scientific assessment, *Journal of Geophysical Research-Atmospheres*, *118*(11), 5380-5552, doi:10.1002/jgrd.50171.
- Bony, S., et al. (2006), How well do we understand and evaluate climate change feedback processes?, *Journal of Climate*, *19*(15), 3445-3482, doi:10.1175/JCLI3819.1.
- Booth, B. B., N. J. Dunstone, P. R. Halloran, T. Andrews, and N. Bellouin (2012), Aerosols implicated as a prime driver of twentieth-century North Atlantic climate variability, *Nature*, *484*(7393), 228-232.
- Burgess, S. D., S. Bowring, and S.-z. Shen (2014), High-precision timeline for Earth's most severe extinction, *Proceedings of the National Academy of Sciences*, *111*(9), 3316-3321.
- Cai, W., P. Van Rensch, T. Cowan, and H. H. Hendon (2011), Teleconnection pathways of ENSO and the IOD and the mechanisms for impacts on Australian rainfall, *Journal of Climate*, *24*(15), 3910-3923.
- Canadell, J. G., C. Le Quéré, M. R. Raupach, C. B. Field, E. T. Buitenhuis, P. Ciais, T. J. Conway, N. P. Gillett, R. Houghton, and G. Marland (2007), Contributions to accelerating atmospheric CO₂ growth from economic activity, carbon intensity, and efficiency of natural sinks, *Proceedings of the national academy of sciences*, *104*(47), 18866-18870.
- Canty, T., N. Mascioli, M. Smarte, and R. Salawitch (2013), An empirical model of global climate - Part 1: A critical evaluation of volcanic cooling, *Atmospheric Chemistry and Physics*, *13*(8), 3997-4031, doi:10.5194/acp-13-3997-2013.
- Carslaw, K., L. Lee, C. Reddington, K. Pringle, A. Rap, P. Forster, G. Mann, D. Spracklen, M. Woodhouse, and L. Regayre (2013), Large contribution of natural aerosols to uncertainty in indirect forcing, *Nature*, *503*(7474), 67-71.
- Carton, J., G. Chepurin, and L. Chen (2018), SODA3: A new ocean climate reanalysis, *Journal of Climate*, *31*(17), 6967-6983.
- Carton, J., and B. Giese (2008), A reanalysis of ocean climate using Simple Ocean Data Assimilation (SODA), *Monthly Weather Review*, *136*(8), 2999-3017, doi:10.1175/2007MWR1978.1.
- Carton, J., and A. Santorelli (2008), Global Decadal Upper-Ocean Heat Content as Viewed in Nine Analyses, *Journal of Climate*, *21*(22), 6015-6035, doi:10.1175/2008JCLI2489.1.
- Ceppi, P., F. Briant, M. D. Zelinka, and D. L. Hartmann (2017), Cloud feedback mechanisms and their representation in global climate models, *Wiley Interdisciplinary Reviews: Climate Change*, *8*(4), e465.
- Charette, M. A., and W. H. Smith (2010), The volume of Earth's ocean, *Oceanography*, *23*(2), 112-114.

- Chavez, F. P., J. Ryan, S. E. Lluch-Cota, and M. Niquen (2003), From anchovies to sardines and back: multidecadal change in the Pacific Ocean, *science*, 299(5604), 217-221.
- Chen, Y., and J. E. Penner (2005), Uncertainty analysis for estimates of the first indirect aerosol effect.
- Cheng, L., K. Trenberth, M. Palmer, J. Zhu, and J. Abraham (2016), Observed and simulated full-depth ocean heat-content changes for 1970–2005, *Ocean Science*, 12(4), 925-935.
- Christy, J. R., and R. T. McNider (2017), Satellite bulk tropospheric temperatures as a metric for climate sensitivity, *Asia-Pacific Journal of Atmospheric Sciences*, 53(4), 511-518.
- Church, J., N. White, L. Konikow, C. Domingues, J. Cogley, E. Rignot, J. Gregory, M. van den Broeke, A. Monaghan, and I. Velicogna (2011), Revisiting the Earth's sea-level and energy budgets from 1961 to 2008, *Geophysical Research Letters*, 38, doi:10.1029/2011GL048794.
- Chylek, P., C. Folland, J. D. Klett, and M. K. Dubey (2020), CMIP5 climate models overestimate cooling by volcanic aerosols, *Geophysical Research Letters*, 47(3), e2020GL087047.
- Chylek, P., J. D. Klett, M. K. Dubey, and N. Hengartner (2016), The role of Atlantic Multi-decadal Oscillation in the global mean temperature variability, *Climate Dynamics*, 47(9-10), 3271-3279.
- Chylek, P., J. D. Klett, G. Lesins, M. K. Dubey, and N. Hengartner (2014), The Atlantic Multidecadal Oscillation as a dominant factor of oceanic influence on climate, *Geophysical Research Letters*, 41(5), 1689-1697, doi:10.1002/2014GL059274.
- Clarke, L., J. Edmonds, H. Jacoby, H. Pitcher, J. Reilly, and R. Richels (2007), Scenarios of greenhouse gas emissions and atmospheric concentrations.
- Coddington, O., J. Lean, P. Pilewskie, M. Snow, and D. Lindholm (2016), A solar irradiance climate data record, *Bulletin of the American Meteorological Society*, 97(7), 1265-1282.
- Collins, M., R. Knutti, J. Arblaster, J.-L. Dufresne, T. Fichet, P. Friedlingstein, X. Gao, W. Gutowski, T. Johns, and G. Krinner (2013), Long-term climate change: projections, commitments and irreversibility, in *Climate Change 2013-The Physical Science Basis: Contribution of Working Group I to the Fifth Assessment Report of the Intergovernmental Panel on Climate Change*, edited by T. Stocker, D. Qin, G. Plattner, M. Tignor, S. Allen, J. Boschung, A. Nauels, Y. Xia, B. Bex and B. Midgley, pp. 1029-1136, Cambridge University Press.
- Collins, W. J., J.-F. Lamarque, M. Schulz, O. Boucher, V. Eyring, M. I. Hegglin, A. Maycock, G. Myhre, M. Prather, and D. Shindell (2017), AerChemMIP: quantifying the effects of chemistry and aerosols in CMIP6, *Geoscientific Model Development*, 10(2), 585-607.
- Comyn-Platt, E., G. Hayman, C. Huntingford, S. E. Chadburn, E. J. Burke, A. B. Harper, W. J. Collins, C. P. Webber, T. Powell, and P. M. Cox (2018), Carbon budgets for 1.5 and 2 C targets lowered by natural wetland and permafrost feedbacks, *Nature geoscience*, 11(8), 568.
- Cowtan, K., Z. Hausfather, E. Hawkins, P. Jacobs, M. Mann, S. Miller, B. Steinman, M. Stolpe, and R. Way (2015), Robust comparison of climate models with observations using blended land air and ocean sea surface temperatures, *Geophysical Research Letters*, 42(15), 6526-6534.
- Cowtan, K., and R. Way (2014), Coverage bias in the HadCRUT4 temperature series and its impact on recent temperature trends, *Quarterly Journal of the Royal Meteorological Society*, 140(683), 1935-1944, doi:10.1002/qj.2297.

- DelSole, T., M. Tippett, and J. Shukla (2011), A Significant Component of Unforced Multidecadal Variability in the Recent Acceleration of Global Warming, *Journal of Climate*, 24(3), 909-926, doi:10.1175/2010JCLI3659.1.
- Deser, C., and J. M. Wallace (1990), Large-scale atmospheric circulation features of warm and cold episodes in the tropical Pacific, *Journal of Climate*, 3(11), 1254-1281.
- Dessler, A. (2010), A determination of the cloud feedback from climate variations over the past decade, *Science*, 330(6010), 1523-1527.
- Dessler, A. (2013), Observations of climate feedbacks over 2000–10 and comparisons to climate models, *Journal of Climate*, 26(1), 333-342.
- Dlugokencky, E. J., L. Bruhwiler, J. White, L. Emmons, P. C. Novelli, S. A. Montzka, K. A. Masarie, P. M. Lang, A. Croswell, and J. B. Miller (2009), Observational constraints on recent increases in the atmospheric CH₄ burden, *Geophysical Research Letters*, 36(18).
- Dolinar, E. K., X. Dong, B. Xi, J. H. Jiang, and H. Su (2015), Evaluation of CMIP5 simulated clouds and TOA radiation budgets using NASA satellite observations, *Climate Dynamics*, 44(7-8), 2229-2247.
- Domingues, C., J. Church, N. White, P. Gleckler, S. Wijffels, P. Barker, and J. Dunn (2008), Improved estimates of upper-ocean warming and multi-decadal sea-level rise, *Nature*, 453(7198), 1090-1093.
- Douglass, D. H., and R. S. Knox (2005), Climate forcing by the volcanic eruption of Mount Pinatubo, *Geophysical Research Letters*, 32(5).
- Duchez, A., J.-M. Hirschi, S. Cunningham, A. Blaker, H. Bryden, B. de Cuevas, C. Atkinson, G. McCarthy, E. Frajka-Williams, and D. Rayner (2014), A new index for the Atlantic Meridional Overturning Circulation at 26° N, *Journal of Climate*, 27(17), 6439-6455.
- Dudok de Wit, T., G. Kopp, C. Fröhlich, and M. Schöll (2017), Methodology to create a new total solar irradiance record: Making a composite out of multiple data records, *Geophysical Research Letters*, 44(3), 1196-1203.
- Edwards, P. N. (2000), A brief history of atmospheric general circulation modeling.
- England, M., S. McGregor, P. Spence, G. Meehl, A. Timmermann, W. Cai, A. Sen Gupta, M. McPhaden, A. Purich, and A. Santoso (2014), Recent intensification of wind-driven circulation in the Pacific and the ongoing warming hiatus, *Nature Climate Change*, 4(3), 222-227, doi:10.1038/NCLIMATE2106.
- Etheridge, D. M., L. P. Steele, R. Francey, and R. Langenfelds (1998), Atmospheric methane between 1000 AD and present: Evidence of anthropogenic emissions and climatic variability, *Journal of Geophysical Research: Atmospheres*, 103(D13), 15979-15993.
- Eyring, V., S. Bony, G. A. Meehl, C. A. Senior, B. Stevens, R. J. Stouffer, and K. E. Taylor (2016), Overview of the Coupled Model Intercomparison Project Phase 6 (CMIP6) experimental design and organization, *Geoscientific Model Development*, 9(5), 1937-1958.
- Fan, S.-M., T. L. Blaine, and J. L. Sarmiento (1999), Terrestrial carbon sink in the Northern Hemisphere estimated from the atmospheric CO₂ difference between Mauna Loa and the South Pole since 1959, *Tellus B: Chemical and Physical Meteorology*, 51(5), 863-870.

- Fawcett, A. A., G. C. Iyer, L. E. Clarke, J. A. Edmonds, N. E. Hultman, H. C. McJeon, J. Rogelj, R. Schuler, J. Alsalam, and G. R. Asrar (2015), Can Paris pledges avert severe climate change?, *Science*, 350(6265), 1168-1169.
- Feng, Y., V. Ramanathan, and V. Kotamarthi (2013), Brown carbon: a significant atmospheric absorber of solar radiation?, *Atmospheric Chemistry & Physics Discussions*, 13(1).
- Ferrari, R., M. F. Jansen, J. F. Adkins, A. Burke, A. L. Stewart, and A. F. Thompson (2014), Antarctic sea ice control on ocean circulation in present and glacial climates, *Proceedings of the National Academy of Sciences*, 111(24), 8753-8758.
- Flato, G., J. Marotzke, B. Abiodun, P. Braconnot, S. Chou, W. Collins, P. Cox, F. Driouech, S. Emori, and V. Eyring (2013), Evaluation of climate models, in *Climate change 2013: the physical science basis. Contribution of Working Group I to the Fifth Assessment Report of the Intergovernmental Panel on Climate Change*, edited by T. Stocker, D. Qin, G. Plattner, M. Tignor, S. Allen, J. Boschung, A. Nauels, Y. Xia, B. Bex and B. Midgley, pp. 741-866, Cambridge University Press.
- Folland, C. K., O. Boucher, A. Colman, and D. E. Parker (2018), Causes of irregularities in trends of global mean surface temperature since the late 19th century, *Science advances*, 4(6), eaao5297.
- Forster, P., T. Andrews, P. Good, J. Gregory, L. Jackson, and M. Zelinka (2013), Evaluating adjusted forcing and model spread for historical and future scenarios in the CMIP5 generation of climate models, *Journal of Geophysical Research-Atmospheres*, 118(3), 1139-1150, doi:10.1002/jgrd.50174.
- Forster, P., A. Maycock, C. McKenna, and C. Smith (2020), Latest climate models confirm need for urgent mitigation, *Nature Climate Change*, 10(1), 7-10.
- Foster, G., and S. Rahmstorf (2011), Global temperature evolution 1979-2010, *Environmental Research Letters*, 6(4), doi:10.1088/1748-9326/6/4/044022.
- Friedlingstein, P., M. Jones, M. O'sullivan, R. Andrew, J. Hauck, G. Peters, W. Peters, J. Pongratz, S. Sitch, and C. Le Quéré (2019), Global carbon budget 2019, *Earth System Science Data*, 11(4), 1783-1838.
- Friedrich, T., A. Timmermann, M. Tigchelaar, O. E. Timm, and A. Ganopolski (2016), Nonlinear climate sensitivity and its implications for future greenhouse warming, *Science Advances*, 2(11), e1501923.
- Fromm, M., G. Kablick III, G. Nedoluha, E. Carboni, R. Grainger, J. Campbell, and J. Lewis (2014), Correcting the record of volcanic stratospheric aerosol impact: Nabro and Sarychev Peak, *Journal of Geophysical Research: Atmospheres*, 119(17), 10,343-310,364.
- Fujino, J., R. Nair, M. Kainuma, T. Masui, and Y. Matsuoka (2006), Multi-gas mitigation analysis on stabilization scenarios using AIM global model, *The Energy Journal*(Special Issue# 3).
- Fyfe, J., N. Gillett, and F. Zwiers (2013), Overestimated global warming over the past 20 years, *Nature Climate Change*, 3(9), 767-769.
- Gerlach, T. (2011), Volcanic versus anthropogenic carbon dioxide, *Eos, Transactions American Geophysical Union*, 92(24), 201-202.
- Gettelman, A., C. Hannay, J. Bacmeister, R. Neale, A. Pendergrass, G. Danabasoglu, J. F. Lamarque, J. Fasullo, D. Bailey, and D. Lawrence (2019), High climate sensitivity in the Community Earth System Model version 2 (CESM2), *Geophysical Research Letters*, 46(14), 8329-8337.

- Giese, B., G. Chepurin, J. Carton, T. Boyer, and H. Seidel (2011), Impact of bathythermograph temperature bias models on an ocean reanalysis, *Journal of climate*, 24(1), 84-93.
- Giles, D. M., B. N. Holben, T. F. Eck, A. Sinyuk, A. Smirnov, I. Slutsker, R. Dickerson, A. M. Thompson, and J. Schafer (2012), An analysis of AERONET aerosol absorption properties and classifications representative of aerosol source regions, *Journal of Geophysical Research: Atmospheres*, 117(D17).
- Gillett, N. P., V. K. Arora, D. Matthews, and M. R. Allen (2013), Constraining the ratio of global warming to cumulative CO₂ emissions using CMIP5 simulations, *Journal of Climate*, 26(18), 6844-6858.
- Glasby, G. P. (2006), Abiogenic origin of hydrocarbons: An historical overview, *Resource Geology*, 56(1), 83-96.
- Goodwin, P., A. Katavouta, V. M. Roussenov, G. L. Foster, E. J. Rohling, and R. G. Williams (2018), Pathways to 1.5 C and 2 C warming based on observational and geological constraints, *Nature Geoscience*, 11(2), 102-107.
- Gouretski, V., and F. Reseghetti (2010), On depth and temperature biases in bathythermograph data: Development of a new correction scheme based on analysis of a global ocean database, *Deep-Sea Research Part I-Oceanographic Research Papers*, 57(6), 812-833, doi:10.1016/j.dsr.2010.03.011.
- Gregory, J. (2000), Vertical heat transports in the ocean and their effect on time-dependent climate change, *Climate Dynamics*, 16(7), 501-515.
- Gregory, J., W. Ingram, M. Palmer, G. Jones, P. Stott, R. Thorpe, J. Lowe, T. Johns, and K. Williams (2004), A new method for diagnosing radiative forcing and climate sensitivity, *Geophysical research letters*, 31(3).
- Gregory, J., C. Jones, P. Cadule, and P. Friedlingstein (2009), Quantifying carbon cycle feedbacks, *Journal of Climate*, 22(19), 5232-5250.
- Gryspeerd, E., J. Muelmenstadt, A. Gettelman, F. F. Malavelle, H. Morrison, D. Neubauer, D. G. Partridge, P. Stier, T. Takemura, and H. Wang (2020), Surprising similarities in model and observational aerosol radiative forcing estimates, *Atmospheric Chemistry and Physics*, 20(1), 613-623.
- Hansen, J., R. Ruedy, M. Sato, and K. Lo (2010), GLOBAL SURFACE TEMPERATURE CHANGE, *Reviews of Geophysics*, 48, doi:10.1029/2010RG000345.
- Hansen, J., M. Sato, P. Kharecha, and K. Von Schuckmann (2011), Earth's energy imbalance and implications, *arXiv preprint arXiv:1105.1140*.
- Hansen, J., M. Sato, R. Ruedy, P. Kharecha, A. Lacis, R. Miller, L. Nazarenko, K. Lo, G. Schmidt, and G. Russell (2007), Climate simulations for 1880–2003 with GISS modelE, *Climate dynamics*, 29(7-8), 661-696.
- Hansen, J., et al. (2005), Efficacy of climate forcings, *Journal of Geophysical Research-Atmospheres*, 110(D18), doi:10.1029/2005JD005776.
- Hartin, C. A., P. L. Patel, A. Schwarber, R. P. Link, and B. Bond-Lamberty (2015), A simple object-oriented and open-source model for scientific and policy analyses of the global climate system—Hector v1. 0, *Geoscientific Model Development (Online)*, 8(PNNL-SA-104722).

- Hausfather, Z. (2008), *The Water Vapor Feedback*, edited, Yale University, Yale Climate Connections.
- Hausfather, Z., H. Drake, T. Abbott, and G. Schmidt (2020), Evaluating the performance of past climate model projections, *Geophysical Research Letters*, *47*(1), e2019GL085378.
- Haustein, K., F. Otto, V. Venema, P. Jacobs, K. Cowtan, Z. Hausfather, R. Way, B. White, A. Subramanian, and A. Schurer (2019), A limited role for unforced internal variability in 20th century warming, *Journal of Climate*(2019).
- Herring, S. C., N. Christidis, A. Hoell, M. P. Hoerling, and P. A. Stott (2020), Explaining extreme events of 2018 from a climate perspective, *Bulletin of the American Meteorological Society*, *101*(1), S1-S140.
- Hirons, L., and A. Turner (2018), The impact of Indian Ocean mean-state biases in climate models on the representation of the East African short rains, *Journal of Climate*, *31*(16), 6611-6631.
- Hopcroft, P. O., and P. J. Valdes (2015), How well do simulated last glacial maximum tropical temperatures constrain equilibrium climate sensitivity?, *Geophysical Research Letters*, *42*(13), 5533-5539.
- Hope, A. P., T. P. Canty, R. J. Salawitch, W. R. Tribett, and B. F. Bennett (2017), Forecasting Global Warming, in *Paris Climate Agreement: Beacon of Hope*, edited, pp. 51-113, Springer.
- Hope, A. P., L. A. McBride, T. P. Canty, B. F. Bennett, W. R. Tribett, and R. J. Salawitch (2020), Examining the human influence on global climate using an empirical model, *Earth's Future*, doi:<https://doi.org/10.1002/essoar.10504179.1>.
- Houghton, J. (2009), *Global warming: the complete briefing*, Cambridge university press.
- Houghton, R. A., J. House, J. Pongratz, G. Van Der Werf, R. DeFries, M. Hansen, C. Le Quéré, and N. Ramankutty (2012), Carbon emissions from land use and land-cover change, *Biogeosciences*(12), 5125-5142.
- Hourdin, F., J.-Y. Grandpeix, C. Rio, S. Bony, A. Jam, F. Cheruy, N. Rochetin, L. Fairhead, A. Idelkadi, and I. Musat (2013), LMDZ5B: the atmospheric component of the IPSL climate model with revisited parameterizations for clouds and convection, *Climate Dynamics*, *40*(9-10), 2193-2222.
- Huber, M., and R. Knutti (2014), Natural variability, radiative forcing and climate response in the recent hiatus reconciled, *Nature Geoscience*, *7*(9), 651-656.
- IPCC (2013), Summary for Policymakers, in *Climate Change 2013 the Physical Science Basis: Working Group I Contribution to the Fifth Assessment Report of the Intergovernmental Panel on Climate Change*, edited by T. Stocker, D. Qin, G. Plattner, M. Tignor, S. Allen, J. Boschung, A. Nauels, Y. Xia, B. Bex and B. Midgley, pp. 3-29, Cambridge University Press.
- Ishii, M., Y. Fukuda, S. Hirahara, S. Yasui, T. Suzuki, and K. Sato (2017), Accuracy of global upper ocean heat content estimation expected from present observational data sets, *SOLA*, *13*, 163-167.
- Ishii, M., and M. Kimoto (2009), Reevaluation of historical ocean heat content variations with time-varying XBT and MBT depth bias corrections, *Journal of Oceanography*, *65*(3), 287-299, doi:10.1007/s10872-009-0027-7.
- Ishii, M., A. Shouji, S. Sugimoto, and T. Matsumoto (2005), Objective analyses of sea-surface temperature and marine meteorological variables for the 20th century using ICOADS and the Kobe collection, *International Journal of Climatology: A Journal of the Royal Meteorological Society*, *25*(7), 865-879.

- Jackson, L. C., K. A. Peterson, C. D. Roberts, and R. A. Wood (2016), Recent slowing of Atlantic overturning circulation as a recovery from earlier strengthening, *Nature Geoscience*, *9*(7), 518-522.
- Jackson, R. B., C. Le Quéré, R. Andrew, J. G. Canadell, J. I. Korsbakken, Z. Liu, G. P. Peters, and B. Zheng (2018), Global energy growth is outpacing decarbonization, *Environmental Research Letters*, *13*(12), 120401.
- Jakob, C. (2014), Going back to basics, *Nature Climate Change*, *4*(12), 1042-1045.
- Jansen, M. F., and L.-P. Nadeau (2019), A toy model for the response of the residual overturning circulation to surface warming, *Journal of Physical Oceanography*, *49*(5), 1249-1268.
- Jo, D. S., R. J. Park, S. Lee, S.-W. Kim, and X. Zhang (2016), A global simulation of brown carbon: implications for photochemistry and direct radiative effect, *Atmos. Chem. Phys*, *16*(5), 3413-3432.
- Jones, P., D. Lister, T. Osborn, C. Harpham, M. Salmon, and C. Morice (2012), Hemispheric and large-scale land-surface air temperature variations: An extensive revision and an update to 2010, *Journal of Geophysical Research-Atmospheres*, *117*, doi:10.1029/2011JD017139.
- Jourdan, F., K. Hodges, B. Sell, U. Schaltegger, M. Wingate, L. Evins, U. Söderlund, P. Haines, D. Phillips, and T. Blenkinsop (2014), High-precision dating of the Kalkarindji large igneous province, Australia, and synchrony with the Early–Middle Cambrian (Stage 4–5) extinction, *Geology*, *42*(6), 543-546.
- Kahn, R. A. (2012), Reducing the uncertainties in direct aerosol radiative forcing, *Surveys in geophysics*, *33*(3-4), 701-721.
- Karl, T. R., A. Arguez, B. Huang, J. H. Lawrimore, J. R. McMahon, M. J. Menne, T. C. Peterson, R. S. Vose, and H.-M. Zhang (2015), Possible artifacts of data biases in the recent global surface warming hiatus, *Science*, doi:10.1126/science.aaa5632.
- Kavvada, A., A. Ruiz-Barradas, and S. Nigam (2013), AMO's structure and climate footprint in observations and IPCC AR5 climate simulations, *Climate Dynamics*, *41*(5-6), 1345-1364, doi:10.1007/s00382-013-1712-1.
- Keeling, C. D., S. C. Piper, R. B. Bacastow, M. Wahlen, T. P. Whorf, M. Heimann, and H. A. Meijer (2005), Atmospheric CO₂ and 13C CO₂ exchange with the terrestrial biosphere and oceans from 1978 to 2000: Observations and carbon cycle implications, in *A history of atmospheric CO₂ and its effects on plants, animals, and ecosystems*, edited, pp. 83-113, Springer.
- Kennedy, J., N. Rayner, R. Smith, D. Parker, and M. Saunby (2011a), Reassessing biases and other uncertainties in sea surface temperature observations measured in situ since 1850: 1. Measurement and sampling uncertainties, *Journal of Geophysical Research: Atmospheres*, *116*(D14).
- Kennedy, J., N. Rayner, R. Smith, D. Parker, and M. Saunby (2011b), Reassessing biases and other uncertainties in sea surface temperature observations measured in situ since 1850: 2. Biases and homogenization, *Journal of Geophysical Research: Atmospheres*, *116*(D14).
- Kiehl, J. (2007), Twentieth century climate model response and climate sensitivity, *Geophysical Research Letters*, *34*(22), doi:10.1029/2007GL031383.
- Kiehl, J., and K. Trenberth (1997), Earth's annual global mean energy budget, *Bulletin of the American Meteorological Society*, *78*(2), 197-208.

- Kirschke, S., P. Bousquet, P. Ciais, M. Saunoy, J. G. Canadell, E. J. Dlugokencky, P. Bergamaschi, D. Bergmann, D. R. Blake, and L. Bruhwiler (2013), Three decades of global methane sources and sinks, *Nature geoscience*, 6(10), 813-823.
- Kirtman, B., S. Power, A. Adedoyin, G. Boer, R. Bojariu, I. Camilloni, F. Doblas-Reyes, A. Fiore, M. Kimoto, and G. Meehl (2013), Near-term climate change: Projections and predictability, in *Climate Change 2013 the Physical Science Basis: Working Group I Contribution to the Fifth Assessment Report of the Intergovernmental Panel on Climate Change*, edited by T. Stocker, D. Qin, G. Plattner, M. Tignor, S. Allen, J. Boschung, A. Nauels, Y. Xia, B. Bex and B. Midgley, pp. 953-1028, Cambridge University Press.
- Klein, S. A., A. Hall, J. R. Norris, and R. Pincus (2017), Low-cloud feedbacks from cloud-controlling factors: a review, in *Shallow Clouds, Water Vapor, Circulation, and Climate Sensitivity*, edited, pp. 135-157, Springer.
- Knight, J. R., R. J. Allan, C. K. Folland, M. Vellinga, and M. E. Mann (2005), A signature of persistent natural thermohaline circulation cycles in observed climate, *Geophysical Research Letters*, 32(20).
- Knutti, R., and G. C. Hegerl (2008), The equilibrium sensitivity of the Earth's temperature to radiation changes, *Nature Geoscience*, 1(11), 735.
- Kosaka, Y., and S. Xie (2013), Recent global-warming hiatus tied to equatorial Pacific surface cooling, *Nature*, 501(7467), 403-+, doi:10.1038/nature12534.
- Köhler, P., R. Bintanja, H. Fischer, F. Joos, R. Knutti, G. Lohmann, and V. Masson-Delmotte (2010), What caused Earth's temperature variations during the last 800,000 years? Data-based evidence on radiative forcing and constraints on climate sensitivity, *Quaternary Science Reviews*, 29(1-2), 129-145.
- Köhler, P., B. de Boer, A. S. von der Heydt, L. Stap, and R. S. van de Wal (2015), On the state-dependency of the equilibrium climate sensitivity during the last 5 million years, *Climate of the Past*, 11, 1801-1823.
- Lamarque, J., G. Kyle, M. Meinshausen, K. Riahi, S. Smith, D. van Vuuren, A. Conley, and F. Vitt (2011), Global and regional evolution of short-lived radiatively-active gases and aerosols in the Representative Concentration Pathways, *Climatic Change*, 109(1-2), 191-212, doi:10.1007/s10584-011-0155-0.
- Le Quéré, C., R. M. Andrew, P. Friedlingstein, S. Sitch, J. Hauck, J. Pongratz, P. A. Pickers, J. I. Korsbakken, G. P. Peters, and J. G. Canadell (2018), Global carbon budget 2018, *Earth System Science Data*, 10(4), 2141-2194.
- Lean, J. L. (2000), Evolution of the Sun's spectral irradiance since the Maunder Minimum, *Geophysical Research Letters*, 27(16), 2425-2428.
- Lean, J. L., and D. H. Rind (2008), How natural and anthropogenic influences alter global and regional surface temperatures: 1889 to 2006, *Geophysical Research Letters*, 35(18), doi:10.1029/2008GL034864.
- Lean, J. L., and D. H. Rind (2009), How will Earth's surface temperature change in future decades?, *Geophysical Research Letters*, 36(15).

- Levitus, S., J. I. Antonov, T. P. Boyer, O. K. Baranova, H. E. Garcia, R. A. Locarnini, A. V. Mishonov, J. Reagan, D. Seidov, and E. S. Yarosh (2012), World ocean heat content and thermosteric sea level change (0–2000 m), 1955–2010, *Geophysical Research Letters*, 39(10).
- Lewis, N., and J. Curry (2018), The impact of recent forcing and ocean heat uptake data on estimates of climate sensitivity, *Journal of Climate*, 31(15), 6051–6071.
- Li, C., J.-S. von Storch, and J. Marotzke (2013), Deep-ocean heat uptake and equilibrium climate response, *Climate Dynamics*, 40(5-6), 1071–1086.
- Lin, Y. J., Y. T. Hwang, P. Ceppi, and J. M. Gregory (2019), Uncertainty in the evolution of climate feedback traced to the strength of the Atlantic Meridional Overturning Circulation, *Geophysical Research Letters*, 46(21), 12331–12339.
- Lindsey, R. (2017), How El Niño and La Niña affect the winter jet stream and U.S. climate, edited, NOAA, Climate.gov.
- Loulergue, L., F. Parrenin, T. Blunier, J.-M. Barnola, R. Spahni, A. Schilt, G. Raisbeck, and J. Chappellaz (2007), New constraints on the gas age-ice age difference along the EPICA ice cores, 0–50 kyr.
- Lynas, M. (2008), *Six degrees: Our future on a hotter planet*, National Geographic Books.
- MacDougall, A. H., T. L. Frölicher, C. D. Jones, J. Rogelj, H. D. Matthews, K. Zickfeld, V. K. Arora, N. J. Barrett, V. Brovkin, and F. A. Burger (2020), Is there warming in the pipeline? A multi-model analysis of the Zero Emissions Commitment from CO₂, *Biogeosciences*, 17(11), 2987–3016.
- Marcott, S. A., T. K. Bauska, C. Buizert, E. J. Steig, J. L. Rosen, K. M. Cuffey, T. Fudge, J. P. Severinghaus, J. Ahn, and M. L. Kalk (2014), Centennial-scale changes in the global carbon cycle during the last deglaciation, *Nature*, 514(7524), 616–619.
- Marvel, K. (2018), **What Does Recent History Teach Us About Equilibrium Climate Sensitivity?**, in *Goddard Scientific Colloquium*, edited, NASA GSFC.
- Marvel, K., R. Pincus, G. Schmidt, and R. Miller (2018), Internal variability and disequilibrium confound estimates of climate sensitivity from observations, *Geophysical Research Letters*, 45(3), 1595–1601.
- Mascioli, N., T. Canty, and R. Salawitch (2012), An empirical model of global climate—Part 2: Implications for future temperature, *Atmospheric Chemistry and Physics Discussions*, 12(9), 23913–23974.
- Masters, G. (1998), *Introduction to environmental engineering and science*, 2nd ed., Prentice Hall Englewood Cliffs, NJ.
- Masters, T. (2014), Observational estimate of climate sensitivity from changes in the rate of ocean heat uptake and comparison to CMIP5 models, *Climate dynamics*, 42(7-8), 2173–2181.
- Masui, T., K. Matsumoto, Y. Hijioka, T. Kinoshita, T. Nozawa, S. Ishiwatari, E. Kato, P. Shukla, Y. Yamagata, and M. Kainuma (2011), An emission pathway for stabilization at 6 Wm⁻² radiative forcing, *Climatic change*, 109(1-2), 59.
- Matthes, K., B. Funke, M. Anderson, L. Barnard, J. Beer, P. Charbonneau, M. Clilverd, T. Dudok de Wit, M. Haberleiter, and A. Hendry (2017), Solar forcing for CMIP6 (v3. 2), *Geoscientific Model Development*, 10(6), 2247–2302.
- Mauritsen, T., and R. Pincus (2017), Committed warming inferred from observations, *Nature Climate Change*, 7(9), 652–655.

- McBride, L. A., A. P. Hope, T. P. Canty, B. F. Bennett, W. R. Tribett, and R. J. Salawitch (2020), Comparison of CMIP6 Historical Climate Simulations and Future Projected Warming to an Empirical Model of Global Climate, *Earth System Dynamics Discussions*, 1-59, doi:<https://doi.org/10.5194/esd-2020-67>.
- McConnell, J. R., A. J. Aristarain, J. R. Banta, P. R. Edwards, and J. C. Simões (2007), 20th-Century doubling in dust archived in an Antarctic Peninsula ice core parallels climate change and desertification in South America, *Proceedings of the National Academy of Sciences*, *104*(14), 5743-5748.
- Medhaug, I., and T. Furevik (2011), North Atlantic 20th century multidecadal variability in coupled climate models: sea surface temperature and ocean overturning circulation.
- Meehl, G. A., J. M. Arblaster, J. T. Fasullo, A. Hu, and K. E. Trenberth (2011), Model-based evidence of deep-ocean heat uptake during surface-temperature hiatus periods, *Nature Climate Change*, *1*(7), 360-364.
- Meehl, G. A., L. Goddard, G. Boer, R. Burgman, G. Branstator, C. Cassou, S. Corti, G. Danabasoglu, F. Doblas-Reyes, and E. Hawkins (2014a), Decadal climate prediction: an update from the trenches, *Bulletin of the American Meteorological Society*, *95*(2), 243-267.
- Meehl, G. A., H. Teng, and J. M. Arblaster (2014b), Climate model simulations of the observed early-2000s hiatus of global warming, *Nature Climate Change*, *4*(10), 898-902.
- Meinshausen, M., N. Meinshausen, W. Hare, S. C. Raper, K. Frieler, R. Knutti, D. J. Frame, and M. R. Allen (2009), Greenhouse-gas emission targets for limiting global warming to 2 C, *Nature*, *458*(7242), 1158.
- Meinshausen, M., S. Raper, and T. Wigley (2008), Emulating IPCC AR4 atmosphere-ocean and carbon cycle models for projecting global-mean, hemispheric and land/ocean temperatures: MAGICC 6.0.
- Meinshausen, M., et al. (2011), The RCP greenhouse gas concentrations and their extensions from 1765 to 2300, *Climatic Change*, *109*(1-2), 213-241, doi:10.1007/s10584-011-0156-z.
- Millar, R. J., J. S. Fuglestedt, P. Friedlingstein, J. Rogelj, M. J. Grubb, H. D. Matthews, R. B. Skeie, P. M. Forster, D. J. Frame, and M. R. Allen (2017), Emission budgets and pathways consistent with limiting warming to 1.5C, *Nature Geoscience*, *10*(10), 741-747.
- Molnár, A. (2018), Leaking away the future: The role of methane emission and natural gas supply chains in global warming, *Energy Policy Studies*.
- Montzka, S., S. Reimann, A. Engel, K. Kruger, W. Sturges, D. Blake, M. Dorf, P. Fraser, L. Froidevaux, and K. Jucks (2011), Scientific assessment of ozone depletion: 2010, *Global Ozone Research and Monitoring Project-Report No. 51*.
- Morgan, M. G., P. J. Adams, and D. W. Keith (2006), Elicitation of expert judgments of aerosol forcing, *Climatic Change*, *75*(1-2), 195-214.
- Myhre, G. (2009), Consistency between satellite-derived and modeled estimates of the direct aerosol effect, *Science*, *325*(5937), 187-190.
- Myhre, G., E. Highwood, K. Shine, and F. Stordal (1998), New estimates of radiative forcing due to well mixed greenhouse gases, *Geophysical research letters*, *25*(14), 2715-2718.

- Myhre, G., J. Nilsen, L. Gulstad, K. Shine, B. Rognerud, and I. Isaksen (2007), Radiative forcing due to stratospheric water vapour from CH₄ oxidation, *Geophysical research letters*, 34(1).
- Myhre, G., D. Shindell, F. Bréon, W. Collins, J. Fuglestedt, J. Huang, D. Koch, J. Lamarque, D. Lee, and B. Mendoza (2013), Anthropogenic and Natural Radiative Forcing, in *Climate Change 2013 the Physical Science Basis: Working Group I Contribution to the Fifth Assessment Report of the Intergovernmental Panel on Climate Change*, edited by T. Stocker, D. Qin, G. Plattner, M. Tignor, S. Allen, J. Boschung, A. Nauels, Y. Xia, B. Bex and B. Midgley, pp. 659-740, Cambridge University Press.
- Nakicenovic, N., J. Alcamo, A. Grubler, K. Riahi, R. Roehrl, H.-H. Rogner, and N. Victor (2000), *Special report on emissions scenarios (SRES), a special report of Working Group III of the intergovernmental panel on climate change*, Cambridge University Press.
- Newman, M., G. P. Compo, and M. A. Alexander (2003), ENSO-forced variability of the Pacific decadal oscillation, *Journal of Climate*, 16(23), 3853-3857.
- Nie, J., P. Wang, W. Yang, and B. Tan (2008), Northern hemisphere storm tracks in strong AO anomaly winters, *Atmospheric Science Letters*, 9(3), 153-159.
- Nijse, F. J., P. M. Cox, and M. S. Williamson (2020), Emergent constraints on transient climate response (TCR) and equilibrium climate sensitivity (ECS) from historical warming in CMIP5 and CMIP6 models, *Earth System Dynamics*, 11(3), 737-750.
- Nisbet, E., M. Manning, E. Dlugokencky, R. Fisher, D. Lowry, S. Michel, C. L. Myhre, S. M. Platt, G. Allen, and P. Bousquet (2019), Very strong atmospheric methane growth in the 4 years 2014–2017: Implications for the Paris Agreement, *Global Biogeochemical Cycles*, 33(3), 318-342.
- Norris, J. R., R. J. Allen, A. T. Evan, M. D. Zelinka, C. W. O'Dell, and S. A. Klein (2016), Evidence for climate change in the satellite cloud record, *Nature*, 536(7614), 72-75.
- O'Neill, B. C., C. Tebaldi, D. P. Van Vuuren, V. Eyring, P. Friedlingstein, G. Hurtt, R. Knutti, E. Kriegler, J.-F. Lamarque, and J. Lowe (2016), The scenario model intercomparison project (ScenarioMIP) for CMIP6.
- Otto, A., et al. (2013), Energy budget constraints on climate response, *Nature Geoscience*, 6(6), 415-416.
- O'Neill, B. C., E. Kriegler, K. L. Ebi, E. Kemp-Benedict, K. Riahi, D. S. Rothman, B. J. van Ruijven, D. P. van Vuuren, J. Birkmann, and K. Kok (2017), The roads ahead: Narratives for shared socioeconomic pathways describing world futures in the 21st century, *Global Environmental Change*, 42, 169-180.
- O'Neill, B. C., E. Kriegler, K. Riahi, K. L. Ebi, S. Hallegatte, T. R. Carter, R. Mathur, and D. P. van Vuuren (2014), A new scenario framework for climate change research: the concept of shared socioeconomic pathways, *Climatic change*, 122(3), 387-400.
- Parrenin, F., V. Masson-Delmotte, P. Köhler, D. Raynaud, D. Paillard, J. Schwander, C. Barbante, A. Landais, A. Wegner, and J. Jouzel (2013), Synchronous change of atmospheric CO₂ and Antarctic temperature during the last deglacial warming, *Science*, 339(6123), 1060-1063.
- Pausata, F. S., L. Chafik, R. Caballero, and D. S. Battisti (2015), Impacts of high-latitude volcanic eruptions on ENSO and AMOC, *Proceedings of the National Academy of Sciences*, 112(45), 13784-13788.

- Pechony, O., and D. T. Shindell (2010), Driving forces of global wildfires over the past millennium and the forthcoming century, *Proceedings of the National Academy of Sciences*, 107(45), 19167-19170.
- Peng, J., Z. Li, H. Zhang, J. Liu, and M. Cribb (2016), Systematic changes in cloud radiative forcing with aerosol loading for deep clouds in the tropics, *Journal of the Atmospheric Sciences*, 73(1), 231-249.
- Penman, D. E., B. Hönisch, R. E. Zeebe, E. Thomas, and J. C. Zachos (2014), Rapid and sustained surface ocean acidification during the Paleocene-Eocene Thermal Maximum, *Paleoceanography*, 29(5), 357-369.
- Pincus, R., P. M. Forster, and B. Stevens (2016), The radiative forcing model intercomparison project (RFMIP): Experimental protocol for CMIP6, *Geoscientific Model Development (Online)*, 9(9).
- Prather, M. J., C. D. Holmes, and J. Hsu (2012), Reactive greenhouse gas scenarios: Systematic exploration of uncertainties and the role of atmospheric chemistry, *Geophysical Research Letters*, 39(9).
- Raftery, A. E., A. Zimmer, D. M. Frierson, R. Startz, and P. Liu (2017), Less than 2 °C warming by 2100 unlikely, *Nature Climate Change*, 7(9), 637-641.
- Rahmstorf, S., J. Box, G. Feulner, M. Mann, A. Robinson, S. Rutherford, and E. Schaffernicht (2015), Exceptional twentieth-century slowdown in Atlantic Ocean overturning circulation, *Nature Climate Change*, 5(5), 475-480, doi:10.1038/NCLIMATE2554.
- Ramanathan, V. (1975), Greenhouse effect due to chlorofluorocarbons: Climatic implications, *Science*, 50-52.
- Randall, D. (2012), *Atmosphere, clouds, and climate*, Princeton University Press.
- Raper, S., J. Gregory, and R. Stouffer (2002), The role of climate sensitivity and ocean heat uptake on AOGCM transient temperature response, *Journal of Climate*, 15(1), 124-130, doi:10.1175/1520-0442(2002)015<0124:TROCSA>2.0.CO;2.
- Rasmusson, E. M., and J. M. Wallace (1983), Meteorological aspects of the El Niño/southern oscillation, *Science*, 222(4629), 1195-1202.
- Riahi, K., A. Grübler, and N. Nakicenovic (2007), Scenarios of long-term socio-economic and environmental development under climate stabilization, *Technological Forecasting and Social Change*, 74(7), 887-935.
- Riahi, K., S. Rao, V. Krey, C. Cho, V. Chirkov, G. Fischer, G. Kindermann, N. Nakicenovic, and P. Rafaj (2011), RCP 8.5—A scenario of comparatively high greenhouse gas emissions, *Climatic change*, 109(1-2), 33.
- Richter-Menge, J., M. Druckenmiller, and M. Jeffries (2019), Arctic Report Card Rep.
- Rieger, L., A. Bourassa, and D. Degenstein (2015), Merging the OSIRIS and SAGE II stratospheric aerosol records, *Journal of Geophysical Research: Atmospheres*, 120(17), 8890-8904.
- Rind, D. (2009), Do Variations in the Solar Cycle Affect Our Climate System?, in *Science Briefs*, edited, NASA GISS.
- Riser, S. C., H. J. Freeland, D. Roemmich, S. Wijffels, A. Troisi, M. Belbéoch, D. Gilbert, J. Xu, S. Pouliquen, and A. Thresher (2016), Fifteen years of ocean observations with the global Argo array, *Nature Climate Change*, 6(2), 145-153.

- Rizzo, A. L., H. J. Jost, A. Caracausi, A. Paonita, M. Liotta, and M. Martelli (2014), Real-time measurements of the concentration and isotope composition of atmospheric and volcanic CO₂ at Mount Etna (Italy), *Geophysical Research Letters*, *41*(7), 2382-2389.
- Robock, A. (2000), Volcanic eruptions and climate, *Reviews of geophysics*, *38*(2), 191-219.
- Rogelj, J., M. Den Elzen, N. Höhne, T. Fransen, H. Fekete, H. Winkler, R. Schaeffer, F. Sha, K. Riahi, and M. Meinshausen (2016), Paris Agreement climate proposals need a boost to keep warming well below 2 C, *Nature*, *534*(7609), 631-639.
- Rogelj, J., D. Shindell, K. Jiang, S. Fifita, P. Forester, V. Ginzburg, C. Handa, H. Kheshgi, S. Kobayashi, and E. Kriegler (2018), Mitigation pathways compatible with 1.5° C in the context of sustainable development. IPCC Special Report on global warming of 1.5° C.
- Rohde, R., R. Muller, R. Jacobsen, S. Perlmutter, A. Rosenfeld, J. Wurtele, J. Curry, C. Wickhams, and S. Mosher (2013), Berkeley Earth Temperature Averaging Process. Geoinfor Geostat: An Overview 1: 2, of, *13*, 20-100.
- Rohling, E., M. Medina-Elizalde, J. Shepherd, M. Siddall, and J. Stanford (2012), Sea surface and high-latitude temperature sensitivity to radiative forcing of climate over several glacial cycles, *Journal of Climate*, *25*(5), 1635-1656.
- Rose, B., K. Armour, D. Battisti, N. Feldl, and D. Koll (2014), The dependence of transient climate sensitivity and radiative feedbacks on the spatial pattern of ocean heat uptake, *Geophysical Research Letters*, *41*(3), 1071-1078, doi:10.1002/2013GL058955.
- Running, S. W. (2006), Is global warming causing more, larger wildfires?, *Science*.
- Rypdal, K. (2015), Attribution in the presence of a long-memory climate response.
- Saji, N., B. Goswami, P. Vinayachandran, and T. Yamagata (1999), A dipole mode in the tropical Indian Ocean, *Nature*, *401*(6751), 360-363, doi:10.1038/43855.
- Salawitch, R. J., B. F. Bennett, A. P. Hope, W. R. Tribett, and T. P. Canty (2017), Earth's Climate System, in *Paris Climate Agreement: Beacon of Hope*, edited, pp. 1-50, Springer, Cham.
- Santer, B., C. Bonfils, J. Painter, M. Zelinka, C. Mears, S. Solomon, G. Schmidt, J. Fyfe, J. Cole, and L. Nazarenko (2014), Volcanic contribution to decadal changes in tropospheric temperature, *Nature Geoscience*, *7*(3), 185-189.
- Santer, B., et al. (2013a), Human and natural influences on the changing thermal structure of the atmosphere, *Proceedings of the National Academy of Sciences of the United States of America*, *110*(43), 17235-17240, doi:10.1073/pnas.1305332110.
- Santer, B., et al. (2013b), Identifying human influences on atmospheric temperature, *Proceedings of the National Academy of Sciences of the United States of America*, *110*(1), 26-33, doi:10.1073/pnas.1210514109.
- Saravanan, R., and J. C. McWilliams (1998), Advective ocean-atmosphere interaction: An analytical stochastic model with implications for decadal variability, *Journal of Climate*, *11*(2), 165-188.
- SATO, M., J. HANSEN, M. MCCORMICK, and J. POLLACK (1993), STRATOSPHERIC AEROSOL OPTICAL DEPTHS, 1850-1990, *Journal of Geophysical Research-Atmospheres*, *98*(D12), 22987-22994, doi:10.1029/93JD02553.
- Saunio, M., R. Jackson, P. Bousquet, B. Poulter, and J. Canadell (2016), The growing role of methane in anthropogenic climate change, *Environmental Research Letters*, *11*(12), 120207.

- Saunoy, M., A. Stavert, B. Poulter, P. Bousquet, J. Canadell, R. Jackson, P. Raymond, E. Dlugokencky, S. Houweling, and P. Patra (2020), The global methane budget 2000–2017, *Earth system science data*, 12(3), 1561-1623.
- Schlesinger, M. E., and N. Ramankutty (1994), An oscillation in the global climate system of period 65–70 years, *Nature*, 367(6465), 723.
- Schmidt, G., D. Shindell, and K. Tsigaridis (2014), Reconciling warming trends, *Nature Geoscience*, 7(3), 158-160, doi:10.1038/ngeo2105.
- Schmittner, A., N. M. Urban, J. D. Shakun, N. M. Mahowald, P. U. Clark, P. J. Bartlein, A. C. Mix, and A. Rosell-Melé (2011), Climate sensitivity estimated from temperature reconstructions of the Last Glacial Maximum, *Science*, 334(6061), 1385-1388.
- Schwartz, S. E. (2012), Determination of Earth's Transient and Equilibrium Climate Sensitivities from Observations Over the Twentieth Century: Strong Dependence on Assumed Forcing, *Surveys in Geophysics*, 33(3-4), 745-777, doi:10.1007/s10712-012-9180-4.
- Schwartz, S. E., R. J. Charlson, R. Kahn, and H. Rodhe (2014), Earth's climate sensitivity: apparent inconsistencies in recent assessments, *Earth's Future*, 2(12), 601-605.
- Shakun, J. D., P. U. Clark, F. He, S. A. Marcott, A. C. Mix, Z. Liu, B. Otto-Bliesner, A. Schmittner, and E. Bard (2012), Global warming preceded by increasing carbon dioxide concentrations during the last deglaciation, *Nature*, 484(7392), 49-54.
- Shen, Z., Y. Ming, and I. M. Held (2020), Using the fast impact of anthropogenic aerosols on regional land temperature to constrain aerosol forcing, *Science Advances*, 6(32), eabb5297, doi:10.1126/sciadv.abb5297.
- Sherwood, S., et al. (2020), An assessment of Earth's climate sensitivity using multiple lines of evidence, *Reviews of Geophysics*, n/a(n/a), e2019RG000678, doi:10.1029/2019rg000678.
- Shindell, D. (2014), Inhomogeneous forcing and transient climate sensitivity, *Nature Climate Change*, 4(4), 274-277.
- Shindell, D., J. Kuylenstierna, E. Vignati, R. van Dingenen, M. Amann, Z. Klimont, S. Anenberg, N. Müller, G. Janssens-Maenhout, and F. Raes (2012), Simultaneously mitigating near-term climate change and improving human health and food security, *science*, 335(6065), 183-189.
- Shindell, D., et al. (2013), Radiative forcing in the ACCMIP historical and future climate simulations, *Atmospheric Chemistry and Physics*, 13(6), 2939-2974, doi:10.5194/acp-13-2939-2013.
- Silver, N. (2012), *The signal and the noise: why so many predictions fail--but some don't*, Penguin.
- Smeed, D., D. Rayner, G. McCarthy, B. Moat, W. E. Johns, M. O. Baringer, C. S. Meinen, and J. Collins (2017), RAPID-MOC time series April 2004 to February 2017.
- Smith, C. J., P. M. Forster, M. Allen, N. Leach, R. J. Millar, G. A. Passerello, and L. A. Regayre (2018), FAIR v1. 3: A simple emissions-based impulse response and carbon cycle model, *Geoscientific Model Development*, 11(6), 2273-2297.
- Smith, S., J. v. Aardenne, Z. Klimont, R. Andres, A. Volke, and S. Delgado Arias (2011), Anthropogenic sulfur dioxide emissions: 1850–2005, *Atmospheric Chemistry and Physics*, 11(3), 1101-1116.
- Smith, S., and T. Bond (2014), Two hundred fifty years of aerosols and climate: the end of the age of aerosols, *Atmospheric Chemistry and Physics*, 14(2), 537-549, doi:10.5194/acp-14-537-2014.

- Smith, S. J., and T. Wigley (2006), Multi-gas forcing stabilization with Minicam, *The Energy Journal*(Special Issue# 3).
- Smith, T., R. Reynolds, T. Peterson, and J. Lawrimore (2008), Improvements to NOAA's historical merged land-ocean surface temperature analysis (1880-2006), *Journal of Climate*, 21(10), 2283-2296, doi:10.1175/2007JCLI2100.1.
- Solomon, S. (2007), *Climate change 2007-the physical science basis: Working group I contribution to the fourth assessment report of the IPCC*, Cambridge University Press.
- Solomon, S., J. Daniel, R. R. Neely, J.-P. Vernier, E. Dutton, and L. Thomason (2011), The persistently variable “background” stratospheric aerosol layer and global climate change, *Science*, 333(6044), 866-870.
- Solomon, S., D. Ivy, D. Kinnison, M. Mills, R. Neely, and A. Schmidt (2016), Emergence of healing in the Antarctic ozone layer, *Science*, 353(6296), 269-274.
- Solomon, S., K. Rosenlof, R. Portmann, J. Daniel, S. Davis, T. Sanford, and G. Plattner (2010), Contributions of Stratospheric Water Vapor to Decadal Changes in the Rate of Global Warming, *Science*, 327(5970), 1219-1223, doi:10.1126/science.1182488.
- Srokosz, M., and H. Bryden (2015), Observing the Atlantic Meridional Overturning Circulation yields a decade of inevitable surprises, *Science*, 348(6241), 1255-1257.
- Steffen, W., W. Broadgate, L. Deutsch, O. Gaffney, and C. Ludwig (2015), The trajectory of the Anthropocene: the great acceleration, *The Anthropocene Review*, 2(1), 81-98.
- Steinman, B. A., M. E. Mann, and S. K. Miller (2015), Atlantic and Pacific multidecadal oscillations and Northern Hemisphere temperatures, *Science*, 347(6225), 988-991.
- Stern, D. I. (2006a), An atmosphere–ocean time series model of global climate change, *Computational statistics & data analysis*, 51(2), 1330-1346.
- Stern, D. I. (2006b), Reversal of the trend in global anthropogenic sulfur emissions, *Global Environmental Change*, 16(2), 207-220.
- Stern, D. I., and R. K. Kaufmann (2014), Anthropogenic and natural causes of climate change, *Climatic change*, 122(1-2), 257-269.
- Stips, A., D. Macias, C. Coughlan, E. Garcia-Gorriz, and X. San Liang (2016), On the causal structure between CO₂ and global temperature, *Scientific reports*, 6, 21691.
- Stocker, T., D. Qin, G. Plattner, M. Tignor, S. Allen, J. Boschung, A. Nauels, Y. Xia, B. Bex, and B. Midgley (2013), IPCC, 2013: climate change 2013: the physical science basis. Contribution of working group I to the fifth assessment report of the intergovernmental panel on climate change *Rep.*, 1535 pp. pp, Cambridge, United Kingdom and New York, NY, USA.
- Storelvmo, T., U. Lohmann, and R. Bennartz (2009), What governs the spread in shortwave forcings in the transient IPCC AR4 models?, *Geophysical Research Letters*, 36(1).
- Stott, P., P. Good, G. Jones, N. Gillett, and E. Hawkins (2013), The upper end of climate model temperature projections is inconsistent with past warming, *Environmental Research Letters*, 8(1), 014024.
- Stouffer, R. J., J. Yin, J. Gregory, K. Dixon, M. Spelman, W. Hurlin, A. Weaver, M. Eby, G. Flato, and H. Hasumi (2006), Investigating the causes of the response of the thermohaline circulation to past and future climate changes, *Journal of Climate*, 19(8), 1365-1387.

- Struthers, H., A. Ekman, P. Glantz, T. Iversen, A. Kirkevåg, E. M. Mårtensson, Ø. Seland, and E. Nilsson (2011), The effect of sea ice loss on sea salt aerosol concentrations and the radiative balance in the Arctic, *Atmospheric Chemistry and Physics*, 11(7), 3459.
- Suckling, E. B., G. J. van Oldenborgh, J. M. Eden, and E. Hawkins (2017), An empirical model for probabilistic decadal prediction: global attribution and regional hindcasts, *Climate Dynamics*, 48(9-10), 3115-3138.
- Tans, P. P., I. Y. Fung, and T. Takahashi (1990), Observational constraints on the global atmospheric CO₂ budget, *Science*, 247(4949), 1431-1438.
- Taylor, J. (1997), *Introduction to error analysis, the study of uncertainties in physical measurements*.
- Taylor, K., R. Stouffer, and G. Meehl (2012), AN OVERVIEW OF CMIP5 AND THE EXPERIMENT DESIGN, *Bulletin of the American Meteorological Society*, 93(4), 485-498, doi:10.1175/BAMS-D-11-00094.1.
- Thomason, L., N. Ernest, L. Millán, L. Rieger, A. Bourassa, J.-P. Vernier, G. Manney, B. Luo, F. Arfeuille, and T. Peter (2018), A global space-based stratospheric aerosol climatology: 1979-2016, *Earth System Science Data*, 10(1), 469-492.
- Thomason, L., J.-P. Vernier, A. Bourassa, L. Millan, and G. Manney (2016), A global, space-based stratospheric aerosol climatology: 1979 to 2014, paper presented at AGU Fall Meeting Abstracts.
- Thompson, D. W., J. M. Wallace, P. D. Jones, and J. J. Kennedy (2009), Identifying signatures of natural climate variability in time series of global-mean surface temperature: Methodology and insights, *Journal of Climate*, 22(22), 6120-6141.
- Thomson, A. M., K. V. Calvin, S. J. Smith, G. P. Kyle, A. Volke, P. Patel, S. Delgado-Arias, B. Bond-Lamberty, M. A. Wise, and L. E. Clarke (2011), RCP4. 5: a pathway for stabilization of radiative forcing by 2100, *Climatic change*, 109(1-2), 77-94.
- Thornhill, G., et al. (2020), Climate-driven chemistry and aerosol feedbacks in CMIP6 Earth system models, *Atmospheric Chemistry and Physics Discussion (in review)*, doi:<https://doi.org/10.5194/acp-2019-1207>.
- Tian, P., L. Zhang, J. Ma, K. Tang, L. Xu, Y. Wang, X. Cao, J. Liang, Y. Ji, and J. H. Jiang (2018), Radiative absorption enhancement of dust mixed with anthropogenic pollution over East Asia, *Atmospheric Chemistry and Physics*, 18(11), 7815-7825.
- Toggweiler, J., and D. W. Lea (2010), Temperature differences between the hemispheres and ice age climate variability, *Paleoceanography*, 25(2).
- Tokarska, K. B., and N. P. Gillett (2018), Cumulative carbon emissions budgets consistent with 1.5 C global warming, *Nature Climate Change*, 8(4), 296.
- Tokarska, K. B., C.-F. Schleussner, J. Rogelj, M. B. Stolpe, H. D. Matthews, P. Pfliegerer, and N. P. Gillett (2019), Recommended temperature metrics for carbon budget estimates, model evaluation and climate policy, *Nature Geoscience*, 12(12), 964-971.
- Tokarska, K. B., M. B. Stolpe, S. Sippel, E. M. Fischer, C. J. Smith, F. Lehner, and R. Knutti (2020), Past warming trend constrains future warming in CMIP6 models, *Science advances*, 6(12), eaaz9549.
- Trenberth, K. (1997), The definition of el nino, *Bulletin of the American Meteorological Society*, 78(12), 2771-2777.

- Trenberth, K., and J. Fasullo (2013), An apparent hiatus in global warming?, *Earth's Future*, 1(1), 19-32.
- Trenberth, K., J. Fasullo, and J. Kiehl (2009), Earth's global energy budget, *Bulletin of the American Meteorological Society*, 90(3), 311-324.
- Tribett, W. R., R. J. Salawitch, A. P. Hope, T. P. Canty, and B. F. Bennett (2017), Paris INDCs, *Paris Climate Agreement: Beacon of Hope*, 115-146.
- Tung, K., and J. Zhou (2013), Using data to attribute episodes of warming and cooling in instrumental records, *Proceedings of the National Academy of Sciences of the United States of America*, 110(6), 2058-2063, doi:10.1073/pnas.1212471110.
- Twomey, S. (1974), Pollution and the planetary albedo, *Atmospheric Environment (1967)*, 8(12), 1251-1256.
- Ummenhofer, C. C., M. H. England, P. C. McIntosh, G. A. Meyers, M. J. Pook, J. S. Risbey, A. S. Gupta, and A. S. Taschetto (2009), What causes southeast Australia's worst droughts?, *Geophysical Research Letters*, 36(4).
- UNFCCC (2015), Paris Agreement, edited, http://unfccc.int/files/essential_background/convention/application/pdf/english_paris_agreement.pdf.
- Van Nes, E. H., M. Scheffer, V. Brovkin, T. M. Lenton, H. Ye, E. Deyle, and G. Sugihara (2015), Causal feedbacks in climate change, *Nature Climate Change*, 5(5), 445-448.
- Van Vuuren, D. P., J. Edmonds, M. Kainuma, K. Riahi, A. Thomson, K. Hibbard, G. C. Hurtt, T. Kram, V. Krey, and J.-F. Lamarque (2011a), The representative concentration pathways: an overview, *Climatic change*, 109(1-2), 5.
- Van Vuuren, D. P., E. Stehfest, M. G. den Elzen, T. Kram, J. van Vliet, S. Deetman, M. Isaac, K. K. Goldewijk, A. Hof, and A. M. Beltran (2011b), RCP2.6: exploring the possibility to keep global mean temperature increase below 2 C, *Climatic change*, 109(1-2), 95.
- Vaughan, M. A., S. A. Young, D. M. Winker, K. A. Powell, A. H. Omar, Z. Liu, Y. Hu, and C. A. Hostetler (2004), Fully automated analysis of space-based lidar data: An overview of the CALIPSO retrieval algorithms and data products, paper presented at Laser radar techniques for atmospheric sensing, International Society for Optics and Photonics.
- Verdon, D. C., and S. W. Franks (2006), Long-term behaviour of ENSO: Interactions with the PDO over the past 400 years inferred from paleoclimate records, *Geophysical Research Letters*, 33(6).
- Vial, J., J. Dufresne, and S. Bony (2013), On the interpretation of inter-model spread in CMIP5 climate sensitivity estimates, *Climate Dynamics*, 41(11-12), 3339-3362, doi:10.1007/s00382-013-1725-9.
- Vincze, M., and I. Jánosi (2011), Is the Atlantic Multidecadal Oscillation (AMO) a statistical phantom?, *Nonlinear Processes in Geophysics*, 18(4), 469-475.
- Voigt, C., R. E. Lamprecht, M. E. Marushchak, S. E. Lind, A. Novakovskiy, M. Aurela, P. J. Martikainen, and C. Biasi (2017), Warming of subarctic tundra increases emissions of all three important greenhouse gases—carbon dioxide, methane, and nitrous oxide, *Global Change Biology*, 23(8), 3121-3138.

- Volodin, E., N. Dianskii, and A. Gusev (2010), Simulating present-day climate with the INMCM4. 0 coupled model of the atmospheric and oceanic general circulations, *Izvestiya, Atmospheric and Oceanic Physics*, 46(4), 414-431.
- Voosen, P. (2019), New climate models forecast a warming surge, *Science (New York, NY)*, 364(6437), 222-223.
- Walker, X. J., J. L. Baltzer, S. G. Cumming, N. J. Day, C. Ebert, S. Goetz, J. F. Johnstone, S. Potter, B. M. Rogers, and E. A. Schuur (2019), Increasing wildfires threaten historic carbon sink of boreal forest soils, *Nature*, 572(7770), 520-523.
- Wang, Y., J. L. Lean, and N. Sheeley Jr (2005), Modeling the Sun's magnetic field and irradiance since 1713, *The Astrophysical Journal*, 625(1), 522.
- Weaver, C., J. Herman, G. Labow, D. Larko, and L.-K. Huang (2015), Shortwave TOA cloud radiative forcing derived from a long-term (1980–present) record of satellite UV reflectivity and CERES measurements, *Journal of Climate*, 28(23), 9473-9488.
- Weaver, C. J., D. L. Wu, P. K. Bhartia, G. J. Labow, and D. P. Haffner (2020), A Long-Term Cloud Albedo Data Record Since 1980 from UV Satellite Sensors, *Remote Sensing*, 12(12), 1982.
- Webb, M. J., T. Andrews, A. Bodas-Salcedo, S. Bony, C. S. Bretherton, R. Chadwick, H. Chepfer, H. Douville, P. Good, and J. E. Kay (2017), The cloud feedback model intercomparison project (CFMIP) contribution to CMIP6, *Geoscientific Model Development*, 2017, 359-384.
- Whiticar, M. J. (1996), Stable isotope geochemistry of coals, humic kerogens and related natural gases, *International Journal of Coal Geology*, 32(1-4), 191-215.
- Wilcox, L. J., E. J. Highwood, and N. J. Dunstone (2013), The influence of anthropogenic aerosol on multi-decadal variations of historical global climate, *Environmental Research Letters*, 8(2), 024033.
- Willis, J. K. (2010), Can in situ floats and satellite altimeters detect long-term changes in Atlantic Ocean overturning?, *Geophysical research letters*, 37(6).
- Wise, M., K. Calvin, A. Thomson, L. Clarke, B. Bond-Lamberty, R. Sands, S. J. Smith, A. Janetos, and J. Edmonds (2009), Implications of limiting CO2 concentrations for land use and energy, *Science*, 324(5931), 1183-1186.
- Wolff, E., et al. (2020), *Climate Change: Evidence and Causes Rep.*, The Royal Society
The National Academy of Sciences.
- Wolter, K., and M. S. Timlin (1993), Monitoring ENSO in COADS with a Seasonally Adjusted Principal, paper presented at Proc. of the 17th Climate Diagnostics Workshop, Norman, OK, NOAA/NMC/CAC, NSSL, Oklahoma Clim. Survey, CIMMS and the School of Meteor., Univ. of Oklahoma, 52.
- Wolter, K., and M. S. Timlin (2011), El Niño/Southern Oscillation behaviour since 1871 as diagnosed in an extended multivariate ENSO index (MEI. ext), *International Journal of Climatology*, 31(7), 1074-1087.
- Wu, L., and Z. Liu (2003), Decadal variability in the North Pacific: the eastern North Pacific mode, *Journal of Climate*, 16(19), 3111-3131.

- Xia, X., H. Che, J. Zhu, H. Chen, Z. Cong, X. Deng, X. Fan, Y. Fu, P. Goloub, and H. Jiang (2016), Ground-based remote sensing of aerosol climatology in China: Aerosol optical properties, direct radiative effect and its parameterization, *Atmospheric environment*, 124, 243-251.
- Yukimoto, S., Y. Adachi, M. Hosaka, T. Sakami, H. Yoshimura, M. Hirabara, T. Y. Tanaka, E. Shindo, H. Tsujino, and M. Deushi (2012), A new global climate model of the Meteorological Research Institute: MRI-CGCM3—Model description and basic performance—, *Journal of the Meteorological Society of Japan. Ser. II*, 90, 23-64.
- Yulaeva, E., and J. M. Wallace (1994), The signature of ENSO in global temperature and precipitation fields derived from the microwave sounding unit, *Journal of climate*, 7(11), 1719-1736.
- Zanchettin, D., M. Khodri, C. Timmreck, M. Toohey, A. Schmidt, E. Gerber, G. Hegerl, A. Robock, F. Pausata, and W. Ball (2016), The Model Intercomparison Project on the climatic response to Volcanic forcing (VolMIP): experimental design and forcing input data for CMIP6, *Geoscientific Model Development*, 9(8), 2701-2719.
- Zeebe, R. E. (2012), History of seawater carbonate chemistry, atmospheric CO₂, and ocean acidification, *Annual Review of Earth and Planetary Sciences*, 40(141), 2012.
- Zelinka, M. D., S. Klein, K. Taylor, T. Andrews, M. Webb, J. Gregory, and P. Forster (2013), Contributions of Different Cloud Types to Feedbacks and Rapid Adjustments in CMIP5, *Journal of Climate*, 26(14), 5007-5027, doi:10.1175/JCLI-D-12-00555.1.
- Zelinka, M. D., T. A. Myers, D. T. McCoy, S. Po-Chedley, P. M. Caldwell, P. Ceppi, S. A. Klein, and K. E. Taylor (2020), Causes of higher climate sensitivity in CMIP6 models, *Geophysical Research Letters*, 47(1), e2019GL085782.
- Zelinka, M. D., C. Zhou, and S. A. Klein (2016), Insights from a refined decomposition of cloud feedbacks, *Geophysical Research Letters*, 43(17), 9259-9269.
- Zeng, N., F. Zhao, G. J. Collatz, E. Kalnay, R. J. Salawitch, T. O. West, and L. Guanter (2014), Agricultural Green Revolution as a driver of increasing atmospheric CO₂ seasonal amplitude, *Nature*, 515(7527), 394-397.
- Zeng, X., and K. Geil (2016), Global warming projection in the 21st century based on an observational data-driven model, *Geophysical Research Letters*, 43(20).
- Zhang, H., J. Lawrimore, B. Huang, M. Menne, X. Yin, A. Sánchez-Lugo, B. Gleason, R. Vose, D. Arndt, and J. Rennie (2019), Updated temperature data give a sharper view of climate trends, *Eos*, 100.
- Zhang, R., T. L. Delworth, and I. M. Held (2007), Can the Atlantic Ocean drive the observed multidecadal variability in Northern Hemisphere mean temperature?, *Geophysical Research Letters*, 34(2).
- Zhang, Y., J. M. Wallace, and D. S. Battisti (1997), ENSO-like interdecadal variability: 1900-93, *Journal of climate*, 10(5), 1004-1020.
- Zharkova, V. V., S. J. Shepherd, E. Popova, and S. I. Zharkov (2015), Heartbeat of the Sun from Principal Component Analysis and prediction of solar activity on a millenium timescale, *Scientific reports*, 5, 15689.
- Zhou, C., M. D. Zelinka, A. E. Dessler, and S. A. Klein (2015), The relationship between interannual and long-term cloud feedbacks, *Geophysical Research Letters*, 42(23).

- Zhou, J., and K. Tung (2013a), Deducing Multidecadal Anthropogenic Global Warming Trends Using Multiple Regression Analysis, *Journal of the Atmospheric Sciences*, 70(1), 3-8, doi:10.1175/JAS-D-12-0208.1.
- Zhou, J., and K. Tung (2013b), Observed tropospheric temperature response to 11-yr solar cycle and what it reveals about mechanisms, *Journal of the atmospheric sciences*, 70(1), 9-14.
- Zhu, J., C. J. Poulsen, and B. L. Otto-Bliesner (2020), High climate sensitivity in CMIP6 model not supported by paleoclimate, *Nature Climate Change*, 10(5), 378-379.